THÈSE EN COTUTELLE PRÉSENTÉE

POUR OBTENIR LE GRADE DE

DOCTEUR DE L'UNIVERSITÉ DE BORDEAUX
ET DE L'INSTITUT NATIONAL DE RECHERCHE SCIENTIQUE
(INRS, CANADA)

ÉCOLES DOCTORALES DES SCIENCES PHYSIQUES ET DE L'INGÉNIEUR DE L'UNIVERSITE DE BORDEAUX ET DES SCIENCES DE L'ÉNERGIE ET DES MATÉRIAUX DE L'INRS

SPÉCIALITÉ : ASTROPHYSIQUE DE LABORATOIRE, ASTROPHYSIQUE, PLASMAS, NUCLÉAIRE

Par Tessa WALTENSPIEL

Investigating in the laboratory particle-magnetized plasma energy exchange processes relevant for astrophysics

Sous la direction de :
Co-directeur : Emmanuel D'HUMIÈRES (Université de Bordeaux)
Co-directeur : Patrizio ANTICI (INRS)
Co-encadrant : Julien Fuchs (École Polytechnique)

Soutenue le 23 juillet 2026 à l'École Polytechnique

Membres du jury :

Alexandre Marcowith, Directeur de recherche	Université de Montpellier	Rapporteur
Claire Michaut, Directrice de recherche	Observatoire de la Côte d'Azur	Rapportrice, Présidente du jury
Bruno Albertazzi, Chargé de recherche	École Polytechnique	Examinateur
François Vidal, Professeur	Institut National de la Recherche Scientifique	Examinateur
Emmanuel d'Humières, Professeur	Université de Bordeaux	Directeur de thèse
Patrizio Antici, Professeur	Institut National de la Recherche Scientifique	Co-directeur de thèse
Julien Fuchs, Directeur de recherche	École Polytechnique	Co-encadrant (invité)

À mes parents, Sabine et Franck

À Gloria et Ruben

Role of the author and acknowledgements

This thesis has been conducted and carried out thanks to the collaboration of three different institutions: CELIA (Centre d'Études des Lasers Intenses et Application) at Université de Bordeaux (France), INRS (Institut National pour la Recherche Scientifique), university of research based in Québec (Canada) and LULI (Laboratoire pour l'Utilisation des Lasers Intenses) at École Polytechnique (France). All the three laboratories and research centers contributed to the finalization of this work. In CELIA, the IFCIA group (Interactions, Fusion, Confinement Inertiel, Astrophysique) has been a core of support and learning for the theoretical part of this work, more particularly for simulations with FLASH and SMILEI. INRS was a hub of shared information and experiments. In LULI, where I was based most of my time during my Phd, I joined the SPRINT group (Sources de Particules et Rayonnement INTenses) and performed experimental campaigns, from planning meetings to analysing the collected data.

Within these groups, my own work consisted in taking part in the realization of the experiments analysed in this manuscript. I worked with my teams to build up the setup and install the diagnostics that will be detailed in here. I participated to the campaigns and performed the needed adjustement to guarantee the accuracy of the results. I then proceeded to the analysis of the data and ran the corresponding simulations. All the results presented in the present manuscript, whether experimental or theoretical, that are not explicitly labeled or referenced as the work of someone else are product of my own.

I also took part into other experiments during my PhD out of the framework of this thesis. These campaigns were performed at the Apollon facility in Paris-Saclay (France) and Rutherford Appleton Laboratory in Oxford (United Kingdom).

I would like to thank my supervisors for helping me navigate in my researches. I am also grateful toward my colleagues and friends from my different laboratories, for their wise advices, their constructives discussions and their kindness. Finally, I want to thank my parents, my dear friends in and outside the academic field, and more generally everybody who supported me during my PhD.

Table of contents

Role of the author and acknowledgements i

Table of contents iii

Chapitre 1 Introduction to laboratory astrophysics 1

1.1 Astrophysical context 1

1.2 Generalities on plasma physics 3

1.2.1 Characteristics 3

1.2.1.1 Definition 3

1.2.1.2 High energy density physics 4

1.2.2 Description of the plasma dynamics 5

1.2.2.1 Fluid description with magnetohydrodynamics 5

1.2.2.2 Limits of the MHD and kinetic description 7

1.2.3 Magnetic field in plasma 8

1.2.3.1 « Frozen in flow » magnetic field or Alfvén theorem 8

1.2.3.2 The Biermann battery effect 9

1.2.4 Plasma parameters and comparison 10

1.2.5 Limits of the *in situ* methods 13

1.3 High-power lasers 14

1.3.1 Development of the laser technology 14

1.3.2 Generation of magnetized plasmas in the laboratory 15

1.3.3 Astrophysical relevance of laser-driven plasmas 18

1.4 Introduction on the studied plasma interactions 19

References 21

Chapitre 2 Magnetic field compression in HED magnetized plasmas 29

2.1 General description of the magnetic compression 29

2.1.1 Definition 29

2.1.2 Astrophysical context 31

2.2 Dynamics of the compression zone 33

2.2.1 Establishment of the compression sheet 33

2.2.2 Characteristic saturation of the magnetic field 34

2.3 Model of the compressed magnetic mirror 35

2.4 Framework of the study 36

2.4.1 Context 36

2.4.2 Aims and structure of the research work 37

References 38

Chapitre 3 Magnetic reconnection between HED magnetized plasmas 41

3.1 Generalities about magnetic reconnection in HED plasmas 41

3.1.1 Definition 41

3.1.2 Astrophysical relevance 43

3.2 Configuration and dynamics of the elongated current sheet 46

3.2.1 Formation of the current sheet 46

3.2.2 Particle kinetics in the current sheet 47

3.2.3 Plasmoid-driven regime 49
3.2.4 Characterisation and parameters of the reconnection 50

3.3 Framework of the study 51

References 53

Chapitre 4 Experimental setups and diagnostics and numerical tools for laboratory astrophysics with high power lasers 55

4.1 Experimental devices in the laboratory 55
4.1.1 The LULI2000 facility 55
4.1.2 Experimental setup for magnetic field compression 57
4.1.2.1 Geometry of the experiment 57
4.1.2.2 Diagnostics 58
4.1.2.2.1 Proton radiography 58
4.1.2.2.2 Interferometry 61
4.1.2.2.3 Optical pyrometry 63
4.1.2.2.4 X-ray spectrometry 64
4.1.3 Experimental setup for magnetic reconnection 65
4.1.3.1 Geometry of the experiment 65
4.1.3.2 Adaptation of the diagnostics 66

4.2 Analytical and numerical tools to model plasmas 68
4.2.1 Hydrodynamical and macroscopic description: the FLASH code 68
4.2.1.1 Numerical setup 68
4.2.1.2 Definition of the setup for magnetic compression 71
4.2.2 Microscopic and kinetic description 72
4.2.2.1 Properties of the Particle-in-Cell code SMILEI 72
4.2.2.2 Architecture of the setups and connection with FLASH 73

4.3 Conclusion 75

References 76

Chapitre 5 Experimental and theoretical investigation of the saturated magnetic field compression between laser-driven plasmas 79

5.1 Characterisation of the plasma 80
5.1.1 Measurement of the electron density 80
5.1.2 Aspect of the magnetic field 84
5.1.3 Estimation of the electron temperature 85

5.2 Evidence of saturated compression between magnetized plasmas 87
5.2.1 Experimental evidence of the compression 88
5.2.2 Hydrodynamical evolution of the compression sheet 91
5.2.2.1 Establishment of the compression sheet 91
5.2.2.2 Global evolution of the saturation 95
5.2.2.3 Plasma parameters 98
5.2.3 Study of the internal dynamics of the compression zone 102
5.2.3.1 Setup of the PIC simulations 102
5.2.3.2 Highlight of the saturation mechanisms at kinetic scales 105

5.3 Influence of the inflow velocity on the inner dynamic of the sheet 108
5.3.1 Establishment of a broken magnetic mirror regime 108
5.3.2 Dynamics of the plasmoids 108
5.3.3 Influence of the velocity on the global evolution of the compression sheet 113

5.4 Conclusion 115

References 117

Chapitre 6 Study of the dynamic of the elongated current sheet for magnetic reconnection in laser-driven plasmas 119

6.1 Characterisation of the current sheet in the laboratory 120
6.1.1 Context of the experiment 120
6.1.2 Experimental highlight of the reconnection 120
6.1.2.1 Case of coplanar targets 120
6.1.2.2 Non-coplanar targets: introduction of an out-of-plane guide field 125
6.1.3 Dynamics of the current sheet 130
6.1.4 Plasma parameters in the current sheet 132

6.2 PIC study of the reconnection process 135
6.2.1 Relevance of PIC simulations over hydrodynamic models 135
6.2.2 Kinetic model of the current sheet 135
6.2.2.1 Numerical setup 135
6.2.2.2 General evolution of the current sheet 136
6.2.2.3 Influence of the guide field 139
6.2.3 Characterisation of the magnetic reconnection 141
6.2.3.1 Evolution of the β_{th} parameter 141
6.2.3.2 Influence of the guide field on the reconnection characteristic parameters 143

6.3 Conclusion 146

References 149

Chapitre 7 General conclusion and perspectives 151

List of figures 155

List of tables 166

Publications 167

Étude en laboratoire des processus d'échange d'énergie particules-plasma magnétisé pertinents pour l'astrophysique 169

Investigating in the laboratory particle-magnetized plasma energy exchange processes relevant for astrophysics 170

Chapitre 1

Introduction to laboratory astrophysics

1.1 Astrophysical context

Astrophysics, as a field of scientific research of its own, differs from the rest of physics by the environment it is applied to. The field reunites the study of diverse objects and events, of several spatio-temporal scales and different natures, embracing various fields from planetology (the study of the formation of planets and their classification) to the study of clusters of galaxies and their dispatching in the Universe [1]. Even if fundamental laws of physics, such as the fundamental principles of classical mechanics, black body radiation or the imposed limit of the celerity of light, govern a large panel of aspects of the known Universe, space objects and events can reach conditions of temperature, pressure or density that are far beyond those that are possible to observe naturally and directly on the surface of the Earth. Adapted physical models and approaches were then needed to understand these environments [2].

The matter as we are familiar with is not the main constituent of the Universe. In fact, the baryonic matter (often described as « visible matter ») outspace is radically different from the solid, liquid and gas states of matter that are mainly encountered on telluric planets like the Earth. To go further, matter only represents approximately 31.5 % of the total mass of the Universe, the rest of the mass being composed of dark energy. Among these 31.5 % of matter, baryonic matter only represents 20 % of the total, the 80 % remaining being composed of dark matter [3]. Dark energy and dark matter are still the subjects of multiple studies as they remain quite little understood. Even if these topics are important to mention to describe the repartition of mass and matter in the Universe, they will not be addressed in this thesis.

The baryonic matter is not distributed equally in the Universe. In a stellar system like ours, 99.86 % of the mass of the system is occupied by the Sun. Indeed, the mass of the Solar System is $1.992.10^{30}$ kg, or 1.0014 $M_{\odot}$, where $M_{\odot} = 1.989.10^{30}$ kg is the mass of the Sun and served as a reference mass unit in Astrophysics. The rest of the baryonic matter within the heliosphere, which designs the volume astrosphere dominated by the solar magnetic field and wind (separated from the interstellar medium by the heliopause), represents only 0.1 % of the total mass of the system and regroups all the other objects within the Solar System, such as telluric and gas planets, objects located in the successive asteroid belts, dwarf planets from the Kepler belt or scattered objects from the Oort cloud [4].

Consequently, the mass of a stellar system in astrophysics is often assimilated to the mass of the star itself. Therefore, the majority of the baryonic matter constituting the Universe is contained in the stars or related to them. Indeed, this mass is principally condensed in the stars during their life cycles [5] but also constitutes the coronal mass ejecta (CME in this manuscript), resulting from the activity in the outer layers of the star and in the corona. These ejectas also feed the permanent the stellar wind which diffuses in the totality of the heliosphere [6].

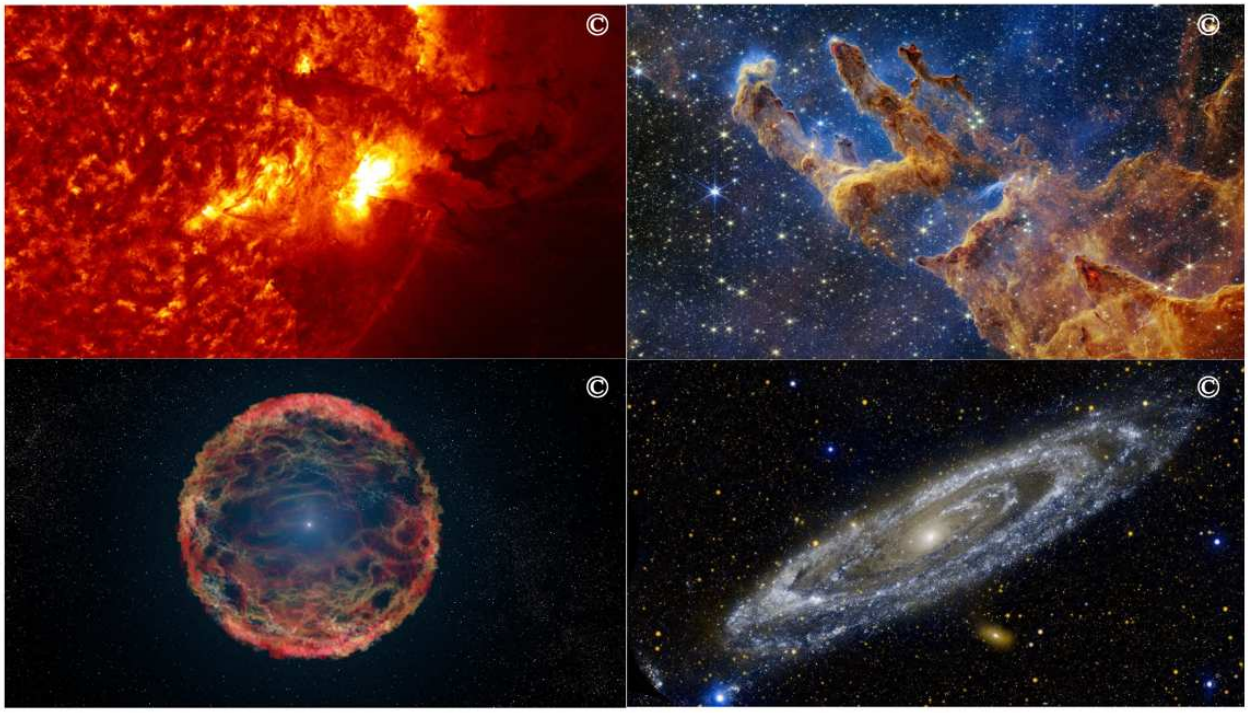

Figure 1. Pannel of examples of the visible matter present under different forms in the Universe. Top left: stellar eruption and ejection of coronal mass from NASA [7]. Top right: gas cloud, place of high stellar formation rate from L. Chemin, C. Carignan and T. Foster [8]. Bottom left: Supernovae remnant hosting a white dwarf in its core. The ejectas are places of turbulences and instabilities from Curtin University [9]. Bottom right: Galaxies concentrate the matter in the Universe and are organised in superclusters from NASA [10].

Stars influence the distribution of matter at every stage of their lifetime, from their formation to their final phases. Stars get formed in specific areas in galaxies, inside star formation dense molecular gas clouds. Stellar objects get formed in these areas when the density of the gas cloud overpasses a threshold value from which the gravitation collapse of the cloud is initiated [11]. Resulting young stellar objects are then composed of the remaining elements composing the cloud, such as hydrogen, helium or iron. These elements constitute the different layers of the star and will

return continuously to the circumstellar medium during the different phases of stellar activities. Stars enrich the medium during their life through stellar winds carrying elements produced by the internal fusion mechanims [12]. Besides, stars whose masses are below the Chandrasekhar limit, which corresponds to the maximum mass a star can reach that can still balance the gravitational collapse, explode in supernovae. Their external layers expand across the interplanetary medium [13], forming supernovae remnants surrounding a highly dense object such as a white dwarf in the core (see Figure 1).

Baryonic matter in the Universe is then dominated by the fourth state of matter which, among else, is the primary component of stars: the plasma. Plasmas constitute the vast majority of visible matter in the Universe. In our Solar System, besides composing the Sun, plasma fills the interplanetary space and dominates even the near-Earth environment [14]. Indeed, the atmospheric gases start to become ionized and transit into the plasma state in the ionosphere, from an altitude of approximately 80 km above sea level [15].

1.2 Generalities on plasma physics

1.2.1 Characteristics

1.2.1.1 Definition

Plasma constitutes the ionized state of matter, different from a neutral gas as it is composed of independent charged particles. In a given volume of a homogeneous plasma, these charged particles are considered free and are numerous enough to allow collective electromagnetic interactions. The number of positive and negative charges are expected to be similar leading to a quasi-neutrality, which is one of the main properties of plasmas. Therefore, the electron density n_e and the ion density n_i are equivalent with $n_e \sim Zn_i$ [16], where Z is the atomic number, and the quasi-neutrality is maintained by the electrostatic forces between the charged particles. This equilibirum is possible because, over a certain length, the local electric fields are screened by the redistribution of the charges in the plasma after a perturbation. This distance is the Debye length. It is characteristic of the plasma and is defined as follows:

$$\lambda_D = \sqrt{\frac{\varepsilon_0 k_B T_e}{n_e e^2}}, \tag{1.1}$$

where ε_0 is the vacuum permittivity (with $\varepsilon_0 = 8.85.10^{-12}$ F.m^{-1}), k_B is the Boltzmann constant (with $k_B = 1.38.10^{-23}$ m^2.kg.s^{-2}.K^{-1}), T_e is the electron temperature, n_e is the electron density and e is the elementary charge (with $e = 1.6.10^{-19}$ C). In the case of an electromagnetic perturbation occuring at a distance d of a charged particle, this perturbation is efficiently screened by the plasma and have an insignificant influence on the particle dynamics as soon as we have $d >> \lambda_D$. Only the electrons are taken into account to calculate the Debye length because they are lighter than the protons and ions and get redistributed faster. More generally, the plasma parameters are most often given for the electron components. As ions are heavier, they are rather immobile and are usually considered as a fixed background of positive charges in the plasma while

the electrons are the mobile part [17]. More generally, for a plasma, the total length L of the system must be $L >> \lambda_D$.

A plasma is constituted of independent charged particles which react when subject to an electromagnetic perturbation. The frequencies at which the electrons and ions oscillate through such fields, respectively ω_{pe} and ω_{pi}, are characteristic of the capacity of the plasma to carry an electromagnetic field and set the inner temporal scales of the plasma. These frequencies depend among else on whether the electron or ion density, as the denser the plasma is, the higher are ω_{pe} and ω_{pi}. They are independent from external perturbations and proper to the plasma, and described by:

$$\omega_{pe} = \sqrt{\frac{n_e e^2}{\varepsilon_0 m_e}}, \tag{1.2}$$

$$\omega_{pi} = \sqrt{\frac{n_i Z^2 e^2}{\varepsilon_0 m_i}}, \tag{1.3}$$

where n_e, n_i are respectively the electron and ion densities, m_e, m_i the electron and ion masses and Z the ionization level. $\tau_{pe} = \omega_{pe}^{-1}$ and $\tau_{pi} = \omega_{pi}^{-1}$ are the characteristic dynamical timescales over which electrons and ions respond respectively to a perturbation in the plasma. As electrons are lighter than ions, their characteristic respond time is much shorter than the ions one, and we have $\omega_{pe}^{-1} << \omega_{pi}^{-1}$. As a result, at timescales close to ω_{pe}^{-1}, the plasma as its whole is dominated by the electrons, while ions are considered as uniform at the earliest stages of a pertubation [18]. Moreover, we also have to take into account the Coulomb collisions within the plasma. Therefore, we define the Coulomb logarithm, set by:

$$\ln \Lambda = 4\pi n_e \lambda_D^3 \tag{1.4}$$

This parameter determines the effect of Coulomb collisions within the Debye sphere, centered on a given particle and with radius λ_D. This value permits to estimate the state of the plasma inside the sphere [19].

1.2.1.2 High energy density physics

Plasmas have already been observed *in situ* in space by satellites since around the late 1950s and early 1960s [20]. If plasmas can be generated now artificially in facilities, space is the medium where plasma is dominant and can be found in the highest volume and under various forms. A large range of temperatures, pressures and densities can be found in space objects of different types (see Figure 2). As this present work is directed to be relevant for astrophysical plasmas, we must remind that these objects can constitute extreme environments under highly energetic conditions. Among them, we can mention stellar combustion, neutron stars [21], supernovae remnants, nuclei of active galaxy [22] or also gamma-ray bursts [23].

In this case, astrophysical plasmas (and consequently their artifical counterparts) are often subject to conditions of high-energy densities (HED in this manuscript), and we then talk about HED plasmas. HED environments imply high conditions of pressure (higher than 10^{11} Pa = 1 Mbar, which corresponds to a million times the terrestrial average atmospheric pressure) and temperature (hotter than $T = 10^7$ K) [24]. Due to the significantly high values of temperature and density

encoutered in HED plasmas, the Debye length is usually very small and can be estimated by $\lambda_D \propto \sqrt{T_e/n_e}$.

It is possible to rank the different types of plasmas presented in astrophysical objects, based on these conditions. Figure 2 shows a temperature-density diagram presenting different objects and environments where plasmas can be encountered in the Universe, showing the various properties they can present. It also mentions the comparison between space plasmas and artificial plasmas in current facilities, showing the parallel between the two types of systems. In this thesis, we only work on classical non-relativistic plasmas, that can be found around planetary magnetospheres or in stellar corona for instance. However, works about relativistic or cold plasmas do exist and are ongoing [25], but they will not be detailed in this manuscript.

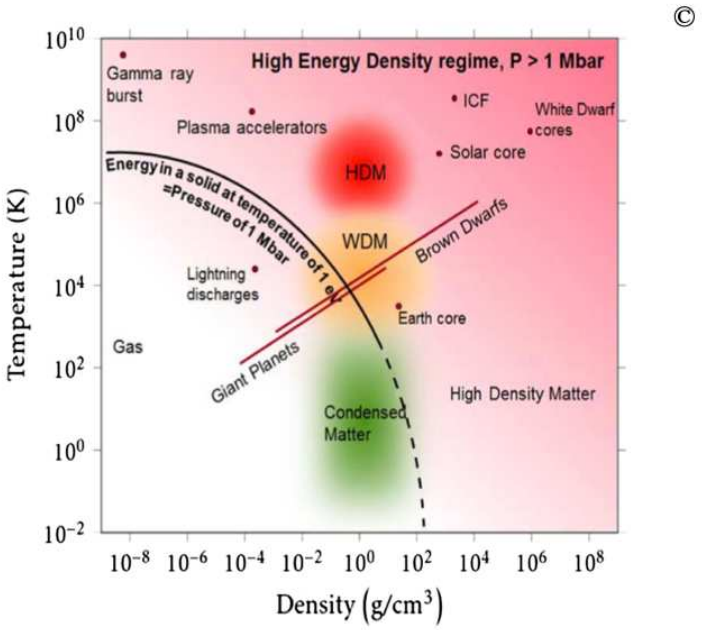

Figure 2. Characterization of the diversity of plasmas in space in a temperature-density-diagram from W. Bang et al *[26]. The HED plasmas are located on the top of the graph, over the black isobar line.*

1.2.2 Description of the plasma dynamics

At macroscopic scales, a plasma exhibits global properties, such as density, temperature, pressure or velocity, that can be described similarly to a fluid. However, a plasma is intrinsically constituted of independent charged particles which interact individually with electromagnetic perturbations. Consequently, the most accurate description that can be made of a plasma is to approach this duality, by detailing both the fluid and the kinetic aspects of the plasma to determine in which configurations one is dominant comparing to the other.

1.2.2.1 Fluid description with magnetohydrodynamics

At large length scales L, such as $L >> \lambda_D$, the evolution of a non-relativistic quasi-neutral plasma does not depend on the oscillations and the proper motion of the particles. At macroscopic scales, a plasma can be modeled as a fluid with a Maxwellian velocity distribution. Its behavior can consequently be approximated by fluid mechanic. As plasmas, and especially space plasmas,

are likely to carry a magnetic field. A magnetized plasma considered in the fluid description is then governed by magnetohydrodynamics laws (MHD in this manuscript). The MHD formalism considers particles as an ensemble rather that individuals and assimilates a plasma to a compressible and conducting fluid in an electromagnetic field. As the plasma is subject to the Maxwell laws at these scales, the MHD model consequently combines both hydrodynamics and electromagnetism to describe the plasma evolution [27].

In this framework, as the plasma is assumed as a maxwellian fluid, we can enunciate the fundamental Euler equations that conduct the plasma evolution [28]. The first of these equations is the mass conservation equation:

$$\frac{\partial \rho}{\partial t} + \nabla . (\rho \mathbf{v}) = 0 \, , \tag{1.5}$$

where ρ is the mass density, $\mathbf{v}$ is the average macroscopic velocity of the plasma, and $\frac{\partial \rho}{\partial t}$ is the mass density rate. Then is the momentum conservation equation:

$$\rho \left(\frac{\partial \mathbf{v}}{\partial t} + \mathbf{v} . \nabla \mathbf{v} \right) = -\nabla P + \mathbf{J} \times \mathbf{B} \, , \tag{1.6}$$

where P is the thermal pressure of the plasma, such as $P = P_e + P_i$, and $P_{e,i} = n_{e,i} k_B T_{e,i}$, $\mathbf{J}$ is the current density, $\mathbf{B}$ is the magnetic field and $\rho \frac{\partial \mathbf{v}}{\partial t}$ is the momentum density rate. The last equation is the energy conservation equation:

$$\frac{\partial P}{\partial t} = -\gamma \nabla \mathbf{v} \, , \tag{1.7}$$

where $\gamma = \frac{C_p}{C_v}$ is the ratio of the calorific capacities (constant pressure over constant volume) and $\frac{\partial P}{\partial t}$ is the energy density rate. In our case, we consider both electrons and ions in the plasma, therefore we place our analysis in the bi-fluid description such as we have:

$$\begin{cases} n_e \left(\frac{\partial n_e}{\partial t} + \nabla . n_e \mathbf{v}_e \right) = 0 \\ n_i \left(\frac{\partial n_i}{\partial t} + \nabla . n_i \mathbf{v}_i \right) = 0 \end{cases} \tag{1.8}$$

The MHD approximation also requires a coherent system of characteristic scales. Beside the conditions of quasi-neutrality enunced previously in 1.2.1.1. and of non-relativity ($v << c$, where v is the macroscopic velocity of the plasma and c is the speed of light), the system must verify:

$$\omega_{ce}^{-1}, \omega_{pe}^{-1} \ll \tau \, , \tag{1.9}$$

where ω_{pe} is the electron plasma frequency (see eq. 1.2), $\omega_{ce} = eB/m_e c$ is the electron cyclotron frequency and the τ the characteristic timescale of the plasma. In order to correspond to the MHD framework, the characteristic timescale of the global system must be much longer than the particle ones. Indeed, a macroscopic equilibrium is longer to achieve as this stable state can be attained only when the collisional behavior of the plasma starts to dominate the dynamics of the plasma over the kinetic one. Besides, longer characteristic timescales ensure time for the electrons to get redistributed in the plasma after an electromagnetic perturbation and therefore to guarantee the quasi-neutrality condition.

In the fluid description, the velocity distribution of the plasma is assumed to be Maxwellian, which implies that the plasma is considered as collisional in the MHD model. By definition, we have:

$$\lambda_{mfp,e},\ \lambda_{mfp,i} << L\ , \tag{1.10}$$

where $\lambda_{mfp,e}$ and $\lambda_{mfp,i}$ are respectively the collisional mean free path of electrons and ions. The mean free path of a particle has to be quantitatively smaller than the total size of the system in order to maintain the hypothesis of the fluid description. This condition joined the one mentioned in 1.2.1.1., stating that, for a plasma, $\lambda_D << L$. In the case of a quasi-neutral fluid plasma, dominated by collective effects and characterized by a Maxwellian velocity distribution, therefore we have $\lambda_D << \lambda_{mfp,ei} << L$.

The MHD model provides a solid macroscopic description of plasmas by modeling them as continuous fluids in electromagnetic fields. Indeed, at sufficiently large scales such as in many astrophysical environments, the collective dynamics of a plasma can be described correctly without expliciting the microscopical aspects and particle dynamics, as the dominant processes governing the plasma evolution are large-scale motions and electromagnetic interactions. Consequently, the magnetohydrodynamic model correctly considers the main observables and plasma parameters, but still only provides a macroscopic view of the system. Therefore, a second formalism needs to be used, this time at the particle scales, in order to have a complete description of the plasma at scales that cannot be described by MHD laws.

1.2.2.2 Limits of the MHD and kinetic description

The MHD model only proposes a fluid aproach to characterize the plasma evolution, in which the particles are modeled as collective and considered with a fully Maxwellian velocity distribution. However, it remains a conditionned approximation, as charged particles are not depicted individually. The thermal motion of the particles, their individual frequency, and more generally all the aspects of the plasma that require to treat the particles individually to be addressed are neglected. This is the limit of the MHD description of plasmas. At smaller scales (typically microscopical scales and below), and as soon as the conditions in eq. 1.9 and eq. 1.10 are not verified, the MHD laws are not efficient anymore [29].

Kinetic effects govern the plasma at timescales close to ω_{pe}^{-1} and ω_{pi}^{-1} for spatial dimensions equivalent or smaller than the mean free path λ_{mfp} of the plasma. The particle-particle collisions that were taken into account by the MHD model are negligeable in the kinetic framework. Furthermore, in this regime, the considered scales for the system are shorter than the mean free path of the particles. As a result, the plasma evolution is then dominated by the inner self-generated electromagnetic fields. In this case, the plasma is treated as collisionless [30].

The kinetic description is based on the proper motion of the particles, such as the statistical distribution function is non-Maxwellian and given by:

$$f_s(t, \mathbf{x}, \mathbf{p}) = \sum_i \delta[\mathbf{x} - \mathbf{x}_i(t)]\delta[\mathbf{p} - \mathbf{p}_i(t)]\ , \tag{1.11}$$

where s is the species (electrons or ions), $\mathbf{x}$ and $\mathbf{p}$ are respectively the position and the momentum, and δ is the Dirac distribution [31]. For each species, we can establish from the distribution function the particle density n_s, the charge current density ρ_s, the average velocity $\mathbf{v}_s$ and the current density $\mathbf{J}_s$:

$$n_s(t, \mathbf{x}) = \int f_s(t, \mathbf{x}, \mathbf{p}) d\mathbf{p}\ , \tag{1.12}$$

$$\rho_s(t, \mathbf{x}) = \sum_s q_s \int d^3_{\mathbf{p}}\, f_s(t, \mathbf{x}, \mathbf{p})\ , \tag{1.13}$$

$$\mathbf{v}_s(t, \mathbf{x}) = \frac{1}{n_s(t,\mathbf{x})} \int \mathbf{v}\, f_s(t, \mathbf{x}, \mathbf{p}) d\mathbf{p}\ , \tag{1.14}$$

$$\mathbf{J}(t,\mathbf{x}) = \sum_s q_s \int d^3_{\mathbf{p}}\, \mathbf{v}\, f_s(t,\mathbf{x},\mathbf{p})\ , \tag{1.15}$$

where $\mathbf{v} = \mathbf{p}/m_s\gamma$, and γ is the relativistic Lorentz factor. As the plasma is considered as quasi-neutral, we can assume that the number of particles for each species is conserved, so $\frac{dn_s}{dt} = 0$. It leads to:

$$\frac{df_s}{dt} = 0 \ \Rightarrow\ \frac{\partial f_s}{\partial t} + \mathbf{v}\,.\nabla f_s + \frac{d\mathbf{p}}{dt}\,.\nabla_{\mathbf{p}} f_s = 0 \tag{1.16}$$

We know that $\frac{d\mathbf{p}}{dt}$ is given by the Lorentz force. Therefore, by rewriting $\frac{d\mathbf{p}}{dt}$ in eq. 1.16, we obtain the Vlasov equation [32]:

$$\frac{\partial f_s}{\partial t} + \mathbf{v}\,.\nabla f_s + q_s(\mathbf{E} + \mathbf{v}\times\mathbf{B}).\nabla_{\mathbf{p}} f_s = 0\ , \tag{1.17}$$

where **E** and **B** are respectively the electric and magnetic fields. As these fields satisfy the Maxwell equations, and as the charged particles constituting the plasma are subject to the Lorentz force, the Vlasov equation (eq. 1.17) is coupled with the Maxwell equations to study the spatio-temporal evolution of the particle distribution function. Consequently, the kinetic description of a collisionless plasma relies on the Vlasov equation (eq. 1.17) and more generally, on all the equations of the Maxwell-Vlasov model (eqs. 1.12 – 1.17) [33].

1.2.3 Magnetic field in plasma

In astrophysics, magnetic fields share a significant place in the studies lead in this domain. They are observed at multiple scales in the Universe and in various high-energy astrophysical events and environments. These events can be interactions between the stellar winds and the planetary magnetospheres, the remnants of supernovae evolving in the circumstellar medium [34] or also interactions of galactic magnetic fields [35]. Thus, we define magnetized plasmas as plasmas carrying a magnetic field, which significantly influence the motion and the trajectories of the charged particles. Therefore, the plasma dynamics is affected by the presence of this magnetic field.

1.2.3.1 « Frozen in flow » magnetic field or Alfvén theorem

In the MHD model, the plasma is considered as a conducting fluid. If we assume that this plasma is an isolated system and consequently not subject to any perturbation or any constraint such as resistivity, the regime can be described by the ideal MHD. In this case, the plasma is modeled as an ideal conductor (so with a supposely infinite conductivity σ). With the hypothesis of the quasi-neutrality of the plasma, we establish that the coupling of electromagnetic fields and the plasma follow the ideal Ohm law [36]:

$$0 = \mathbf{E} + \mathbf{v} \times \mathbf{B} \tag{1.18}$$

By injecting the ideal Ohm law (eq. 1.18) in the Maxwell-Faraday law ($\frac{\partial \mathbf{B}}{\partial t} = -\nabla \times \mathbf{E}$), we obtain the continuity equation for the magnetic field in the plasma:

$$\frac{\partial \mathbf{B}}{\partial t} = \nabla \times (\mathbf{v} \times \mathbf{B}) \tag{1.19}$$

This equation shows that, in ideal MHD, the evolution of the magnetic field within the plasma depends on its velocity. As a consequence, the plasma and the magnetic field are coupled together and form a conductive regime, as the magnetic field is advected by the plasma. By integrating eq. 1.19 over a mobile surface S(t), we establish the relation governing the magnetic flux:

$$\int \frac{\partial \mathbf{B}}{\partial t} d\mathbf{S} = \int \nabla \times (\mathbf{v} \times \mathbf{B}) d\mathbf{S} = \int_{\delta S} \mathbf{B} d\mathbf{S} \tag{1.20}$$

These two equations eq. 1.19 and eq. 1.20 show that the magnetic field is carried by the plasma and that the transported magnetic flux Φ is conserved through any surface. Therefore, we have $\frac{d\phi}{dt} = 0$ and, as they carry an electrical conductivity, the charged particles composing the plasma become « frozen-in » the magnetic field. This is valid for every surface S(t) whose dimensions may vary with the time as the magnetic field is advected by the plasma (see Figure 3).

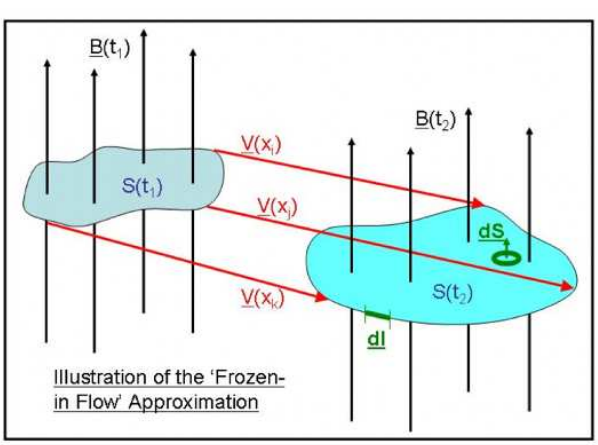

Figure 3. Illustration of the « Frozen-in-flow » magnetic field approximation. This shows that the magnetic flux going through $S(t_1)$ and $S(t_2)$ is the same (see lectures by N. Murphy for Harvard-Smithsonian Center for Astrophysics [37]).

This property of magnetic fields in plasmas is known as the Alfvén theorem: magnetic field lines are « frozen-in » the ideal plasma throughout the whole evolution of the system. Therefore, the charged particles composing the plasma remain on the same field line they were initially attached to. An ideal plasma flow delimited by a surface S(t) can be distorted but the field lines cannot break and the continuity of the magnetic flux will be conserved over time. It is still important to mention that this theorem is only valid for the framework of the ideal MHD, as described at the beginning of this section. Indeed, the « frozen-in » aspect of the magnetic field can break if the plasma encounters a pertubation (such as a non negligeable resistivity) that would alter the topology of the field lines and then modify the ideal aspect of the MHD regime [38].

1.2.3.2 The Biermann battery effect

As plasmas are composed of charged particles, they are consequently subjects to electric fields and can get magnetized. It was mentioned before that this magnetic field can come from an external source [39]. However, an initially unmagnetized plasma can get spontaneously magnetized. This comes from the inner electron pressure of the plasma, such as the electric field is governed by:

$$\mathbf{E} = -\frac{\nabla P_e}{q n_e}, \tag{1.21}$$

where P_e is the electron pressure and n_e is the electron density. From the Maxwell-Faraday law, we know that the variations of a magnetic field can induce an electric field. Therefore, with eq. 1.21, we can enunciate:

$$\frac{\partial \mathbf{B}}{\partial t} = -\nabla \times \mathbf{E} = \frac{1}{q} \nabla \times \left(\frac{\nabla P_e}{n_e} \right) \tag{1.22}$$

We know that $P_e \propto n_e T_e$, therefore we can write:

$$\frac{\partial \mathbf{B}}{\partial t} = \frac{1}{q n_e} (\nabla n_e \times \nabla T_e) \tag{1.23}$$

The inner gradients of electron density and temperature of the plasma generate the apparition of a magnetic field. Eq. 1.23 is the fundamental relation governing the effect known as the Biermann battery effect [40]. In a situation when the gradients of electron density and electron temperature are crossed and non-colinear in the plasma (so if $\nabla n_e \times \nabla T_e \neq 0$), the plasma gets magnetized spontaneously, without any form of interaction with an external field. The Biermann battery effect is extremely important for astrophysical plasmas since it takes place as soon as the required conditions on temperature and density are met [41]. It appears and intervenes naturally in many astrophysical objects, from localized fields in the stellar magnetic loops monitoring the ejecta of stellar wind [42] to galaxies [43]. Consequently, the Biermann battery effect is thought to be a source of necessary initial magnetic fields at different scales in the Universe, even for the larger ones such as in galactic fields for instance [44].

The Biermann battery effect, and more generally magnetized plasmas, can be modeled by using the MHD description at macroscopic scales. Their effects on the ambiant global magnetic fields in space are known, but besides that, these fields are also a known means of particle acceleration [45]. Indeed, the magnetic field can rearrange the local particle distribution and interactions between two or more magnetized plasmas can modify the aspects of these fields, by inducing perturbations in zones where the MHD becomes locally resistive and where the Alfvén theorem is not valid anymore. Particles traveling alongside the field lines can then be accelerated in these regions of perturbations, following the variations of flux and energies due to the interactions between plasmas and as a result, rearrangements of field lines can even be observed [46]. These mechanisms will be detailed later in this manuscript.

1.2.4 Plasma parameters and comparison

The Euler equations introduced earlier for the MHD fluid description permit to set key parameters from the plasma properties such as its density, temperature or other characteristic scales in order to describe quantitatively the dynamics of a system. The plasma parameters are established dimensionless quantities used to estimate the different physical properties of the plasma. Their numerical values permit to ensure the validity of the hydrodynamic Euler equations (eqs. 1.5 – 1.7), but also to provide a quantitative comparison between different plasmas. Besides describing the plasma in an electromagnetic field, similarities in the Euler equations for two plasmas correspond to equivalences between their characteristic physical quantities mentioned above. In these conditions, it is legitimate to establish and acknowledge similarities between two different systems.

We first define here the Euler number Eu. Usually, in the classical fluid mechanics framework, we define $Eu = \Delta P/(\rho v^2)$, where ΔP is the pressure difference at distinct states of the evolution of the system, ρ is the mass density and v is the velocity of the fluid. However, in HED physics, the definition and normalisation commonly used of the Euler number is different, in order to transcribe efficiently the plasma dynamics and exhibit similarities between plasma systems (see Section 1.3.3.). Therefore, here we define the Euler number by Eu [47]:

$$Eu = v\sqrt{\frac{\rho}{p}}, \tag{1.24}$$

where v is the velocity of the fluid, ρ is the mass density and p is the pressure. Consequently, two plasmas present a similar behavior in regard of the Euler equations if their respective Euler numbers Eu are equivalent. In this section, we are going to detail the parameters that we calculated to characterize our plasmas as well as their interaction in our works. The calculations were later made for both experimental and numerical studies (see Chapter 5 and Chapter 6). To quantify the velocity of mechanical waves, like the sound, comparing to the velocity of the plasma, we determine the Mach sound number M_S [48]:

$$M_S = \frac{v}{c_S}, \tag{1.25}$$

$$c_S = \sqrt{\frac{\gamma P}{\rho}} = \sqrt{\frac{\gamma Z k_B T_{e,i}}{m_i}}, \tag{1.26}$$

where c_S is the sound speed, γ is the ratio of the calorific coefficients, Z is the atomic number of the species, k_B is the Boltzmann constant and m_i is the mass of the ions. If $M_S < 1$, the fluid velocity is slower than the perturbation that propagates isotropically in the plasma. From $M_S \sim 1$ and above, the system becomes supersonic, which induces the formation of internal shock waves that compress locally the plasma and can trigger particle acceleration. In parallel, we make a similar analysis for electromagnetic waves in the plasma by estimating the Alfvén Mach number M_A and velocity v_A [49]:

$$M_A = \frac{v}{v_A}, \tag{1.27}$$

$$v_A = \frac{B}{\sqrt{\mu_0 m_i n_i}}, \tag{1.28}$$

where v_A is the Alfvén velocity, μ_0 is the vacuum permeability and n_i is the density of the ion. In the ideal MHD framework, the Alfvén waves are incompressible and transverse waves, resulting from the coupling between the plasma motion and the magnetic tension, as shown in eq. 1.19, and consequently propagating along the magnetic field lines. Electromagnetic perturbations induce the motion of the plasma alongside modifying the inner magnetic field carried by the plasma. The plasma and the field evolve together, as stated by the Alfvén theorem (see section 1.2.3.1.). The topology of the magnetic field carried by a plasma can be distorted by the propagation and the motion of this plasma through the waves but the magnetic flux is conserved. Besides, the plasma and the field evolve jointly along the direction of propagation and the Alfvén Mach number M_A determines which component governs these dynamics. If $M_A > 1$, then $v_A < v$ therefore the plasma flow carries the expansion of the field and globally the evolution of the system. In this case, the plasma is considered as a super-Alfvénic plasma. On the contrary,

$M_A < 1$ implies a sub-Alfvénic regime in which the magnetic field governs the plasma dynamics. We also estimate the viscosity aspects of the plasma, which can be quantified by the Reynolds number R_e [50]:

$$R_e = \frac{\text{inertial forces}}{\text{viscous forces}} = \frac{v\,L}{\nu}, \tag{1.29}$$

where ν is the scalar viscosity of the plasma, calculated in m^2/s, such as $\nu = \mu/\rho$, where μ is the dynamic viscosity. However, here in this thesis, we are working with an approximation of the Braginskii viscosity [51] already used in previous HED plasma physics studies [52]. Therefore, here $\nu = 2e{+}8T_e/(ZB)$, where Z is the ionization level of the plasma ions and B is the magnetic field expressed in Gauss (we precise here that, even if some calculations in this thesis have been initially made in the CGS unit system, all the final results presented in the following chapters have been correctly converted to the SI unit system). In the ideal MHD framework, the viscous effects are expected to be negligeable therefore R_e is supposed to be larger than the unity, such as $R_e >> 1$. In the presence of a magnetic field in the medium, the induction and the diffusion of the field in the moving plasma also require to be addressed, therefore we determine the analogue magnetic Reynolds number R_{em} [53]:

$$R_{em} = \frac{\text{magnetic induction}}{\text{magnetic diffusion}} = \frac{v\,L}{\eta}, \tag{1.30}$$

where η is the magnetic diffusivity of the plasma, calculated in m^2/s, such as $\eta = 1/\mu_0\sigma_0$, where σ_0 is the electronic conductivity. Here, we use the Spitzer resistivity [54], such as $\eta = 8.2e{+}5\ln\Lambda Z T_e^{-3/2}$, where $\ln\Lambda$ is the Coulomb logarithm and Z the ionization level. Like previously for the Reynolds number R_e, the magnetic Reynolds number R_{em} is expected to be larger than the unity ($R_{em} >> 1$) in a case where the advection of a magnetic field by a propagating plasma is dominant over the diffusion of the field. Then, the capacity of a plasma to transport and conduct the heat is characterized by the Péclet number P_e [55]:

$$P_e = \frac{\text{convective transport}}{\text{thermal diffusivity}} = \frac{v\,L}{\chi}, \tag{1.31}$$

where χ is the thermal diffusivity of the electrons, calculated in m^2/s, such as $\chi = \kappa/C_p\,\rho$, where κ is the thermal conductivity and C_p is the heat capacity. Here, we use the approximated expression $\chi = 8{,}6.10^9\,A^{1/2}T_e/(ZB)$ [56], where A is the mass number of the plasma ions, Z the ionization level and B the magnetic field expressed initially in Gauss. The system corresponds to the MHD framework when the condition $P_e >> 1$ is respected, which means that the heat transport is governed by the advection within the plasma while the thermal diffusion is negligeable. Consequently, in this regime, the heat is carried by the plasma in a quasi-adiabatic manner. Finally, we determine the β_{th} parameter [57]:

$$\beta_{th} = \frac{\text{thermal pressure}}{\text{magnetic pressure}} = \frac{n_{e,i}k_B T_{e,i}}{B^2/2\mu_0}, \tag{1.32}$$

where the thermal pressure depends on both electrons and ions. If $\beta_{th} << 1$, the plasma is considered as highly magnetized as the magnetic pressure dominates the interactions in the plasma, while the inner thermal pressure is negligeable. If $\beta_{th} >> 1$, the thermal pressure governs the dynamics of the plasma, which advects the magnetic field. We notice some similarities about the

evolution of the plasma between both the Mach and Alfvén numbers and the β_{th} parameter. Consequently, we can write:

$$\beta_{th} = \frac{2\mu_0 n_{e,i} k_B T_{e,i}}{B^2} = \frac{2}{\gamma}\left(\frac{c_S^2}{v_A^2}\right), \tag{1.33}$$

$$M_A = \sqrt{\frac{\gamma\beta_{th}}{2}}\, M_S \tag{1.34}$$

When $\beta_{th} << 1$, we have $M_S > M_A$, therefore a plasma dominated by the magnetic field is more likely to be supersonic than super-Alfvénic. All these plasma parameters will be calculated and given for each of our studies in the following chapters (Chapter 5 and Chapter 6). These calculations of the plasma parameters are adapted to the study of HED laser-driven plasmas. Therefore, it allows us to use the approximated formulas detailed in this paragraph. Moreover, these dimesionless parameters will permit to exhibit similar behaviors between laser-driven laboratory plasmas and their astrophysical counterparts.

1.2.5 Limits of the *in situ* methods

Currently, astrophysical studies are often slowed down by environmental constraints (for instance, it is difficult to study X-rays emissions directly on the ground, because the Earth atmosphere stops most of these wavelengths), by the occurence of these events (plasma interactions at the edges of the magnetosphere are spatially localized and short in time), and more generally by the distances between the Earth or the observation point and the object (such as the Sun corona or other sources in the Universe). Besides, observations and conclusions made about astrophysical events can be indirect, relying on diagnostics like spectral emissions and absorptions. In cases where no direct measurements can be made, uncertainties cannot be neglected when it comes to the interpretation of these results. Plus, by staying in an observation role, there are no possibilities to modify any parameters of any possible space plasma interaction [58].

Still, the study of astrophysical magnetized plasmas stay of great interest since they proceed on vast scales in systems involving among the highest levels of energy densities. The interactions between these plasmas shape their environment but these transient processes remain difficult to observe in space. However, these phenomena can be investigated under controlled experimental conditions in laboratory experiments. Indeed, if astrophysical studies used to be mainly dominated by observational studies, with terrestrial or spatial telescopes whose results depend on the observed objects, the growth of powerful lasers is a huge step forward for astrophysics and, in our present case, for the study of magnetic fields in plasma. This technology leads to new possibilities in the field of laboratory astrophysics [59], here by using high power lasers which generate plasmas via the laser-matter interaction, presenting similar properties to astrophysical plasmas. Besides, laboratory experiments allow direct measurements and diagnostics, with the asset of adjustable parameters providing precise information about the experimental conditions for each laser shot, as well as repeatatibility properties.

Modern laboratory experiments, as well as numerical models relevant for astrophysics, provide complementary information to address and complete the classical observational methods. Indeed, a technology capable to bring a substantial amount of energy in a plasma flow to reach the HED conditions that exist in space needed to be developed and this became possible with high-power lasers [60].

1.3 High-power lasers

In this part, we are going to mention the key points about high-power lasers that are required in this study. We will describe the different important parameters that we take into account in our work as well as the mechanisms engaged in the formation of plasmas in the laser-matter interaction. Also, it is crucial, in order to validate the results of our study that will be enounced later in this manuscript, to explicit the link between space plasmas and the laser-driven ones

1.3.1 Development of the laser technology

The laser technology started growing in the 1960s, as the first laser was a ruby laser built by the american physicist T.H. Maiman [61]. It relies on the principle of spontaneous and stimulated emission of photons. Lasers provide coherent, monochromatic and collimated light sources. However, it was only during the 1970s and early 1980s that high-power lasers were developped to reach energy at a kilojoule level during a nanosecond-long pulse, as well as intensities on targets around $I \sim 10^{14} - 10^{16}$ W/cm^2. This is the technology that leads to the study of HED physics with lasers in the laboratory [62].

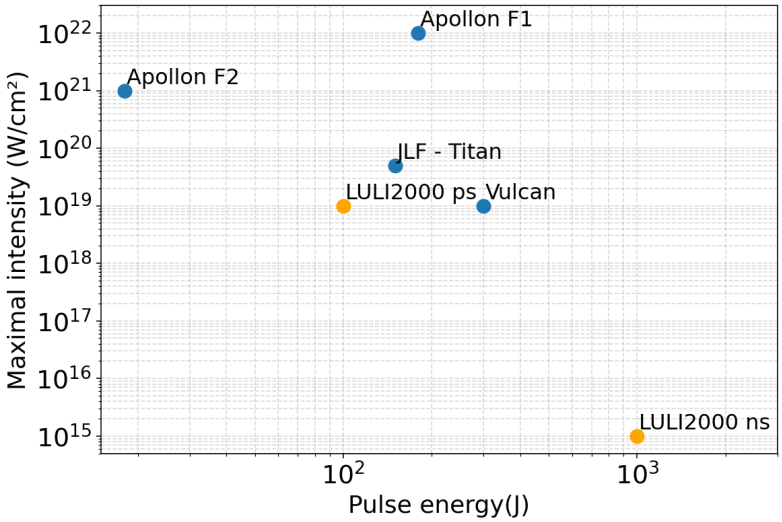

Figure 4. Properties of different laser facilities in the world, presenting high-power and high-intensity lasers. This is a selection among the different laser installations worldwide, all with specific beam characteristics. To ease the reading, we only show here the facilities where the author participated in experiments during the thesis. The lasers that will be later described in the present manuscript and that were used for the experiments for this thesis are marked with orange dots.

The laser is characterized by its amplitude, the duration of its pulse and its frequency ω. The pulse can be considered as a Gaussian shaped pulse in space and in time. The intensity of the beam is then determined by:

$$I(\mathbf{r}, z) = \frac{P}{\pi w(z)^2} \, e^{-2\frac{r^2}{w(z)^2}}, \tag{1.35}$$

where P is the optical power of the beam and w(z) is the weight characterising the beam radius as the distance from the beam propagation axis where the intensity drops to $1/e^2$, which is approximately 13.5 % of the maximal value. Here, the intensity is measured at the position (**r**, z), where z is the coordinate longitudinal to the propagation axis of the beam and **r** the 2D vector characterizing the transversal position. Laser beam pulses are mostly used range from a few femtoseconds (1 fs = 10^{-15} s, « short », « ultrashort » pulses) to a few nanoseconds (1 ns = 10^{-9} s, « long » pulses). Short and intense pulses were made possible during the 1980s with the perfectionning of the Chirped Pulse Amplification (CPA) developed by G. Mourou and D. Strickland who earned the Nobel Price of Physics in 2018 [63]. This technique consists in producing a fs-long and low-energy pulse, that will be stretch to 50 – 200 ps and amplified, before being compressed back to its original duration but carrying the increased energy. With this method, it is possible to develop high intensity lasers, reaching high intensities over I ~ 10^{18} W/cm^2, as the energy is increased while sustaining a short pulse duration (see Figure 5). This paves the way for the studies of new regimes like proton acceleration or relativistic plasmas [64]. Currently, modern facilities like the LULI2000 (see Chapter 4) can combine the two types of beams, with long and short pulses.

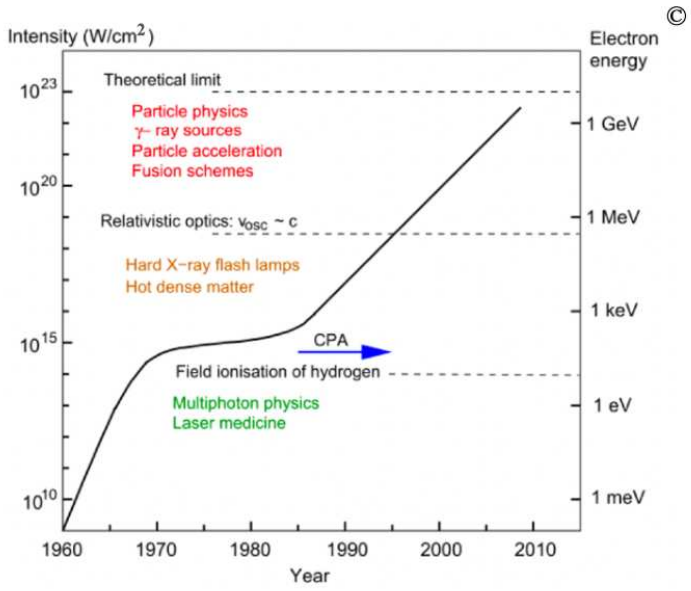

Figure 5. History of laser intensity, showing the progress acceleration made possible with the CPA and the different regimes avoilable (see lectures by M. Borghesi for Queen's University of Belfast [65]).

1.3.2 Generation of magnetized plasmas in the laboratory

Modern high-power lasers are major means to deliver a crucial amount of energy on a selected target. During an interaction of such a pulse with matter (concentrating kilojoule level of energy on a few micron-wide focal spot) not longer than a few nanoseconds, matter is subject to a brutal and high rise of the temperature on its surface, reaching hundreds electron-volts eV, and attaining pressures equivalent to Mbars (10^6 bars). Consequently, the irradiation of targets with high power lasers can generate dense plasmas directly from the target ionization and create HED

conditions, similar to those measured in space, on the surface of the target due to the laser-matter interaction.

Magnetic field strength	$B \sim 10^2$ T
Plasma density for T < 1 keV	$d \sim 10^{26}$ part/m^3
Laser intensity at $\lambda = 1$ μm	$I > 10^{13}$ W/cm^2
Electric field strength	$E \sim 10^{11}$ V/m

Tableau 1. Examples of physical quantities in a HED regime with a pressure of 1 Mbar [66].

The plasma is formed through the ionization of a target irradiated by a high-power laser, which deposits a large amount of energy on its surface. This energy is absorbed via inverse Bremsstrahlung [67]. As the laser beam ionizes the target surface, the free electrons located within the first few layers of the material are excited by the deposited photons and gain energy via collisions with the surrounding ions. These electrons that used to be unperturbed before the pulse acquire an important kinetic energy within an extremely short timescale (with $t < t_{pulse}$). The surface of the target is rapidly ionized, forming a hot and dense plasma.

Electrons are much lighter than ions and protons (with $m_p/m_e = 1836$), so they respond to the perturbation induced by the laser more rapidly than the ions. Consequently, the electrons heated in the focal spot area are quickly accelerated away from the interaction region. This rapid motion of the electrons creates therefore a charge separation between the hot accelerated electrons and the ions that still remain nearby the target surface. Electric fields, that can reach strong values in HED conditions (see Table 1), get formed on the irradiated surface and accelerate the remaining ions, contributing to the plasma ablation from the surface of the target. This ion acceleration leads therefore to the expansion of a dense plasma plume from the target, which is sustained during the whole duration of the laser pulse.

The density of the plasma typically decays exponentially with the distance of expansion away from the target and the level of ionization of the plasma depends on the material composing the target. When irradiated with a laser, light materials like plastic alloys (with a low atomic number Z) produces lighter ions and form a less dense and more rapidly ionized plasma, alongside faster losses of energy. On the contrary, heavier materials like copper (with a higher Z) get more levels of ionization and lead to the generation of denser plasmas [68].

The plasma ablation mechanism described here corresponds to a front-side ablation, where the laser deposits energy and ablates matter on the irradiated side of the target. Back-side ablation is also common in laboratory, where the plasma expands from the opposite side of the target (see Figure 6). In this configuration, if the target is irradiated with a high-power laser carrying a moderate intensity (see Figure 4), the electrons are accelerated and transported through the target by thermal conduction and a hydrodynamic shock wave induced by the energy deposited by the laser. Once the shock wave reaches the back of the target, it triggers the plasma expansion [69].

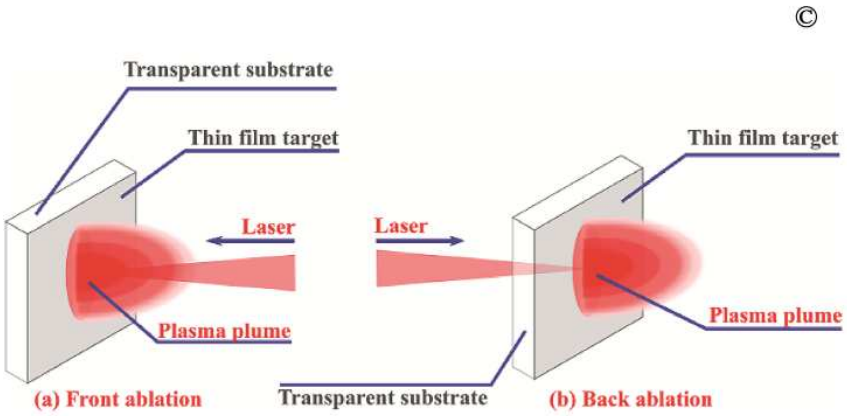

Figure 6. Plasma ablation by laser-matter interaction achievable in laboratory from A. Mondal, R.K. Singh and H.C. Joshi [70].

The plasma expansion resulting from the ablation process of the target by the laser generates and carries the crossed gradients necessary for the generation of a Biermann battery magnetic field. The gradient of electron density n_e is longitudinal to the plasma expansion axis and normal to the target surface while the gradient of electron temperature T_e is transversal and in the target surface plane (see Figure 7) [71]. These are the non-colinear gradients that imply the spontaneous magnetization of the plasma via the Biermann battery effect with no auxiliary magnetic field sources.

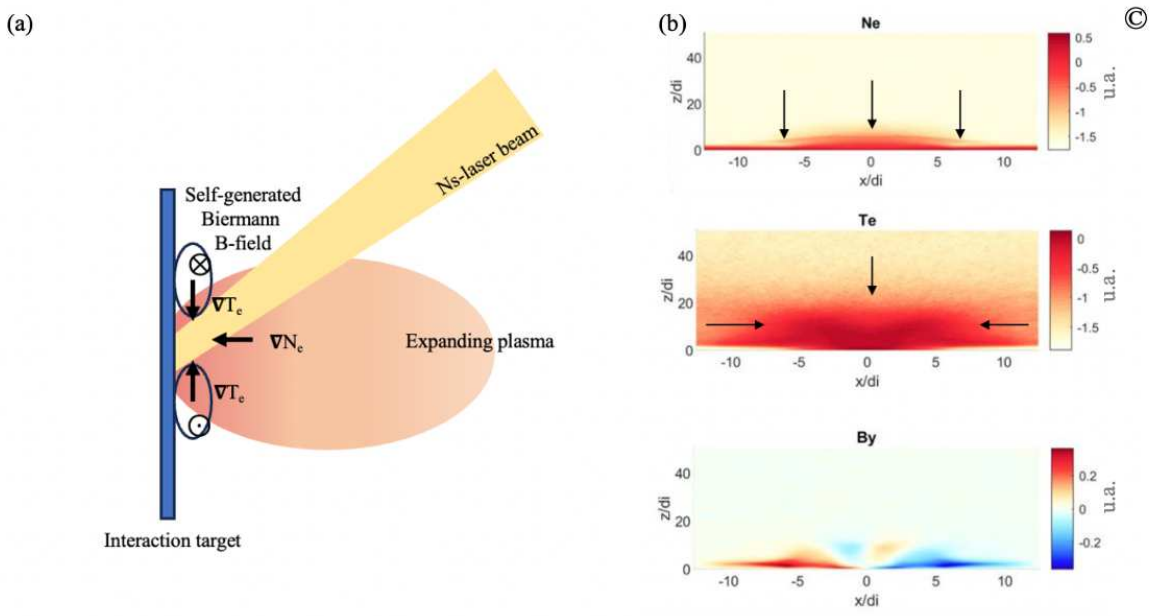

Figure 7. Modeling of the Biermann battery effect in laser-driven plasmas. (a) Schematization of the laser-matter interaction inducing gradients of electron density n_e and temperature T_e during the plasma expansion. The rotation axis of the toroidal magnetic field is represented by the out-of-plane vectors. (b) Kinetic simulations by J. Peery [72] showing the spatial evolution of the electron density and temperature gradients, and consequently the development of the out-of-plane toroidal magnetic field.

The field expansion presents a decaying profile akin to the plasma one, with the strongest amplitude around the laser irradiation zone and a weaker one in less energetic zones at the edges of the plasma plume. Indeed, during the laser-matter interaction, the strongest and sharpest gradients are located all around the borders of the focal spot of the laser beam. Consequently, the Biermann battery magnetic field is an out-of-plane toroidal field, evolving around the axis of expansion of the plasma and the laser focal spot [73].

High power long-pulse lasers permit to investigate Biermann battery self-generated magnetic fields in plasmas in the laboratory, by producing magnetic fields reaching amplitudes of a few hundreds of Teslas on the target surface and expanding jointly with the plasma. In these conditions, the magnetic field is generated and maintained during the entirety duration of the laser pulse, as the continious energy deposition by the laser during the impulsion sustains the required conditions and gradients for the magnetic flux production.

1.3.3 Astrophysical relevance of laser-driven plasmas

Plasmas can be produced nowadays artificially in dedicated facilities such as laser facilities. However, laser-driven plasmas are generated by laser pulses lasting no longer than a few nanoseconds and generally expand on short distances (around 1 mm). These spatial and temporal scales are radically different from their astrophysical counterparts that can expand over thousands of kilometers, which is of course unreachable in the laboratory. In order to be able to draw a legitimate parallel between these two types of plasmas and apply conclusions on the studies of laser-driven plasmas that are relevant for Astrophysics, it is crucial to underline the similarities between experimental and astrophysical conditions, despite evident scale differences.

Scaling laws permit to estimate how comparable two systems are. In the case of laboratory astrophysics, it is possible to assimilate the laser-driven plasmas to the astrophysical ones. Indeed, the physical phenomena occuring on such disparate temporal and spatial scales can be compared since the equations that govern their dynamics show a certain degree of similarity. These levels of similarity are usually classified into classes [74], from exact invariance (exact thermodynamical conditions, regardless temporal or spatial scales [75]) to perfect or partial similarity (experiments only conserve a part of the equations [76]). We also talk about « resemblance » when it comes to laboratory experiments that are not directly comparable to any specific event but provide help to understand a certain physical process.

Consequently, two distinct systems that present comparable dynamical evolutions are described by the same hydrodynamic equations, so then the MHD laws are applicable to both. This similarity allows a comparison of the plasma parameters detailed in 1.2.4. These dimensionless parameters represent the behaviour of the plasma under certain conditions and show the dominant mechanisms and physical processes in the plasma (heat conduction, thermal pressure, magnetic field, …). Furthermore, many astrophysical systems are characterized among else by high conductivity and low diffusivity, which permit to assimilate them to ideal conductive fluids on which ideal MHD laws and the Alfvén theorem can be applied. By comparing laser-driven plasmas with astrophysical plasmas that present the same values for these parameters despite of their dimensions and timescales, it is possible to accurately reproduce relevant physical processes with laboratory plasmas and provide a valid experimental model.

For astrophysics, laboratory experiments are an asset to study mechanisms that are challenging to track with classic instruments and *in situ* observations (such as magnetic rearrangements or particle acceleration) [77]. Modern high-power lasers are a major means to deliver a crucial amount of energy on a selected target and the irradiation of these targets permits to produce dense plasmas as well as the conditions of high energy density that are required on the target surface. Currently, many astrophysical phenomena can be investigated with high-power lasers [78]: active galactic nuclei [79], turbulences and collisionless shocks in supernova remnants [80] and Earth magnetosphere bow shock [81], or collision of galactic clouds [82]. Furthermore, the development of short-pulse and high intensity lasers widens the possibilities of studies to the relativistic plasmas and related astrophysical events, such as relativistic jets [83].

Moreover, the diagnostics used during the experiments in the laboratory, like interferometry or X-ray spectroscopy, provide direct measurements of the different observables (such as the density or the temperature) whereas the classic methods are often performed through indirect observations. These tools give the possibility to realise precise measurements on the plasmas which could not be doable otherwise, as well as a control of the operator over key parameters of the experimental setup, such as the duration or the energy of the laser pulse, the target properties or the delays between the diagnostics and the laser beams. Besides, unlike the astrophysical events which are occasional, infrequent and hard to predict, producing laser-driven plasmas in the laboratory permits the repeatability of the events, by generating multiple times plasmas in similar. Finally, it is crucial to complete the experimental results with simulations to validate the outcome of the experiment and propose a model reliable for both the experimental situation and its astrophysical equivalent.

1.4 Introduction on the studied plasma interactions

We introduced previously that plasmas, whether it is in space or in the laboratory via laser-matter interaction, can be magnetized spontaneously via the Biermann battery effect. This plasma which carries the magnetic field is likely to interact with others magnetized plasmas, which is highly susceptible to happen in space in turbulent regions like the stellar corona and realized in the laboratory with several laser-driven plasmas generated simultaneously. When happening, the interaction between the magnetic fields alters the characteristics of the plasmas in the zone of perturbations, accelerates the charged particles that are subject to the local modification of the electromagnetic fied; and generally, rearranges the magnetic fields involved.

More precisely, in an isolated plasma the magnetic field remains unpertubed, and « frozen-in », as it can be described by the ideal MHD framework. However, in a zone of interaction with another magnetized plasma, each magnetic field is distorted by the encountered external electromagnetic perturbation. In between the plasmas a zone of interaction is formed, within which the MHD model is not ideal anymore and the Alfvén theorem is not effective. The density of magnetic flux is altered, leading to the variation of several quantities like the electron density, the energy distribution, the particles velocities and trajectories, or the pressure.

As plasmas constitute the quasi-entirety of the visible matter in the Universe, interactions and collisions between magnetized plasmas are common and represent an active area of research [84]. Magnetic field redistribution and particle acceleration are still constituting open questions, especially in regard of extreme and high energy densities environments observed in space. Due to the major impact of magnetic fields at every scale of the Universe (from planetary magnetospheres to galaxies), their fluctuations have a crucial role in these intense phenomena. Consequently, magnetic field rearrangements and reconfiguration are expected to be a major answer when it comes to high energy carried and transfered to particles.

In this thesis, we focused on the study of two of these interactions that have an important impact on their medium and on the dynamics of the particles involved in the process: magnetic field compression and magnetic reconnection. Both of these mechanisms have been the subjects of numerical studies through simulations investigating the plasma at different time and spatial cases. Moreover, distinct experimental campaigns have been performed to reproduce and characterise the plasma and the impact of these interactions on the magnetic field. In this work, the plasma is only magnetized via the Biermann battery effect, as it happens in space. No other source of magnetic field has been added in order to observe the evolution of these interactions between self-generated magnetic fields only. Here, we show how we can trigger magnetic compression and reconnection in the laboratory using high power lasers. We also investigate the energy exchanges occuring during the processes, as well as the regime changes between expanding plasmas and the zone of interaction, affecting both the dynamics of the plasma and the topology of the magnetic fields.

Magnetic compression and the properties of the mechanism will be addressed in Chapter 2 alongside the astrophysical context. Similarly, magnetic reconnection will be detailed in Chapter 3. All the characteristics of the facility, the laser beams and the experimental diagnostics used during our experiment, as well as the state-of-the-art of the numerical codes used for our simulation work will be brought forward in Chapter 4, in order to introduce the methods that permitted to get our results. Both these experimental and simulations results about magnetic compression will be presented in Chapter 5 while we will focus on our results and conclusions (once again experimental and theoretical) about magnetic reconnection in Chapter 6.

References

[1] A. Acker, Astronomie Astrophysique, 5th edition, Dunod (April 2019).

[2] R.P. Drake, High-Energy-density Physics: Fundamentals, Inertial Fusion, and Experimental Astrophysics, Springer (January 2006).
https://doi.org/10.1007/978-3-319-67711-8

[3] B. Ryden, Introduction to Cosmology, 2nd edition, Cambridge University Press (November 2016).
https://doi.org/10.1017/9781316651087

[4] NASA, https://science.nasa.gov/solar-system/solar-system-facts/ (website still available in April 2026).

[5] N. Langer and R.P. Kudritzki, « The spectroscopic Hertzsprung-Russell diagram », Astronomy & Astrophysics, Volume 564, A52, (April 2014).
https://doi.org/10.1051/0004-6361/201423374

[6] E.N. Parker, « Dynamics of the Interplanetary Gas and Magnetic Fields », The Astrophysical Journal, Volume 128, 664 (November 1958).
https://doi.org/10.1086/146579

[7] NASA, https://svs.gsfc.nasa.gov/ (website still available in April 2026).

[8] L. Chemin, C. Carignan and T. Foster, « HI kinematics and dynamics of Messier 31 », The Astrophysical Journal, Volume 705, 1395 (September 2009).
https://10.1088/0004-637X/705/2/1395

[9] Curtin University, https://www.curtin.edu.au/news/media-release/curtin-researcher-helps-find-largest-supernova-remnant-by-looking-in-right-place/ (website still available in April 2026)

[10] NASA, https://science.nasa.gov/solar-system/skywatching/night-sky-network/catch-andromeda-rising/ (website still available in April 2026).

[11] B.T. Draine, Physics of the Interstellar and Intergalactic Medium, Princeton University Press (January 2011).

[12] D.D. Clayton, Principles of Stellar Evolution and Nucleosynthesis, University of Chicago Press (January 1984).

[13] D. Martizzi, C-A. Faucher-Giguère, E. Quataert, « Supernova feedback in an inhomogeneous interstellar medium », Monthly Notices of the Royal Astronomical Society, Volume 450, 1, p. 504-522 (June 2015).
https://doi.org/10.1093/mnras/stv562

[14] E.N. Parker, Cosmical Magnetic Fields: Their Origin and their activity, Oxford University Press (1979).

[15] P. Stubbe and T. Hagfors, « The Earth's ionosphere: a wall-less plasma laboratory », Surveys in Geophysics, Volume 18, p. 57-127 (January 1997).
https://doi.org/10.1023/A:1006583101811

[16] M-B. Kallenrode, Space physics: an Introduction to Plasmas and Particles in the Heliosphere and Magnetospheres, Springer (January 2001).
https://doi.org/10.1007/978-3-662-09959-9

[17] F.F. Chen, Introduction to Plasma Physics and Controlled Fusion, 3rd edition, Springer (January 2016).
https://doi.org/10.1007/978-3-319-22309-4

[18] N.A. Krall and A.W. Trivelpiece, Principles of Plasma Physics, Amaerican Journal of Physics, Volume 41, 12 (January 1973).
https://doi.org/10.1119/1.1987587

[19] J.A. Krommes, « An introduction to the physics of the Coulomb logarithm, with emphasis on quantum-mechanical effects », Journal of Plasma Physics, Volume 85, 1 (January 2019).
https://doi.org/10.1017/S0022377818001319

[20] G. Ganguli, M.A. Reynolds and M.W. Liemohn, « The plasmasphere and advances in plasmaspheric research », Journal of Amospheric and Solar-Terrestrial Physics, Volume 62, 17 – 18, p. 1647-1657 (November 2000).
https://doi.org/10.1016/S1364-6826(00)00117-6

[21] G. Briozzo and E. Gallo, « Analytical expressions for pulse profile of neutron stars in plasma environments », The European Physical Journal C, Volume 83, 165 (February 2023).
https://doi.org/10.1140/epjc/s10052-023-11331-2

[22] B. Czerny *et al*, « Dusty plasma in active galactic nuclei », The European Physical Journal D, Volume 77, 56 (April 2023).
https://doi.org/10.1140/epjd/s10053-023-00630-8

[23] A. Pe'er, « Plasmas in Gamma-Ray Bursts: Particle Acceleration, Magnetic Fields, Radiative Processes and Environments », Galaxies, Volume 7, 33 (February 2019).
https://doi.org/10.3390/galaxies7010033

[24] National Academies, Fundamental research in high energy density science (Chapter 1), Washington DC: The National Academies Press (February 2023).
https://doi.org/10.17226/26728

[25] C.N. Danson *et al*, « Petawatt and exawatt lasers worldwide », High Power Laser Science and Engineering, Volume 7, 54 (August 2019).
https://doi.org/10.1017/hpl.2019.36

[26] W. Bang *et al*, « Review of laser-plasma physcis research and applications in Korea », Fluids, Plasma and Phenomenology, Volume 80, p. 698-716 (January 2022).
https://doi.org/10.1007/s40042-021-00391-w

[27] P.A. Davidson, An Introduction to Magnetohydrodynamics, Cambridge University Press (February 2010).
https://doi.org/10.1017/CBO9780511626333

[28] L.D. Landau and E.M. Lifshitz, Fluid Mechanics, Oxford Pergamon Press (1987).
https://doi.org/10.1016/B978-0-08-033933-7.50009-X

[29] R.M. Kulsrud, Plasma Physics for Astrophysics, Princeton University Press (December 2004).

[30] A. Hruska, « Fluid description of a collisionless plasma and electric current systems in cosmic plasmas », Astrophysics and Space Science, Volume 62, p. 491-508 (May 1979).
https://doi.org/10.1007/BF00645483

[31] Y.L. Klimontovich, « Physics of collisionless plasma », Physics-Uspekhi, Volume 40, 1 (1997).
https://doi.org/10.1070/PU1997v040n01ABEH000200

[32] A.A. Vlasov, Many Particles Theory and its Application to Plasma, U.S. Atomic Energy Commission, Technical Information Service Extension (1961).

[33] V. Vedenyapin, A. Sinitsyn and E. Dulov, « Kinetic Boltzmann, Vlasov and related Equations », Chapter 3, p. 19-28 (June 2011).
https://doi.org/10.1016/C2011-0-00134-5

[34] R.M. Williams *et al*, « Supernova Remnants in the Magellanic Clouds. I. The Colliding Remnants DEM L316 », The astrophysical Journal, Volume 480, p.618-632 (May 1997).
https://doi.org/10.1086/303990

[35] A. Müller, B. M. Poggianti *et al*, « Highly ordered magnetic fields in the tail of the jellyfish galaxy JO206 », Nature Astronomy, Volume 5, p.159-168 (January 2021).
https://doi.org/10.48550/arXiv.2009.13287

[36] E.R. Most, J. Noronha and A.A. Philippov, « Modelling general-relativistic plasmas with collisionless moments and dissipative two-fluid magnetohydrodynamics », Monthly Notices of the Royal Astronomical Society, Volume 514, 4, p.4989-5003 (August 2022).
https://doi.org/10.1093/mnras/stac1435

[37] N. Murphy, « Conservation Laws in Ideal MHD », Harvard-Smithsonian Center for Astrophysics (February 2016).
https://lweb.cfa.harvard.edu/~namurphy/Lectures/Ay253_2016_03_Conservation_Laws.pdf

[38] H. Alfvén, « Existence of Electromagnetic-Hydrodynamic Waves », Nature, Volume 150, 3805, p. 405-406 (October 1942).
https://doi.org/10.1038/150405d0

[39] Z. Chen, « Influence of external magnetic field on the electronic structure and radiative properties in plasm-embedded multi-electron atomic systems », Journal of Electron Spectroscopy and Related Phenomena, Volume 258, 147223 (July 2022).
https://doi.org/10.1016/j.elspec.2022.147223

[40] L. Biermann and A. Schlüter, « Cosmic radiation and cosmic magnetic fields. II. Origins of cosmic magnetic fields », Physical Review, Volume 82, 6, (June1951).
https://doi.org/10.1103/PhysRev.82.863

[41] L. Biermann, « Origin of magnetic fields on stars and in interstellar space », Naturforsch, Volume 5, p. 65-71 (1950).

[42] V.B. Belakhovsky *et al*, « Geomagnetic and ionospheric response to the interplanetary shock on January 24, 2012 », Earth, Planets and Space, Volume 69, 105 (August 2017).
https://doi.org/10.1186/s40623-017-0696-1

[43] F. Zhao, M. Alvarez and T. Abel, « The Biermann battery and early Structure Formation », AIP Conf. Proc., 990, p.39-41 (March 2008).
https://doi.org/10.1063/1.2905616

[44] K.M. Schoeffler, N.F. Loureiro *et al,* « The generation of magnetic fields by the Biermann battery and the interplay with the Weibel instability », Phys. Plasmas, 23 (April 2016).
https://doi.org/10.1063/1.4946017

[45] A.R. Bell *et al*, « Cosmic-ray acceleration and escape from supernova remnants », Monthly Notices of the Royal Astronomical Society, Volume 431, 1, p. 415-429 (May 2013). https://doi.org/10.1093/mnras/stt179

[46] A. Riols and G. Lesur, « Dust settling and rings in the outer regions of protoplanetary discs subject to ambipolar diffusion », Astronomy & Astrophysics, Volume 617, 117 (September 2018). https://doi.org/10.1051/0004-6361/201833212

[47] D.D. Ryutov *et al*, « Similarity Criteria for the Laboratory Simulation of Supernova Hydrodynamics », The Astrophysical Journal, Volume 518, 821 (June 1999). https://doi.org/10.1086/307293

[48] L.D. Landau & E.M. Liftshitz, *Fluid mechanics*, Volume 6 of Course of Theoretical Physics, Second Edition (Janvier 1985).

[49] D.D. Ryutov, R.P. Drake and B.A. Remington, « Criteria for scaled laboratory simulations of astrophysical MHD phenomena », Astrophysical Journal Supplement Series, Volume 127, 465 (April 2000). https://doi.org/10.1086/313320

[50] A.S. Richardson, NRL Plasma Formulary, Plasma Physics Division, Naval Research Laboratory (2019 edition).

[51] S.I. Braginskii, Transport processes in a plasma, Review of Plasma Physics, Volume 1, pp. 205-311 (M.A. Leontovich, New York, 1965).

[52] D.D. Ryutov *et al*, « Similarity criteria for the laboratory simulation of supernova hydrodynamics », Astrophysical Journal, Volume 518, 821 (June 1999). https://doi.org/10.1086/307293

[53] K. Jadhav and A.J. Chandy, « Large eddy simulations of high-magnetic Reynolds number magnetohydrodynamic turbulence for non-helical and helical initial conditions: A study of two sub-grid scale models », Physics of Fluids, Volume 33, 085131 (August 2021). https://doi.org/10.1063/5.0060925

[54] L. Spitzer, Physics of fully ionized gases, Interscience Publishers (2nd edition, 1962).

[55] D.D. Ryutov, « Scaling laws for dynamical plasma phenomena », Phys. Plasmas, Volume 25, 100501 (October 2018). https://doi.org/10.1063/1.5042254

[56] D.D. Ryutov, R.P. Drake and B.A. Remington, « Criteria for scaled laboratory simulations of astrophysical MHD phenomena », Astrophysical Journal Supplement Series, Volume 127, 465 (April 2000). https://doi.org/10.1086/313320

[57] H.E.J. Koskinen and E. Kilpua, Physics of Earth's Radiation Belts, Chapter 1, p. 1-25, Springer (October 2021). https://doi.org/10.1007/978-3-030-82167-8_1

[58] S. Lebedev *et al*, « Laboratory Astrophysics and Collimated Stellar Outflows: The Production of Radiatively cooled Hypersonic Plasma Jets », The Astrophysical Journal, Volume 564, 1, p. 113-119 (August 2001).
https://doi.org/10.1086/324183

[59] H. Takabe and Y. Kuramitsu, « Recent progress of laboratory astrophysics with intense lasers », High Power Laser Science and Engineering, Volume 9 (July 2021).
https://doi.org/10.1017/hpl.2021.35

[60] B.A. Remington, R.P. Drake and D.D. Ryutov, « Experimental astrophysics with high power lasers and Z pinches », Reviews of Modern Physics, Volume 78, 755 (September 2006).
https://doi.org/10.1103/RevModPhys.78.755

[61] T.H. Maiman, « Stimulated Optical Radiation in Ruby », Nature, Volume 187, p. 493-494 (August 1960).
https://doi.org/10.1038/187493a0

[62] R.P. Drake, High-Energy-Density Physics, 1st edition, Springer (August 2006).
https://doi.org/10.1007/3-540-29315-9

[63] D. Strickland and G. Mourou, « Compression of amplified chirped optical pulses », Optics Communications, Volume 56, 3, p. 219-221 (December 1985).
https://doi.org/10.1016/0030-4018(85)90120-8

[64] A.J. Gonsalves *et al*, « Petawatt laser guiding and Electrom beam Acceleration to 8 GeV in a Laser-heated Capillary discharge waveguide », Phys. Rev. Lett., Volume 122, 084801 (February 2019).
https://doi.org/10.1103/PhysRevLett.122.084801

[65] M. Borghesi, « Ion Acceleration: TNSA and beyond », Lecture 1, Queen's University of Belfast.
https://ilil.ino.cnr.it/wp-content/uploads/2018/06/LPACAPRI2017-part1_Borghesi.pdf

[66] R. Davison *et al,* Frontiers of High Energy Density Physics, National Academies Press (2004).

[67] J.G. Lunney and R. Jordan, « Pulsed laser ablation of metals », Applied Surface Science, Volumes 127-129, p. 941-946 (May 1998).
https://doi.org/10.1016/S0169-4332(97)00770-8

[68] J.F. Young, Experimental Methods in the Physical Sciences, Academic Press (1997).

[69] K. Jakubowska, « Short-pulse Laser-driven strong shock waves », in Progress in Ultrafast Intense Laser Science XIV, Springer, Volume 118, p. 271 – 286 (December 2018).
https://doi.org/10.1007/978-3-030-03786-4_15

[70] A. Mondal, R.K. Singh and H.C. Joshi, « Neutral and ion composition of laser produced lithium plasma plume in front and back ablation of thin film », Journal of Analytical Atomic Spectrometry, Issue 9 (June 2019).
https://doi.org/10.1039/C9JA00158A

[71] Y. Ohira, « The Biermann battery driven by a streaming plasma », The Astrophysical Journal, Volume 911 (Avril 2021).
https://doi.org/10.3847/1538-4357/abec41

[72] J. Peery *et al*, « Kinetic simulation of magnetic field generation via the Biermann Battery effect for laser-driven HED experimental conditions » (Poster presentation).
https://suli.pppl.gov/2018/2018%20SULI%20deliverables%20%281%29/Peery/Su_p.pdf

[73] K.M. Schoeffler, N.F. Loureiro *et al*, « The generation of magnetic fields by the Biermann battery and interplay with the Weibel instability », Phys. Plasmas, Volume 23, 056304 (April 2016).
https://doi.org/10.1063/1.4946017

[74] E. Falize, C. Michaut and S. Bouquet, « Similarity properties and scaling laws of radiation hydrodynamic flow in laboratory astrophysics», The Astrophysical Journal, Volume 730, 2 (March 2011).
https://doi.org/10.1088/0004-637X/730/2/96

[75] H. Takabe, « Astrophysics with Intense and Ultra-Intense Lasers – Laser Astrophysics », Progress of Theoretical Physics Supplement, Volume 143 (July 2001).
https://doi.org/10.1143/PTPS.143.202/1875851

[76] D.D. Ryutov and B.A. Remington, « A 'perfect' hydrodynamic similarity and effect of the Reynolds number on the global scale motion », Phys. Plasmas, Volume 10, p. 2629-2632 (July 2003).
https://doi.org/10.1063/1.1578488

[77] D.D. Ryutov, B.A. Remington *et al*, « Magnetohydrodynamic scaling: from astrophysics to the laboratory », Phys. Plasmas, Volume 8, p. 1804-1816 (May 2001).
https://doi.org/10.1063/1.1344562

[78] B.A. Remington *et al*, « A review of astrophysics experiments on intense lasers », Phys. Plasmas, Volume 7, p. 1641-1652 (May 2000).
https://doi.org/10.1063/1.874046

[79] A. Levinson and R. Blandford, « Raman scattering in high-radio-brightness astrophysical systems: application to active galactic nuclei », Monthly Notices of the Royal Astronomical Society, Volume 274, 3, p.717-729 (June 1995).
https://doi.org/10.1093/mnras/274.3.717

[80] N.C. Woolsey *et al*, « Collisionless shock and supernova remnant simulations on VULCAN », Phys. Plasmas, Volume 8, p. 2439-2445 (May 2001).
https://doi.org/10.1063/1.1351831

[81] A.R. Bell *et al*, « Collisionless shock in a laser-produced ablating plasma », Phys. Rev. A, Volume 38, 1363 (August 1988).
https://doi.org/10.1103/PhysRevA.38.1363

[82] T.S. Perry *et al*, « Opacity Measurements in a Hot Dense Medium », Phys. Rev. Lett, Volume 67, 3784 (December 1991).
https://doi.org/10.1103/PhysRevLett.67.3784

[83] R. Bingham, Laser-plasma interactions, Chapter 8, CRC Press (March 2009).

[84] A.H. Boozer, « Physics of magnetically confined plasmas », Rev. Mod. Phys., Volume 76, 1071 (January 2005).
https://doi.org/10.1103/RevModPhys.76.1071

Chapitre 2

Magnetic field compression in HED magnetized plasmas

In this chapter, we are going to focus in more details on the first mechanism mentioned previously, which is magnetic field compression. Here, we will present the main properties of the process and introduce the subjects of our work. The experimental devices and simulation codes will be addressed in chapter 4, while the results will be discussed in chapter 5. Here we are going to develop the physical mechanisms occuring during the compression of magnetic fields, how it influences the plasma involved in the process and how we build our experimental campaign on this subject. Moreover, we will define the objectives of our work as well as the physical mechanisms that interviene in the magnetic compression we focused on.

2.1 General description of the magnetic compression

2.1.1 Definition

We consider two identical HED magnetized plasmas, counter-propagating toward each other with a velocity **v**. As long as the plasmas remain unperturbed, their magnetic field are frozen as described in 1.2.3.1. However, in the case where the plasmas interact with each other, the field of each plasma alters the other. Consequently, the Alfvén theorem is not verified anymore in the zone of interaction and variations of the magnetic flux happen. In a configuration where two HED magnetized plasmas interact and collide, magnetic compression occurs when the plasmas collide if the magnetic fields they carry are oriented parallel to each other in the zone of interaction [1]. The zone of collision is known as the compression region, and a distinct and localized compression sheet appears in this area.

During the collision, each plasma plume penetrates the magnetic field carried by the opposite plasma, with a velocity **v** perpendicular to the magnetic flux. As plasmas are conductors, the collision results in the formation of a motional electric field $\mathbf{E} = -\mathbf{v} \times \mathbf{B}$ in the zone of interaction that modifies the dynamics of the plasma in the compression zone. As the interacting plasmas counterpropagate toward each other, the magnetic flows converge toward the interaction zone where they accumulate. Therefore, the magnetic flied strength increases quickly in the compression zone, forming the distinct compression sheet with a significantly higher magnetic pressure (see Figure 8).

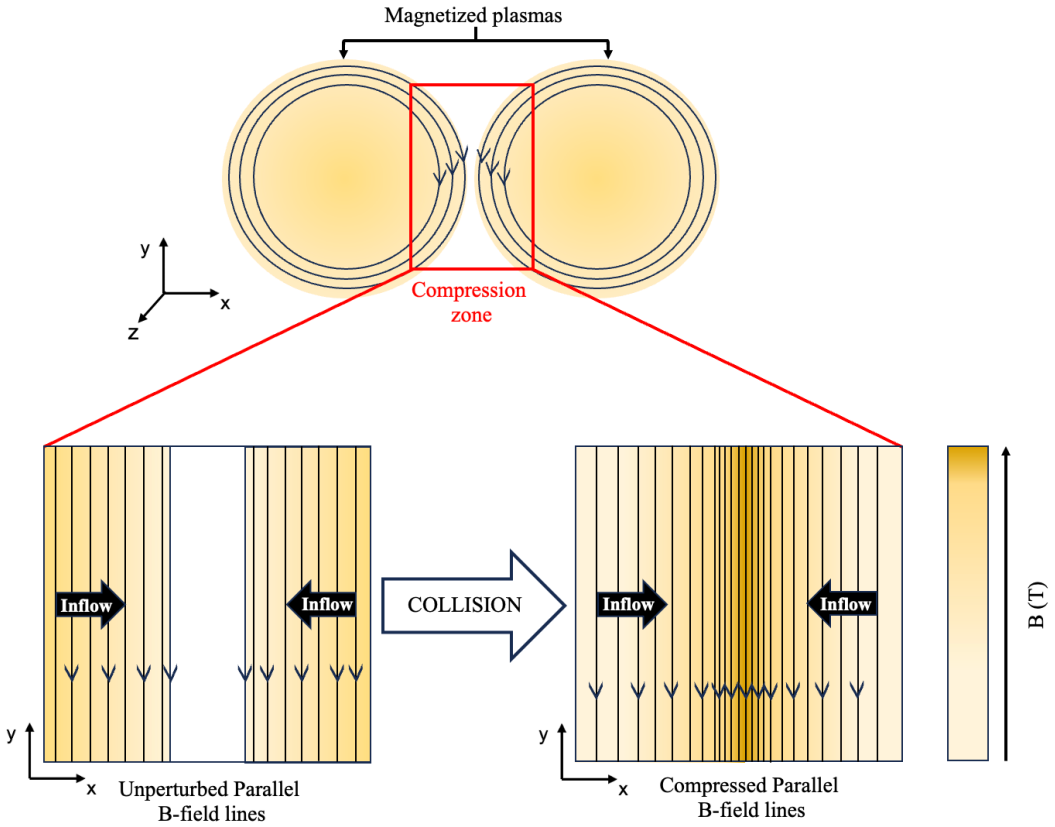

Figure 8. Schematization of the magnetic compression mechanism in the compression zone between two magnetized plasmas. The field lines are represented by the thin black arrows, oriented along the y-axis. A close-up of the compression zone shows the field lines before and after the interaction between the two plasmas that induce the compression. The plasma motion and the inflows of particles they brought in the compression are represented by the large symmetrical arrows along the x-axis.

The compressed field lines behave as a bottleneck for particles in the compression zone. As the charged particles composing the plasma follow these lines, the particle density increases too in the compression sheet. Consequently, the arising magnetic field and density of field lines lead to an accumulation of magnetic flux. The plasma flows converge in the zone and for such magnetized plasmas colliding with a velocity **v**, we have $\nabla \cdot \mathbf{v} \leq 0$. In the MHD model, the evolution of the the internal pressure of a system is given by the following Euler equation:

$$\frac{\partial \mathrm{P}}{\partial \mathrm{t}} = -\gamma \nabla \mathbf{v} \qquad (2.1)$$

As $\nabla \cdot \mathbf{v} \leq 0$, the pressure rate $\frac{\partial P}{\partial t} \geq 0$ and the pressure in the compression sheet increases jointly with the amplitude of the magnetic field and the field lines and particles densities [2].

2.1.2 Astrophysical context

Magnetic compression is an active area of research in Astrophysics as it is suspected to play a key role among the various interactions occurring between HED magnetized plasmas in the Universe. These interactions mainly take place in highly energetic and turbulent environments. As mentioned previously, compression occurs as soon as the conditions on the magnetic field geometry are met and the magnetic flux accumulates in the compression sheet. The resulting local amplification of the magnetic field strength is associated with a rising magnetic pressure. Both the magnetic pressure gradients and the motional electric field located within the compression sheet are major means for transfers of energy from the plasma bulk to the particles, leading in particle acceleration [3]. Besides, the mechanism magnetic compression and its effects on local aspects and topologies of magnetic fields are ubiquitous and can take place over a wide range of spatio-temporal scales and environments across the Universe. In each case, the dynamics of the involved plasmas is deeply influence by the converging magnetic flows as well as by the resulting energy exchanges. Therefore, magnetic compression is a fundamental process playing a key role in the magnetic field amplification and the particle energization that can intervene in plasma interactions throughout various astrophysical systems [4].

Magnetic compression can be observed in near-Earth events, at the edges of the magnetosphere where it interacts with the solar wind [5]. The surface of the Sun, called the photosphere, is turbulent and favourable to plasma interactions, and the plasma flows can get locally even more magnetized through mechanims as the Biermann battery effect. Due to the dynamic of this region, the magnetic fields can induce a local compression in the plasma if they happen to be in the required configuration. In this case, the plasma becomes locally unstable, which leads to the amplification of the magnetic field. It has been observed that, as the matter is compressed, this mechanism can result in intense solar activity as solar flares, inducing plasma ejections in the corona. The corona is the nonuniform external layer of the Sun atmosphere, highly magnetized by the magnetic field of the Sun [6]. When solar eruptions occur, two magnetized mediums interact. The plasma eruptions can either reconnect with the local field on the surface of the Sun within the photosphere or be released in the corona toward the circumstellar medium. In this case, these coronal mass ejectas (CME in this manuscript) contribute to nurtur the solar wind which carries the interplanetary magnetic field (IMF in this manuscript) from the Sun until the limits of the heliopause. The IMF is frozen in the solar wind and is advected by the plasma [7] within the Solar System.

We call « magnetosphere » the domain of influence of the inner magnetic field of a planet or a star, delimited by the magnetopause. For the planets in the Solar System presenting a magnetic field and then a magnetosphere, the field lines are oriented from the South Pole to the North Pole but are shaped by the interaction with the solar wind. Upstream the magnetosphere on the daylight side we find the bow shock, defining the magnetosheath. Magnetic field rearrangements occur in this area. The amount of plasma interacting with the magnetosphere shapes the magnetic field around the Earth. The collision between the solar wind and the plasma contained within a planetary

magnetosphere will shape the field lines of the magnetic field and redistribute the plasma inside the limits of the magnetopause [8]. As the two magnetic fields interact, the plasma inflows are redistributed at the edges of the magnetosphere. This phenomenom can lead to a local compression of the magnetic field lines around the planet, depending on how the field lines are oriented (see Figure 9). These phenomena have already been measured by on-ground facilities and spacecrafts located near the compression zone [9], exhibiting a local amplification of the magnetic field as well as a change of the plasma parameters in the zone.

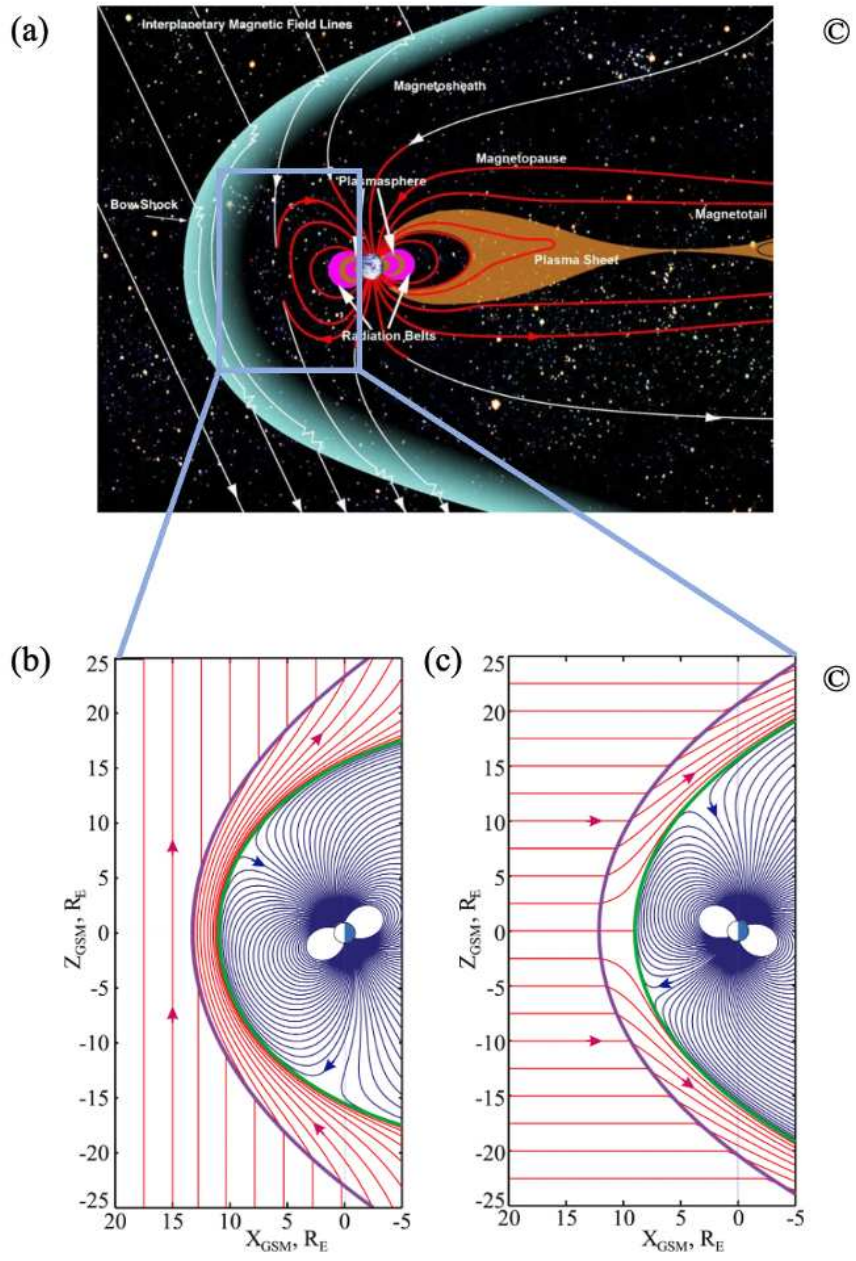

Figure 9. Scheme of the Earth magnetosphere (a) from NASA [10] and representation of the interaction between the IMF (red arrows) and the planetary field (blue arrows) in the cases where the IMF field lines are parallel (b) or perpendicular (c) to the Earth field lines. The magnetopause is represented by the thick green line and the bow shock upstream the magnetosphere by the purple line. The plots are represented in the Geocentric Solar Magnetospheric (GSM) coordinates and scaled with the radius of the Earth (R_E) as a reference. From N.A. Tsyganenko et al *[11].*

The pattern of magnetic fields leading to magnetic compression is a common feature in the propagation of the stellar winds, as well as in diverse turbulent environements implying magnetized astrophysical plasmas. For instance, as for CME and stellar wind, compression can occur around supernovae remnants, between its expansions and the ISM [12]. More generally, different types of magnetized plasmas can be submitted to magnetic field compression, including plasmas under relativistic regimes [13].

As mentioned previously, we dispose of spacecrafts orbiting in specific regions in the Earth magnetosphere, as well as on-ground technologies like telescopes able to measure the compression and its effects in space. Despite these devices, observations and measures of compressed magnetic fields in space are constrained by the occurrence of the interactions that generate them, as well as by their limited spatio-temporal scales. For instance, CME only last a few hours and their interactions with the Earth magnetosphere remain spatially localized [14]. Consequently, *in situ* measurements require a certain proximity with the interaction regions and are generally difficult to obtain. As a result, laboratory experiments using high-power lasers, associated to numerical works, provide the possibility to generate magnetized plasmas in a controlled environment and under reproducible conditions in order to set up the magnetic compression. Besides, previous works have shown that it is possible to recreate magnetic compression in laboratory between laser-driven magnetized plasmas presenting parameters (see 1.2.4.) close to the astrophysical ones [15].

2.2 Dynamics of the compression zone

2.2.1 Establishment of the compression sheet

The plasmas collide in the zone of interaction designated as the compression zone. This specific area of the system contains the accumulated magnetic flux carried by the growing density of field lines. This mechanism leads to the formation of a compression sheet, characterized by a distinct increase of the amplitude of the magnetic field, marking a clear transition with the surrounding plasma. This compression sheet is located at the edges of the plasmas and is oriented following a preferential axis, parallel to the compressed lines. It is maintained over the whole duration of the compression by the continuous flows of charged particles incoming with the colliding plasmas.

As each plasma penetrates the magnetic field **B** of the other one with an inflow velocity **v**, perpendicular to the field lines and consequently orthogonal to the preferential axis of the forming compression sheet, these non-colinear vectors lead to the apparation of a longitudinal convection electric field $\mathbf{E}_{//} \neq 0$, along the compression sheet. It appears on each side of the compression sheet, as both plasmas collide with each other with a certain velocity and carry a magnetic field. The electric field is oriented along and parallel to the compression sheet, and is induced by $-\mathbf{v} \times \mathbf{B}$ [16].

Consequently, the inflow charged particles brought in the compression zone are redirected in the sheet by following the inner electromagnetic field [17]. Indeed, as the colliding plasmas are considered as ideal before the start of the compression process, the field lines are frozen and the

ideal MHD laws imply an infinite conductivity (ie $\mathbf{E} \sim 0$). The apparition of $\mathbf{E}_{//} \neq 0$ in the sheet and the compression of the field highlight a change toward a non-ideal regime in the sheet, inducing there a finite conductivity. An anisotropy in the particle distribution is established within the compression zone and therefore establish a transit of particles through the sheet. As a result, particles are accelerated and ejected out of the zone, creating a corresponding outflow of particles [18]. This particular motion of the particles, associated to the local high density of field lines, leads to a confinement of the magnetic field in the compression sheet.

2.2.2 Characteristic saturation of the magnetic field

We consider that the plasmas expand freely before the interaction (such as the Alfvén theorem is verified), while the compressed plasma is confined in the compression sheet, which is a zone of interaction and energy exchanges. Consequently, there is a clear transition between the two regimes, from a dynamic where the magnetic field is first advected by the plasma to a configuration where the magnetic field guides the flow.

However, the amplitude of the compressed magnetic field does not increase linearly nor indefinitely with the incoming plasma flux during the interaction. Instead, both experimental and numerical studies, as well as astronomical observations, have shown that the amplification of the magnetic field in the compressed plasma reaches a defined saturation value [19]. The saturation of the amplification of the magnetic field strength in the compression sheet reflects the existence of inner mechanisms that counterbalance the plasma inflows. Moreover, the link between magnetic compression and the acceleration and ejection of particles out of the compression sheet through the motional electric field reveals that a constant flux of particles transits through the interaction zone, which compensates the accumulation of magnetic flux in the sheet. As a result, the saturation of the compressed field is reached when the compression sheet attains a dynamical equilibrium state where the different mechanisms shaping the sheet are balanced. Consequently, it is crucial to estimate the different limiting processes, the energy exchanges operating in the compression zone, as well as the influence of the different involved parameters on the saturation to understand correctly the dynamics of the compressed plasma in the sheet.

Therefore, we also define the compression rate to characterize the compression, by calculating the ratio between the amplitudes of the compressed field and the unpertubed reference field measured in the absence of compression. This saturation property of the magnetic field in the compression zone is a means to predict the strength of the compression but also to compare different plasma configurations and their parameters.

2.3 Model of the compressed magnetic mirror

A compression sheet reaches a state of equilibrium as the amplitude of the compressed magnetic field saturates. In a magnetized plasma, a magnetic field B is considered stable in the kinetic framework if it evolves over spatial characteristic scales that are larger than the ion Larmor radius but also if its temporal variations remain slower than the characteristic ion timescales (where $t >> \omega_{pi}^{-1}$). Therefore, ions and their trajectories remain adjusted with the evolutions of the magnetic field. In this case, the individual ion-electron scalar magnetic momentum μ_B is considered as an invariant of the system and is conserved in the compression sheet, so μ_B is defined by [20]:

$$\mu_B = \frac{m v_\perp^2}{2B} = \text{constant}\ , \tag{2.2}$$

where m is the mass of the charged particle and $v_\perp$ is the perpendicular component of the particle velocity with respect to the magnetic field direction. Indeed, when a charged particle oscillates along a magnetic field line, the motion of the particle is gyrotropic and the particle global velocity can be written $\mathbf{v} = v_\perp + v_\parallel$, where $v_\parallel$ is the parallel component. In a zone where the amplitude of B increases, like in the compression sheet, then $v_\perp$ is expected to raise jointly in order to guarantee the conservation of the magnetic momentum μ_B. However, in a collisionless plasma governed by the magnetic field, the total kinetic energy $E = \frac{1}{2} m v^2$ is conserved so $v_\perp^2 + v_\parallel^2$ is constant. Consequently, if $v_\perp^2$ increases to maintain a constant magnetic momentum, therefore $v_\parallel^2$ decreases. For a sufficiently high value of the amplitude of the magnetic field B in the sheet, the velocity of a particle is entirely defined by its component perpendicular to the field $v_\perp^2$ as the parallel component of the energy E is entirely converted. Therefore, for an increasing B, we have $v_\parallel^2 \rightarrow 0$. In this case, the particle is entirely reflected out of the compression zone, which then behaves like a magnetic mirror [21].

We mentioned previously that the motion of the particle flow in the compression sheet is highly anisotropic due to the motional electric field. As particles still go through the sheet, the anisotropy implies that particles incoming in the compression region enters the sheet only if they are aligned with the magnetic field and therefore, it exists an angle above which a particle is deflected out and prevented from entering the sheet. We can then define this limit angle θ_0 above which a particle is reflected (see Figure 10). In the case of an increasing amplitude caused by magnetic field compression, we have $B_{comp} >> B_0$, where B_0 is the average magnetic field in the incoming plasma flow. We have [22]:

$$\sin^2 \theta_0 = \frac{B_0}{B_{comp}} \tag{2.3}$$

A particle is deflected by the strong compressed magnetic for an angle θ such as $\theta_0 < \theta$. Therefore, we have the condition:

$$\theta_0 = \sin^{-1}\left(\sqrt{\frac{B_0}{B_{comp}}}\right) < \theta \tag{2.4}$$

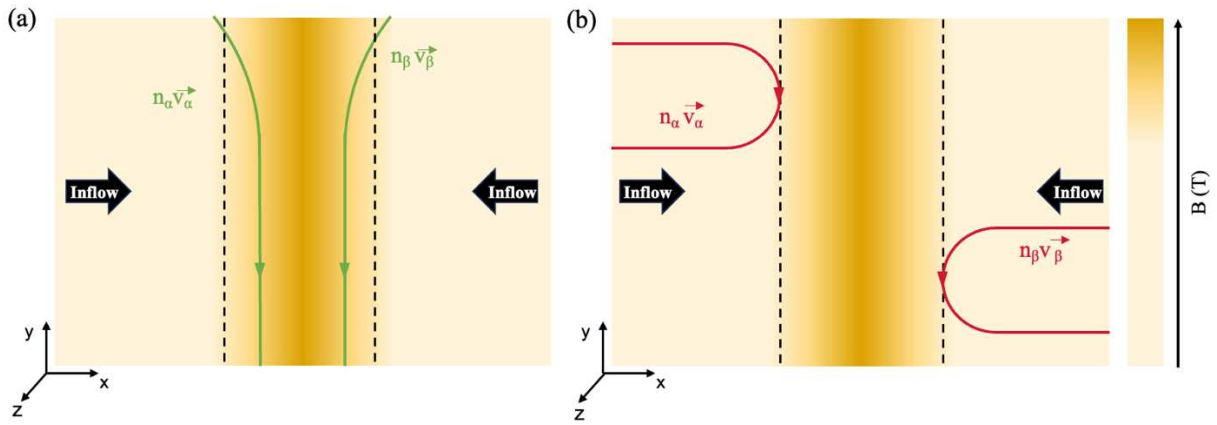

Figure 10. Schemes of the two situations in the case of the interaction of particles of densities n_α, n_β and velocities v_α, v_β with the magnetic mirror. (a) The inflow particles, whose trajectories are modeled by the green lines, have an incident angle $\theta < \theta_0$ and enter the compression sheet. (b) The inflow particles, whose trajectories are modeled by the red lines, have an incident angle $\theta > \theta_0$ and are reflected.

As the magnetic field strength B_{comp} increases in the compression sheet, the ratio B_0/B_{comp} decreases and, as established with eq. 2.4, so does the value of the limit angle θ_0. Therefore, an increasing proportion of the incoming particles does not enter the compression sheet, inducing that the compression sheet becomes less accessible to the plasma inflow. This mechanism limits the transport of particles through the sheet, which reduces the efficiency of the compression process as well as reinforce the confining aspects of the compression sheet.

2.4 Framework of the study

2.4.1 Context

Our study of magnetic field compression is grounded into the study of interactions between magnetized astrophysical plasmas in the laboratory by generating laser-driven plasmas. Previous works in the field have already proved that the plasmas generated via laser-matter interaction present similar characteristic parameters with space plasmas, despite radically smaller spatio-temporal scales which make them possible to handle. The *in situ* observations of magnetic compression in space are limited partly by the probability of detection of the process by nearby instruments, as well as by the succint and localized aspects of the mechanism.

These are precisely the circumstances under which the laboratory study of the mechanism is legitimate. Here, we focus on magnetic compression between two expanding plasmas, as it can happen naturally in the Universe (see 2.1.2.). Consequently, we rely experimentally on the self-generation of magnetic field via the Biermann battery effect. In this situation, the expanding plasma resulting from the laser-matter interaction carries a toroidal spontaneous magnetic field.

Today, it is possible to generate such plasmas in the laboratory and to establish a complete setup to prompt the compression. Besides, the use of experimental diagnostics enables to track the evolution of the different physical quantities affected by the compression, and the repeatability of the conditions of the experiment can confirm their recurring behaviors during the compression process. Consequently, the study of magnetic field compression is a suitable subject for the laboratory astrophysics framework to provide relevant results, complementary to the classical methods of measurements.

2.4.2 Aims and structure of the research work

In this thesis, we are going to describe our study of magnetic field compression in the laboratory using plasmas generated by high power lasers, from the experimental setup to the analysis of the collected data and the supporting numerical simulations. The aim of the study is to characterize the experimentally observed compression as well as the expected saturation of the compressed field. In this study, we chose to rely entirely on the Biermann battery effect to magnetize the plasmas that will induce the compression process during their interaction.

We will present the different diagnostics used during the experiment and then describe the evolution of the sheet through its density, its temperature or the amplitude of the compressed field. Furthermore, the analysis of the experimental data is directly linked to numerical simulations that were run to model mechanisms encountered during the process. Both hydrodynamic and particle-in-cell (PIC in this manuscript) simulations (see Chapter 4, section 4.2) were used to draw a complete analysis of the compression sheet at different scales. Finally, the theoretical part of our study constitutes a continuity of hybrid simulations published by Sladkov *et al* [23] (alongside our experimental results). Not only will our simulations support the experimental observations and the first theoretical results but will also describe the compression process in both MHD and kinetic frameworks.

The description and the parameters of the setup of our experiment, the experimental diagnostics, as well as the numerical codes used to perform our simulations will be detailled in Chapter 4. The different results, both experimental and theoretical, will be addressed in Chapter 5.

References

[1] O.V. Gotchev *et al*, « Laser-driven magnetic flux compression in high energy density plasmas », Phys. Rev. Lett., Volume 103, 215004 (November 2009).
http://doi.org/10.1103/PhysRevLett.103.215004

[2] D.A. Gurnett and A. Bhattacharjee, Introduction to Plasma Physics: With Space and Laboratory Applications, Cambridge University Press (2005).
https://doi.org/10.1017/CBO9780511809125

[3] G.L. Siscoe, « Aspects of global coherence of magnetospheric behavior », Journal of Atmospheric and Solar-Terrestrial Physics, Volume 73, 4, p. 402-419 (March 2011).
https://doi.org/10.1016/j.jastp.2010.11.005

[4] Y.B. Zeldovich and Y.P. Raiser, Physics of Waves and High-temperature Hydrodynamic Phenomena, Academic Press (1967).
https://doi.org/10.1016/B978-0-12-395672-9.X5001-2

[5] J. Zhong and Y. Wang, « Global magnetic field properties in the solar wind interaction of Mercury from MESSENGER measurements », Astronomy & Astrophysics, Volume 692, 136 (December 2024).
https://doi.org/10.1051/0004-6361/202451926

[6] J.T. Gosling, Encyclopedia of the Solar System, Academic Press (2nd edition), p. 99-116 (2007).
https://doi.org/10.1016/B978-012088589-3/50009-8

[7] C. Scolini *et al*, « CME-CME Interactions as sources CME Geoeffectiveness: The formationsof the complex ejecta and intense geomagnetic storm in 2017 early September », The Astrophysical Journal Supplement Series, Volume 247, 1 (February 2020).
https://doi.org/10.3847/1538-4365/ab6216

[8] Y. Chen *et al*, « Anomalous response of Mercury's magnetosphere to Solar wind compression: Comparison to Earth », The Astrophysical Journal, Volume 957, 1 (October 2023).
https://doi.org/10.3847/1538-4357/acf655

[9] S. Ye *et al*, « Solar wind compression of planetary magnetospheres revealed by radio and plasma wave observations », AGU Fall Meeting (December 2021).

[10] https://science.nasa.gov/blogs/the-sun-spot/2023/09/26/earths-magnetosphere-and-plasmasheet/ (website still available in April 2026).

[11] N.A. Tsyganenko *et al*, « Magnetic fields and electric currents around the dayside magnetopause as inferred from data-constrained modeling », Frontiers in Astronomy and Space Sciences, Volume 11 (July 2024).
https://doi.org/10.3389/fspas.2024.1425165

[12] D.A. Prokhorov *et al*, « Evidence for a shock-compressed magnetic field in the northwestern rim of Vela Jr. From X-ray polarimetry », Astronomy & Astrophysics, Volume 692, A59 (December 2024).
https://doi.org/10.1051/0004-6361/202452062

[13] T. Shahbaz *et al*, « Evidence for magnetic field compression in shocks within the jet of V404 Cyg », Monthly Notices of the Royal Astronomical Society, Volume 463, 2, p.1822-1830 (December 2016).
https://doir.org/10.1093/mnras/stw2171

[14] J. Zhang *et al*, « Earth-affecting solar transients: a review of the progresses in solar cycle 24 », Progress in Earth and Planetary Science, Volume 8, 56 (October 2021).
https://doi.org/10.1186/s40645-021-00426-7

[15] M.J. Rosenberg *et al*, « First experiments probing the collision of parallel magnetic fields using laser-produced plasmas », Phys. Plasmas, Volume 22, 042703 (April 2015).
https://doi.org/10.1063/1.4917248

[16] J. Lemaire and M. Scherer, « Ionosphere-plasma sheet field-aligned currents and parallel electric fields », Planetary and Space Science, Volume 22, 11, p. 1485-1490 (November 1974).
https://doi.org/10.1016/0032-0633(74)90013-0

[17] C. Gabrielse *et al*, « Utilizing the Heliophysics/Geospace System Observatory to understand particle injections: Their scale sizes and propagation directions », Journal of Geophysical Research: Space Physics, Volume 124, 7, p. 5584-5609 (July 2019).
https://doi.org/10.1029/2018JA025588

[18] D.P. Higginson, Ph. Korneev *et al*, « Laboratory investigation of particle acceleration and magnetic field compression in collisionless colliding plasma flows », Nature Communications Physics, Volume 2, 60 (June 2019).
https://doi.org/10.1038/s42005-019-0160-6

[19] A. Brandenburg and K. Subramanian, « Astrophysical magnetic fields and nonlinear dynamo theory », Physics Reports, Volume 417, 1-4 (October 2005).
https://doi.org/10.1016/j.physrep.2005.06.005

[20] H.-J. Fahr and M. Siewert, « Revisiting the role of magnetic moments in heliospheric plasmas », Astronomy & Astrophysics, Volume 552, A38 (April 2013).
https://doi.org/10.1051/0004-6361/201220965

[21] Ph. Korneev, E. d'Humières and V. Tikhonchuk, « Collisionless plasma interpenetration in a strong magnetic field for laboratory astrophysics experiments », Phys. Plasma, Volume 21, 022117 (February 2014).
https://doi.org/10.1063/1.4866598

[22] D.J. Rose, « General criterion for mirror instability of a plasma », Phys. Fluids, Volume 8, p. 951-955 (May 1965).
https://doi.org/10.1063/1.1761339

[23] A. Sladkov *et al*, « Saturation of the compression of the two interacting magnetized plasma toroids evidenced in the laboratory », Nature Communications, Volume 15, 10065 (November 2024).
https://doi.org/10.1038/s41467-024-53938-

Chapitre 3
Magnetic reconnection between HED magnetized plasmas

In this chapter, we are going to focus on magnetic reconnection, which is the second mechanism we worked on during this thesis, once again both experimentally and theoretically. The experimental devices and simulation codes will be addressed in chapter 4, while the results will be discussed in chapter 6. Here we will set the physical basis needed to study the process and detail the configuration we studied, which is the elongated current sheet configuration. We will describe in this state-of-the-art all the necessary aspects of magnetic reconnection to justify our experimental work and to show it is anchored in the domain of research on magnetic reconnection.

3.1 Generalities about magnetic reconnection in HED plasmas

We saw in the previous chapter that magnetic field compression occurs when HED magnetized plasmas interact such as magnetic field flows are parallel to each other within the compression zone. Now, with the magnetic reconnection, we are going to describe what happens when the flows are anti-parallel in the region of interaction.

3.1.1 Definition

We consider two identical HED magnetized plasmas propagating toward each other with a velocity **v**, such as **v** is orthogonal to the direction of the magnetic field **B**. Once again, in the absence of perturbations and according to ideal MHD framework, the magnetic field is frozen in the plasma flow. We suppose that each interacting magnetized plasma carries its own embedded magnetic field so, when they collide, the magnetic flows are aligned and anti-parallel between each other (see Figure 11). In this specific configuration, the magnetic fields are directed toward opposite directions, inducing magnetic tearing and the dissipation of the opposed fields

components in the center of the reconnection zone (so |B| ~ 0 T). Consequently, a current sheet oriented perpendicularly toward **v** and carrying an electric field $\mathbf{E}_{//}$ is formed in the reconnection zone between the two plasmas [1].

However, such a configuration between expanding magnetized plasmas induces a disruption of the magnetic flux and the frozen-in conditions are not valid anymore in the reconnection region. Indeed, the electric field induces resistive effects along the current sheet, leading to tearing and distortion of the magnetic field in this area. The plasma localized in the current sheet and within the direct outer parts enters a resistive MHD regime, allowing magnetic diffusion. Therefore, the magnetic fields disconnect and reconnect between each other. This model of resistive reconnection is known as the Sweet-Parker model [2].

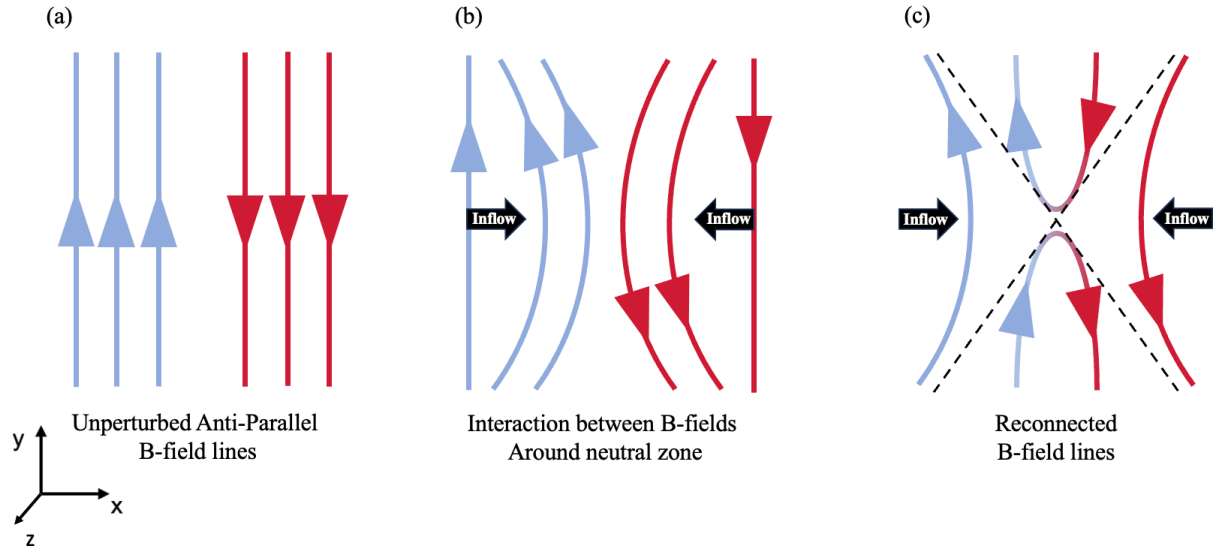

Figure 11. Schematization of magnetic reconnection between two magnetized plasmas. The magnetic field and their opposed directions are represented by the blue and red arrows, oriented along the y-axis. The converging inflows are modeled by the large symetrical arrows along the x-axis. (a) shows the system before the beginning of the reconnection process, when the magnetic fields are frozen in the plasma flows. (b) represented the beginning of the process. Contrary to magnetic compression during which the magnetic flux accumulates in the interaction region, in magnetic reconnection we observe a neutral zone between the interacting magnetic fields. (c) Close-up of the reconnected field lines in the reconnection sheet, inducing the formation of a crossed-magnetic field.

Magnetic reconnection is a fundamental mechanism between magnetized plasmas, resulting from the connection of the involved magnetic fields. The reconnection zone is a place of energy conversion, more particularly magnetic energy is converted into kinetic and thermal energy. We initially have a converging motion of the plasmas toward the reconnection zone, analogous to magnetic compression. Consequently, during the initial phase of the reconnection, the pressure increases in the reconnection zone and leads to magnetic flux accumulation. However, the rising pressure in the sheet is counterbalanced by the dissipation of the magnetic field within the reconnection sheet, due to the antiparallel orientation of the fields. Consequently, the magnetic pressure remains low in the sheet and the total pressure is dominated by the plasma pressure.

This imbalance between the plasma pressure and magnetic field strength implies magnetic diffusion and the reconnection of the field lines, along a release of energy. The magnetic energy

released through the modification of the topology of the field is converted into various mechanisms, such as toward thermal or kinetic energy transferred to the incoming charged particles entering the current sheet, or as well as a source of acceleration along the magnetic field lines for these same particles. As a consequence, the plasma is ejected from the reconnection sheet with a high-velocity **v'** through ouflow regions, oriented perpendicularly to the incoming plasma flows. In these specific regions then, the plasma flow becomes divergent and satisfies $\nabla \cdot \mathbf{v}' > 0$.

3.1.2 Astrophysical relevance

Magnetic reconnection is a ubiquitous mechanism that can take place at various scales in the Universe. As it enables sudden releases of energy in its surrounding environment and a rapid diffusion of the magnetic flux and rearrangement of the field topology, it is evidenced in different astrophysical events as well as reproducible in laboratory experiments on plasmas. As a consequence, magnetic reconnection is an important topic of research in the field of space plasmas and their interactions.

In astrophysics, magnetic reconnection can be measured and observed directly in the near Earth medium [3], similarly to magnetic field compression as the two mechanisms both rely on the fields alignment in the interaction zone. Consequently, magnetic reconnection is a well observed mechanism implied in solar activity and interactions with planetary magnetospheres. As mentioned in Chapter 2, the Sun photosphere is a turbulent region constituted of magnetized plasma whose magnetization can locally varied. Particle acceleration and matter ejection via CME are known phenomena associated to plasma interaction on the surface of the Sun and within the corona, supplying the solar wind. Magnetic reconnection is one of the predominant supposed mechanisms at play in these processes which can result in the release of the stored energy contained in the reconnection region formed in between magnetized plasmas. Among else, magnetic reconnection plays a key role in the plasma ejection from the Sun through solar arches [4].

Solar arches are magnetic structures connecting two zones of opposite magnetic polarity (see Figure 12a)). They come from the formation of magnetic flux tubes within the photosphere that, as they expand within the solar corona, form a closed magnetic loop. As the resulting arch extends above the surface, it evolves in the highly magnetized corona where it interacts with the surrounding magnetic field. Magnetic reconnection first occurs in between the field contained in the arch and around in the corona, restructuring the topology of the magnetic field carried by the arch [5]. As the plasma is strongly magnetized, it remains coupled with the field inside of the arch.

Solar arches contribute to the solar wind because their structure is continuously evolving in their environment due to the plasma flows in both the photosphere and the corona. Consequently, converging flows can interfere directly with the structure of the arch and distort the arch, leading to the formation of a current sheet within the structure of the arch. As a result, magnetic reconnection sites appear directly in between the branches of the arch (see Figure 12b)). Magnetic reconnection can isolate portions of the magnetized plasma contained in the arch by forming closed magnetic structures known as plasmoids. These plasmoids are plasma structures that are confined by their own magnetic field and are consequently commonly formed during magnetic reconnection involving several sites of reconnection in the current sheet where field lines

reconnect (only one site of reconnection is schematized on Figure 1c)). Plasmoids are usually appearing at the latest times of the process, once the current sheet starts to be fragmented in between these several reconnection sites [6]. As magnetic dissipation is possible and the fields reconnect with one another, the reconnection process within the arch not only leads to the expected particle acceleration and plasma heating, but it also results in the ejection of plasmoids into the circumstellar medium, sustaining the continuous the solar wind.

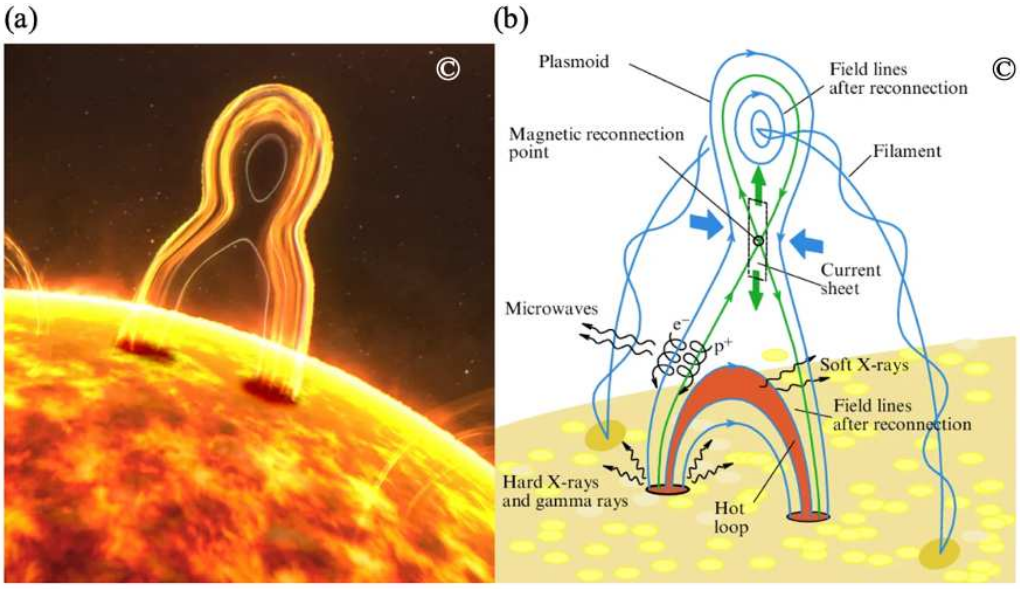

Figure 12. Solar arches and magnetic reconnection. (a) Visualization of a solar arch distorted by the interaction with the corona from NASA [7]. A plasmoid is getting formed as magnetic reconnection is occuring inside of the arch. (b) Scheme of the same process from A. Lysenko et al *[8].*

As mentioned previously, the solar wind propagates and the IMF interacts directly with planetary magnetospheres. The plasma interacting with the magnetosphere shapes the magnetic field of the Earth. In Chapter 2, Figure 9a) showed a representation of the magnetosphere around the Earth. We notice that the shape of the magnetic fields within the magnetopause (the limit of the zone of influence of the terrestrial magnetic field) schematized in red is highly asymetric from each side of the Earth rotational axis. On day side, as the solar wind is directly colliding with the magnetosphere, the field carried by the solar wind becomes flatten. The plasma flow is redirected as magnetic reconnection (or compression, depending on the field local orientation) already takes place there. In this case, the fields reconnect and the solar wind plasma merges with the Earth magnetic field. However, as the plasma flows are redirected by the direct collision, the solar wind propagates around the magnetosphere and stretches and elongates the Earth field on the night side. This part of the magnetosphere is known as the magnetotail [9].

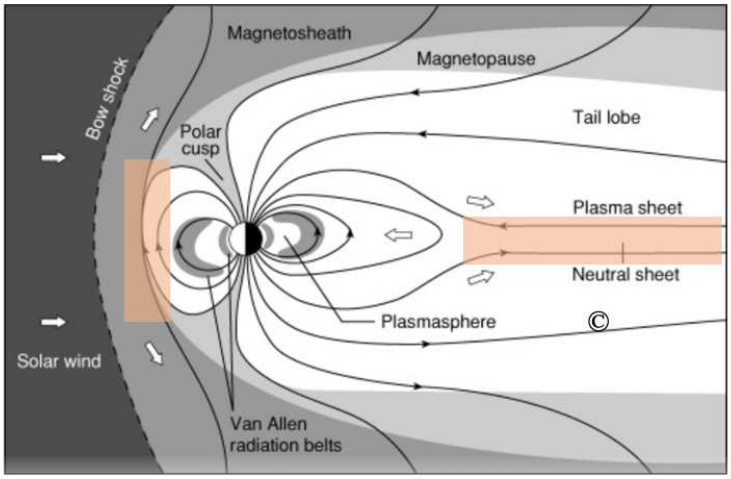

Figure 13. Scheme of the Earth magnetosphere. The zone where magnetic reconnection is the most likely to occur (on day side and within the plasma sheet in the magnetotail on night side) are highlighted in orange. From R.A. Treumann et al *[10].*

Consequently, the fields of opposite directions are brought closer to one another, forming an elongated current sheet (see Figure 13). There is an observed storage of plasma in this specific region of the magnetosphere. However, the current sheet is, by definition, unstable. Its elongated configuration allows multiple sites of reconnection where the magnetic field lines reconnect, forming plasmoids between each site. As a consequence, the magnetic energy stored in the magnetotail is released and converted. The plasma is then accelerated away from both sides of the current sheet, forming outflows in both directions. Therefore, one part is redirected toward the Earth poles, which contributes to inject energetic particles into the ionosphere, inducing and intensifying auroral activities [11]. The other part is ejected down the tail, releasing plasmoids that get detached from the magnetotail during the magnetic reconnection processes into the interplanetary medium.

Nowadays, magnetic reconnection can be detected in space environments, like in the plasma sheet within the magnetotail. For instance, plasmoid-dominated reconnection can be detected by measuring accelerated particle flows or the emissivity of the plasma. However, it is important to underline that, just like for magnetic field compression, reconnection events are difficult to observe *in situ* in space. Indeed, even though we dispose of multiple devices and satellites orbiting within the magnetosphere capable to track and measure the variations of physical quantities related to magnetic reconnection such as the current density, the probability to detect a reconnection current sheet remains low. The dimensions of the current sheets and the particle outflows generated by magnetic reconnection events are extremely small in comparison with the total volume of the magnetosphere. Besides, all the reconnection events are succinct in time (they last at best for a few hours) and are hardly previsible, making the detections of these phenomena very rare [12]. Furthermore, these *in situ* observations imply that reconnection processes have only been observed yet in Earth nearby regions or more generally within the limits of the heliopause, due to the current limits of spacecraft technology. Therefore, even if magnetic reconnection is expected to happen in more violent and far events, such as in accretion disks around neutron stars or black holes, direct observations of reconnection events remain impossible in these specific cases.

Consequently, as magnetic reconnection can happen under very different conditions and scales, it is currently possible to evidence the mechanism in the laboratory [13]. By investigating

laser-driven plasmas, in our case magnetized by self-generated Biermann battery magnetic fields to model the spontaneous magnetic fields in space plasmas, we have the opportunity to study the reconnection process in systems with laboratory sized dimensions, within experimental setup that allows to observe the temporal evolution of magnetic reconnection as well as to reproduce the conditions of its generation.

3.2 Configuration and dynamics of the elongated current sheet

We describe here the dynamics and the mechanisms implied in the reconnection current sheet, especially in the elongated current sheet configuration. Indeed, as we anchor our work in the laboratory astrophysics framework, we focus on the most frequent configuration observed in space.

3.2.1 Formation of the current sheet

The current sheet is formed as soon as the frozen-in condition of the plasma magnetic field breaks. Indeed, when a magnetized plasma verifies the Alfvén theorem, it is supposed that it behaves like an ideal fluid in the ideal MHD framework, so consequently, its conductivity is considered as ideal and infinite. However, as the plasmas start interacting within the reconnection zone, magnetic flux accumulation increases the magnetic energy density in this region, leading to a local decrease in the plasma conductivity. As the plasmas can not be considered as ideal anymore, the non-ideal terms in the Ohm's law cannot be neglected anymore, so we then have:

$$\mathbf{E} + \mathbf{v} \times \mathbf{B} = \mathbf{R}\,, \tag{3.1}$$

where $\mathbf{R}$ are the non-ideal terms, such as $\mathbf{R} \neq 0$. Indeed, magnetic reconnection can only occur if we have $\mathbf{E} + \mathbf{v} \times \mathbf{B} \neq 0$, as it is the presence of non-ideal terms that allows the rupture of the frozen-in condition on the magnetic fields in the plasmas which permit fields reconnection in the current sheet. In the framework of resistive MHD, we can approximate $\mathbf{R}$ with $\mathbf{R} = \eta\mathbf{J}$, where η is the plasma resistivity coefficient and $\mathbf{J}$ is the current density, normal to the reconnection plan.

The fields reconnect with each other at a specific location of the current sheet known as an X-point, due to the topology of the inflow and reconnected field lines in this region (here the field lines represented in the neutral sheet correspond to the magnetic flux isolines). The reconnected lines are strongly bent and contribute to the release of magnetic energy. As mentioned earlier, this magnetic energy is converted into thermal energy that heats the plasma but also into kinetic energy that redirects the plasma flows. Consequently, the reconnected fields contribute in expelling the plasma inflows out of the reconnection sites, establishing two reconnection outflows on either side of the X-point, perpendicular to the inflow direction [14] (see Figure 14a)).

We often consider that there are two main configurations for magnetic reconnection. The single X-point that we described constitutes the basis magnetic structure of the reconnection process and can occur independantly. However, as mentioned before, this isolated configuration is not the most likely to happen in space plasmas. Indeed, like for the magnetotail of the Earth magnetosphere, a current sheet formed during the reconnection is more likely to contain several X-points, organized as a chain of multiple reconnection sites in between which plasmoids are formed (see Figure 14).

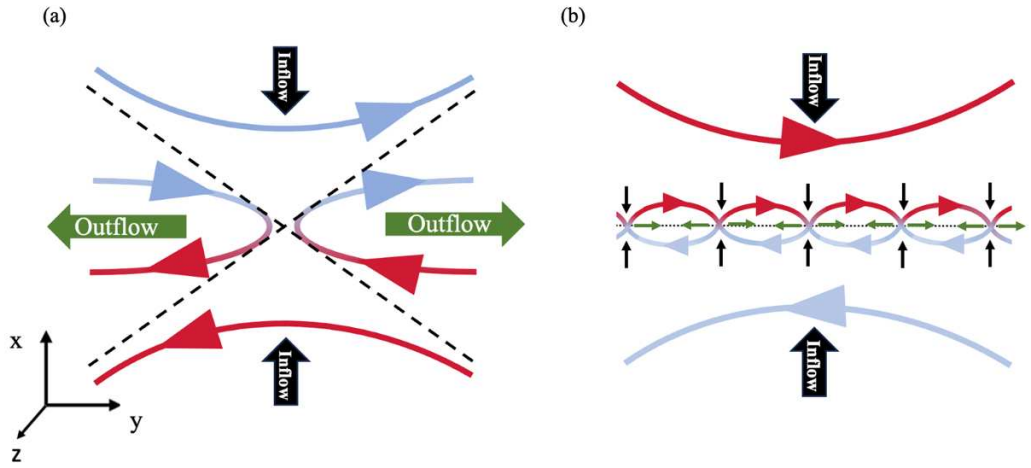

Figure 14. Schematic view of the structure of magnetic reconnection in (a) an isolated X-point magnetic configuration and in (b) an elongated current sheet constituted by a succession of multiple reconnection sites and plasmoids.

An elongated current sheet is an unstable configuration as the plasmoid chain is induced by the fragmentation of the sheet. Indeed, plasmoids do not remain confined in the sheet, as the magnetic energy they contain is rapidly converted and the particles trapped inside the plasmoids are accelerated along the sheet toward the outflows. As the energy conversion process gets developed, the plasmoids progressively merge with one another, leading to their coalescence.

While we expressed Ohm's law in the framework of resistive MHD to justify the breaking of the frozen magnetic field and the reconnection of field lines in the current sheet, the energy conversion and more generally the inner dynamics are mostly related to the charged particles motion, as they are injected in the sheet by the plasma inflows. Consequently, the current sheet grows thinner structures reaching spatio-temporal scales where the kinetic effects are dominant and where the MHD conditions are no longer valid. The particle dynamics require to be addressed to characterise the evolution of the elongated current sheet.

3.2.2 Particle kinetics in the current sheet

In order to describe the charged particle dynamics in the current sheet, we consider the sheet at kinetic scales, such as the electron and ion inertial lengths to characterise its temporal evolution after its formation. To do so, we define the sheet in the kinetic regime, within which the plasma is considered as collisionless.

The charged particles entering the reconnection sheet are brought in by the incoming plasma flows. As the magnetized plasmas are initially considered as ideal, the particles are frozen in the magnetic field. However, once these particles, especially electrons, are entering the current sheet where the magnetic field is dissipated, particles are influenced by the electric field within the sheet. The Larmor radius of the particles ($R_L = m_{part}v/eB$) increases significantly as the magnetic field tends to $|B| \sim 0$ T in the core of the current sheet [15]. Consequently, particles are not frozen-in on the field anymore and get demagnetized. Electrons are accelerated away by the electric field faster than the ions. We observe a separation between ions and electrons, and this decorrelation is known as the Hall effect. Consequently, we locally have $\mathbf{J} \cdot \mathbf{E} > 0$, and the magnetic energy is transferred from the field to the particles [16].

All these effects are only occuring at kinetic scales but are crucial to describe the dynamics of the current sheet. Therefore, we adapt Ohm's law by accounting for kinetic effects to highlight the totality of the encountered mechanisms:

$$\mathbf{E} + \mathbf{v} \times \mathbf{B} = \eta \mathbf{J} + \frac{1}{n_e}(\mathbf{J} \times \mathbf{B} - \nabla p_e) + \frac{m_e}{ne^2}\frac{\partial \mathbf{J}}{\partial t}, \tag{3.2}$$

where $\frac{1}{n_e}\mathbf{J} \times \mathbf{B}$ is the Hall term reflecting the electron-ion separation, ∇p_e is the electron pressure gradient and $\frac{m_e}{ne^2}\frac{\partial \mathbf{J}}{\partial t}$ is the electron intertia term. Both types of particles are still anisotropically accelerated by the electric field toward the outflows but their trajectories are different (see Figure 15). Indeed, as ions are heavier than electrons, they have different spatio-temporal scales, like the Larmor radius which is larger for the ions than for the electrons in similar conditions. Consequently, ions are less confined by the current sheet while the electrons stay magnetized for a longer time. As a result, electrons decouple from the fields only in the core of the current sheet, where they are strongly accelerated [17].

The separated motions of electrons and ions in the current sheet play a key role in the reconnection process, as it leads to the formation of local currents within the sheet and the Hall electromagnetic field gets formed (see the Hall term in Eq. 3.2). This field has a quadripolar structure, which is one characteristic signature of magnetic reconnection.

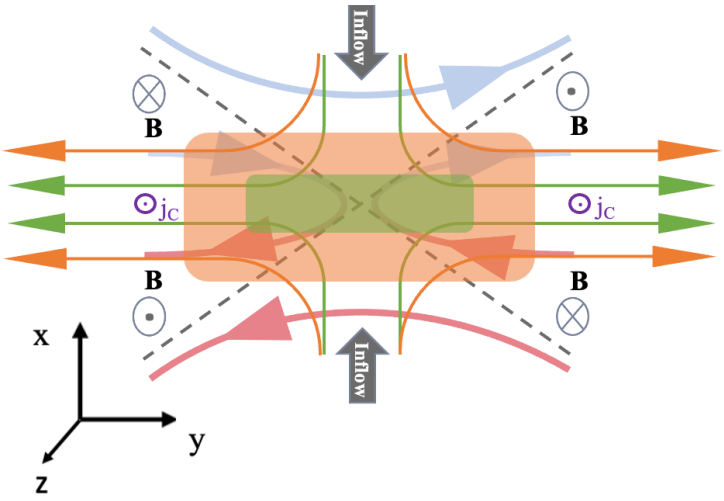

Figure 15. Schematic representation of electrons (in green) and ions (in orange) decoupled trajectories in the current sheet. The electron diffusion layer (light green) is much thinner than the ion one (light orange). The quadripolar Hall magnetic field B is represented in grey on each side of the separative axis (black dashed lines) and the uniform current density j_C orientation is in purple.

The particle acceleration within the sheet contributes to nurtur the high current that can be measured in the sheet. Indeed, this is related to the charge difference implied by the decoupling of the electron and the ion dynamics, as it induces a secondary electric field, which is the Hall field. In this case, the particle distribution within the reconnection sheet becomes non-Maxwellian, confirming the necessity of a kinetic description of the plasma in the sheet.

3.2.3 Plasmoid-driven regime

As mentioned before, the current sheet is unstable during the plasmoid phase. Indeed, the plasmoid regime is triggered by the growing tearing instabilities in the current sheet. These perturbations destabilize locally the magnetic field structure in the sheet, which fragments the current sheet into a chain of multiple reconnection sites. Reconnected magnetic field lines form then the closed plasmoids within which the charged particles are traped and confined. As plasmoids get developed from instabilities, they only get formed in the configuration of the elongated current sheet. Indeed, we need to have $\delta << L$, where δ is the width of the sheet and L its length. The current sheet gets more unstable the longer and thinner it becomes as instabilities are more likely to appear. Therefore, the establishment of plasmoids requires a large aspect ratio L/δ. The plasmoid regime transcribes a particular dynamic regime of the current sheet that we can quantify by introducing the Lundquist number [18] defined by:

$$S = \frac{\mu_0 L v_A}{\eta}, \tag{3.3}$$

where μ_0 is the vacuum permeability, L is the length of the sheet, v_A is the Alfvén velocity and η is the plasma resistivity. The Lundquist number is a dimensionless parameter that compares the advection and the diffusion of the flux. If $S >> 1$, the advection aspect of the plasma dominates the sheet. This implies that the field does not diffuse in the sheet through the resisitivity effects

within the flow and that the plasma is highly conducting. Consequently, a high Lundquist number represents an unstable reconnection sheet where instabilities appear, and the plasmoid regime can only be established if S >> 1 [19].

3.2.4 Characterisation and parameters of the reconnection

The dimensionless plasma parameters described in Chapter 1, section 1.2.4., are important to characterize the dynamics of the plasma in the reconnection sheet. Moreover, we dispose of proper parameters to quantify magnetic reconnection as a process itself. Indeed, the different regimes of reconnection (with or without plasmoids) depend on several quantities that set the conditions on the reconnection. Among these parameters is the reconnection rate R. Its calculation provides a direct measurement of the efficiency of the magnetic flux transport in the sheet as well as of the conversion of magnetic energy during the process. The reconnection rate [20] is dimensionless like the rest of the plasma parameters we have already mentioned. Indeed, it is usually normalised to a reference electric field E_0, which is often:

$$E_0 = v_A B_0 \,, \tag{3.4}$$

where v_A is the Alfvén velocity (see Chapter 1, eq. 1.29) and B_0 is the amplitude of the reconnecting magnetic field in the incoming plasma. Consequently, in the case of a bidimensional reconnection, the reconnection rate R is defined by:

$$R = \frac{1}{E_0} \frac{\partial \phi_{rec}}{\partial t} \,, \tag{3.5}$$

where φ_{rec} is the flux in the reconnection sheet. We consider a half-plane delimited by the surface S and the contour C, perdicular to the reconnection plane x0y (see Figure 16).

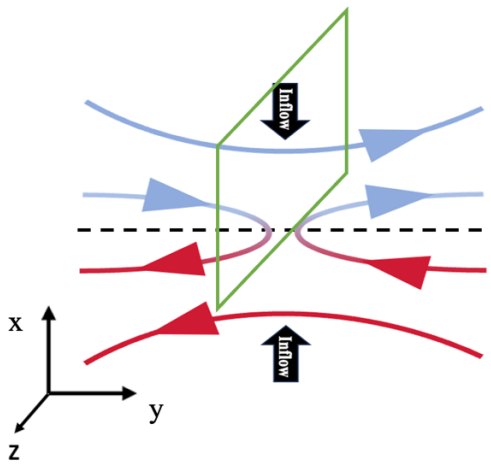

Figure 16. Magnetic reconnection in the plane (x0y). The surface S through which we estimate the flux is represented in green in the plane (y0z).

With the Maxwell-Farady equation and the Stockes theorem, we write the relation between the flux and the magnetic field as:

$$\frac{\partial \varphi_{\mathrm{rec}}}{\partial t} = \int_S \frac{\partial \mathbf{B}}{\partial t}\, dS = \int_S \nabla \times \mathbf{E}\, dS = \oint_C \mathbf{E}\, d\mathbf{l} \tag{3.6}$$

Because the reconnecting electric field $\mathbf{E_{rec}}$ is colinear to the z-axis, perpendicular to the reconnection plane, $\mathbf{E}d\mathbf{l} = 0$ on the sides that are perpendicular to the z-axis. Besides, the top side of the surface is located outside of the reconnection sheet so we can also consider $\mathbf{E}d\mathbf{l} = 0$ there. Consequently, we can write:

$$R = \frac{E_z(x=0)}{v_A B_0} \tag{3.7}$$

Finally, it is important to acknowledge the possible presence of a guide field in the reconnection sheet. Indeed, for a magnetic reconnection process as shown on Figure 16, we can express the magnetic field that interact with the current sheet as:

$$\mathbf{B} = B_0(x)\, \bar{\mathbf{y}} + B_z \bar{\mathbf{z}}\,, \tag{3.8}$$

where B_z is the guide field [21]. The guide field corresponds to the component of the magnetic field that is perpendicular to the reconnection plane. The reconnection process is influenced by this out-of-plane component which can attain strength that are higher, smaller or comparable to the reconnecting field B_0. This component of the magnetic field plays a crucial role in the dynamics of the reconnection. Indeed, in astrophysical contexts such as once again in the case of the Earth magnetotail, strong guide fields have been measured. Besides, the presence of the guide field does not affect directly the in-plane force balance. However, it maintains the magnetization of the charged particles within the sheet. Consequently, their zones of diffusion (see Figure 15) are reduced, which leads to more confined particle dynamics in the current sheet.

3.3 Framework of the study

This work presents our study of the temporal evolution of the elongated and long aspect ratio current sheet as well as the development of plasmoids during the reconnection. Indeed, the spatial and temporal evolution of the elongated current sheet is still an open question [22], to which we propose an answer thanks to laboratory astrophysics methods. We designed our experimental setup to recreate the necessary conditions for magnetic reconnection in the laboratory. By generating laser-driven plasmas magnetized via the Biermann battery effect, our aim is in a first time to investigate the formation and the evolution of the current sheet in the laboratory, on which we dispose of significant control over the different parameters of the experiment as well as reproductibility. Moreover, relying on the Biermann battery effect to magnetize the plasmas permits to easily generate the expected conditions between magnetic flows to trigger the reconnection. Even though elongated current sheets are the most frequent configuration for magnetic reconnection, it is still little explored in laser-driven experiments.

In this work, we will present how we managed to provide for the first time observations of the temporal evolution of the current sheet and its fragmentation in a chain of plasmoids, by using exprimental diagnostics. These measurements permit to calculate the plasma parameters related to the current sheet and the reconnection process, as well as to investigate the different inner mechanisms happening within the sheet.

We will also focus on the kinetic-timescale aspects of magnetic reconnection by running particle-in-cell simulations that will support the experimental results and complete our experimental measurements with theoretical conclusions. Once again, and similarly to our study of magnetic compression, both of our experimental and simulation works permit to reproduce plasma conditions and parameters relevant to astrophysical environments and to study magnetic reconnection and the plasmoid dynamics between magnetized plasmas through controlled settings and diagnostics in the laboratory. As mentioned, before the probability to observe correctly magnetic reconnection directly in space remains rare and depends on too many factors that cannot be controlled and precisely predicted. Consequently, our work will serve for future experiments and modeling of the reconnection current sheet.

As our work on magnetic reconnection consists in both experimental setup and analysis as well as numerical simulations, we will describe the setup of the experiment, as well as the different diagnostics (most of them were already used for the experimental measurements of magnetic compression so their efficiency has been proven by our team) and the specifities of the PIC code that we used for simulations in Chapter 4. Our results and conclusions will be depicted in Chapter 6.

References

[1] S. Bolanos *et al*, « Laboratory evidence of magnetic reconnection hampered in obliquely interacting flux tubes », Nature Communications, Volume 13 (September 2022). https://doi.org/10.1038/s41467-022-33813-9

[2] E.N. Parker, « Sweet's mechanism for merging magnetic fields in conducting fluids », Journal of Geophysical Research, Volume 62, 4, p. 509 – 520 (December 1957). https://doi.org/10.1029/JZ062i004p00509

[3] J.P. Reistad *et al*, « Separation and quantification of ionospheric convection sources: 2. The dipole tilt angle influence on reverse convection cells during Northward IMF », Journal of Geophysical Research: Space Physics, Volume 124 (July 2019). https://doi.org/10.1029/2019JA026641

[4] L. Li *et al*, « Magnetic reconnection between a solar filament and nearby coronal loops », Nature Physique, Volume 12, p. 847 – 851 (May 2016). https://doi.org/10.1038/nphys3768

[5] J. Lin *et al*, « Direct observations of the magnetic reconnection site of an eruption on 2003 November 18 », The Astrophysical Journal, Volume 622, 2 (April 2005). https://doi.org/10.1086/428110

[6] X. Yan *et al*, « Fast plasmoid-mediated reconnection in a solar flare », Nature Communications, Volume 13 (February 2022). https://doi.org/10.1038/s41467-022-28269-w

[7] https://svs.gsfc.nasa.gov/20310 (website still available in April 2026).

[8] A. Lysenko *et al,* « X-ray and gamma-ray emission of solar flares », Physics-Uspekhi, Volume 63 (June 2019). https://doi.org/10.3367/UFNe.2019.06.038757

[9] M. Palmroth *et al*, « Magnetotail plasma eruptions driven by magnetic reconnection and kinetic instabilities », Nature Geoscience, Volume 16, p. 570 – 576 (June 2023). https://doi.org/10.1038/s41561-023-01206-2

[10] K.R. Lang, Encyclopedia of Geology, Chapter « Solar system: the Sun », Elsevier, p. 209 – 220 (2005). https://doi.org/10.1016/B0-12-369396-9/00078-2

[11] R.A. Treumann *et al*, « Auroral evidence for multiple reconnections in the magnetospheric tail plasma sheet », Europhysics Letters, Volume 85, 4 (February 2009). https://doi.org/10.1209/0295-5075/85/49001

[12] M. Oieroset *et al*, « *In situ* detection of collisionless reconnection in the Earth's magnetotail », Nature, Volume 412, p. 414 – 417 (July 2001). https://doi.org/10.1038/35086520

[13] J.B. Taylor, « Relaxation anf magnetic reconnection in plasmas », Rev. Mod. Phys., Volume 58, 741 (July 1986). https://doi.org/10.1103/RevModPhys.58.741

[14] C.S. Arridge *et al*, « Cassini *in situ* observations of long-duration magnetic reconnection in Saturn's magnetotail », Nature Physics, Volume 12 (November 2015). https://doi.org/10.1038/nphys3565

[15] E.G. Zweibel and M. Yamada, « Magnetic reconnection in astrophysical and laboratory plasmas », Annual review of Astronomy and Astrophysics, Volume 47, p. 291 – 332 (September 2009). https://doi.org/10.1146/annurev-astro-082708-101726

[16] S. Zenitani *et al*, « The inner structure of collisionless magnetic reconnection: the electron-frame dissipation measure and Hall fields », Phys. Plasmas, Volume 18 (December 2011). https://doi.org/10.1063/1.3662430

[17] W. Daughton *et al*, « Role of electron physics in the development of turbulent magnetic reconnection in collisionless plasmas », Nature Physics, Volume 7, p. 539 – 542 (April 2011). https://doi.org/10.1038/nphys1965

[18] A. Bhattacharjee *et al*, « Fast reconnection in high-Lundquist-number plasmas due to the plasmoid instability », Phys. Plasmas, Volume 16 (November 2009). https://doi.org/10.1063/1.3264103

[19] N.F. Loureiro *et al*, « Magnetic reconnection and stochastic plasmoid chains in high-Lundquist-number plasmas », Phys. Plasmas, Volume 19 (April 2012). https://doi.org/10.1063/1.3703318

[20] Y. Liu *et al*, « First-principles theory of the rate of magnetic reconnection in magnetospheric and solar plasmas », Communications Physics, Volume 5, 97 (April 2022). https://doi.org/10.1038/s42005-022-00854-x

[21] M. W. Kunz, « Lecture notes on Introduction to Plasma Astrophysics », Part XI.

[22] Y.M. Huang, L. Comisso and A. Bhattacharjee, « Plasmoid instability in evolving current sheet and onset of fast reconnection », The Astrophysical Journal, Volume 849, 2 (November 2017). https://doi.org/10.3847/1538-4357/aa906d

Chapitre 4

Experimental setups and diagnostics and numerical tools for laboratory astrophysics with high power lasers

In this chapter, we are going to describe the different tools used for our researches on magnetic field compression and magnetic reconnection in laboratory astrophysics. This thesis presents theoretical work, experimental settings and data analysis. We used several experimental diagnostics and simulation codes that present their own specificities and assets for plasma physics. On the first hand, we are going to detail the parameters of our experimental campaigns, how our experimental setups were designed to observe either compression or reconnection, but also the different diagnostics installed during our experiment. On the second hand, we will introduce the different numerical codes used for the theoretical part of the study.

4.1 Experimental devices in the laboratory

4.1.1 The LULI2000 facility

Both of the experimental campaigns were conducted at the LULI2000 facility, in the experimental room n°1, at École Polytechnique [1] (see Figure 17). This facility is built around both a high-power nanosecond laser and a high intensity picosecond line, then users can combine nanosecond-long and picosecond-long pulses within the target chamber. The long pulse line is

called the North line, set here in a square shaped pulse that can be split into sub-beams in the experimental room. The short pulse is the South line. In our case, it was used as reference for time synchronization. The facility also provides auxiliary laser beams used for the experimental diagnostics (see 4.1.2.2).

During our experiments, the two lines were set at the frequency $f_1 = 1\ \omega$. In this configuration, the North line delivers an energy around $E_{North} \sim 1000$ J at a wavelength of $\lambda = 1.053$ µm at the end of the amplification line, on a 2 ns or 5 ns pulse, for an intensity of $I \sim 10^{14}$ W/cm^2, while the South line, thanks to the CPA technique [2], is set to deliver $E_{South} \sim 100$ J while being compressed on 1 ps. At these energies, the rate of shooting is of 1 shot per 90 minutes, leading to 5 and 6 shots per day for a total of around 80 shots per campaign. As mentioned previously, the North beam can be divided with beamsplitters in the optical path, creating two beams respectively called North and North bis in this manuscript. As both the North and South beams are transported between the exit of the compressor and the target, there is a loss of energy in the route, such as it is estimated that only approximately 50% of the total energy of the North line hits the target, which is around 25% for each sub-beam North and North bis. Similarly, only 46% of the energy of the South line reaches the target.

In parallel, an auxiliary beam, called the Blue line in this manuscript, was used for the Thomson scattering diagnostic (see 4.1.3.2.1) and delivers an energy around $E_{Blue} \sim 20$ J in a few nanoseconds (with t = 1.5 ns to t = 5 ns, depending on the shots). This line has been set at both $f_1 = 1\omega$ and $f_2 = 2\omega$ frequencies (so $\lambda_1 = 1.053$ µm and $\lambda_2 = 0.532$ µm) during the experiments. Finally, a Nd:YAG (Neodynium doped Yttrium Aluminium Garnet) Quantaray laser [3], set at the frequency $f_2 = 2\omega$, was turned on before each shot for the interferometry diagnostic (see 4.1.2.2). All the laser beams were synchronized with one another at the time of the shot, using the South line as reference time t_0, except for the Nd:YAG which is started manually before the shot. As a result, it is also possible to delay the laser beams toward one another to investigate the plasma at different times and track the temporal evolution of the different quantities with the diagnostics.



Figure 17. Photographs of the LULI2000 facility. On the left: the laser hall with the North and South beams. On the right: the experimental room n°1 of the facility with the target chamber, the diagnostics, the North and South lines, the Quantaray laser and the Blue line.

4.1.2 Experimental setup for magnetic field compression

4.1.2.1 Geometry of the experiment

The experimental campaign focused on the study of magnetic field compression was conducted in 2022 at the LULI2000 facility. To reproduce the necessary conditions enabling magnetic compression between two encountered plasmas, two opposed and identical 5 µm thick copper targets were irradiated by the two identical long pulse laser beams North and North Bis. The two laser beams were aligned to irradiate the targets during 2 ns while coming from opposite directions and a 45° angle of incidence. The scheme of the target configuration is presented in Figure 18. This configuration was chosen to generate two counter-propagating magnetized plasmas, each advecting a toroidal self-generated Biermann battery field toward each other. With this geometry, opposed magnetic field will be similarly oriented in between the targets where they collide and induce the phenomena of compression between the targets.

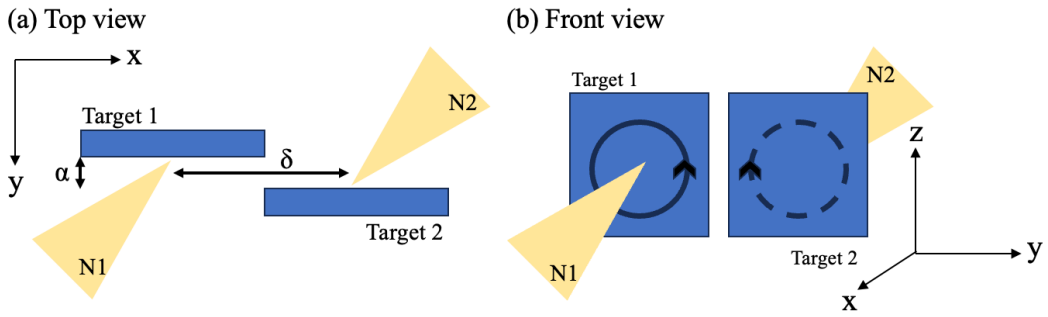

Figure 18. Scheme of the double target configuration and the magnetic field disposition for the investigation of the compression. a) Top view of the setup (in the x0y plane). α and δ, respectively the distance between the two targets surfaces and between the centers of the two focal spots, are the two geometrical parameters that varied during the experiment.

A third laser, in our case the picosecond-long South line, was shot on a 23 µm thick plastic (PET) target to generate a proton beam by Target Normal Sheath Acceleration (TNSA) [4] (see Figure 19). This mechanism consists in irradiating a target on one side with a high intensity laser, such as the energy of the beam is transferred to the hot electrons on the surface. These electrons move accross the target and escape through its back face. This creates a separation of the charges on the back surface of the target, leading to the formation of an electrostatic field that will ionize the atoms composing the target. Therefore, protons (and more generally ions) will be accelerated [5]. Here, this beam was produced to generate a proton beam for our proton radiography diagnostic (see 4.1.2.2.1), and the use of PET for the TNSA target permitted to reduce the background X-rays on the detectors. These protons then propagate through the two plasmas produced by the irradiation of the two copper targets by the North and North Bis beams and will be deflected by the two self-generated Biermann battery magnetic fields advect by the expanding plasmas. The trajectories of the probing protons are altered by the structure of the compression that occurs when the plasmas collide [6].

These self-generated magnetic fields are maintained during the total duration of the laser pulse (so around 2 ns). As the deflection of the field stays limited by the combination of the Righi-Leduc [7] and Nernst [8] effects, the targets in the experiment have to be close enough from each

other to enable the observation of the compression. As a consequence, the targets were often replaced during the experiment in order to increase or decrease the height α between them to observe the variations of the amplitude of the compressed magnetic field.

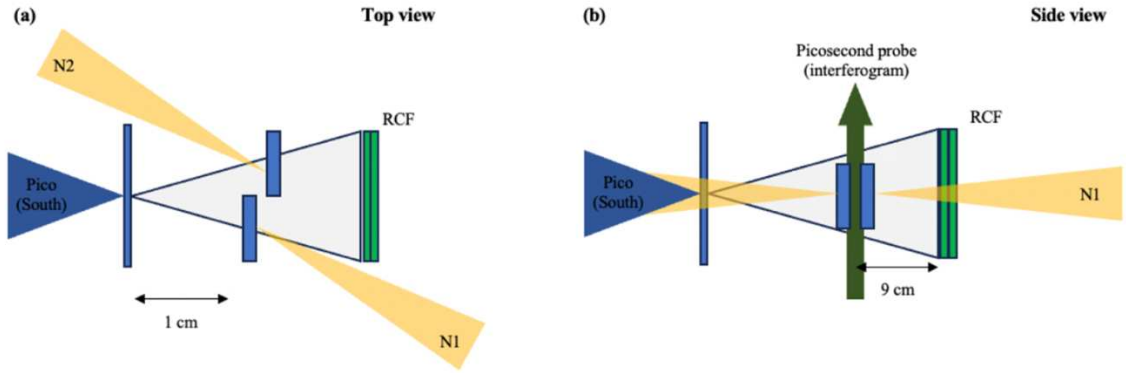

Figure 19. Scheme of the experimental setup used for the magnetic compression experiment with the top view (a) and the side view (b). The nanosecond-long lasers are represented in yellow (here named N1 and N2 to ease the visibility), the picosecond laser in dark blue, the three targets in light blue and the Quantaray laser, the probe used for the interferometry diagnostic, in dark green.

This geometry has been designed by the group SPRINT and the three targets have been mounted on 3D printed holders conceived at the target laboratory at École Polytechnique. Alongside this specific configuration for the targets and the resulting lasers alignments, several diagnostics were installed inside and outside the target chamber to characterize the spatial and temporal evolution of the laser-driven plasmas as well as of the compression process. These diagnostics permitted to measure experimentally physical quantities such as the densities, the topology of the compression or the temperatures.

4.1.2.2 Diagnostics

In this section, we will describe the different experimental diagnostics used during the campaign. We will present their different functions, their setup in the laboratory and the type of results that can be obtained. The analysis of the experimental results and the associated discussions will be addressed in Chapter 5.

4.1.2.2.1 Proton radiography

Proton radiography is a diagnostic commonly used to characterize the magnetic field topology by using the deflection of protons propagating through magnetized expanding plasmas created from the laser-matter interaction [9]. The aim was to use the TNSA proton beam generated by the irradiation of the PET target with the high intensity line to probe the magnetic fields in the expanding plasmas and the evolution of the compression structure in formation between the targets. A proton beam created via TNSA presents good qualities to probe these electromagnetic fields [10], such a small source size and a good spatial resolution [11]. Besides, the pulse has a picosecond-long duration which is shorter than the characteristic evolution time of the topology of the magnetic field. The TNSA proton beam is non-relativistic and spreads longitudinally.

Therefore, it can probe the temporal evolution of the magnetic field that appears motionless in the proton beam referential.

Besides, the available settings at the LULI2000 also permit to introduce a delay between the creation of the nanosecond-long beam and of the picosecond-long beam from shot to shot. During our experiment, this delay was set between $\Delta t = 0.5$ ns and $\Delta t = 4.5$ ns. This method allows to track both the spatial and temporal evolution of the compression structure between the two interacting plasmas over longer time intervals than the differences of time-of-flights between protons of different energies contained in a TNSA beam.

To image the compression structure, we used radiochromic films (RCF) [12], which darken when exposed to the radiations from the proton beam. They are a useful means in laser-driven plasma experiments, as it is possible to measure the dose deposited in each film and, consequently, map the dose distribution in 2D. The RCFs are usually disposed in stacks of several layers of films, each layer corresponding to one discrete level of kinetic energy. Each proton will deposit more energy in one specific film according to its own energy, as for each level of kinetic energy, the Bragg peak of the proton (the peak of energy released by a proton shortly before being stopped while travelling in a material) is located at a different depth [13]. Consequently, it is possible to get the complete proton spectra for every shot. Also, as the films can saturate when exposed to a high dose of radiation, plastic filters were interposed between and in front of the films to attenuate the incoming energy.

As mentioned before, the protons are deflected by the magnetic fields when they propagate through the plasmas. A beam created via TNSA is usually composed of protons whose trajectories are contained in a solid angle formed by a 30°- 40° aperture cone [14]. In a case where the beam does not interfer with any electromagnetic field, the trajectories of the protons remain unperturbated. However, the protons are deflected by the Lorentz force $\mathbf{F} = e(\mathbf{v} \times \mathbf{B} + \mathbf{E})$ during the interaction with a magnetic field, therefore here the initial proton distribution in the beam is affected by the magnetic compression structure. The fluctuations of the proton repartition and of the dose on the films correspond to the line-integrated deflections of the protons. A strong magnetic field will locally deflect the protons, leading to a local accumulation such as around the magnetic loops. Consequently, the darkest parts on the RCF film reflect this proton accumulation while the lighter zones on the film correspond to the areas of strong magnetic fields from which protons have been reoriented.

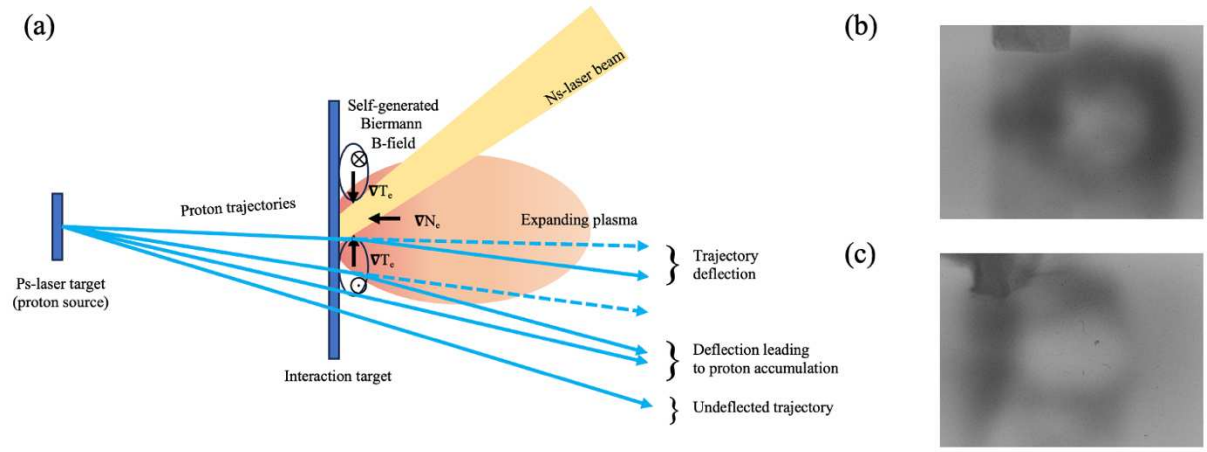

Figure 20. (a) Scheme of the TNSA protons deflection through the interaction with the self-generated magnetic field on the surface of the target. The original unbothered proton trajectories (showing the proton path without magnetic field) are modeled by the dotted arrows and the deflected trajectories are represented by the plain ones. (b) and (c): Raw RCFs exhibiting the proton deflection and the compression structure at (b) 1 ns and (c) 2.25 ns after the beginning of the interaction. The topology of the compression structure on RCFs will be detailed in the next chapter.

Calibrations have been made [15] to know how different materials slow down protons and how to determine the level of energy corresponding to each film, depending on the configuration of the stack. Therefore, we establish the different levels of energy measured with different possibilities of stacks by relying on the existing works of calibration. Here, the stacks were constituted of both types of RCFs, 3 HDV2 films and 3 EBT3 films, in which HDV2 are put on top of the stack for lower levels of energy, and EBT3 on the back for higher energies. All the stacks were wrapped in a 10 µm thick aluminum foil to maintain it and protect it from debris coming from the laser-target interaction, but also to constitute a first filter for the incoming radiation. Each RCF film is separated from the next one by 80 µm thick plastic filters to get regular and well distinct steps of energies. A laser such as the South line at the LULI2000 facility can produce protons whose energies reach until around $E_p \sim 20$ MeV, so the aim of the chosen configuration for the RCF stack was to cover the entire energy range (see Figure 21).

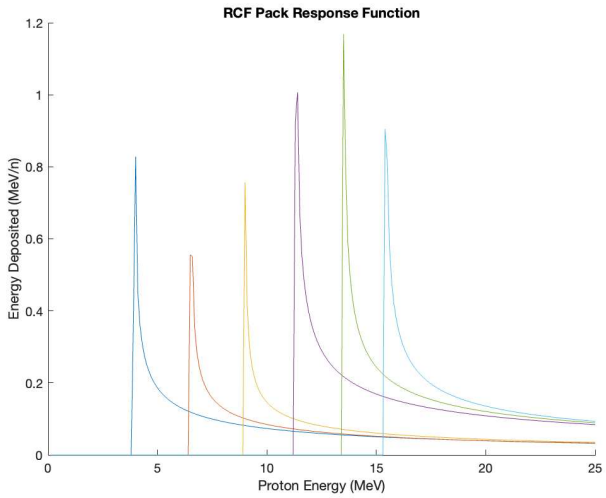

Figure 21. Response curves of the RCF stack showing the energy levels deposited by the incident protons in each RCF film. Each Bragg peak corresponds to a RCF film. Protons with the lowest energies will irradiate the HDV2 films closest to the targets while protons with highest levels of energy will propagate and reach the EBT3 films at the back of the stack.

We use RCFs and proton radiography to capture the projection of the protons deflected by the compression of the magnetic fields in plasmas generated from the interacting targets. The structure of the protons is projected on the RCFs and we can determine numerically the dose in Gray received by each RCF during the propagation of the proton beam [16]. During the experiment, the stack was set and remained in the axis of propagation of the TNSA beam. Alongside the time delay between the North and the South line that was regularly changed to track the temporal evolution of the compression, the distance between the interaction targets and the RCF stack has also been varied during the experiment, from 5 cm to 8.4 cm, to adjust the magnification of the interaction figure on the film.

4.1.2.2.2 Interferometry

In order to characterize the plasma created during the laser-target interaction, we used spatially and temporally resolved optical interferometry to probe the expanding plasmas and measure the electron density. GOI cameras (Gated Optical Imager) were set to capture the plasma evolution at different times during the interaction to track the temporal evolution of the electron density. The choice to use these camera devices ensures a temporal resolution around 80 ps. As mentioned before, the characteristic evolution time of the topology of the magnetic field is larger than this temporal resolution, therefore the diagnostic permits, to capture a specific moment in the evolution of the magnetic field compression structure.

The optical path was built to constitute a Mach-Zehnder interferometer [17]. With a beam splitter, we split the Nd:YAG auxilliary laser beam into two identical sub-beams, with the same phase, frequency and wavefront, which recombine at the exit of the interferometer. However, they were aligned with a phase difference to exhibit the interference fringes seen on the GOI cameras (see Figure 22). The beam propagating in the unaltered optical path is set as the reference beam. The other one is probing the plasmas and is perturbed by their expansion during the shot. Indeed, even if the two arms of the interferometer are aligned such as both beams go through the same distances to conserve the same optical length, the probing beam goes through the plasmas created by the ablation of the targets and is momentarily propagating into a medium with a lower refractive

index N, with $N = \frac{c}{v_\varphi}$, where v_φ is the phase velocity. In parallel, the reference beam remains unperturbated in the vacuum where N = 1. In a plasma, the refractive index and consequently the phase of the probing beam depend on the electron density n_e. Therefore, we observe a distortion of the fringes on the interferogram, correlated with the electron density n_e (see Figure 22b) and 22c)).

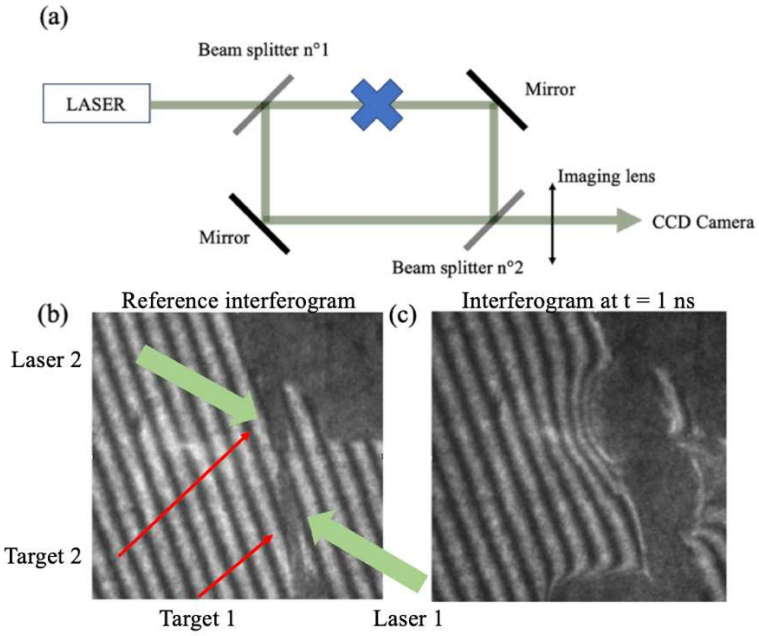

Figure 22. (a) Scheme of the Mach-Zehnder interferometer as it was setup during the experiment. Along the path within the interferometer, the beam coming from the Nd :YAG laser is collimated. It is being focused by the imaging lens upstream the CDD camera. The arms of the interferometer are aligned such as the interferogram appears focused on the CCD captor. (b) Interferogram without perturbations before the shot (reference image). The black block on the top right corner corresponds to the targets and their holder. (c) Interferogram 1 ns after the shot, the fringes are distorted by the presence of the plasma on the probing arm.

The expansion of the plasma on Figure 22c) is revealed by both the distortion of the interferometric fringes and the black area close to the target surfaces. This particularly zone corresponds to the region where the plasma is the densest. It appears opaque for the cameras because the laser probe propagating in the interferometer is entirely refracted by the strong gradients of electronic density.

To analyse the interferograms (Figure 22b) and 22c)), we used the software Neutrino [18], developed at LULI. Thanks to this software, and starting from the reference image, we obtain the spatial expansion of the plasma, the surface and volume density maps and the 2D profiles of the electron density n_e in the plasma. In order to get the volume density map from the surface distribution, we define an axis on the 2D map around which the system presents a cylindrical or a spherical symmetry in order to compensate the lack of information along the axis normal to the surface plane. This operation is done through Abel Inversion [19]. The complete methodology that leads to the volume density of the plasma starting from the interferograms will be detailed in Chapter 5.

4.1.2.2.3 Optical pyrometry

As the aim of our setup was to be able to observe the compression zone, it was also interesting to track the self-emission of the plasma and its temporal evolution. As mentioned in 4.1.2.1, the compression zone is confined within the targets area so it is possible to determine an axis along which we can measure this observable via optical pyrometry [20].

We tracked the evolution of the plasma heating during the compression process. Therefore, an optical path was aligned with the center of the targets area. The plasma generated via the laser-target interaction is heated through the laser energy deposition mechanisms such as the inverse Bremsstrahlung effect. During the interaction and the excitation of the copper atoms composing the targets, a photon resulting from the thermal heating of the electrons and of atomic de-excitation processes is emitted as a measurable signal. The emitted light during the shot and the compression process is reflected, in our case as a backscatter coming from one of the two long-pulse laser beams [21]. A beamsplitter divided the reflected light so only a fraction was redirected toward the camera to avoid any saturation of the image, as the pyrometry beam was focused through a converging lens. As we were interested in the temporal evolution of the plasma emission, the optical path was coupled with a streak camera Hamamatsu©. In order to only select a wavelength corresponding to a 2ω frequency, we added a green filter BG38 (red suppression filter) in front of the streak camera entrance, as well as an optical density whose attenuation could vary from one shot to another.

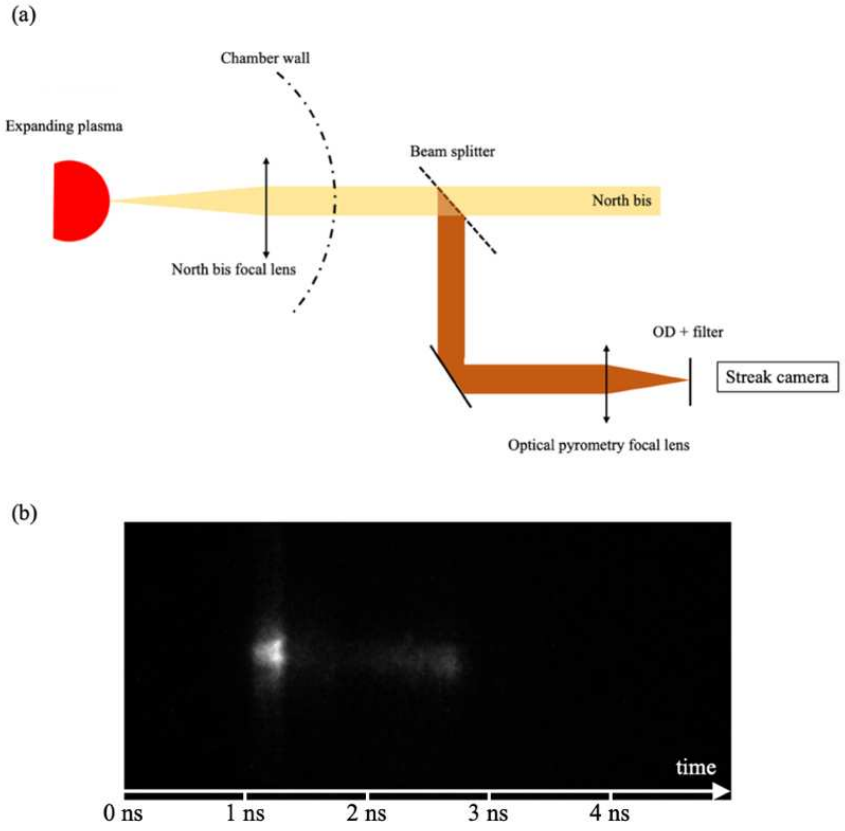

Figure 23. (a) Scheme of the optical pyrometry diagnostic as it was setup during the experiment. The light coming from the compression zone was divided by the beam splitter so only half of it reached the streak camera. (b) Image of the plasma visible light emission obtained with the streak camera for the configuration when both of the targets were irradiated by the two laser beams to induce the compression. During this shot, the time window of the streak camera was of 5 ns and an OD of 2.1 was placed in front of the camera entrance.

4.1.2.2.4 X-ray spectrometry

The last diagnostic for this experiment was an X-ray spectrometer used to measure the time integrated electron temperature of the plasmas produced during each shot, in the different tested configurations. We used a Focusing Spectrometer with Spatial Resolution (FSSR) [22], that was aligned toward the direction of propagation of the North bis beam, so with a 45° angle regarding on the target. The FSSR was placed in the chamber and was made of a spherical bent mica crystal that permitted to diffract the X-rays radiation and obtain the emission spectra of the ions coming directly from the ionization of the targets. The mica crystal presented a lattice spacing of $2d = 19.9149$ Å and a curvature radius of $R = 150$ mm. The spectral resolution over $\lambda/d\lambda = 1000$ was coupled to a spatial resolution of $\delta x = 120$ µm.

The crystal reflects the light due to its curvature and the resulting spectra were recorded on a fluorescence detector Fujifilm Image Plate (IP in this manuscript) [23]. The IP was placed under the crystal, which was aligned with the TCC height. It is a passive diagnostic as IPs were removed after each shot and it was possible to visualize the spectra (see Figure 24) by scanning them. As they are photosensitive, it was important to prevent them from being exposed to any kind of light after removing them from the FSSR box, in order to not pollute the information. Both the crystal and the IP were covered by a 2 µm thick PET filter as well as an aluminium filter whose thickness varied from shot to shot, following the level of saturation observed. These prevented from any reflections other than the X-rays on the IP that would pollute the emission spectra. Also, the filters protected the device from any debris coming from the laser-target interaction, like we did previously to protect the RCF stacks. The measurements of the plasma electron temperature were made by analysing the 4d-2p and 4s-2p electron transitions for Ne-like and Na-like ions. Indeed, the transitions peaks visible while analysing the spectra are sensitive to the variations of the temperature, the density and the thickness of the plasma.

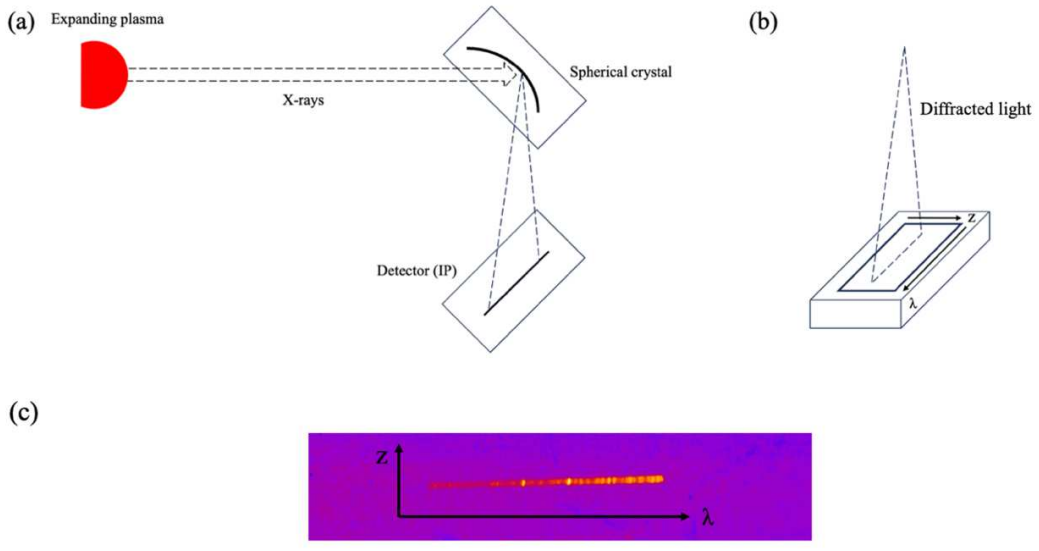

Figure 24. (a) Scheme of the side view of the FSSR setup with the expanding plasma (X-rays source), the spherical crystal aligned on the same height than the target and the detector (IP) below. The distance between the crystal and the detector was equivalent to the crystal curvature radius. (b) Close up in cavalier perspective of the IP inside its box. The different filters disposed on the top of the box are not represented here. (c) An IP processed with ImageJ for a single shot with the North bis beam only on a copper target, showing the emission spectrum.

Here, we described the different diagnostics used in the laboratory to characterize experimentally magnetic field compression. The experimental data and results will be associated to a theoretical work with hydrodynamic and PIC simulations. The codes used to run these simulations and their specificities will be described in detail in 4.2.

4.1.3 Experimental setup for magnetic reconnection

4.1.3.1 Geometry of the experiment

The experimental campaign focusing on magnetic reconnection took place in 2023 at the LULI2000 facility, in the same experimental room as the campaign focusing on magnetic compression. To generate the reconnection in the laboratory, we used a two targets configuration like we did for magnetic field compression, and we adapted the previous setup for the spatial needs of the reconnection experiment. Once again, two identical coppers targets (5 µm thick each) were irradiated by the two identical nanosecond-long laser beams North and North Bis. This time, the two beams were aligned to enter the chamber with the same direction of propagation, so both of them interact with the targets on the same face (see Figure 25). However, they are still oriented with a 45° angle of incidence. With this new setup, the plasmas created by the laser-target interaction interacted and collided in front of the two targets, such as the magnetic fields within each plume collide toward each other in their zone of interaction with opposed orientations. This configuration of anti-parallel fields induces magnetic reconnection between the two expanding magnetized plasmas.

Otherwise, besides the disposition of the targets and the beams adapted to orientate the fields in the required anti-parallel configuration, we adapted this setup in order to extend the zone of reconnection and then create an elongated current sheet between the interacting plasmas. Therefore, the North and North Bis beams were aligned such as they irradiated the targets with elliptical focal spots, whose dimensions were approximately 600 µm by 80 µm. Finally, the target holder was designed to permit to introduce an angle to tilt the targets toward each other. This angle varied from shot to shot (from 0° for coplanar targets to 30°) [24]. This method can induce an out-of-plane guide field that can alter the reconnection process. This was helpful to track the evolution of the current sheet at different times of the reconnection process.

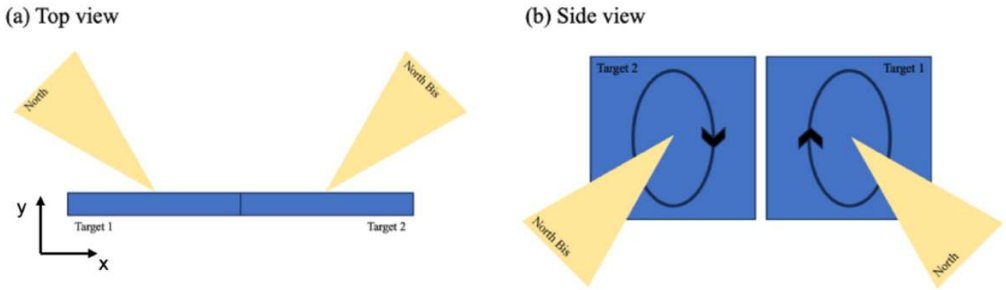

Figure 25. Schemes of the target and beam configuration and of the magnetic field disposition for the magnetic reconnection experiment. The North and North Bis beams were irradiating the targets in a symmetric configuration about the axis normal the two target surfaces, with an incident angle of 45° each. Here, the targets represented are coplanar.

The South beam line delivering the picosecond-long pulse was used as a third beam to generate a TNSA proton beam similarely to the magnetic compression experiment, and the target used remains the same as previously (23 µm thick and PET target). The magnetic reconnection figure is going to be formed by protons that are deflected by the interaction of the plasmas magnetized by the Biermann battery effect, using proton radiography as in the compression experimental setup. During the campaign, the distance between the interaction targets and the TNSA plastic target varied in regard with the different configurations that were tested. This distance varied from 4.7 mm for a 15° tilting angle to 1 cm for a 30° angle and coplanar targets (see Figure 26).

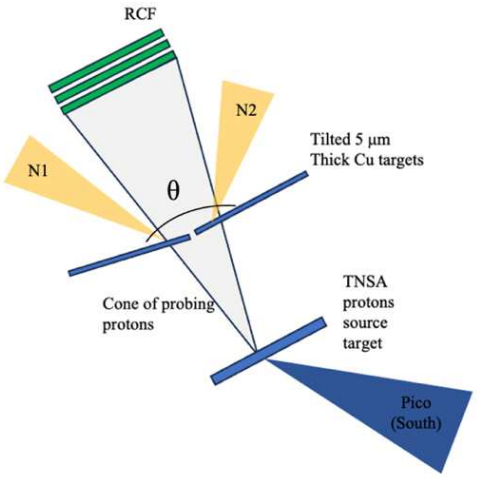

Figure 26. Scheme of the experimental setup with the targets represented in light blue, the two nanosecond-long lasers in yellow (here named N1 and N2 to ease the visibility), the laser generating the proton beam in dark blue and the RCF stack in green. The angle θ corresponds to the aperture angle between the two targets and varied from shot to shot.

The geometry of this experiment was also made possible by using target holders conveived at the target laboratory of École Polytechnique and, diagnostics have also been installed to characterize both the plasmas and the reconnection process, as well as to track to evolution of the current sheet. The functionings of most of the diagnostics we used during this second experiment (like proton radiography, optical pyrometry and interferometry) has already been described in 4.1.2.2., and will not be repeated here in this section. However, we will explain how we adapted these diagnostics to the new configuration and also, we will address the complementary diagnostic that has been added for the present campaign.

4.1.3.2 Adaptation of the diagnostics

The same diagnostics used for the magnetic compression experiment were used for the one about magnetic reconnection. Consequently, we are not going to describe their functionings again (see 4.1.2.2) but here we will emphasize the modifications made to adapt them to the study of magnetic reconnection and the characterization of the current sheet between the two plasmas.

First, the proton radiography diagnostic was installed such as the stack faced the targets in front of the ionization side. Plus, the stack remained in the axis of propagation of the TNSA proton

beam. Here, proton radiography was used to image both the figures of reconnection and to focus on and visualize the elongated current sheet and the formation of plasmoids. The distance between the targets and the first RCFs of the stack moved from 4.2 cm to 5.2 cm during the experiment depending on the target configuration and the expected level of magnification. We used a stack composed of 3 HD-V2 films for the first levels of energy and 3 EBT films for the highest energies. Each time, the films are separated from each other by two 80 µm thick PET filters. Also, a 10 µm thick aluminium filter is placed at the top of the stack to prevent from the saturation of the first films and to protect them from possible debris from the laser-target interaction. The energy levels corresponding to the different films have also been recalculated (see Figure 27).

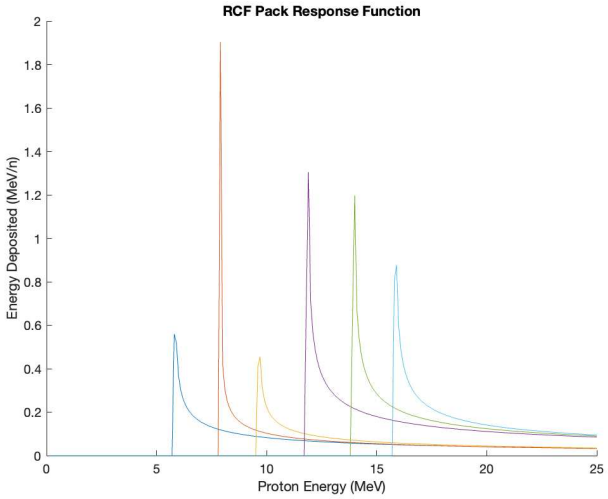

Figure 27. Response curves of the RCF stack showing the energy levels deposited in each film from the stack in the reconnection experiment.

For the interferometry diagnostic, we built again a Mach-Zehnder interferometer, using the Nd:YAG Quantaray laser as optical probe. The interaction arm is set to go through the plasma expanding in front of the interaction targets. For optical pyrometry, we once again used the optical return of one long-pulse beam partially redirected toward a streak camera with a beam splitter. This time, optical pyrometry was used to measure the temporal evolution of the plasma along the reconnection sheet and the optical path was aligned with the current sheet direction axis.

We described in this first part all the different diagnostics and equipments used and needed for the experimental campaigns for this thesis. We will detail the experimental results in Chapter 5 for magnetic compression and Chapter 6 for magnetic reconnection, along how we observed the targeted phenomena and how we analysed and put together the different data collected with the diagnostics. For both experimental studies, a work of numerical simulation was performed to complete the diagnostic measurements and support the interpretation of the experimental results. Therefore, we also provide a computational study of the plasma dynamics in the observed mechanisms.

4.2 Analytical and numerical tools to model plasmas

We worked with two different simulation codes, as each of them are designed to simulate specific physical processes, in order to provide a comprehensive theoretical description of the plasma evolution. Indeed, a complete characterization of the plasma is required on both the field-based and particle-based approaches. Consequently, a code relying on the fluid description of the plasma, programmed to solve the MHD equations, will only allow to investigate the macroscopical aspects of the system, where particles are not treated individually but rather as a continuous fluid. In parallel, magnetic compression and magnetic reconnection are phenomena resulting among else in particle acceleration, implying that individual charged particles are directly involved in the energy exchanges that shape the plasma in the interaction zone for both cases. As the particle kinetic cannot be describe by the MHD framework, a kinetic description is therefore required here to address the microscopical effects and to resolve the motion of the individual particles during the evolution of the system.

Whether numerical codes are designed for the MHD or particle description of the plasma, each one is set differently and relies on fundamentally different numerical and physical frameworks, such as a single code would not be able to simulate simultaneously the macroscopical and microscopical aspects of a same system. An MHD-based hydrodynamic code does not resolve kinetic effects and PIC simulations cannot model the large-scale evolution of the plasma dynamics. As a result, the two studies are distinct but completementary. In the following part, we will introduce and describe the two simulation codes used to run our simulations to support our experimental results. Simulation results for magnetic field compression and for magnetic reconnection will be respectively developed in Chapter 5 and Chapter 6 along with experimental results.

4.2.1 Hydrodynamical and macroscopic description: the FLASH code

4.2.1.1 Numerical setup

FLASH is a FORTRAN90-written code based on the CGS unit system, developed by the University of Chicago and then carried on by the University of Rochester at the FLASH Center for Computational Science (USA) [25]. It is a multi-physics code which carries several packages able to solve many physical issues, mainly linked to astrophysics, plasma physics and HED physics, but also related to fluid instabilities and laser-plasma interactions. We ran our simulations using the FLASH4.7.1 version since this was the latest version available. This version contains all the previous packages mentioned, as well as those requested to model the experiments, such as the conductivity or the magnetic field related packages.

FLASH is a Eulerian code [26], its approach is oriented to solve fluid dynamic problems over a large range of situations, whose frameworks are suited to obtain an MHD description of the studied systems. Therefore, FLASH relies on and solves the general governing equations of MHD (see Euler equations in Chapter 1, eqs. 1.5 – 1.9), and can be used to describe both ideal MHD or resistive MHD regimes. Indeed, the specificity of the MHD approach is that a hydrodynamical code like FLASH will consider both the electrons and the ions as a compressible fluid, rather than individual and single particles. The MHD approximation of a fluid used by FLASH assumes that

the particle velocity distribution is Maxwellian, providing only a solution to MHD equations. The macroscopic variables, such as densities or temperatures, are modeled over time by the code by approximating numerically the MHD equations. As a hydrodynamical code, FLASH neglects the possible kinetic or microscopic effects like particle acceleration or any non-Maxwellian velocity distributions.

FLASH was used in our study of magnetic field compression to give the macroscopic aspect of the evolution of the compressed magnetic field and to reproduce the experimental results at these scales. In this work, FLASH was run to simulate the expansion of the plasma, model the evolution of the electron density and the magnetic field in the compression sheet, as well as to measure the temperatures and, more generally, all the quantities evaluated within the MHD framework. The laser energy was deposited in the cells constituting the first layers of the target through inverse Bremsstrahlung, as it happens in the laboratory. Solid matter, like in the interaction targets, is not considered in a solid state but instead represented by an overcritical plasma, that becomes temporally underdense in order to deposit the laser energy where the beam meets the cells constituting the target surface. The amount of energy deposited on these cells can be determined with an energy balance calculation.

For this thesis, simulations were performed in the cartesian geometry but FLASH also provides cylindrical or spherical geometries. Morever, the code includes dedicated solvers for hydrodynamics and, more generally, for MHD systems, as well as all the implicit solvers based on the HYPRE library. These allow to model various plasma processes, such as magnetic field evolution, electron thermal conduction or anisotropic transport. Besides, in order to model correctly the temperature in HED plasmas, a single temperature model in the ideal MHD framework is insufficient. Indeed, various physical processes such as laser heating, transport or radiation absorption and emission, can cause fluctuations from the electron-ion-radiation thermal equilibrium and bring the system out of its stable state. To include all these effects, FLASH extends the standard MHD system of equations by treating the electron, ion and radiation temperatures separately. This approach permits a more complete model of the plasma dynamics and this description of the plasma and is known as the “3T” description (for “3 temperatures”).

The cells that compose the simulation domain remain stationary and for every timestep, each quantity occupies the entirety of the cell. Diffusion is then allowed when a flux simulated by FLASH crosses the boundary between two consecutive cells. In this case, the quantity allocated to each cell varies with the evolution of the system. Consequently, some areas of the simulation grid present shaper gradients of different physical quantities (like higher gradients of temperature in the focal spot area and axis of propagation of the laser beam or brutal density gradients on the target surface). Consequently, to prevent from an accumulation of information in one cell and a possible numerical failure, FLASH allows to define an adapative grid, called an adaptative mesh refinement (AMR in this manuscript) [27]. An AMR grid enables to increase locally the resolution of the simulation in a specific zone where it is necessary to do so, as depicted in Figure 29.

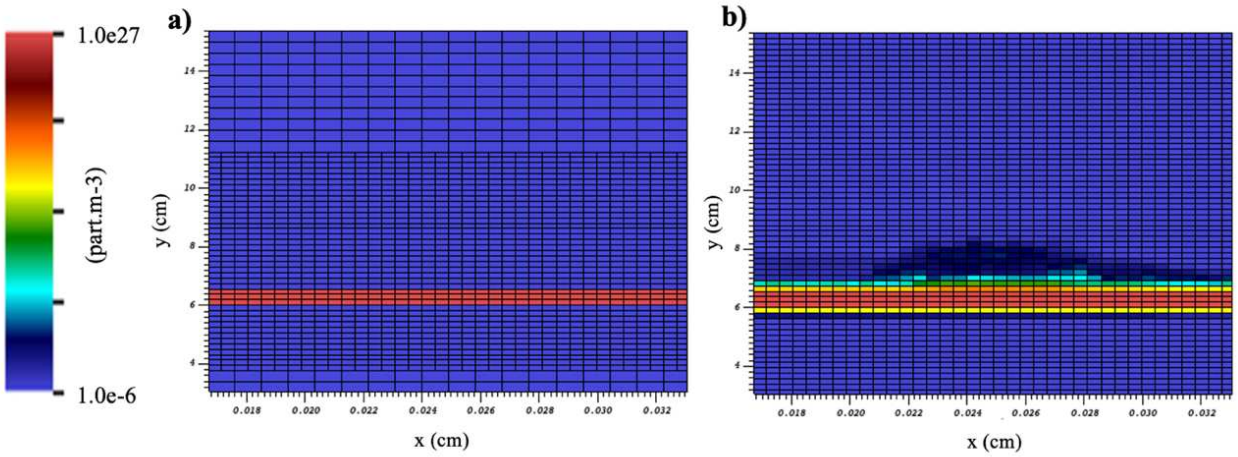

Figure 28. Example of the adaptation of the mesh around the target hit by the laser in cartesian coordinates in 2D FLASH simulations. a) represents a copper target at t = 0 ns. The mesh around the target is smaller because of the difference of density between the target and the vacuum. b) represents the first step of the simulation. The mesh adapted itself as the laser beam propagates and the target starts to be ionized and the plasma to expand.

Each cell, whether it is affected by the AMR process during the simulation, is composed of logically cartesian arranged blocks. In 2D, each cell is subdivided into a number nxb of blocks along **x** and a number nyb along **y**. Each block is identified by a coordinate (i, j) such as $i \in [1, nxb]$ and $j \in [1, nyb]$. This subdivision is efficient in the three systems of coordinates and the numbers of blocks nxb, nyb are chosen by the user in order to adapt the global resolution of the simulation. A higher number of blocks per cells increases the resolution of the simulation and can reduce possible risks of mismatch between two zones presenting too different gradients. However, a higher resolution also slows down the simulation.

Another important parameter to set for the grid is the refinement level, which defines the maximal internal refinement of each block composing a cell in the AMR. It corresponds to the highest spatial resolution achievable during the simulation (see Figure 30). Consequently, each refinement level corresponds to the number of subdivisions of a cell. The refinement value is carried by the variable **refinement_max,** which value is set between 1 and 4 and defined by the user. This parameter plays a key role in the resolution of fine plasma structures or areas of the simulations carrying important gradients. However, like the global resolution itself described in the previous paragraph, a high value of **refinement_max** increases the computational cost.

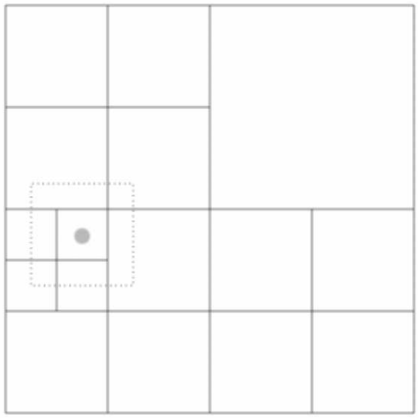

Figure 29. Scheme of the adaptative mesh refinement process in a FLASH simulation [28] showing the adaptation of the dimension of the cells, subdivided by blocks. The refinement process ensures that every cell in the computational grid is systematically probed and refined if needed.

4.2.1.2 Definition of the setup for magnetic compression

FLASH was used in this work to characterize magnetic compression in the MHD framework, as defined in Chapter 2 and to support the experimental settings and conclusions. Therefore, we implemented the beam parameters for the lasers, in order to correspond to the beam characteristics of the LULI2000 (see section 4.1). The copper targets (with an atomic number Z = 29 and a mass number A = 64) were set with a length of 350 µm and a width of 5 µm to match the dimensions of the targets used during the experiment. To model solid copper, we defined the target with the volume density of copper n_{copper} = 8.96 g/cm^3. As FLASH cannot represent the vacuum numerically, it has to be defined as a proper species. Consequently, we set the copper targets in a low-density hydrogen gas (Z = A = 1), with $n_{gas} = 10^{-6}$ g/cm^3, to reproduce as close as possible the conditions of plasma expansion in vacuum. In order to guarantee the stability of the simulation and more particularly to prevent from overstated temperature gradients between the copper target (high Z) and the pseudo-vacuum (low Z), the Courant-Friedrichs-Lewy (CFL) condition was put to 0.1 and the numerical setup was initialized at T_0 = 500 K. This value for the temperature was chosen following multiple tests and remains cold enough to not wrongfully influence the thermic evolution of the system but stable enough to prevent from numerical issues during the run of the simulation.

We defined a 1 x 1 mm simulation domain, with a 10 block-per-mesh resolution, a maximal refinement **refine_max** = 3, and all the boundaries were set to the "outflow" condition. The typical timestep of such a numerical setup is 1 ps and all the simulation results presented in this manuscript are in a 2D cartesian geometry. Besides, the only module used for magnetic field generation is the Biermann battery module, associated to the diffusion and the conductivity for electrons and ions. Furthermore, it is crucial to implement the equations of state of copper and hydrogen constituting the targets and the vacuum, in order to model the laser-matter interaction correctly. Indeed, these equations govern the evolution of the interactions between the species and the laser beam, as they exhibit the dynamics of the material and the observables. We built these equations of state with the software MPE, developed by Jean-Luc Dubois at CELIA. Defining the equations of state with MPE is a preliminary work done before running a FLASH simulation as it generates IONMIX tables containing the distribution of energy for both the target and vacuum covering the entire energy range expected during the simulation in order to describe correctly the variations of the laser-driven plasma [29]. All the materials in the simulation must be described with the same energy repartition in order to not induce a mismatch in the energy transport between

the target and the vacuum. In the present case, the energy was partitioned in ranges between 1 eV and 100 keV.

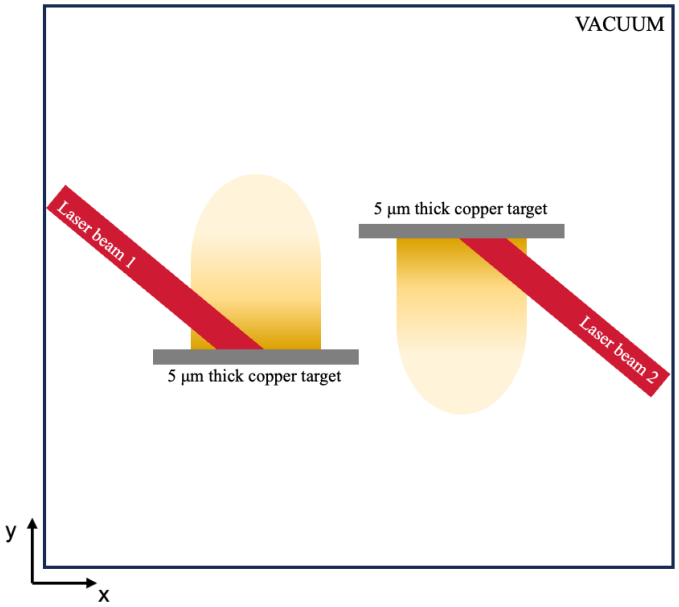

Figure 30. Schematic illustration of the experimental setup for magnetic compression with the expanding plasmas, reproduced and adapted for FLASH simulations in 2D cartesian geometry. The black border represents the limits of the simulation domain.

As mentioned in Chapter 1, the MHD description of plasma expansion determines the global and macroscopical evolution, by considering the plasma flows as compressive fluids. This specific framework enables to solve the Euler equations but still remains restricted. Indeed, the system has to meet certain conditions over its spatio-temporal scales for the MHD description to be applied accurately. Otherwise, the MHD equations are not valid anymore.

However, a plasma is composed of charged particles with their proper motion and kinetic properties, which can influence the plasma, this time at smaller scales. At these scales, the collisionless aspect of the plasma is dominant and the velocity distributions are non-Maxwellian. Since these mechanisms are outside of the MHD framework, they are not described by hydrodynamical codes such as FLASH, they need to be addressed using a different theoretical framework. Consequently, we model the kinetic effects by using Particle-in-cell codes.

4.2.2 Microscopic and kinetic description

4.2.2.1 Properties of the Particle-in-Cell code SMILEI

Particle-in-Cell codes are suited to describe magnetized plasmas at scales where they are governed by kinetic effects. PIC codes are commonly used in plasma physics to model the motion of charged particles in electromagnetic fields with non-Maxwellian velocity distributions [30]. As the collisionless aspect of the plasma dominates in the kinetic framework, we use a PIC code to solve the coupled system of Maxwell-Vlasov equations.

We ran simulations using SMILEI [31], a C++ based PIC code, designed especially for plasma simulations and partially developed at LULI. It disposes of various important modules for plasma physics simulations, as well as several Maxwell solvers. The PIC method used by SMILEI consists in the discretization of the distribution function (see Chapter 1, eq. 1.11) in a finite sum of N_s numerically modeled particles, such as [32]:

$$f_s(t, \mathbf{x}, \mathbf{p}) = \sum_{p=1}^{N_s} \frac{w_p}{V_c} S(\mathbf{x} - \mathbf{x}_p(t))\delta(\mathbf{p} - \mathbf{p_p(t)}) , \quad (4.1)$$

where $\mathbf{x}_p$ and $\mathbf{p}_p$ are the position and the momentum of a particle, V_C is the volume of a cell composing the simulation grid, S is the shape function which represents the implementation of the particles in the simulation grid, δ is the Dirac distribution, and w_p is the weight, defined by:

$$w_p = \frac{n_\alpha(x_p(t=0))}{N_\alpha(x_p(t=0))} , \quad (4.2)$$

where n_α is the particle density for a specific species α (electrons or ions), and N_α is the total number of particles contained in a single cell of the grid. Indeed, PIC codes integrate the Vlasov equation (see Chapter 1, eq. 1.17) along the continuous trajectories of the particles within an electromagnetic field and solve the Maxwell equations on a discrete numerical grid subdivided in cells. SMILEI enables to interpolate the electric and magnetic fields for the position of each particle, as well as to compute and track the position and the velocity of a particle at each timestep. Consequently, the components of the electromagnetic field are defined with SMILEI by:

$$\mathbf{E}_p = \int S(x - x_p)\mathbf{E}(x)dx \quad (4.3)$$

$$\mathbf{B}_p = \int S(x - x_p)\mathbf{B}(x)dx \quad (4.4)$$

The electromagnetic fields are entirely discretized in the physical and phase space, and by combining the discretized distribution function (eq. 4.1) with the Vlasov equation, we obtain the equations of motion of the particles in the non-relativistic regime:

$$\frac{d\mathbf{x_p}}{dt} = \mathbf{v_p} \quad (4.5)$$

$$\frac{d\mathbf{v_p}}{dt} = \frac{q_p}{m_p}(\mathbf{E}_p + \mathbf{v}_p \times \mathbf{B}_p) \quad (4.6)$$

At each timestep, SMILEI interpolates the electromagnetic field and the other necessary physical quantities such as the position and the velocity of the particles, as well as the charge and current densities. The new electromagnetic field is then recomputed on the grid, solving the discretized Maxwell equations. These fields are then taken as a field reference for the new interpolation made by the code at the next timestep, creating a recursive loop at each timestep.

4.2.2.2 Architecture of the setups and connection with FLASH

Whether SMILEI simulations were run in order to study magnetic compression or magnetic reconnection, the aim was to simulate the evolution of the interaction zone and of the particle distribution when the two laser-driven magnetized plasmas propagate and collide. As two distincts mechanisms are studied here, the specificities of each setup will be described and detailed in

Chapter 5 and Chapter 6 respectively, but there are still some similarities. As we focus each time on both electrons and protons, we chose a realistic mass ratio between the two species, such as $m_i/m_e = 1836$. Besides, to recreate the magnetized plasmas, we initialized a background magnetic field that represents the orientation of the colliding fields in each experiment. As magnetic compression occurs when the fields are oriented parallel to each other, we implement a uniform magnetic field to model this alignment. On the contrary, we initialize a hyperbolic tangential profile for the magnetic reconnection case to model the anti-parallel topology of the interacting fields.

The motion of the plasmas is exhibited by a double-gaussian density profile on each side of the simulation domain, modeling the converging flows of particles. The particles are advected toward each other in the center of the domain by a hyperbolic tangent shaped velocity profile. This specific profile for the velocity enables to have, for $y < y_0$, (where $y_0 = L_y/2$ and L_y is the transverse dimension of the simulation domain), a particle velocity such as $\vec{v} = v\vec{y}$, and $\vec{v} = -v\vec{y}$ for $y > y_0$.

We relied on experimental observations (as well as FLASH results in the case of magnetic compression) to set the different parameters of the PIC simulations, like the initial velocity or the electron and ion temperatures. These parameters varied from one topic to the other and will be described later. However, the numerical parameters implemented for the two sets of SMILEI simulations are similar: the typical timestep was 0.3 fs and the resolution of the simulation grid was set to 1024 x 512 so that the length $l_{x,y}$ of each cell in each dimension was $l_{x,y} \sim \lambda_D$, where λ_D is the Debye length. Each cell contained initially at least 64 particles and were distributed on at least 8 x 4 patches on the grid. All the SMILEI simulations presented in this manuscript are in a 2D cartesian geometry, like the FLASH results.

SMILEI simulations enable to solve numerically mechanisms occuring out of the framework of the MHD that cannot be observed with hydrodynamic codes like FLASH. Conducting a theoretical study covering both the fluid and the kinetic approach of the plasma permits to give a complete view of the dynamics of the plasma, as well as the evolution of the different quantitites altering the topology of the magnetic field during the interaction over large temporal and spatial scales. The disparities between the two methods are summarized in Table 2.

	Hydrodynamic description	**Kinetic description**
Global function	Describes the plasma as a fluid (MHD)	Describes the motion of particles in the plasma
Expected results	Models macroscopic observables	Solves the distribution function of particles
Field of efficiency	Large and global systems	Local non-linear effects
Microscopic effects	Not explicitly modeled	Self-consistently resolved

Tableau 2. Summary of the main differences of the two descriptions and of the complementarity of the two studies.

4.3 Conclusion

We presented in this chapter the different tools and diagnostics needed in our studies of interactions between laser-driven magnetized plasmas. For both magnetic field compression and magnetic reconnection, we needed to establish a precise experimental setup in order to conduct our studies in the laboratory. We presented the role of the different diagnostics, as well as the physical quantities that were investigated and observed.

In parallel of data analysis, we conducted a theoretical study using the simulation codes FLASH and SMILEI for both the hydrodynamic and the kinetic descriptions of our systems. The numerical setup of the simulations and the choice of the correct parameters have taken an important time of this thesis work to provide the closest results to the reality of the experiment. This included different phases of test, benchmarking and variations of the parameters. However, we came to relevant results to support the experimental ones. The two following chapters will consist on the presentation of these results, both for experimental data and simulations.

References

[1] M. Koenig et al., « Recent laboratory astrophysics experiements at LULI », Plasma and Fusion Research, Volume 4, 044 (March 2009).
https://doi.org/10.1585/pfr.4.044

[2] D. Strickland and G. Mourou, « Compression of amplified chirped optical pulses », Optics Communications, 56(3) :219–221 (December 1985).
https://doi.org/10.1016/0030-4018(85)90120-8

[3] B. Zhou *et al*, « Efficient, frequency-stable laser-diode-pumped Nd:YAG laser », Opt. Lett. 10, Issue 2, 62-64 (1985).
https://doi.org/10.1364/OL.10.000062

[4] R.A. Snavely *et al*, « Intense high-energy proton beams from petawattlaser irradiation of solids », Physical Review Letters, 85(14):2945 (October 2000).
https://doi.org/10.1103/PhysRevLett.85.2945

[5] S.C. Wilks, S. C. *et al*, « Energetic proton generation in ultra-intense laser–solid Interaction », Physics of plasmas, 8(2):542–549 (February 2001).
https://doi.org/10.1063/1.1333697

[6] W. Fox, G. Fiksel and D.B. Schaeffer, « Proton deflectometry analysis in magnetized plasmas: magnetic field reconstruction in one dimension », Phys. Rev. E, Volume 110, 015206 (July 2024).
https://doi.org/10.1103/PhysRevE.110.015206

[7] Y. Cui *et al*, « The importance of Righi-Leduc heat flux to the ablative Rayleigh-Taylor instability during a laser irradiating target », High Power Laser Science and Engineering, Volume 12, e24 (Janvier 2024).
https://doi.org/10.1017/hpl.2024.3

[8] A. Nishiguchi *et al*, « Convective amplificationf of magnetic field in laser-produced plasmas by the Nernst effect », Phys. Rev. Lett., Volume 62, article 3 (Juillet 1984).
https://doi.org/10.1103/PhysRevLett.53.262

[9] T.E. Cowan *et al*, « Ultralow emittance, multi-MeV proton beams from a laser virtual-cathode plasma accelerator », Phys. Rev. Lett. 92, 204801 (May 2004).
https://doi.org/10.1103/PhysRevLett.92.204801

[10] M. Borghesi *et al*, « Proton imaging detection of transient electromagnetic fields in laser-plasma interactions », Rev. Sci. Instrum. 74, 1688-1693 (March 2003).
https://doi.org/10.1063/1.1534390

[11] M. Borghesi *et al*, « Multi-MeV proton source investigations in ultraintense laser-foil interactions », Phys. Rev. Lett. 92, 055003 (February 2004).
https://doi.org/10.1103/PhysRevLett.92.055003

[12] S.N. Chen *et al*, « Absolute dosimetric characterization of Gafchromic EBT3 and HDv2 films using commercial flat-bed scanners and evaluation of the scanner response function variability », Rev. Sci. Instrum., 87(7):073301 (July 2016).
https://doi.org/10.1063/1.4954921

[13] V. Istokskaia *et al*, « Proton Bragg curve and energy reconstruction using an online scintillator stack detector », Rev. Sci. Instrum., 94 073305 (July 2023).
https://doi.org/10.1063/5.0146554

[14] A. Mancic *et al*, « Isochoric heating of solids by laser-accelerated protons: Experimental characterization and self-consistent hydrodynamic modeling », High Energy Density Physics, Volume 6, Issue 1, p.21-28 (January 2010).
https://doi.org/10.1016/j.hedp.2009.06.008

[15] C.A. Cecchetti *et al*., "Magnetic field measurements in laser-produced plasmas via proton deflectometry", Phys. Plasmas, Volume 16, 043102 (Avril 2009).
https://doi.org/10.1063/1.3097899

[16] S.A. Gaillard *et al*, « Study of saturatin of CR39 nuclear track detectors at high ion fluence and of associated artifact patterns », Rev. Sci. Instrum., 78(1):013304 (February 2007).
https://doi.org/10.1063/1.2400020

[17] M. BORN and E. WOLF, « Elements of the theory of interference and interferometers », Principles of Optics, p.256-369, Elsevier, 1980.

[18] GitHub NeutrinoToolkit/Neutrino. image analysis for plasma physics. https://gith ub.com/NeutrinoToolkit/Neutrino. (Website still accessible in April 2026).

[19] P. Tomassini and A. Giulietti, « A generalization of Abel inversion to non-axisymmetric density distribution », Optics Communications, Volume 199, Issue 1-4, p.143-148 (Novembre 2001).
https://doi.org/10.1016/S0030-4018(01)01575-9

[20] P. Bertrand *et al*, « Pyrometry applications in thermal plasma processing », Vacuum, Volume 56, Issue 1, p.71-76 (January 2000).
https://doi.org/10.1016/S0042-207X(99)00168-2

[21] S. Bolanos *et al*, « Laboratory evidence of magnetic reconnection hampered in obliquely interacting flux tubes », Nature Communications, 13:6426 (October 2022).
https://doi.org/10.1038/s41467-022-33813-9

[22] A.Y. Faenov *et al*, « High-performance X-ray spectroscopic devices for plasma microsources investigations », Physica Scripta, Volume 50, Number 4, 333 (March 1994).
https://doi.org/10.1088/0031-8949/50/4/003

[23] N. Izumi *et al*, « Application of imaging plates to X-ray imaging and spectroscopy in laser plasma experiments », Rev. Sci. Instrum., 77, 10E325 (October 2006).
https://doi.org/10.1063/1.2351924

[24] S. Bolanos, « Étude expérimentale de la dynamique de la reconnexion magnétique induit par laser de puissance », Doctoral thesis defended at École Polytechnique (December 2019).

[25] P. Tzeferacos et al., « FLASH MHD simulations of experiments that study shock generated magnetic fields », High Energy Density Physics, Volume 17, Part A, p.24-31 (December 2015). https://doi.org/10.1016/j.hedp.2014.11.003

[26] M. Shoucri, « Eulerian codes for the numerical solution of the Vlasov equation », Communications in Nonlinear Science and Numerical Simulation, Volume 13, Issue 1, p.174-182 (February 2008).
https://doi.org/10.1016/j.cnsns.2007.04.004

[27] D. DeZeeuw and K.G. Powell, « An adaptively refined cartesian mesh solver for the Euler Equations », Journal of Computational Physics, Volume 104, Issue 1, p. 56-68 (January 1993).
https://doi.org/10.1006/jcph.1993.1007

[28] FLASH User's Guide, FLASH 4.7.1.
https://flash.rochester.edu/site/flashcode/user_support/flash4_ug_4p71/ (website still available in April 2026).

[29] S. Bilyk & M. Grinfeld, « Operational equations of state for hydrocode: computer implementation », Procedia Engineering, Volume 58, p. 424 – 432 (December 2013).

[30] C.K. Birdsall and A.B. Langdon, Plasma Physics via Computer Simulation, Series in Plasma Physics (January 1991).
https://doi.org/10.1201/9781315275048

[31] J. Derouillat *et al*, « SMILEI : A collaborative, open-source, multi-purpose particle-in-cell code for plasma simulation », Computer Physics Communations, Volume 222, p. 351-373 (January 2018).
https://doi.org/10.1016/j.cpc.2017.09.024

[32] https://smileipic.github.io/Smilei/ (website still available in April 2026).

Chapitre 5

Experimental and theoretical investigation of the saturated magnetic field compression between laser-driven plasmas

In this chapter, we detail our study of magnetic field compression conducted both experimentally in the laboratory and theoretically through hydrodynamic simulations to evaluate the macroscopic evolution of the process and PIC simulations to investigate the dynamics of the compression sheet at smaller scales to assess the influence of kinetic effects. If the saturation of the compressed magnetic field has already been observed, we will here bring new elements to describe the mechanisms inducing this saturated aspect of the compression. In this part, we will first describe and characterize the plasma generated by the laser-matter interaction during our experimental campaign. We experimentally proved the saturation of the compressed magnetic field during the collision of two counter-propagating plasmas carrying spontaneous Biermann battery magnetic fields whose orientations are similar in the zone of interaction. Here, there is no external sources of magnetic field. Then, we will focus on the dynamics of the compression process, as well as on the formation and the evolution of the compression sheet. We performed hydrodynamic simulations to build a complete representation of the process and to corroborate the experimental conclusions, as well as PIC simulations to deepen our understanding of the inner topology of the compression zone and the ensuing particle acceleration. This combined approach was conducted to distinguish the different regimes occuring during the compression of two HED laser-driven magnetized plasmas, and to describe the dynamics of the compression sheet. Here, we detail the dynamics of the compression zone in both the macroscopic and particle-scale frameworks.

5.1 Characterisation of the plasma

Establishing the main characteristics of the plasma ablated by the laser-target interaction is the first step to analyse quantitatively the characteristics of the compression zone. In this part of our study, we aim to determine the macroscopic values defining the plasma, such as the electron density, the electron temperature, the characteristic length and the profile of expansion of the laser-driven plasmas. These observations not only allow to be assured of a correct ionization of the target by the laser and to validate the experimental observations, but also, these physical quantities will permit to calculate the characteristic dimensionless plasma parameters. We will be able to draw similarities between space plasmas and plasmas created in our laboratory to make analogies and also compare our experimental plasmas to our simulation results.

5.1.1 Measurement of the electron density

As described in section 4.1.2.2.2., our interferometry diagnostic consisted in a Mach-Zehnder interferometer. One of the arms went through the zone of interaction between the nanosecond-long laser beams and the targets in order to image the expanding plasmas, both before the shot (serving as reference interferograms) and during the target ionization (see Figure 31). We observe visually the expansion of the plasma on the experimental interferograms, represented by the black area (the zone where the light of the laser is refracted by the strongest gradients of density and where the plasma is opaque), as well as by the perturbations of the interference fringes (see Figure 31a)).

Interferometry was used to measure both the surface and the line-integrated volume electron densities by probing the plasma in the interaction region. For each shot, the ablated plasma is probed at different times after the beginning of the laser-target interaction to track the temporal evolution of the expansion. The interferograms are analyzed using the software Neutrino described previously in Chapter 4. By associating the reference and shot interferograms to extract the phase shift induced by the expanding plasma plume on the probe beam, the spatial topology of the electron density can be reconstructed, providing both the surface and the volume density map. We underline that this analysis conducted to extract the density maps and the characteristic length was done for a single target configuration, so in this present case, only one target was irradiated by a single nanosecond-long laser beam. In order to characterize the free expansion of the plasma, we needed a configuration where the magnetic compression was not occuring.

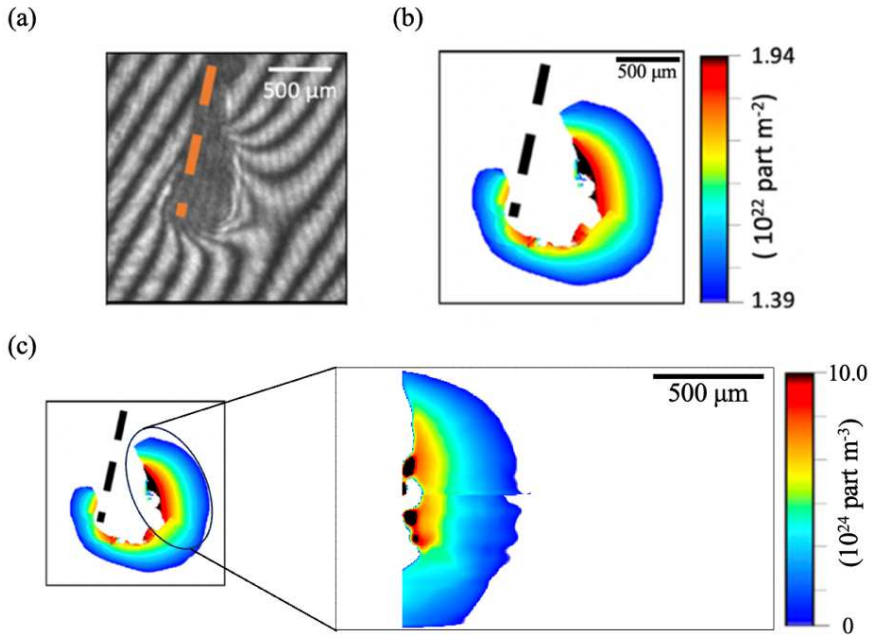

Figure 31. Expansion of the plasma captured with the interferometry diagnostic in the configuration where only one target is irradiated by a laser beam. The analysis was made with Neutrino here at t = 1 ns after the beginning of the laser pulse. a) Raw image of the interferogram during the shot as it was captured by the GOI camera. The target is represented by the orange dotted line. b) Map of the corresponding electron surface density obtained from the raw interferogram with Neutrino. Here the target is modeled by the black dotted line. c) Map of the electron volume density obtained from the surface density map via Abel inversion. The section of the surface density map used to integrate the density with Abel inversion is circled in black.

We get the map of the electron volume density (Figure 31c)) by applying an Abel inversion [2] on the electron surface density, on a section where it is possible to establish an axis of symmetry. An Abel inversion is an integral transform consisting in the projection of an axisymetrical function. It permits to reconstruct the volume density distribution by integrating the surface density along a normal axis of cylindrical symmetry [3] to construct the volume expansion of the plasma from the 2D density map.

The plasma generated by the target ionization has an exponential shaped expansion profile in vacuum, that can be modeled by a function $f(x) = e^{-x/L}$, where x is the distance along the axis of propagation, normal to the target surface, and L is the characteristic length of the plasma. We measure the evolution of the electron density profile along the thin black line with Neutrino as shown on Figure 32a) for a copper target ($Z_{copper} = 29$). The electron density map and the profile shown on Figure 33 were measured for a time t = 1 ns after the beginning of the shot. The profile on Figure 32b) does present an exponential decay, here with a characteristic length of L = 1/0.006 = 167 µm. We used copper-made targets in this experiment because copper is an element with a relatively high atomic number and mass compared to other materials that can be used in the laboratory, such as aluminium or plastics. Not only is copper a material which presents multiple ionization states and absorbs a large fraction of the energy deposited by the laser, but its irradiation produces heavier ions, inducing a slower plasma expansion. Consequently, the plasma ablated from a copper target remains denser for a longer time. Moreover, a slower expansion implies also a slower dissipation of the thermal energy, reducing the energy losses.

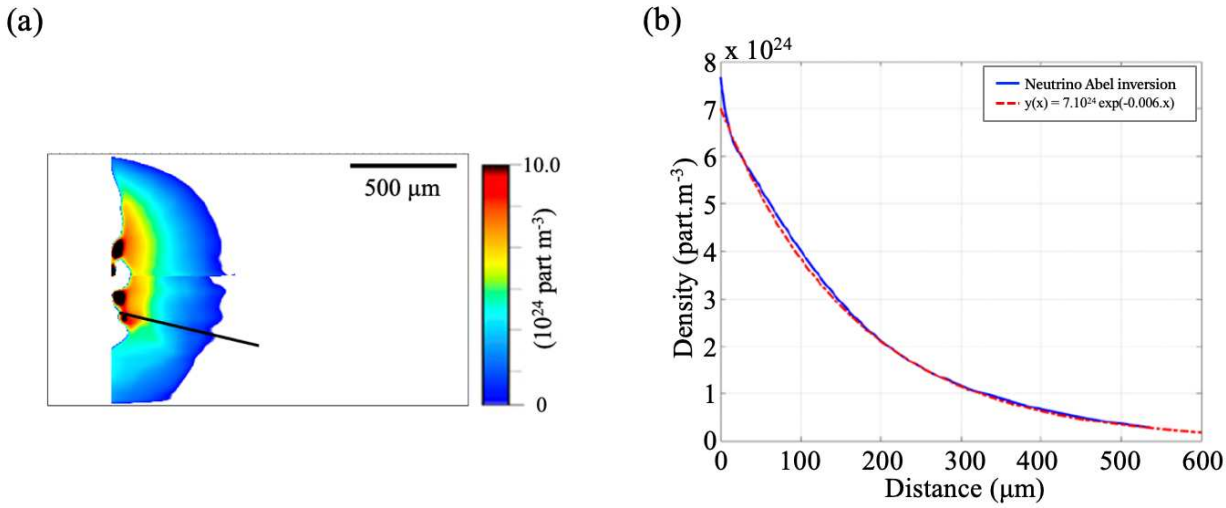

Figure 32. a) Electron volume density map used for the estimation of the exponential decay of the spatial expansion of the plasma. b) Profile of the electron density along the line of measurement following the direction of propagation of the plasma. The experimental curve calculated with the Neutrino analysis (in blue) is fitted with an exponential model (dashed red curve), whose expression is written in the legend.

However, the interferometry diagnostic coupled with the cameras, as well as Neutrino, have resolution limitations. Indeed, it is not possible to measure a density whose order of magnitude is over $n_e = 10^{25}$ part/m^3 with the interferometry diagnostic and consequently with Neutrino. This corresponds to the maximum value above which the laser probe used for the interferometry cannot propagate in the plasma (see the opaque part on the interferogram on Figure 31a)). Consequently, we complete the experimental characterisation of the electron density with simulations, especially in the densest parts close to the target surface.

The numerical results obtained with FLASH give a more complete view of the evolution of the plasma density. Using FLASH, it is possible to reproduce the spatial evolution of the plasma density like we did with the interferometry diagnostic but also temporally. We implement the parameters listed in 4.2.1.2. in the case of a single cooper target configuration. The pseudo-vacuum is still constituted by a low-density hydrogen gas and we conserve the modules of Biermann battery magnetic field, diffusion and conductivity for electrons and ions as previously described.

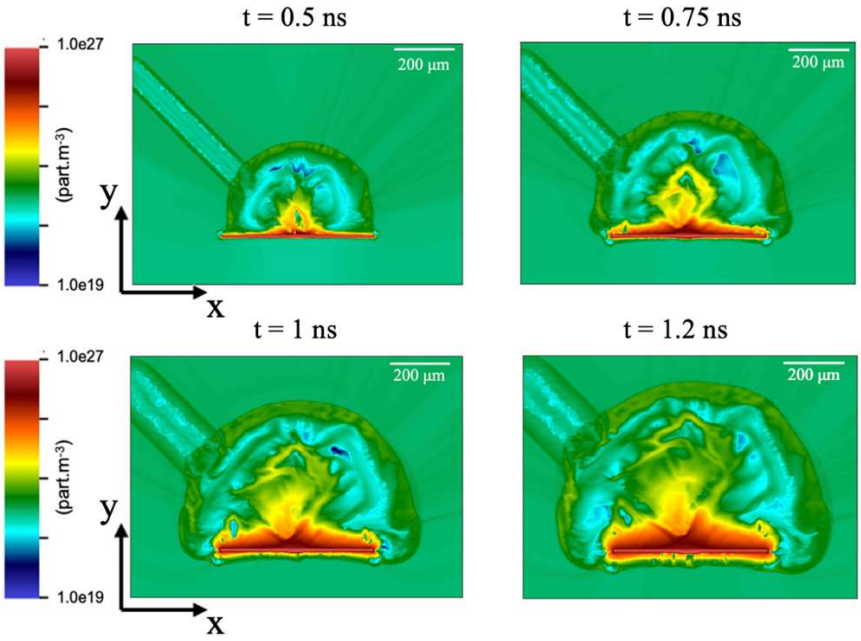

Figure 33. 2D cartesian FLASH simulations modeling the temporal and spatial evolution of the electron density. The simulated copper target is irradiated by a 2 ns long pulse laser (visible on the left side of the simulation domain), with a power of P = 10^{10} W, a wavelength λ = 1 µm, a focal spot with a 25 µm diameter and a 45° incidence angle.

Figure 33 shows the temporal and spatial evolution of the electron density n_e carried by the expanding plasma, similarely to what was observed in the laboratory. To draw a direct comparison between the simulated theoretical plasma expansion and the experimental one, we extract a corresponding lineout over regions where the electron density lies within the measurement range provided by Neutrino (see Figure 34).

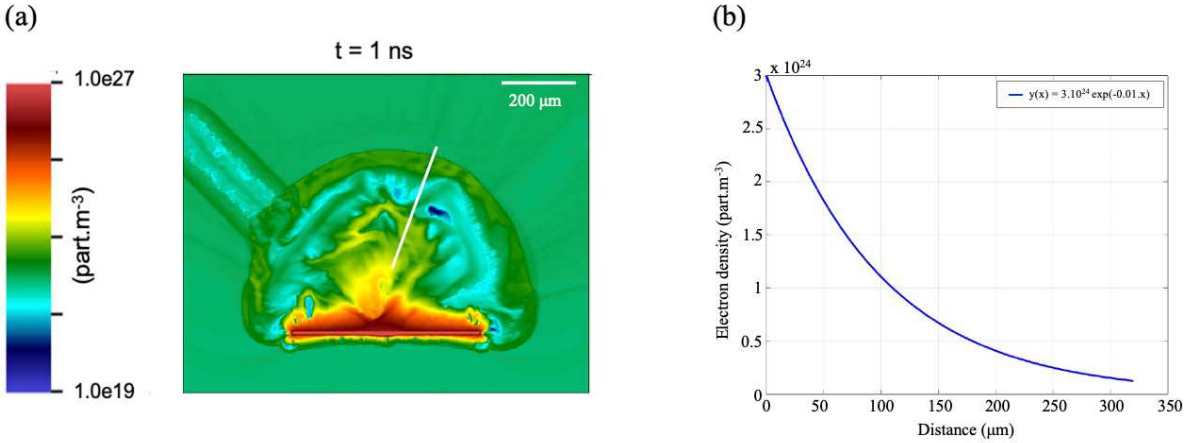

Figure 34. Measurement of the plasma electron density profile on 2D cartesian simulations with FLASH at t = 1 ns. The electron density along the white line drawn on (a) is fitted with the exponential function represented on (b).

The electron density profile shown here is approximated by an exponential function, in order to extract the characteristic length of the expanding plasma. The length obtained with this method is about L = 100 µm. This value falls within the same order of magnitude than the

experimental length obtained with Neutrino but a difference is still noted. Indeed, the plasma modeled with FLASH is more compact and may underline a less extended redistribution of the energy deposited by the laser through the different mechanisms used in the 2D simulations, such the electron heat transport or the radiative effects. Moreover, hydrodynamical simulations performed with codes like FLASH are subject to flux limiters, which can reduce the expansion of the plasma. However, the quantitative similarities still enable us to have a decent comparison for the experimental plasma but also to validate the setup and its results.

5.1.2 Aspect of the magnetic field

We remind that we focused on the interaction of two laser-driven plasmas magnetized via Biermann battery spontaneous magnetic fields. As a consequence, to simulate those self-generated magnetic fields with FLASH 4.7.1., the only module related to the magnetic field generation used was the Biermann battery module. No other magnetic field related numerical packages were used in the simulations as no other external sources of magnetic field were provided during the experiment. Similarely as we did with the density of the expanding plasma, we model the magnetic field carried by the expanding plasma during the laser-target interaction.

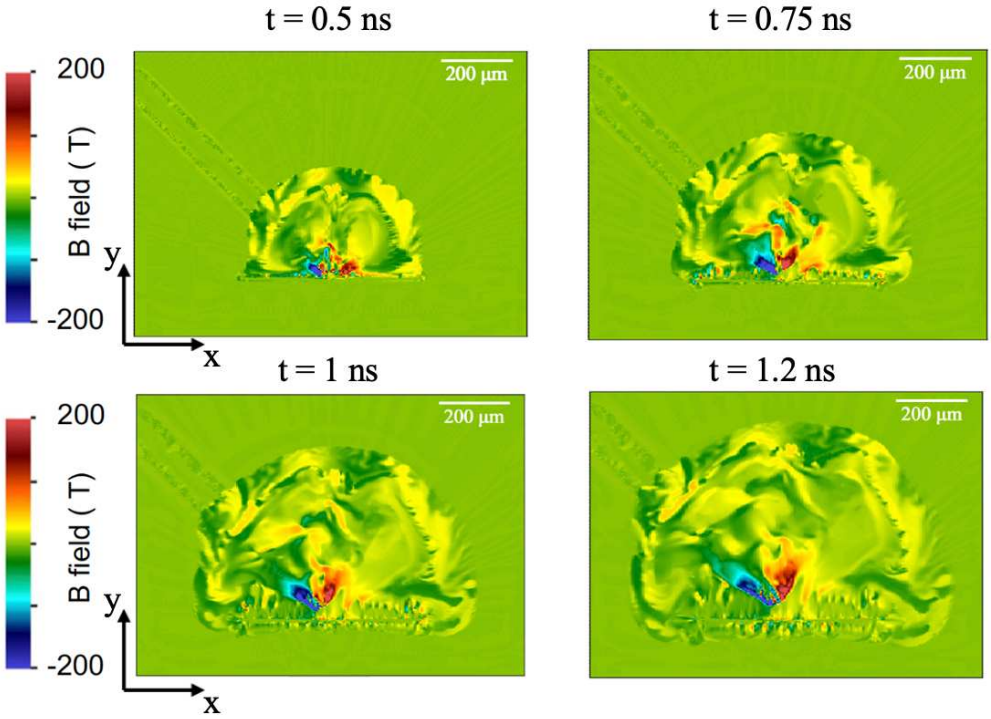

Figure 35. 2D cartesian FLASH simulations of the temporal evolution of the z-component B_z of the magnetic field generated by Biermann battery. The simulated copper target is irradiated by a 2 ns long laser beam (slightly visible on the left side of the simulation domain) with a power of $P = 10^{10}$ W, a wavelength $\lambda = 1$ µm, a focal spot with a 25 µm diameter and a 45° incident angle.

The laser-target interaction generates a toroidal self-generated magnetic field, whose temporal and spatial evolution is represented on Figure 35. The plasma expansion is maintained during the whole duration of the laser pulse, and the magnetic field is advected by the plasma away from the target surface along the normal y-axis. The magnetic field strength on the target surface reaches around $B_z \sim 200$ T in the region around the laser focal spot in the energy deposition zone. Even if the version FLASH4.7.1. used for the simulations in this manuscript does not include the Nernst effect, which compresses the magnetic field near the target surface, but only the Righi-Leduc effect, the strongest parts of the magnetic field still remain confined near the focal spot area and stay close to the target surface for the entire duration of the laser pulse. The radial plasma expansion velocity is estimated around ~ 500 µm/ns, so 500 km/s with FLASH and the analogous velocity in the experiment measured in the laboratory was around ~ 300 µm/ns. Even if the two velocities measured in the simulations and the experiment are both of the same order of magnitude, a few hundreds of micrometers per nanosecond, a noticeable difference subsists. Similarly to our previous observations on the characteristic plasma length, this difference may reflect the modeling and numerical approximation performed by the different modules involved in the 2D FLASH simulations. Furthermore, the hydrodynamic framework does not resolve kinetic-related mechanisms or collisionless phenomena that contribute to the redistribution of the energy deposited by the laser during the experiment but also to a decelerated plasma expansion. Finally, we remind that we manually rose the initial temperature to prevent from numerical failures (see Chapter 4, section 4.2.1.2.).

As the magnetic field is advected by the plasma, its strength decreases until it drops to values close to $B_z \sim 10$ - 30 T at the edges of the plasma plume, where the plasma density is still sufficiently high to support it. This evolution of the magnetic field is characteristic of the Biermann battery effect. Furthermore, the simulated strength of B_z falls within the expected range for self-generated magnetic fields in laser-driven plasmas with similar parameters [4].

5.1.3 Estimation of the electron temperature

The maximum electron temperature T_e was measured experimentally with the X-rays spectrometer FSSR by estimating the intensity ratios of the spectrally resolved emission lines. The analysis of the FSSR data was made by our collaborator E. Fillipov [5]. For a single target configuration, the plasma was characterized at a distance d = 410 µm from the target surface and integrated over a 250 µm wide region. The plasma is probed in a region located sufficiently far away from the target surface to avoid the region where the temperature gradients in the plasma are the highest due to the non-local thermal equilibrium of the expansion around the interaction zone. Indeed, we showed that the electron density n_e is the highest in this specific zone, which would alter the emission lines captured by the FSSR and consequently prevent the calculation of the temperature T_e. On the contrary, in the region where our measurements were done, the plasma is optically thiner and more stable, while still emitting strong enough lines to still be detected by the spectrometer [6].

The electron temperature measured with the FSSR is $T_e = 200$ eV, with an accuracy of ± 30 eV. Once again, we compare this result with the FLASH simulations for the single target

configuration. Figure 36 shows the temporal and spatial evolution of the electron temperature T_e in the plasma during its expansion.

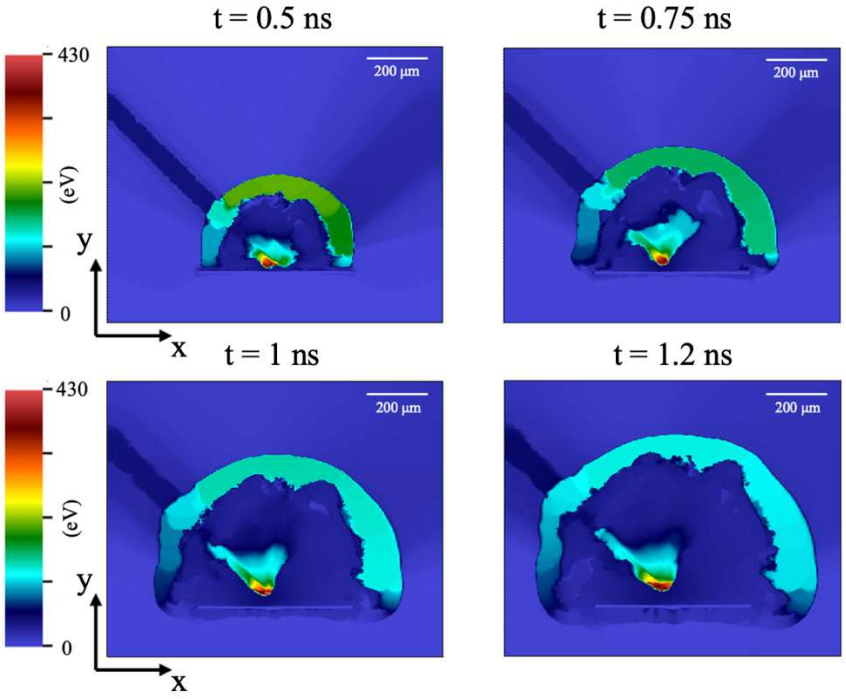

Figure 36. 2D cartesian FLASH simulations of the temporal and spatial evolution of the electron temperature Te in eV. The copper-made target was irradiated with a 2 ns long laser beam (visible on the left side of the simulation domain) with a power of P = 10^{10} W, a wavelength λ = 1 µm, a focal spot with a 25 µm diameter and a 45° incident angle.

FLASH 2D simulations show indeed a notably higher peak of electron temperature in the interaction zone with the laser, reaching around $T_e \sim 430$ eV near the target surface. Besides, this considerably higher temperature remains very localized during the whole duration of the laser pulse, confined in the laser energy deposition area. It is interesting to notice that most of the high electron temperature is carried whether in the laser-target interaction region or in the corona of the plasma plume, reaching in this specific area values around $T_e \sim 150$ - 200 eV. Therefore, the electron temperature as simulated by FLASH falls in the same range than the one measured with the FSSR. Indeed, as the radial expansion of the plasma is around 500 µm/ns, we can estimate that the corona is the area of the plasma probed by the FSSR.

Besides, we observe that the electron temperature in the corona reaches a peak of value at the early stages of the expansion (at around t ~ 500 ps on Figure 36) before decreasing as the expansion continues. FLASH simulations also show a similar evolution for the ion temperature T_i. Indeed, ion temperature T_i reaches its peak early like T_e does before stabilizing at later times (see Figure 37). As we notice, even if they are also heated during the laser-target interaction, ions are considerably heavier than electrons such as, over a similar timescale, they remain initially colder. Moreover, as the deposition of energy in the target is made through the electrons, electrons are heated first and a later thermal equilibrium becomes reachable once electrons transfer a part of this energy to the ions via Coulomb collisions. However, the timescales measured here do not cover this delay.

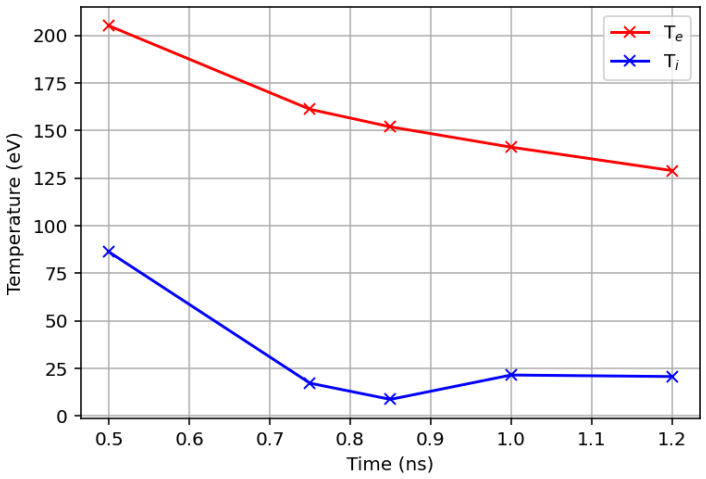

Figure 37. Temporal evolutions of both the average electron temperature T_e and ion temperature T_i measured in the corona of the plasma plume for the single target configuration in 2D cartesian FLASH simulations. Ions stay colder than electrons because more energy and time would be needed to heat the ions at a similar temperature than the electrons.

In this first part, we showed the evolution of the plasma for the single target configuration, using both experimental and FLASH simulations results. In this configuration, the plasma expands unperturbed in the vacuum. This part of the study is important because, on one hand, it will consist in a reference for the two-target configuration and on the other hand, these first results allowed us to validate the experimental setup and the characterization of the plasma created in the laboratory. Now that we proved that the plasmas present the same characteristics in both the experimental and numerical cases, we can rely on our diagnostics and numerical simulations to study the compression process.

5.2 Evidence of saturated compression between magnetized plasmas

In this part, we are going to focus on the formation of the compression sheet between magnetized plasmas in the two targets configuration. The aim is to show how the compression was indeed observed in the laboratory, as well as to detail the dynamics of the compressed plasmas in the case of the interaction of plasmas magnetized via the Biermann battery effect. Also, these experimental results will be compared to two types of simulations: first, with the hydrodynamical code FLASH, to describe the global and macroscopic evolution of the system; and then with the PIC code SMILEI to focus properly on the influence of kinetic effects on this process. Both of these codes were described in Chapter 4, section 4.2. This theoretical work was conducted to support the experimental conclusions about the compression process but also to distinguish the different regimes and inner mechanisms occuring during the compression of two HED laser-driven magnetized plasmas.

5.2.1 Experimental evidence of the compression

In the case of magnetic compression, the two counter-propagating magnetized plasmas collide and a localised compression zone appears quickly after this interaction. For this configuration, we adopted the two-target configuration described in 4.1.2.1, with two identical nanosecond-long laser beams irradiating two identical copper targets with opposite directions of propagation. Indeed, the expected rise of the magnetic field strength between the targets only appears when two magnetized plasmas collide in the zone in between the targets. Experimentally, the compression structure can be visualized with proton radiography.

The targets are irradiated on their opposite surfaces, such as the plasmas carry self-generated Biermann battery magnetic fields who are oriented parallel to each other in the interaction zone in between the targets. For proton radiography, the field advected by the plasma originating from the first target and interacting with the proton beam coming from the TNSA plastic target (irradiated by the 1 ps long beam) is focusing this beam, concentrating the protons in a condensed area. In contrast, for the second target, the magnetic field and the plasma are expanding in the same direction as the one the proton beam is propagating to. Thus, the protons interact with the rear side of the expanding plasma plume, which induces a defocus of the beam and a divergence of the proton trajectories. The disposition of the targets and their ionization by the long-pulse laser beams provide magnetic fields which have opposite directions relatively to the TNSA proton beam and therefore alter the trajectories of the probing proton in opposite ways. In the case of compression between the two expanding plasmas, the resulting proton structure visualized with proton radiography combines the focused protons that are expanded in an arc-shape as well as the defocused protons forming a vertically stretched and disrupted halo (see Figure 38a)). This pattern reflects the propagation of the protons through the compression zone in between the targets. The darker area on the RCF suggest that the compressed magnetic field deflects the protons toward a localized and focused zone.

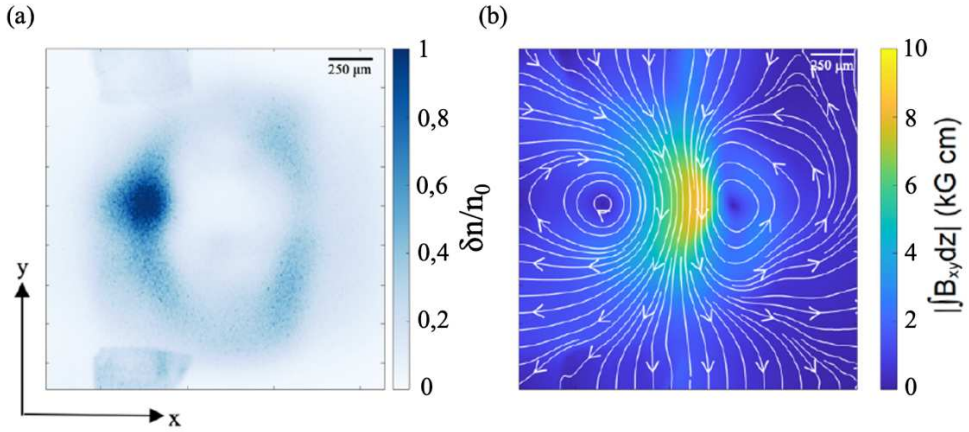

Figure 38. Highlight of the magnetic compression imaged on experimental RCF, analyzed by Conor Fegan [7]. (a) Proton flux measured on RCF at t = 1.25 ns after the beginning of the laser pulse, for the two targets configuration (the two target surfaces are separated by a distance α = 400 µm and the laser focal spots are distant of δ = 500 µm). (b) Corresponding intensity map of the path-integrated magnetic field. The white arrows correspond to the field lines modeling the polarity of the field in the x0y plan, the colorbar represents the intensity of the line-integrated field toward the normal z-axis. The RCF were analysed with PROBLEM.

Figure 38 shows the maps of the proton flux and of the path-integrated magnetic field obtained experimentally with proton radiography and RCFs. To extract this information from the raw films in the RCF stack, we used PROBLEM (PROton imaged B-field non-linear Extraction Module) [8], a Matlab code developed by the team of Archie Bott at the University of Oxford. The first step is to develop a routine to convert a scan of the raw RCF into a dose map (in Gy) and to apply a gaussian blur on the zone of proton energy deposition on the RCF. This blur permits to extract an average background from the scan of the analysed RCF which corresponds to the shape of the unperturbated proton beam, in the absence of any magnetic structure [9]. This reference background is then substracted from the initial RCF to only keep the relevant information about the protons deflected by magnetic compression. This new version of the RCF is the entry file for PROBLEM.

Then, the method first consists in using the parameters of the experiment, in particular the energy range of the RCF and the distance between the RCF stack and the proton source, to determine the proton trajectories. A high-pass filter is also applied to remove the long wavelength variations in the proton flux, as they are not associated with the expected magnetic deflections. The second step is to reconstruct the magnetic field in the probed zone through an inversion algorithm which is running iteratively until convergence. This allows to extract a map of the deflected proton distributions, which is inversely related to the proton flux estimated previously. The regions with a low proton flux on the film are represented by an expanded mesh, while regions with a high proton flux are more focused. In this work, we processed 10^6 iterations to guarantee a correct convergence toward a stable solution. Otherwise, an insufficient convergence leads to distortions in the reconstructed field topology, by overlooking locally the magnetic field strength and consequently affecting the accuracy of the results.

Finally, the reconstructed perpendicular path-integrated magnetic field is obtained from the reconstructed deflection potential [10]. This is shown on Figure 39b), where a clear rise of the strength of the magnetic field along the z-axis is observed in between the interacting fields. This local amplification of the magnetic field strength is due to the compression process. We note that, in the region of the enhanced strength of the magnetic field, the field lines represented by the white arrows are indeed aligned parallel between each other and their density is specifically higher, which implies a convergence of the magnetic flux in this zone.

With this disposition, similarly to the single target configuration, each plasma carries a toroidal magnetic field self-generated via Biermann battery, whose amplitudes range from $B_z \sim 10$ T to $B_z \sim 200$ T locally. As the two targets configuration was chosen especially to trigger magnetic compression, we consequently observe a density peak on the interferometry diagnostic corresponding to the local accumulation of magnetic flux, resulting in the increase of the magnetic field amplitude B_z. The area presenting this density peak is following a 45° angle in between the targets, due to the initial incidence angle the nanosecond-long laser beams hit the targets with.

This has been observed experimentally and theoretically (see Figure 39). In the laboratory, a strong localized electron density n_e is observed on the interferograms obtained with the Mach-Zehnder inteferometer. The plasma confined in the compression zone has a density higher than the maximal capacities of the experimental devices and Neutrino, so the plasma appears opaque in this zone. Consequently, FLASH simulations are used to reproduce and detail the variations of the density of the compressed plasma. This accumulation and stagnation of the plasma in the compression sheet remains for the entirety of the compression process and this structure is characteristic of the compression mechanism.

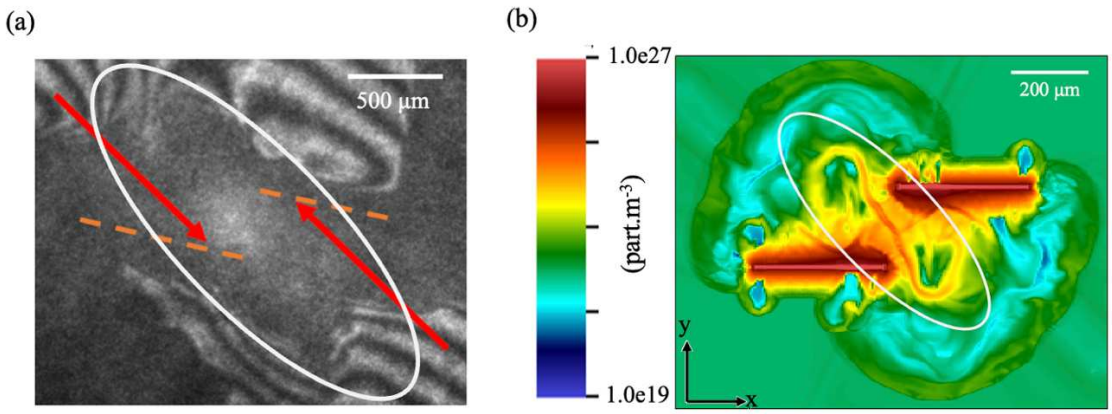

Figure 39. Structure of the plasma electron density during the compression process. (a) Experimental interferogram showing magnetic compression occuring in between two targets (schematized by the two orange doted lines) separated by a distance α = 200 µm. The densest parts of the plasma correspond to the dark zones on the interferogram around the targets. The dark area between the targets and close to their surfaces corresponds to the zone where the laser probe cannot propagate anymore due to the strong gradients of electron density. (b) Corresponding FLASH simulation representing the electron density for the same double targets configuration at t = 0.9 ns. The same tilted structure (circled in white) corresponding to the accumulation of plasma in the compression zone is observed for parameters similar to the experiment.

To further investigate experimentally the characteristics of the compression zone, we measure the plasma emissivity in the sheet with the diagnostic of optical pyrometry. As magnetic compression induces a local modification of the magnetic field and therefore of the plasma conditions, it is supposed to produce a characteristic visible emission. Consequently, we can compare the self-emission in the optical visible domain of a freely expanding plasma in the single target configuration and the emissivity of the compressed plasma in the sheet when two magnetized plasmas are generated. As the experimental diagnostic is coupled to a streak camera, the plasma emissivity is time-resolved on a 2 nanosecond-long time window. The emissivity can be defined by [11]:

$$\epsilon \propto n_e^2 E(T_e) , \qquad (5.1)$$

where E is the emission function that depends on the electronic temperature T_e. Previously, we have shown that, for an unperturbed plasma propagating in the vacuum, the FSSR measurements exhibit that, except in the zone of irradiation close to the target surface, the plasma is stable and does not present strong gradients of temperature or density. In parallel, as shown now on Figure 40, in the case where only one target is irradiated by a single laser beam, the emissivity of the plasma remains low during the entire duration of the pulse. This emissivity profile corresponds to the typical expansion of a hot plasma generated by the laser-matter interaction, evolving in the absence of any perturbation such as plasma interaction or magnetic compression.

However, we observe a totaly different emission profile in the presence of two converging plasmas leading to compression. We showed the characteristic increasing electron density n_e in Figure 39 within the compression zone as the plasma is compressed by the accumulation of magnetic flux. As $\epsilon \propto n_e^2$, and since the electron density starts to increase rapidly after the compression begins, the emissision rises considerably as soon as the compression starts (around t ~ 0.4 – 0.5 ns), reaching values around 40 times higher than the single target case in the first peak

of emission. Furthermore, the gradients are strong in the compression sheet at the early stages of the process and the compressed plasma is not stabilized yet, leading to the important succint peak. Later, the emissivity becomes a little bit more stable but remains still enhanced compared to the single target configuration. The peaks are visible for both distances between the targets, with $\alpha = 100$ µm and $\alpha = 200$ µm.

Moreover, these enhanced emissions detected experimentally are also a signature of the particle acceleration implied in the compression sheet. Indeed, the higher emissivity coming from the compression region is not only the result of the increasing electron density but also highlights phases of plasma heating as well as emission resulting from the internal dynamics of the compression sheet.

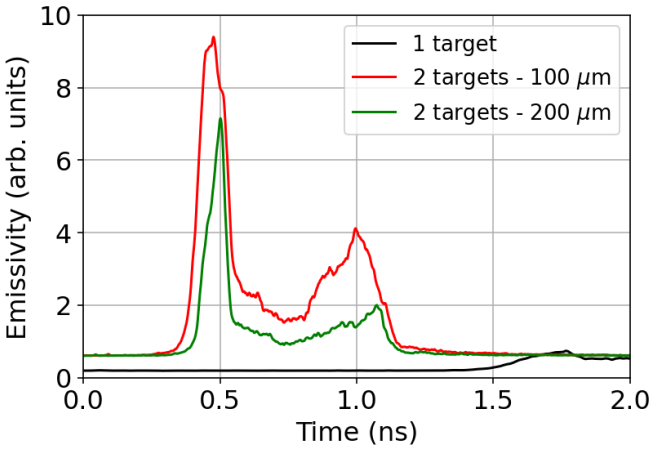

Figure 40. 1D lineouts showing the temporal evolution of optical pyrometry measurements of plasma self-emission, integrated along the compression sheet direction axis, in the two-target configuration (with compression) and in the single target configuration (without compression). The initial time t = 0 ns corresponds to the beginning of the laser pulse and the irradiation of the targets.

The analysis of the experimental data shows that the diagnostics provided complementary results, highlighting the characteristics of magnetic compression between magnetized plasmas. We exhibited the confined density accumulation in the compression sheet as well as the thermal variations of the compressed plasma. By comparing unperturbed expanding plasma and interacting plasmas inducing the compression, we experimentally showed the effects of the mechanism on the plasma evolution and dynamics. Furthermore, these results show that laser-driven magnetized plasmas can trigger magnetic compression similarly to their astrophysical counterparts, even in case of self-magnetization. The following step is now to characterize theoretically the internal dynamics of the compression sheet as well as the variations of the different plasma characteristics.

5.2.2 Hydrodynamical evolution of the compression sheet

5.2.2.1 Establishment of the compression sheet

The compression of magnetic fields in a confined zone of compression alters the characteristics of the plasmas involved. The increasing local density shown in Figure 39 in the zone of compression occurs jointly with a rise of the strength of the magnetic field. These

variations of the different observables were measured both with experimental diagnostics and in simulations recreating the experimental setup as we simulated with FLASH the formation of the compression sheet.

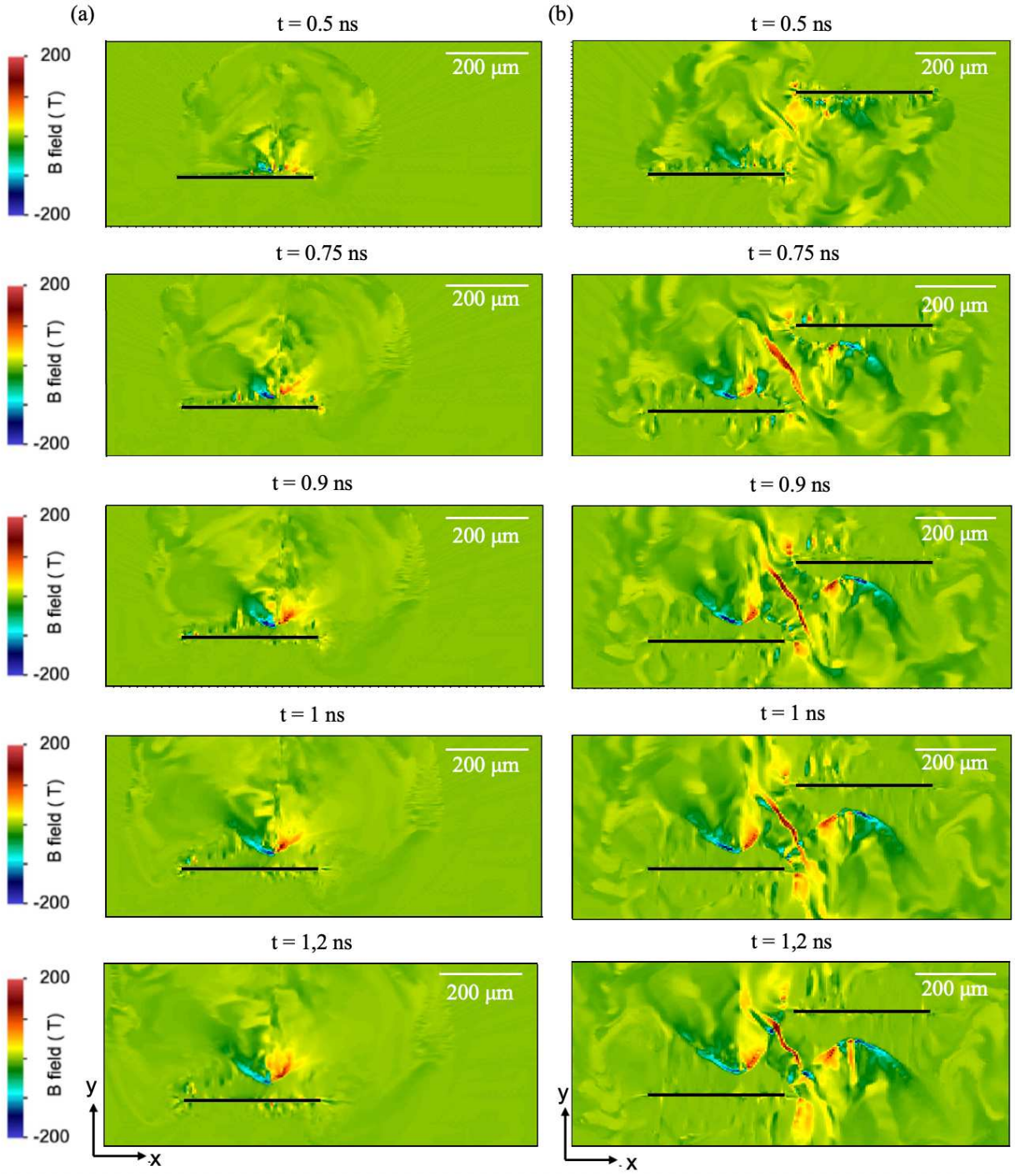

Figure 41. 2D FLASH cartesian simulations of the temporal evolution of the out-of-plane component B_z of the magnetic field. (a) The single target configuration showing the evolution of the magnetic field from the laser ionization of one target. (b) The two target configuration presenting the expansion of the two magnetic fields and the resulting formation of the compression sheet in between the targets. The targets are represented by the black plain lines.

Here, we simulate the case $\alpha = \delta = 200$ µm, where the distances between the two laser focal spots and the target surfaces are the same. This configuration has been tested during the experiment. Figure 41 shows the 2D cartesian FLASH simulation results of the temporal evolution of the out-of-plane component B_z of the toroidal magnetic field. We compare here the two different configurations, with one (Figure 41a)) and with two (Figure 41b)) irradiated targets. The numerical setup and the parameters of the plasmas and the laser beams remain the same in both cases. Figure 41a) shows how a single laser-driven plasma expands unperturbed in a situation where there is no interaction with any other magnetized plasma. The strength of the field is the highest on the surface of the target, with a maximum amplitude around $B_z \sim 180$ T, and decreases with the distance as expected for a Biermann battery generated field. In Figure 41b), the second target is irradiated by an identical laser beam, so two magnetized plasmas are generated. The plasmas collide between the targets, inducing an accumulation of magnetic flux in a contained area. We also notice that the compression sheet is indeed aligned on a 45° tilted axis already observed in the laboratory (see Figure 39).

The strengths of the interacting magnetic fields are low in the edges of the expanding plasmas when they collide (with $B_0 \sim 5$ - 15 T), but the local high magnetic flux implies field accumulation in the zone. This leads to a local and intense increase of the magnetic field strength, reaching around $B_z \sim 200$ T in the compression sheet. Whether it is for the magnetic field strength showed on Figure 41b) or for the electron density on Figure 39b), we do observe the characteristic stagnation of the plasma during the compression process. Figure 42 shows the temporal evolution of the local increase of B_z in the compression sheet for the configuration presented in Figure 41b). The highly compressed magnetic field is contained in a confined sheet, with a full width half maximum (FWHM) around ~ 10 - 15 µm.

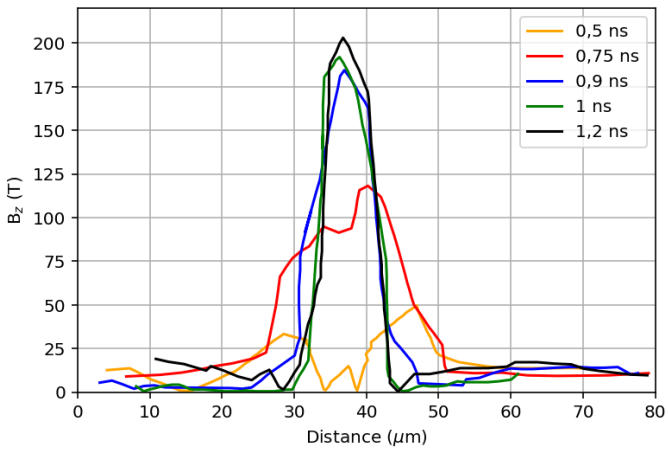

Figure 42. 1D lineouts showing the temporal evolution of the accumulated field in the compression zone in the 2D cartesian FLASH simulations. The 1D lineouts were taken at the center of the compression sheet and perpendicular to it.

This compression zone is clearly delimited and separated from the outer plasma at the edges of the plasma plumes where the advected magnetic field remains almost unperturbed. The compression sheet stays contained during the whole laser pulse, despite the continuous converging flux of plasma flux coming from the target irradiation. We can also notice on Figure 42 that the strength of B_z tends to a maximum limit value. This is consistent with the experimental measurements but it is also revealing of the saturation of the compressed magnetic field amplitude.

Indeed, as shown on Figure 42, the strength of B_z does not increase linearly during the process and, starting from t ~ 0.9 ns, we clearly notice that the growth of B_z slows down until reaching its maximal value. Moreover, we remind that the laser pulse is a 2 nanosecond-long pulse, so the strength of the compressed field saturates even while the irradiation of the targets is still ongoing.

The saturation of the compressed magnetic field amplitude and the increasing density of magnetic flux imply that the electronic density n_e saturates jointly. As the plasma accumulates in the compression sheet, its inner electron density first increases significantly, which makes the zone much denser than the outer parts of the interacting plasmas. Indeed, on Figure 33, the electron density in the expanded plasma close to the edges of the plume is around $n_e \sim 10^{21} - 10^{22}$ part/m^3, while a considerable rise of the electron density until around $n_e \sim 10^{25}$ part/m^3 is showed on Figure 43.

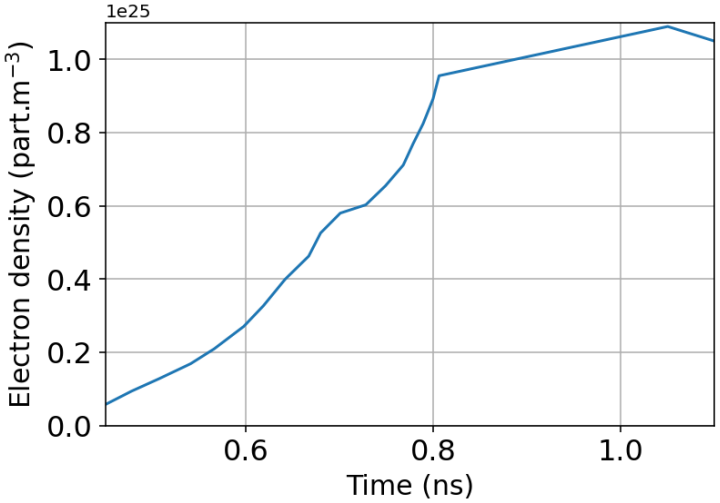

Figure 43. Temporal evolution of the electronic density n_e in the center of the compression zone in the 2D cartesian FLASH simulations.

However, the magnetic field strength increases in the compression zone due to the accumulation of magnetic flux. As the compressed field is confined inside the sheet (see Figure 42), the corresponding magnetic pressure $P_B = B^2/2\mu_0$ grows too in the compression sheet. This increasing magnetic pressure slowly starts to prevent the plasma flow from entering the sheet, which consequently reduces the efficiency of the compression mechanism. Therefore, the plasma and magnetic flux accumulation slows down, and the sheet evolves toward a regulated equilibrium regime between the plasma thermal pressure and the magnetic field pressure, such as $n_e k_B T_e \sim B^2/2\mu_0$ inside the compression sheet.

Furthermore, the amplification of the compressed magnetic field in the compression sheet contributes significantly to reduce the electron Larmor radius $r_{L,e}$ in this zone. We know that $r_{L,e} = \sqrt{2\, m_e k_B T_e} / eB$. The evolution of the electron temperature T_e will be detailled later in this chapter, but for an average temperature T_e = 100 eV and an average compressed magnetic field B_{comp} = 180 T, we have $r_{L,e} \sim 0.2$ µm. From Figure 42, we know that the average width of the compression sheet is ~ 10 – 15 µm. Consequently, the fact that the electron Larmor radius is smaller than the thickness of the compression sheet of two orders of magnitude reflects that the electrons are highly magnetized and confined in the sheet, inducing a density accumulation.

Besides, Figure 42 and Figure 43 show a correlation between the evolutions of the magnetic field strength and the electron density in the compression sheet. Indeed, Figure 44 shows that the electron density n_e in the compression sheet increase rapidly, starting at t ~ 0.4 – 0.5 ns, which corresponds with the formation of the sheet. However, after t ~ 0.8 ns, the density growth slows down and reaches a maximal value, which is similar to the evolution of magnetic field strength. This dynamics of the electron density reveals that the accumulation in the sheet becomes limited by the equilibrium regime of pressure described previously that regulated the saturation aspects of the compression sheet.

5.2.2.2 Global evolution of the saturation

By measuring the strength of the compressed field in the sheet, we compare it to the reference magnetic field B_0 in the plasma surrounding the compression zone and we calculate the compression rate B_z/B_0 to characterize quantitatively the mechanism. Experimental measurements presented in Sladkov *et al* defined the compression rate B_z/B_0 with:

$$\frac{B_z}{B_0} \approx \frac{\int_{in} B\,dz}{\int_{out} B\,dz} \times \frac{\alpha}{h} - \frac{\alpha}{h}, \tag{5.2}$$

where $\int_{in} B\,dz$ and $\int_{out} B\,dz$ are respectively the integrated magnetic field in the compression zone and at the edges of the expanding plasmas. The compression sheet is confined and contained so it is only formed on a fraction h of the maximum length (here α = 200 µm, see Figure 41b) between the targets. Different values of α have been investigated experimentally and the average compression rates were estimated within B_z/B_0 ~ 7 - 23.

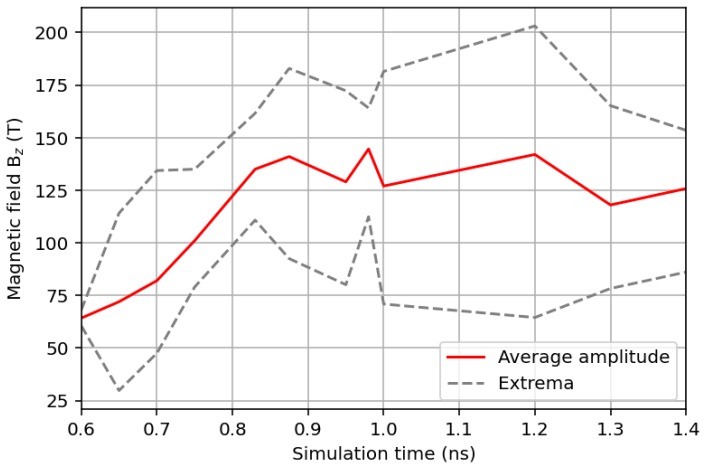

Figure 44. Temporal evolution of the magnetic field B_z in the compression region for α = δ = 200 µm in the 2D cartesian FLASH simulations. As the strength of the magnetic field varies in the sheet, we can estimate an average strength (red plain line) as well as the extrema values (grey dashed lines).

The observed saturation of the compression field in the sheet implies that the compression rate is increasing until a certain maximum limit value, and this is general for every configuration experimentally tested. Figure 45 represents the compression rate in the sheet in the FLASH simulation and illustrates the range of B_z strength measured in the compression sheet and showed

in Figure 44. The average compression rate in FLASH increases and stabilizes at around $B_z/B_0 \sim 16$ - 17. The two dashed lines transcribe the compression rate for the lowest and highest measurements of B_z in the sheet. Indeed, FLASH simulations showed that the compressed magnetic field is not uniform inside the sheet, presenting sections with higher values of B_z usually located in the core of the sheet, and where the compression rate reach $B_z/B_0 \sim 25$. Therefore, the compressed magnetic field strength fluctuates in the compression zone, and the calculation of the average compression rate can overlook the strength of the process. The rate measured in regions of lower values of the compressed magnetic field, like near the edges of the sheet or at early stages of the process, is estimated around $B_z/B_0 \sim 8 – 10$ in the FLASH simulations and around ~ 7 - 8 in both the experiment and the hybrid simulations presented in Sladkov *et al*. Meanwhile, these same hybrid simulations evaluate the global average rate in the sheet at approximately 14.

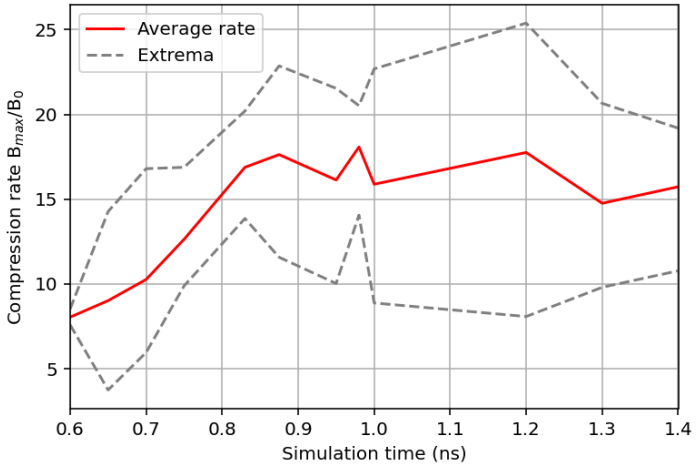

Figure 45. Temporal evolution of the compression rate in the compression region for $\alpha = \delta = 200$ µm in the 2D cartesian FLASH simulations. As the strength of the magnetic field varies in the sheet, the average rate (red plain line) corresponds to the average strength of the field in the zone while the extrema (gray dashed lines) represent the lowest and highest values of B_z.

The compression rate predicted with FLASH reaches a maximal value, meaning that the field amplitude saturates in the compression sheet, as it was observed experimentally. Therefore, B_z/B_0 remains close within the interval 7 – 23 throughout the process. The average and lowest compression rates are slightly above the experimental and hybrid corresponding results, saturating respectively around ~ 16 – 17 and ~ 10, but remain of the same order of magnitude. In addition, this saturation occurs for $t < 2$ ns, while the irradiation of the targets is still ongoing. As a result, the compression sheet reaches a quasi-stationary state even while the plasma inflows are still converging toward the zone. The saturation reflects then the establishment of the hydrodynamic equilibrium we described in 5.2.2.1. within the sheet, where the magnetic flux accumulation is no longer increasing significantly.

The results of the simulations previously described in this section were for the two targets separated by $\alpha = \delta = 200$ µm but the saturation of the compressed magnetic field is a common characteristic, regardless of the choice of α, as shown in Figure 46. The saturation is observed for all values of α however B_z/B_0 does vary with this parameter. For $\alpha = 100$ µm, the targets are too close to each other and the plasmas start to collide before the Biermann battery magnetic fields are fully established. Therefore, the compression process is less effective. For highest values of α, the

plasmas carry weaker magnetic fields B_0 at their edges than those for $\alpha = 200$ µm. In these cases, less magnetic energy is involved in the process. However, for all values of α, the average compression rates all fall within the same interval 4 – 16, which is consistent with the experimental findings.

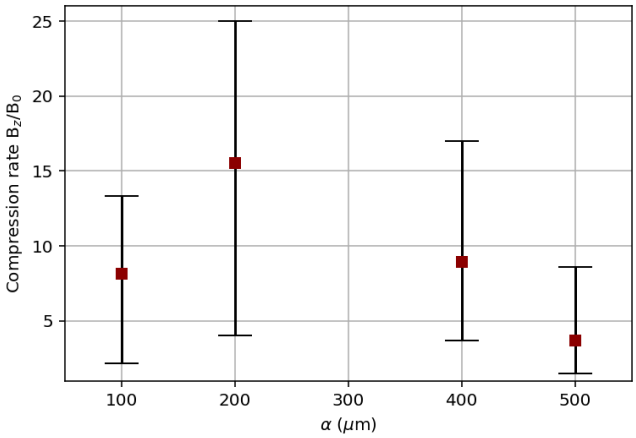

Figure 46. Evolution of the compression rate for different α in 2D cartesian FLASH simulations, α representing the distance between the irradiated target surfaces. The bars correspond to the extrema values of B_z measured in the sheet during the time of the simulation.

We showed in Section 5.2.2.1 that the saturation of the compressed magnetic field and the increasing density of magnetic flux imply that the electron density n_e saturates jointly. However, Figure 48 shows that the electron temperature T_e decreases in the sheet during the process. Indeed, T_e only reaches a peak of high temperature at the beginning of the compression when the plasmas collide, similarly to the emission profiles observed experimentally with optical pyrometry. The electron temperature attains $T_e \sim 750$ eV around 40 ps after the collision. A second lower peak at $T_e \sim 220$ eV around $t \sim 0.5$ ns corresponds to the beginning of the formation of the compression sheet confining the compressed magnetic field (see Figure 43). This profile of temperature is highly similar to the plasma emissivity profile measured experimentally with the optical pyrometry diagnostic (see Figure 40).

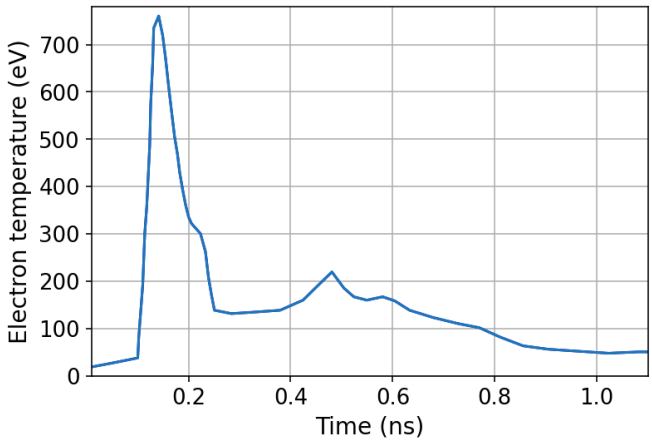

Figure 47. Temporal evolution of the electron temperature measured in the 2D cartesian FLASH simulations in the center of the compression zone for α = 200 µm .

In parallel, we remind that β_{th} is defined by:

$$\beta_{th} = \frac{P_{th}}{P_B}, \tag{5.3}$$

where the β_{th} parameter is the ratio of the thermal and the magnetic pressures. In the converging plasmas simulated with FLASH, $\beta_{th} \sim 50$. β_{th} is significantly higher than the unity, therefore the expanding plasmas are dominated by the thermal pressure P_{th}. The magnetic fields are advected by the plasmas and the magnetic flux increases when the converging flows collide. However, the same calculation of β_{th} with FLASH gives $\beta_{th} \sim 0.15$ inside the compression sheet, where the plasma becomes magnetically dominated by the field. A regime change operates in between the expanding plasmas and the compression zone, where the dynamics is governed by the magnetic pressure P_B that contains the plasma and structures the inner field. We observe here that the compression of the magnetic field on a confined zone, associated with the constant incoming plasma flows accumulating particles in the sheet, induces a significant raise of the magnetic pressure P_B (see Chapter 2, eq. 2.1), dominating henceforth the compressed plasma.

5.2.2.3 Plasma parameters

We showed the difference of regimes between the expanding plasmas and the compression sheet with the radically different values of β_{th} calculated with FLASH in each zone. The plasma dynamics is significantly different whether it is propagating or confined. In order to go further into the characterization of the mechanisms governing the plasma and to underline the specificities of the compression sheet, we determine the dimensionless plasma parameters in each zone of the system.

The plasma parameters (described in Chapter 1, section 1.2.4) allow to evaluate quantitatively the results of the FLASH simulations. Besides, as we place our study in the framework of laboratory astrophysics, we can compare the plasma parameters calculated with the FLASH results with both the experiment and astrophysical events. In our case, we compare our work with the plasma parameters corresponding to magnetic compression between CMEs (see Chapter 2, section 2.1.2.), calculated through satellite measurements [12].

The plasmas expand with a velocity of $v_{plasma} = 500$ km/s according to the FLASH simulation results (the experimental measurement of the plasma velocity is $v_{exp} = 300$ km/s). To establish the plasma parameters, we start by calculating the Alfvén velocity:

$$v_A = \frac{B}{\sqrt{\mu_0 m_i n_i}}, \tag{5.4}$$

where m_i and n_i are respectively the mass and the density of the copper ions. We obtain $v_A = 25$ km/s, so the self-generated Biermann battery fields simulated with FLASH propagate toward each other at a super-Alfvénic velocity. This confirms that, in the expanding plasma, the flow advects the magnetic field, as it implies $v_{plasma} > v_A$. Consequently, in this zone we have $M_A > 1$, where M_A is the Alfvén Mach number. As we have:

$$\beta_{th} = \frac{P_{th}}{P_B} \approx \frac{M_A^2}{M_S^2}, \tag{5.5}$$

where M_S is the Mach number. Then, we can compare these quantities in the expanding plasma and in the compression sheet.

	Expanding plasma	Compression sheet
Mach number (M_S)	1.2	1.13
Alfvén Mach number (M_A)	8.4	0.4
β_{th}	57	0.15

Tableau 3. Comparison of the Mach and Alfvén numbers in the expanding plasma and within the compression sheet in 2D cartesian FLASH simulations.

Although the value of M_S barely fluctuates during the transition from the plasma plume to the compression sheet, we observe a radical regime change for M_A. In the compression sheet, $M_A < 1$, which is typical of a low velocity magnetized plasma. Indeed, if $M_A < 1$, then $v < v_A$ as v_A increases jointly with the magnetic field B and the magnetic pressure P_B. The strong dominating magnetic field slows down the plasma at a sub-alfvénic speed in the compression sheet.

Besides, the calculation of M_S gives $M_S \sim 1.13 – 1.2$ so M_S remains stable even during the regime change. With $M_S \sim 1$, the system is in an early supersonic regime. In the compression sheet, we have then $M_S > M_A$, which implies $v_A > c_S$, where c_S is the sound velocity. We know from eq. 1.26 in Chapter 1 that $c_S \propto \sqrt{T_e}$. We showed on Figure 47 that T_e briefly increases at the time of the collision of the plasmas before decreasing rapidly in the compression sheet during its evolution. Then if the value of T_e drops in the compression zone, so is c_S. Consequently, if M_s remains quite constant in the transition between the expanding plasmas and the confined compression sheet, this reflects a slower velocity v of the plasma in the compression sheet. The plasma entering the sheet is slowed down by the magnetic flux accumulation and the associate magnetic pressure gradient that behaves as an opposing force to the incoming plasma flows. A growing magnetic pressure resulting from the confined amplification of the magnetic field strength contributes to diminish the efficiency of the compression process and to install the stable saturation regime.

These observations validate our model of the dynamics of the plasma but is also coherent with eqs. 1.33 and 1.34 from Chapter 1. Also, calculating the plasma parameters allows to support the MHD approach of the compression sheet. Therefore, we determine the Reynolds numbers as well as the Peclet and Euler numbers.

	Expanding plasma	Compression sheet
Reynolds number (R_e)	37	700
Magnetic Reynolds number (R_{em})	27	40
Peclet number (P_e)	0.11	2
Euler number (Eu)	1.6	1.5

Tableau 4. Comparison of plasma parameters in the MHD framework in the expanding plasma and inside the compression sheet in 2D cartesian FLASH simulations.

The Euler numbers are comparable in both regions, indicating that both the plasma plume and the compression sheet can be correctly described by the Euler equations, within the framework of ideal MHD (see Chapter 1, eqs. 1.5 – 1.7). Moreover, the other dimensionless plasma parameters bring more precisions about the conditions of the magnetic field in the plasma. We notice that the Reynolds number R_e is one order of magnitude higher in the compression sheet than in the expanding plasma. It reflects that the viscosity effects are less significant in the sheet, which favors the increase of the magnetic field strength. In contrast, the magnetic Reynolds number R_{em} fluctuates way less, even if R_{em} is slightly higher in the compression zone, indicating a reduced magnetic diffusion in the sheet. This observation is consistent with the evolution of the Peclet number P_e, which also underlines the regime change. Indeed, $P_e = 2$ within the compression sheet while $P_e < 1$ in the outer regions of the expanding plasmas. This shows a transition from a diffusion-dominated regime to an advection-dominated one in terms of heat transport. As the compression sheet is governed by the stronger compressed magnetic field, the heat transport is highly anisotropic. The compressed field induces the parallel electric field $E_{//}$ mentioned in Chapter 2, which favors a preferential direction for the transport. Consequently, the thermal transport is less efficient across the compressed magnetic field than it is in the expanding plasma, supporting once again the temperature profile calculated with FLASH in the compression zone. Finally, we can compare these parameters with their counterparts in space and in the laboratory.

	CME	Experiment	Simulations
Alfvén velocity (v_A [km/s])	250	50	25
Magnetic field (B [T])	3e-8	450	200
Electron density (n_e [part/cm^3])	2	$1.3.10^{21}$	10^{21}
Mach number (M_S)	1.4	3	1.2
Alfvén Mach number (M_A)	1.6	10	8.4
Characteristic spatial scale (L[cm])	$1.5.10^{12}$	3.10^{-2}	10^{-2}
Reynolds number (R_e)	5.10^5	8.10^2	$6.4.10^2$
Magnetic Reynolds number (R_{em})	10^{17}	63	27
Peclet number (P_e)	10^4	2.3	2
Thermal beta (β_{th})	0.18	0.12	0.14
Euler number (Eu)	1.8	3.7	1.6

Tableau 5. Comparison of selected plasma parameters adapted from Sladkov et al, in the case of magnetic compression for interaction between CMEs (astrophysical reference), for the experimental laser-driven plasmas and for the plasmas simulated with 2D cartesian FLASH simulation.

Table 5 shows the comparison between selected plasma parameters in the three different studied cases: interactions in space between coronal mass ejecta, laser-driven plasmas generated in the laboratory and the associated simulated plasmas in FLASH. The different Euler numbers remain in the same order of magnitude, justifying the descriptions of the plasmas in all situations by the Euler equations as well as the comparison between the experimental and simulated plasmas with their astrophysical counterparts. Moreover, the dimensionless parameters as the Reynolds and Peclet numbers are all larger than the unity (so R_e, R_{em}, $P_e >> 1$), therefore we can justify that the global evolution of the presented systems can be correctly described in the ideal MHD framework. Besides, we can also estimate the electron mean free path $\lambda_{mfp,e}$ in the expanding plasma plumes. Here, we have $\lambda_{mfp,e} \sim 20$ µm, so the condition on the ratio $\lambda_{mfp,e}/L$, where L is the characteristic length, verifies the condition $\lambda_{mfp,e}/L << 1$, highlighting the validity of the ideal MHD model. The mean free path for ions is expected to be even smaller, as plasma produced from copper are dense and present a high collision rate. Finally, we show here that both the numerical and experimental plasmas present the same inner characteristics than their astrophysical counterparts, despite significantly different spatial scales. Consequently, we can affirm that our results are relevant for the study of magnetic compression between space plasmas, and that the comparison of plasma dynamics is accurate. Furthermore, we exhibit strong similitudes between the experimental measurements and the FLASH simulation results. Consequently, we developed a valid experimental setup showing a consistent process, providing good agreements with the simulations.

We knew from previous studies that the magnetic compression process between two magnetic fields oriented parallel to each other in their interaction zone saturates, as it has already been measured in space environments. In this work, we showed experimentally and numerically that the saturation is intrasequential to the compression mechanism. It is directly linked to the dynamics of the compressed magnetic field, whose amplification does not increase linearly with the incoming plasma flows but instead rapidly reaches a maximal saturation value. We also demonstrated that this saturation is resulting from the magnetic pressure accumulation, that tends to oppose the incoming plasma flows. The magnetic field amplification is then limited by its own strength, and the saturation reflects the progressive establishment of a balanced and stable regime within the sheet. Consequently, we can state the saturation is the completion of a self-regulated process. We showed in our work that an increasing strength of the magnetic field and the confined aspect of the compression sheet lead automatically to an increasing magnetic pressure in the compression zone that slows down the compressed plasma and reduces the entering flows. In a few words, the strong magnetic field amplified by the compression process is playing a key role in the reduced efficiency of the process.

The FLASH simulations relying on the MHD framework provide a solid global and macroscopic description of the formation and the evolution of the compression sheet. The hydrodynamic simulations reproduce the main observables and parameters of the experiment and model the general dynamics of the compressed plasma. However, FLASH only provides an approach based on the fluid description of the plasma and does not resolve explicitly any particle-scales effects such as collisionless effects or non-Maxwellian velocity distributions. Consequently, a second complementary study needs to be conducted to address the microscopic effects influencing the compression process.

5.2.3 Study of the internal dynamics of the compression zone

5.2.3.1 Setup of the PIC simulations

To build the SMILEI setup, we use at the plasma parameters obtained with the FLASH simulations, such as the velocity or the strength of B_z at the edges of the compression zone. To match the results presented on Fig. 41b), we set an initial and uniform magnetic field along the z-axis, such as we have $B_0 = 30$ T at t = 0 ps. This value of the initial field corresponds to the field B_0 at the edges of the compression sheet observed in FLASH simulations. The simulations were set in a 180 µm x 90 µm domain, for a 1024 x 512 resolution (8 x 4 patches) and 64 particles per cell. The typical timestep is 0.3 fs and the boundaries conditions were set to "periodic" to maintain the particle flows. The simulations were performed in 2D, cartesian like for FLASH simulations. As units are normalized in SMILEI [13], to make the comparison with the FLASH and experiment results we chose to explicit the results in the SI system of units, by implementing a reference frequency ω_r via the **reference_angular_frequency_SI** variable. For the following SMILEI results, we chose $\omega_r = 1.74.10^{14}$ rad/s.

The initial electron temperature was set at $T_e = 750$ eV and the initial ion temperature at $T_i = T_e/3$. We chose a realistic mass ratio between protons and electrons to have $m_i/m_e = 1836$, and in order to simulate the incoming plasmas, we applied a double gaussian density profile n_{ei} for both electrons and ions. Therefore, we initially have:

$$n_{e,i} = n_0 \left(e^{\frac{(y-\frac{L_y}{6})^2}{2\sigma^2}} + e^{\frac{(y-\frac{5L_y}{6})^2}{2\sigma^2}}\right) \quad (5.6)$$

We remind that L_y is the tranverse dimension of the simulation domain and $\sigma = L_y/3$. $n_0 = 20$ is the initial density in the normalized units of SMILEI and correspond to $n_0 = 10^{19}$ part/m^3. To model the velocity of the particles and to advect these particle flows toward the center of the simulation domain to induce the compression in the middle of the simulation domain, we chose a hyberbolic tangent shaped velocity profile:

$$v_{e,i} = -v_0 \tanh \frac{(y-y_0)}{\frac{L_y}{4}}, \quad (5.7)$$

where the amplitude of the velocity was set to $v_0 = 0.0015c$, so $v_0 = 500$ km/s. A peak of magnetic field amplitude appears in the first few hundreds of femtoseconds. Figure 49 shows the state of the compression at t = 12 ps for the B_z component of the magnetic field, a time when the compression sheet is still in formation and when the compressed magnetic field is still increasing before stabilizing. The 1D profiles taken in the compression sheet along the y-axis (see Figure 48b) and Figure 49 for the temporal evolution of the compressed magnetic field strength) are similar to the ones obtained with FLASH (see Figure 42). We also note that the value of B_0 out of the edges of the contained compression zone remains close to its initial value, around $B_0 \sim 20$ T, once again joining the FLASH results.

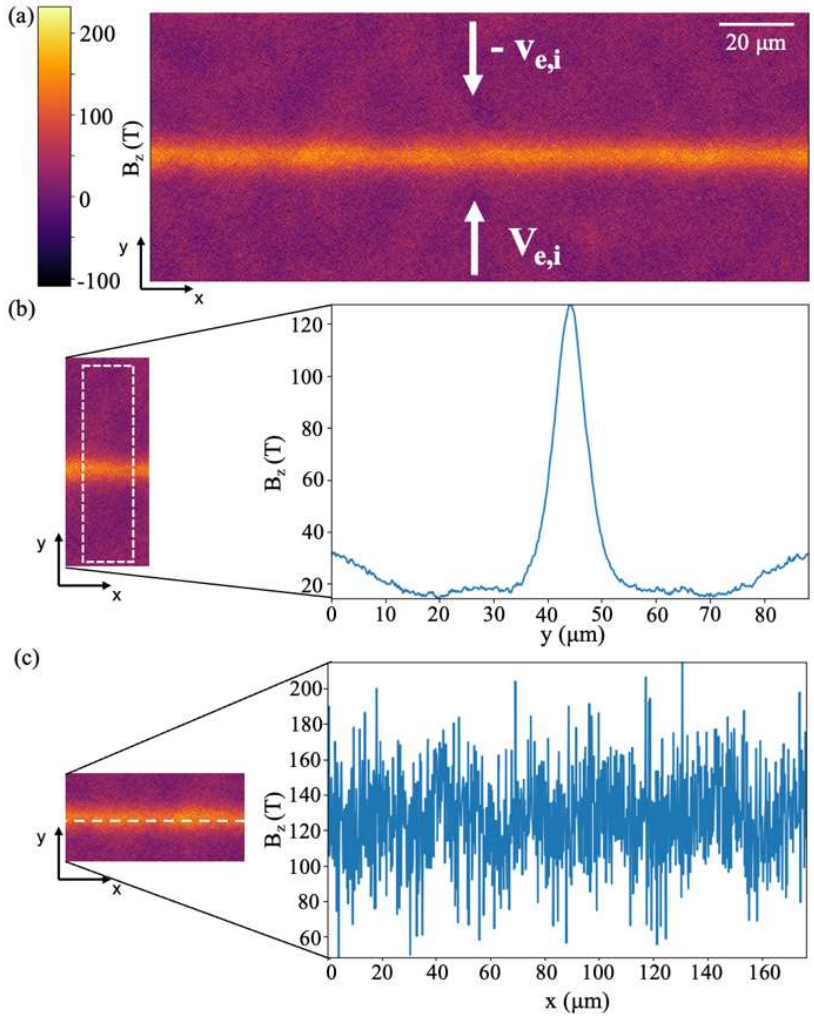

Figure 48. Modeling of the compression sheet at t = 12 ps after the collision between the magnetized plasmas in 2D cartesian SMILEI simulations for B_0 = 30 T and v_0 = 0.0015c. (a) General view of the compression sheet and the strength of B_z. The particle inflows and their velocities are represented by the white arrows. (b) 1D profile along the y-axis of the average accumulated field in the compression zone. The profile showed here corresponds to the white dashed box as the calculation was averaged over the entire x-axis. (c) 1D profile of the fluctuations of B_z in the core of the sheet along the x-axis (white dashed line).

It is also interesting to notice that the 1D profile of B_z along the compression sheet direction axis following the x-axis is very fluctuating (see Figure 48c)), as B_z can vary over a factor 3 for nearby positions for one given time (with B_z ~ 60 - 200 T). Inner variations of B_z were also measured with FLASH but the fluctuations presented on Figure 48c) are more localized and spread over the whole sheet. Indeed, the hydrodynamic description shows a more global repartition of the strength of the compressed field, with the strongest values of B_z being more likely to be measured in the center of the sheet. Yet, with the choice of geometry and boundary conditions in our PIC simulations, we note that these variations of B_z are localized and recurring over the compression sheet.

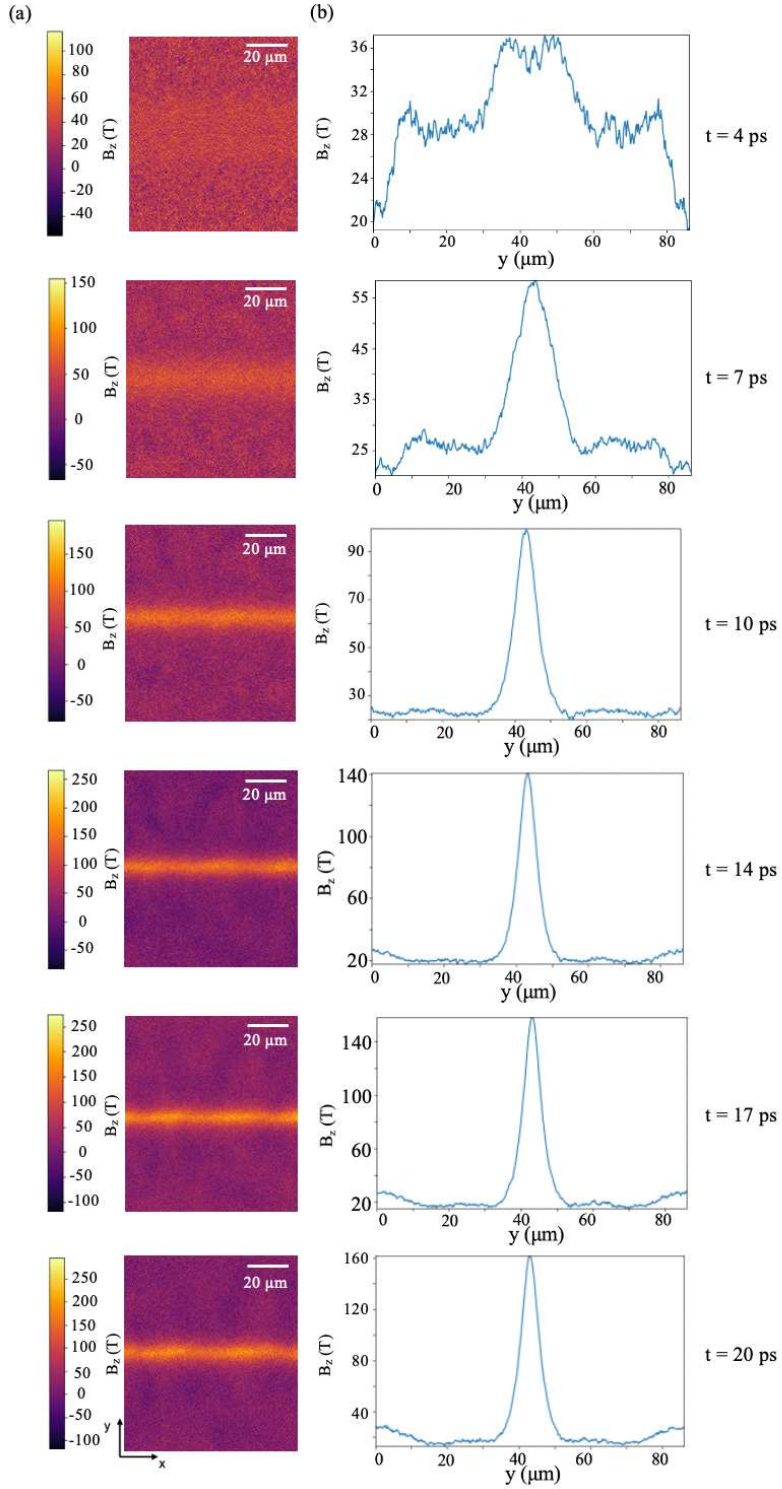

Figure 49. Temporal evolution of the compression process in 2D SMILEI simulations. (a) General view of the formation and the evolution of the compression sheet and its amplitude B_z. At t = 4 ps, the compression sheet is still getting formed and in a transition stage while after t = 7 ps, the compression is established and the dimensions of the sheet stay constant. (b) Profiles of the average accumulated field in the compression zone. The profiles showed here correspond to measurements along the y-axis.

The values of β_{th} calculated in Section 5.2.2.2. exhibit the transition between freely expanding plasmas resulting from the targets irradiation and a highly magnetized confined and compressed plasma in the compression sheet. The important increase of magnetic pressure that we

demonstrated previously is dominant enough to govern the internal plasma dynamics within the compression sheet. We underlined previously that the strong and amplified magnetic field induces the magnetization of electrons, as electrons contained in a high magnetic field have a smaller Larmor radius. The particle transport in the sheet is then strongly influence by the topology of the compressed magnetic field and its interactions with the local electromagnetic forces generated by the motion of these particles. Besides, at spatial scales close to the electron inertial length $d_e = c / \omega_{pe}$, electrons decouple from the ion motion and kinetic effects, such as non-Maxwellian velocity distribution or charged separation induced by the electromagnetic fields, become gradually more important than the global MHD description. The decoupling of electrons from ions induces particle diffusion that alters the magnetic field through the generation of local currents in the sheet and affects directly the structure of the compressed magnetic field. Consequently, the internal dynamics of the compression sheet is dominated by the complementary evolutions of the charged particles and the electromagnetic fields.

5.2.3.2 Highlight of the saturation mechanisms at kinetic scales

In this framework, we also estimate the compression rate in the sheet. As shown in Figure 44 and Figure 45, the calculation of the average compression rate with FLASH underestimates the highest values of B_z. This is similar with SMILEI, as $B_{average} \sim 125$ T in Figure 48b) for $B_{max} > 200$ T on Figure 48c). Consequently, we calculate again both the average compression rate and the corresponding rate for the highest values of B_z measured in the sheet (see Figure 50). We ran several tests with SMILEI changing only the strength of the initial field B_0 to estimate the influence of this parameter on the process. Each time the compression saturates and stabilizes around a similar maximal value. The average rate converges toward around $B_z/B_0 \sim 5$ - 6, while the highest one remains stable around $B_z/B_0 \sim 8$ - 9, which is close to the experimentally measured compression rate in the same conditions ($B_z/B_0 \sim 7$ - 8).

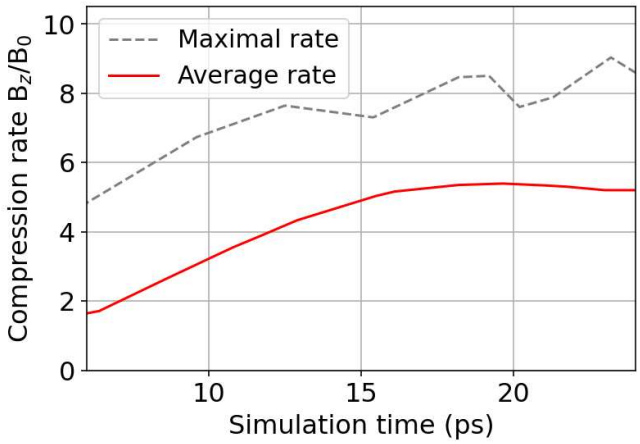

Figure 50. Temporal evolution of the compression rate in the compression region in 2D SMILEI simulation for B_0 = 30 T and v_0 = 0.0015c. As the strength of the magnetic field varies in the sheet, the average compression rate (red plain line) corresponds to the average strength of the field in the zone (presented on Fig. 49b)) while the extrema (grey dashed lines) represent the compression rate for the highest values of B_z measured in the sheet.

The electrons become involved quasi-instantly and, as $\omega_{pe}^{-1} < \omega_{pi}^{-1}$, they react to the plasma interaction in an even shorter time than the ions [14]. In both cases, electron and ion plasma frequencies are shorter than the typical temporal hydrodynamic scales and the duration needed for a hydrodynamic regime to be established. Besides, SMILEI calculates directly the local currents and electromagnetic fields created by the electrons and ions. As a result, the PIC code approach provides the immediate coupling between the magnetic field and the charged particles. Therefore, during the first stages of the process, the compression sheet is entirely shaped by the individual interactions of electrons and ions with the magnetic field.

We can also estimate the evolution of the electron kinetic energy in the sheet, shown on Figure 51. The electron kinetic energy increases with B_z/B_0 and grows until reaching a maximum value, before stabilizing starting from t ~ 15 ps until increasing slowly to E ~ 900 eV around t ~ 40 ps. This time corresponds to the duration over which T_e increases to its maximal value in FLASH (see Figure 47). The B_z component of the compressed magnetic field and the inflow velocity v_{ei}, perpendicular to the direction axis of the sheet, are non-colinear and induce the longitudinal oriented motional electric field $E_{//}$ on both sides of the sheet. These electric fields redirect the incoming flows and once particles enter the compression sheet, they are accelerated along the direction axis of the sheet by these motional electric fields, gaining kinetic energy. Moreover, the field impacts directly the particle proper dynamics by redirecting the initial inflows toward each extremity of the sheet along its direction axis, establishing anisotropic continuous flows. The incoming particles do not remain confined in the compression zone, but they are transported along it by the plasma flow.

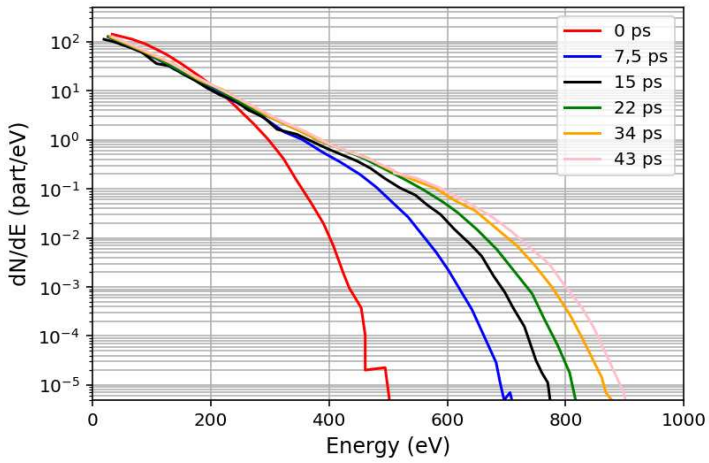

Figure 51. Temporal evolution of the energy spectrum of electrons in 2D cartesian SMILEI simulation. The energy cutoffs tend to a stable value (around E = 900 eV), sign of an equilibrium within the sheet.

The dynamics of the compression zone is dominated by the high strength of the compressed magnetic field which confined the incoming particles within the sheet. However, they are also subject to the motional electric fields $E_{//}$, parallel to the direction axis of the sheet and which establish strong anisotropic flows of particles along this axis. Figure 51 shows how the incoming electrons are gaining kinetic energy by being accelerated along the sheet. But we demonstrated previously that the electron Larmor radius $r_{L,e}$ was smaller by two orders of magnitude than the width of the sheet. This difference of scales explains the density accumulation in the sheet, observed in the experiment and confirmed by the FLASH simulations. Still, we also highlighted

the saturation aspect of the compression caused by the magnetic pressure accumulation in the sheet and leading to a similar saturation of the density in the sheet (see Figure 43). As the density in the compression sheet reaches a saturation value while incoming plasma flows are still converging toward the zone, the deviation of particles induced by $E_{//}$ and their acceleration constitutes an inner mechanism of balance.

This results into outflows expelling particles and preventing the plasma from accumulating in the sheet, which induces that the density value tends to saturate during the process akin to the magnetic field strength. As the ejected particles exit the sheet carrying their own kinetic energy, the sheet enters a stable regime where the energy supplied by the particle inflows is balanced by the energy carried away from the sheet by outflows. The dynamics of the compression zone is then governed by these internal anisotropic particle flows traversing the zone, guided by the strong electromagnetic field.

Therefore, a part of the incoming energy is converted into particle acceleration rather than contributing directly to the compression process. Consequently, the efficiency of the compression is limited and the converted energy is not involved in plasma heating. These internal redistributions of energy, following the transition between the expanding plasma and the compression sheet, are consistent with both the saturation of the compressed magnetic field amplitude and the overall decrease in electron temperature T_e observed at later timescales in the FLASH simulations. Besides, the compression sheet is approximately ~ 15 μm wide. Its dimensions are comparable to the estimated ion inertial length, which is d_i = 16.7 μm. At this scale, the ion dynamics decouple from the plasma bulk, which emphasizes the predominance of particle-scaled and kinetic effects within the sheet. Moreover, at dimensions such as the width of the compression sheet, similar to the ion inertial length d_i, we are at the spatial limits of the MHD model. In this case, it is not sufficient to describe the system using only the fluid description without addressing the kinetic effects. As a result, it is crucial to also conduct a kinetic analysis using PIC simulations to model the entire evolution of the compression zone and complete the results in the MHD framework obtained with FLASH.

The compression is therefore subject to both kinetic and hydrodynamic regimes. The two models are complementary, describing the dynamics of the sheet at different spatial and temporal scales. This part of the numerical study relying on the PIC approach allowed at first to bring support to the previous conclusions made with FLASH. The 2D SMILEI simulations exhibit both the compression and the rapid saturation of the magnetic field strength. Plus, the dimensions of the sheet in the kinetic framework remain coherent with the global model proposed by FLASH.

Moreover, the PIC study mostly permitted to resolved explicitly the particle dynamics in order to complete the hydrodynamic description. We show here that the motional electric fields, parallel to the sheet and naturally generated by the converging magnetized plasmas, participate in both the confinement of the particles within the sheet and their energization. Anisotropic flows of accelerated particles along the sheet are deviated and redirected outside of the sheet, which constitutes another mechanism regulating the accumulation in the sheet and therefore inducing a saturation. Finally, simulations with both FLASH and SMILEI present compression rates range from a few unities to between twenty and thirty. This is consistent with the current measurements made for space plasma and it reinforces the relevancy of our laboratory approach for the study of interactions between astrophysical plasmas.

5.3 Influence of the inflow velocity on the inner dynamic of the sheet

5.3.1 Establishment of a broken magnetic mirror regime

We showed on Figure 46 that the compression rate remains in the same range for different initial values of B_0 and we came to the same conclusions by running several simulations with SMILEI. The sheet evolves toward a quasi-steady and therefore, we observe a conservation of the magnetic momentum. In this section, we go further than our experimental framework by choosing to modify our initial velocity for the inflow plasma in SMILEI. By rising the velocity, we investigate the topology of the compression sheet in a case where involved plasmas are closer to be in a relativistic regime, as magnetic field compression has already been observed between such plasmas in violent astrophysical events like gamma-ray burst [15]. The aim of this part of the study is to track the topology of the compressed magnetic field in a sheet subject to high velocity inflows and how this excessive amount of kinetic energy is redistributed in the compression zone.

We showed in Chapter 2 Section 2.3 that the compression zone behaves as a magnetic mirror, incorporating the inflow particles to the sheet or deflecting toward the outflow. This mechanism balances the flux of charged particles in the sheet and contributes to its stability. This ideal situation of magnetic mirror guarantees the conservation of the magnetic momentum μ_B (see Chapter 2, eq. 2.3). As the amplitude of the initial incoming magnetic field does not change fundamentally the value of the compression rate, we ran SMILEI simulations using the same setup with $B_0 = 20$ T, in order to stay in the range of field relevant for Biermann battery field. However, this time we varied the inflow velocity. In these cases, where two magnetized plasmas similar as previously collide, a highest inflow velocity v_0 brings consistent modifications of the topology of the sheet. The same simulation parameters were applied as previously (see Section 5.2.3), except that the number of particles per cell was raised to 128 to improve the statistics in the sheet. The following results were obtained with $v_1 = 0.02c$, therefore $v_1 = 6000$ km/s, and $v_2 = 0.05c$, therefore $v_2 = 15000$ km/s, instead of $v_0 = 0.0015c$ as shown previously.

5.3.2 Dynamics of the plasmoids

Increasing the inflow velocity modifies significantly the structure of the compression sheet, the magnetic flux distribution and the global dynamics of the plasma. The field is compressed very rapidly, leading to a rapid and strong rise of the strength of the field in the zone in less than 1 ps. In this case, the magnetic momentum is not conserved in the totality of the sheet like it was previously but only locally, and the reflection of incoming particles is not guaranteed anymore. Indeed, we showed with eq. 2.5 in Chapter 2 that the conservation of the magnetic momentum implies a condition of reflexion on the incident angle θ of the incoming particle as there is a limit angle above which the particle is reflected out of the compression sheet. However, this property relies on the conservation of μ_B. Otherwise, the condition on θ is not efficient anymore.

As a consequence, the sheet is fragmented by broken inner magnetic field lines, isolating plasmoids of high magnetic field strength (where μ_B is still conserved). Between the plasmoids,

the magnetic mirror effect is not efficient anymore and the anisotropy of the sheet is broken. Particles that are still reflected are not directed toward the outflow but instead toward the plasmoids where they are trapped.

This phase, called the broken mirror regime, is established early into the compression process due to the higher incoming particle velocity. Figure 52 shows the temporal evolution of the plasmoids for $v_1 = 0.02c$. Their positions are fixed by the broken mirror configuration, and the compressed magnetic field trapped inside them reaches high values (around $B_{max} \sim 250$ T). However, the phenomenon does not persist over time and the regime remains unstable. The particle kinetic energy evolves with v^2 then consequently, rising the velocity v from $v_0 = 0.0015c$ to $v_1 = 0.02c$ increases significantly the kinetic energy carried by the fast-incoming particles. The compression sheet is fragmented and the high magnetic energy stored in the plasmoids dissipates in a few picoseconds, as the plasmoids are progressively merging. The dissipation of the plasmoids allows to dissipate the excessive kinetic energy brought in by the inflows. A slow homogenization of the field is then observed, as the sheet evolved toward a more stable regime.

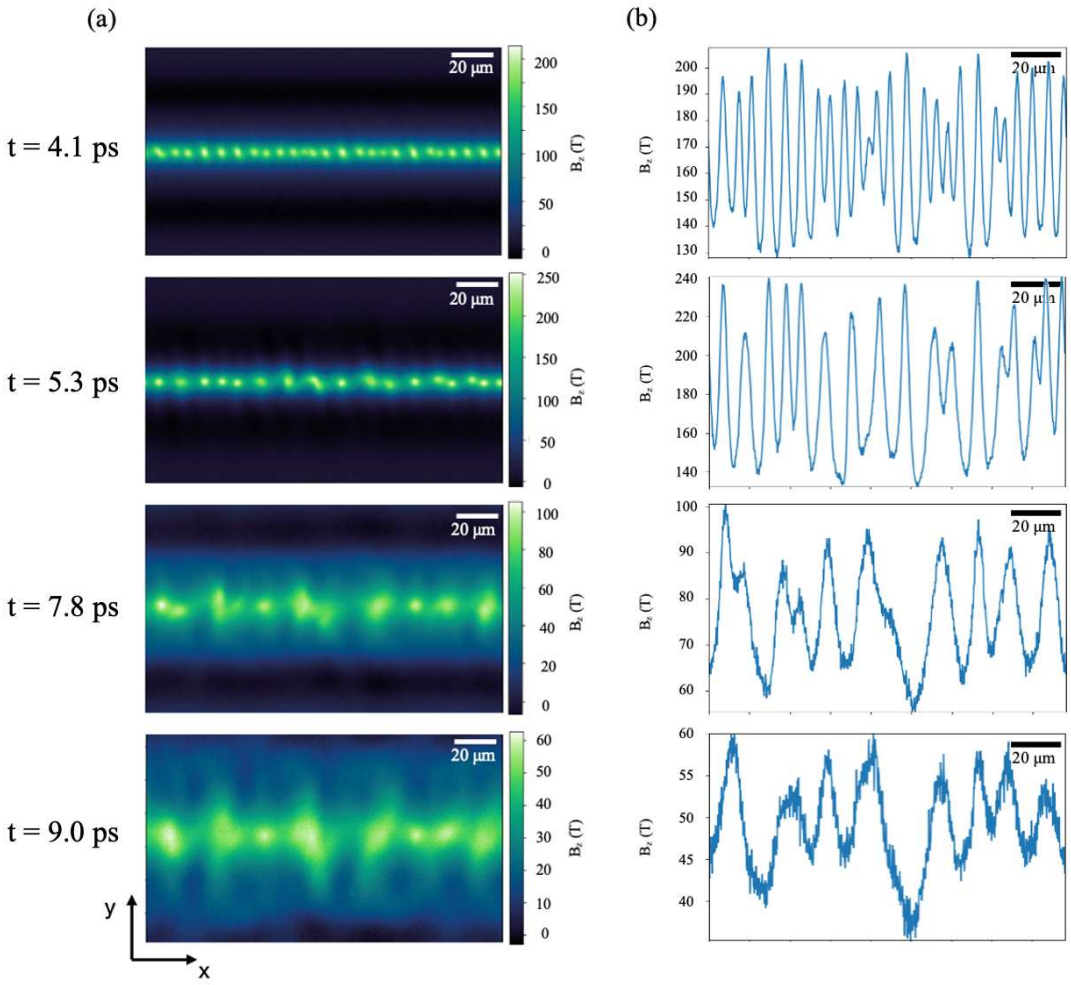

Figure 52. Formation and temporal evolution of the compression sheet in the broken mirror configuration in 2D cartesian SMILEI simulations for $B_0 = 20$ T and $v_1 = 0.02c$. The plasmoids are formed quickly after the beginning of the compression due to the high velocity of the inflows. They first present a regular pattern before being dissipated. (a) 2D map of the magnitude field strength B_z. (b) 1D profiles along the x-axis in the center of the compression sheet showing the evolution of the period of apparition of the plasmoids.

We ran another set of simulations in the same conditions, but this time with $v_2 = 0.05c$. As the new velocity is even higher than the previous one, we expect again a broken magnetic mirror phase during the compression with stronger fluctuations of the magnetic field strength in between the plasmoids.

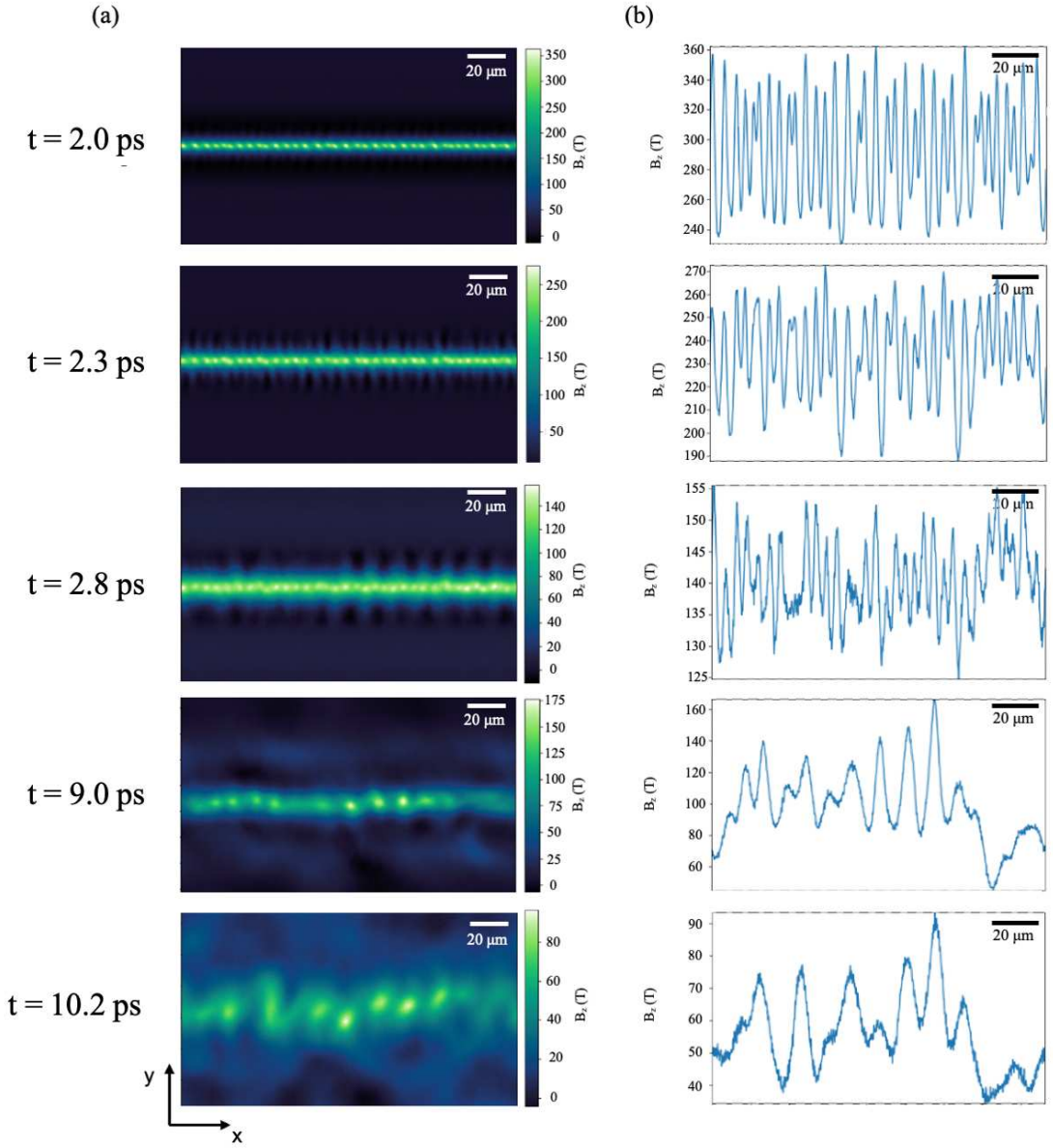

Figure 53. Formation and temporal evolution of the compression sheet in a broken mirror configuration in 2D cartesian SMILEI simulations for $B_0 = 20$ T and $v_2 = 0.05c$. The plasmoids are formed quickly after the beginning of the compression due to the high velocity of the inflows. (a) 2D map of the magnitude field amplitude B_z. (b) 1D profiles along the x-axis of the center of the compression sheet showing the evolution of the period of apparition of the plasmoids.

Plasmoids remain in the compression sheet for only 2 - 6 ps and we will show later in this section that this is independent of the initial magnetic field strength B_0. Indeed, in our study of the case of the broken magnetic mirror, the only varying parameter affecting the non-conservation of the magnetic momentum and implying the formation of plasmoids was the inflow velocity. Figure 53 shows the evolution of the compression for the same initial field $B_0 = 20$ T for the velocity v_2. In both cases, the magnetic field contained in the plasmoids during the phases of broken magnetic

mirror is significantly higher than in the rest of the sheet, leading to a temporary rise of the average compression rate. Once the plasmoids begin to dissipate, the compression sheet returns to a more stable regime, with an average compression rate $B_z/B_0 \sim 2$, which is smaller than the one measured for a compression sheet in a stationary regime. As shown on Figure 53, the compression sheet widens as the plasmoids energy dissipates, reaching a width of approximately 50 µm at the end of the phase, while the sheet was thin and contained at the beginning of the plasmoid formation. As a result, after the broken magnetic mirror phase, the compression process is not as efficient as it is for a smaller inflow velocity.

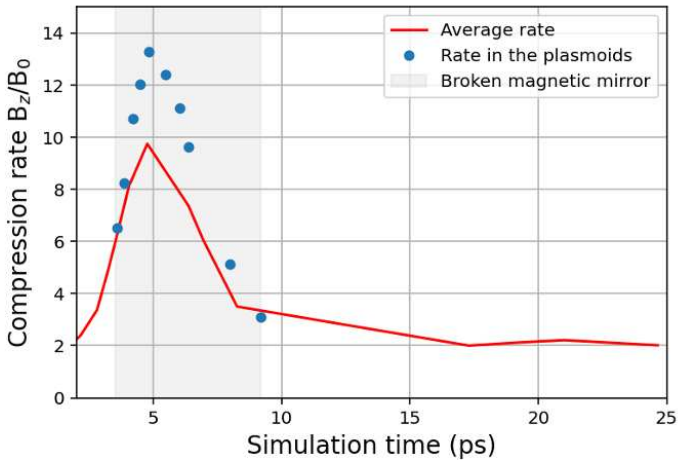

Figure 54. Temporal evolution of B_z/B_0 in the broken magnetic mirror configuration in 2D cartesian SMILEI simulation for B_0 = 20 T and v_0 = 0.02c. The time interval when the enter sheet enters the broken magnetic mirror configuration is highlighted in gray. This period is characterized by a peak of the average compression rage and a strong compressed field contained in the plasmoids.

Indeed, even in the more stable final regime reached after the dissipation of the plasmoids, the sheet still presents turbulent structures, especially around the plasmoid remnants. The establishment of the broken magnetic mirror phase and the formation of plasmoids occur from a rupture of the transport anisotropy inside the sheet, as the particles entering the compression zone are not advected toward the outflows anymore but gather instead into plasmoids. When the plasmoids begin to dissipate, the energy and particle releases are still not anisotropic and propagate longitudinally and transversely, leading to the widening of the sheet. Globally, the electromagnetic field is disorganized by the merging of the plasmoids at the end of the broken magnetic mirror regime. Therefore, the compressed field is not contained in plasmoids anymore but it is also not homogeneous over the totality of the sheet.

Besides, if the incoming flows are too fast and if the resulting particles kinetic energy is too high, we notice several consecutive phases of broken magnetic mirror in the sheet. These phases are separated by relaxation time and are required to achieve a more stable regime. In this case, the successive phases contribute to the progressive dissipation of the energy accumulated in the compression zone and stored in the plasmoids. Figure 55 shows this gradual mechanism in the case where v_2 = 0.05c, for which we observed two concise broken magnetic mirror phases. Both present the same characteristics, except that the peaks of the average compression rate and the amplitude of the magnetic field trapped in the plasmoids slowly decrease toward a different final stable value.

Figure 55 also presents the temporal evolution of the compression rate for two distinct initial values of the magnetic field. These two amplitudes of field were voluntary chosen to not be

too close to each other to highlight that this process of phased compression is established for a certain inflow velocity and, in this case, remains similar regardless the initial value of the magnetic field. We note that the average compression rate varies with the velocity during the phases of broken magnetic mirror but remains quite similar to what we measured for $v_1 = 0.02c$. The value of the initial field B_0 does not impact this specific behavior from the sheet but, for $B_0 = 50$ T, the plasma has a lower β_{th} parameter than in the case where $B_0 = 20$ T, as a higher magnetic pressure is applied on the sheet. The plasma is less compressible and the average compression rate during the phases of broken magnetic mirror is lower than for $B_0 = 20$ T.

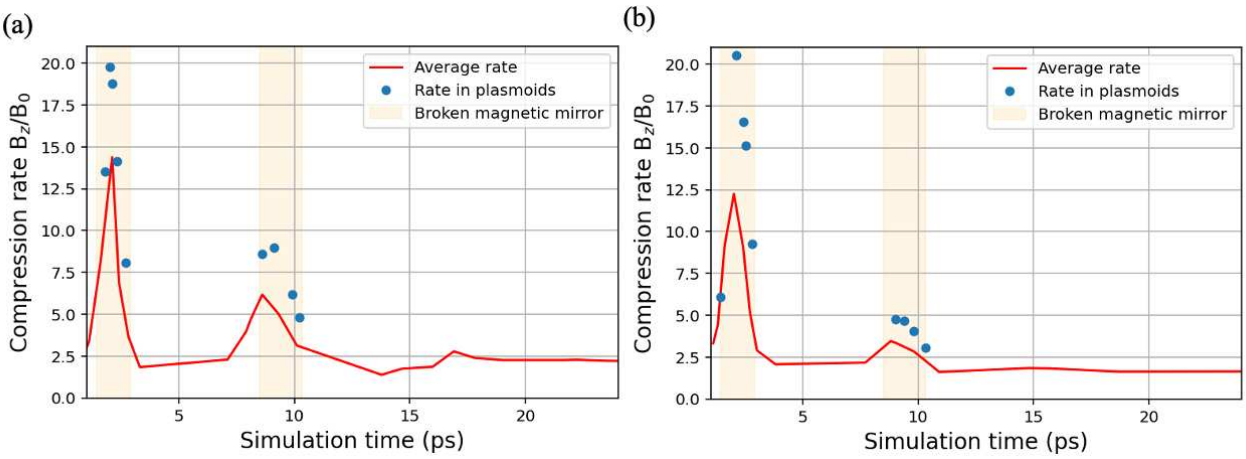

Figure 55. Temporal evolution of B_z in the compression in the broken magnetic mirror configuration in 2D cartesian SMILEI simulations for (a) $B_0 = 20$ T and for (b) $B_0 = 50$ T. In both cases, we have $v_2 = 0.05c$. The time intervals when the sheet enters the broken magnetic mirror configuration are highlighted in beige.

With 1D profiles along the x-axis of the compression sheet in the broken magnetic mirror regime, we measured the amplitude of the magnetic field oscillations of the compressed field within the plasmoids and we determined the frequency of apparition of the plasmoids. We apply 1D spatial Fourier transforms at different times during the broken magnetic mirror phases to extract the dominant k_{max} modes (see Figure 56) during the plasmoid regime. An increasing inflow velocity has a direct impact on k_{max}. Indeed, for $v_1 = 0.02c$, the plasmoids have a quasi-constant space distribution, represented by stable values of k_{max} ($k_{max} \sim 0.03 - 0.05$ on $t \sim 3.5$ - 9 ps). In this case, the broken magnetic mirror may still be unstable but reaches a dominant instability mode leading to more coherent particle dynamics in between the plasmoids. For $v_2 = 0.05c$, k_{max} values are more heterogeneous during the phases of broken magnetic mirror than for $v_1 = 0.02c$. This suggests that an even higher inflow velocity leads to a more turbulent evolution of the compression sheet, even during the broken magnetic mirror phases. Consequently, the sheet is unstable for a longer time and a single broken magnetic mirror phase is not efficient enough to install a stable regime in the sheet.

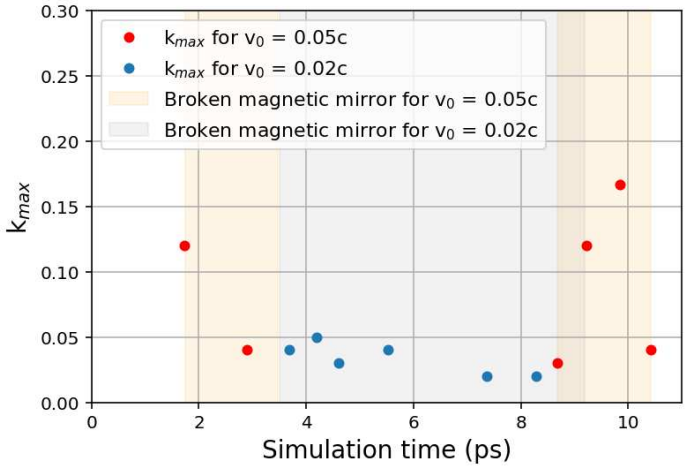

Figure 56. Comparison of the dominant modes of the broken magnetic mirror in 2D cartesian SMILEI simulations for the two different velocities v_1 = 0.02c and v_2 = 0.05c, and for B_0 = 20 T.

Finally, the electron inertial length in the compression sheet is d_e = 0.4 µm while the average distance between plasmoids measured in the sheet is $\lambda_{plasmoid}$ ~ 10 - 25 µm. The characteristic spacing of the plasmoids corresponds to approximately $\lambda_{plasmoid} \sim 25 - 50\ d_e$. Besides, $\lambda_{plasmoid} \sim d_i$. We note that $\lambda_{plasmoid}$ is significantly bigger than d_e but similar to the ion inertial length. Consequently, by falling between these two values, $\lambda_{plasmoid}$ remains close to kinetic scales. Therefore, the plasmoid evolution is still influence by the particle dynamics. Moreover, the fact that $\lambda_{plasmoid}$ corresponds to several electron skin depths close to the ion skin depth is typical of collisionless tearing instabilities implying an unstable regime [16].

5.3.3 Influence of the velocity on the global evolution of the compression sheet

Due to the establishment of a broken magnetic mirror regime during the compression, we observe instabilities growing within the sheet that do not appear in the case of a compression sheet in a stable and stationnary regime as presented in Section 5.2. Among these instabilites, are the tearing effects directly responsible for the fragmentation of the sheet. As mentioned before, the relaxation phase following the broken magnetic mirror phase is more stable than the plasmoid regime but not similar to the stationnary regime. We observe the subsistence of remnants of the plasmoids regime. The compressed field is not contained in plasmoids anymore but still not homogeneous and regions of higher compressed fields can remain. As shown in Figure 52a) and in Figure 53a), the redistribution of energy post-unstable regime widens the compression zone, which becomes less efficient.

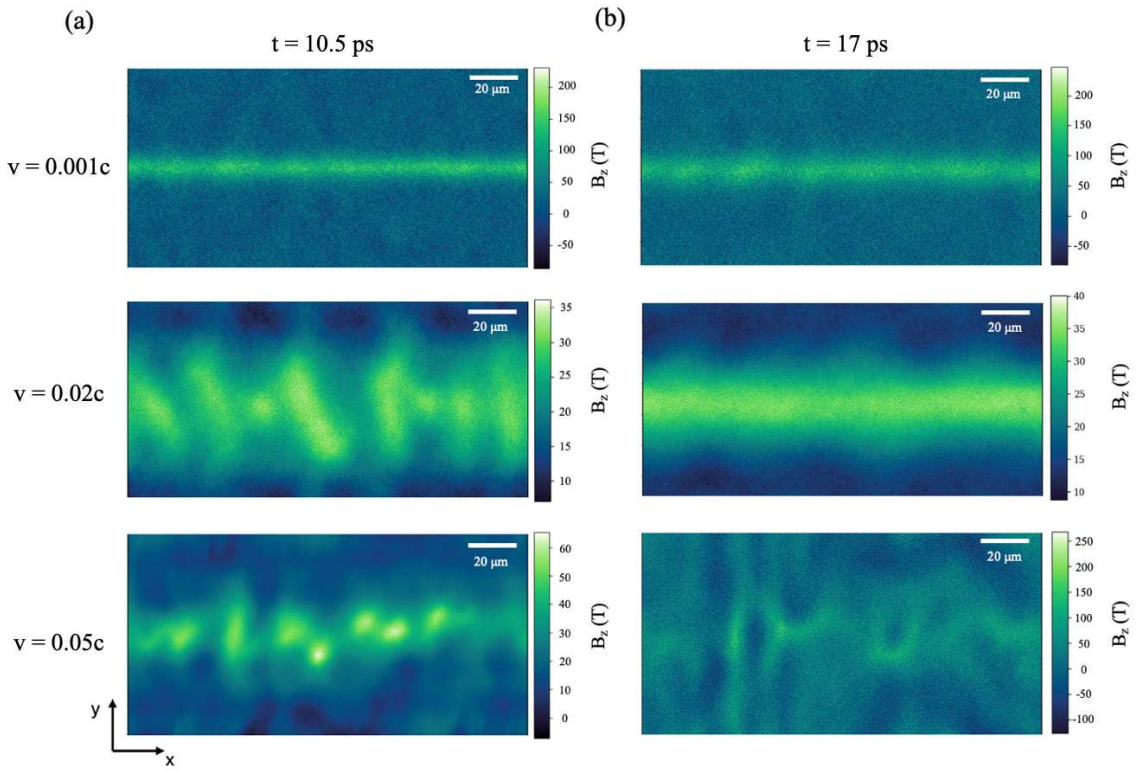

Figure 57. Comparison of the temporal evolution of the compression sheet for the three different velocities in 2D cartesian SMILEI simulations, for B_0 = 20 T at (a) t = 10.5 ps and (b) t = 17 ps, showing the temporal evolution of the topology of the sheet whether it went through one or several broken magnetic mirror phase or not.

Figure 58 presents the same case of magnetic compression for an initial field B_0 = 20 T, for the three different velocities investigated previously. The time t = 10.5 ps (Figure 57a)) corresponds to the time when the broken magnetic mirror phase ends in the configurations where it occurs, for v_1 = 0.02c and v_2 = 0.05c. The second time (Figure 57b)) represents the behavior of the sheet on longest timescales, when the sheet is supposed to have reached a stable regime in every cases. Indeed, at t = 17 ps, the compression rate is stable in the three configurations.

The case v_0 = 0.001c corresponds to the stable configuration as discussed in Section 5.2. Here, the compression sheet is perfectly stable over time, both in terms of spatial dimensions and of strength of the compressed magnetic field. In this stable regime, the flow of particles is well balanced like we demonstrated and ensures the stationnarity of the regime in the sheet during the time interval in which the charged particles govern the evolution of the compression process. Consequently, the high magnetic field remains confined within a narrow and orderly compression region.

In constrast, we showed that for v_1 = 0.02c, the compression sheet first underwent an unstable phase of broken magnetic mirror during the early times of the process. We observe that, even if the sheet is still very turbulent while exiting the plasmoids regime, it relaxes toward a stable regime similar to the low velocity stationary and stable case. The magnetic energy previously contained in the plasmoids dissipates and is redistributed all along the sheet, and the compressed magnetic field tends to present a rather homogeneous distribution in the sheet. However, we still note noticeable differences compared to the unperturbed case at late stages of the process. At t = 17 ps, the compression zone remains broader than for the stable case, with a width around

35 μm (so approximately twice the width than for $v_0 = 0.001c$). As a consequence, the compression mechanism is less efficient, even if the sheet tends to achieve a stable regime. The widening of the sheet indicates that part of the magnetic energy is redistributed through turbulent motions and slightly contributes to the compression process itself. Indeed, we do observe in this case fluctuations at the edges of the compression sheet at t = 17 ps. They are remains of the previous unstable regime, as the magnetic energy was released in a non anisotropic manner through the sheet when the plasmoids are dissipating. This irregular redistribution of the energy generates turbulent structures along the direction axis of the compression sheet following the x-axis leading to the merging of the structures, but also transversally toward the boundaries of the zone. These patterns perturb the structure of the sheet and also slow down the compression mechanism.

The case where $v_1 = 0.02c$ can be considered as an intermediate model between a fully stable compression sheet and a strongly perturbed sheet whose final regime no longer presents a homogeneous compressed magnetic field. For $v_2 = 0.05c$, although the plasmoids dissipate around t = 10.5 ps as expected at the end of the unstable regime, this time corresponding to the second phase of the broken magnetic mirror (see Figure 55), as in this case, the strong particle inflow required two phases to regulate the energy entering in the compression zone. Consequently, the dissipation of the magnetic and kinetic energies becomes too turbulent to maintain a consistent inflow-outflow balance, which weakens the stability of the structure of the sheet itself. The fluctuations on the edge already observed for $v_1 = 0.02c$ are stronger and distort the sheet. The compression zone is still marked by a low but remaining average compression rate ($B_z/B_0 \sim 2$, see Figure 56), but does not recover a coherent and contained structure after the broken magnetic mirror phase, and the zone stays perturbed by inner turbulent motions.

5.4 Conclusion

Our aims were to observe and define the magnetic field compression, both experimentally and theoretically by relying entirely on self-generated magnetic fields via the Biermann battery effect. We showed that interactions between laser-driven plasmas magnetized via the Biermann battery effect, can trigger the magnetic compression process. The resulting compression sheet is shaped by the collision of plasmas and the continuous flow of particles transiting along it. It is characterized by a local accumulation of the magnetic flux, that is compressed by the converging plasma flows. The magnetic field strenght rises in the compression zone, jointly with the electron density. The balance between inflows, the particle redistribution and the energy in the compression sheet limits the compression process, leading to saturation of the compressed magnetic field. As it is possible to generate Biermann battery fields via the laser-matter interaction, we designed a setup to recreate situations leading to compression as it can be detected in space.

We showed that the compression sheet can be observed in laboratory, and we measured the phenomena through our diagnostics, as the compression structure itself is clearly visible on both RCF and interferograms, and plasma and particle motions were captured by optical pyrometry and spectroscopy. We observed experimentally the saturation of the compressed field in the sheet and supported these results with numerical studies. Previous theoretical studies relied on hybrid

simulations treating ion following the PIC description but considering electrons as a fluid, near a MHD formalism. Here, we conducted two distinct numerical studies, each of them presenting their proper description (either hydrodynamic or kinetic) for both electrons and ions. Our simulations permitted to model both the general evolution of the sheet and its internal dynamic.

The MHD description conducted with FLASH was a helpful means to support our experimental results but also to characterize the compression aspect as well as the saturation of the amplitude of the compressed magnetic field that has already been observed. Our work permitted to exhibit the key role of the increasing magnetic pressure as an inner source of saturation in the sheet. Therefore, we manage to highlight that the saturation aspect is self-regulated process and that an amplification of the magnetic field strength in the compression sheet implies a reduction of the inflow due to the high magnetic pressure.

Complementary to the hydrodynamic description, the PIC simulations with SMILEI allowed to focus on the proper motions of the particles and to underline their dynamics in the compression sheet. We showed that the motional electric fields generated by the interacting magnetized plasmas deflect the inflow particles along the sheet, toward a prefered direction, and install a highly anisotropic continuous particle flow within the sheet. The charged particles are accelerated out of the sheet by their interaction with the local electromagnetic field, which contribute to the establishment of a balanced state, reflected by the saturation of the compressed magnetic field. Furthermore, all parts of our study, experimental or theoretical, conduct the quantitative conclusions about the magnetic field in the compression zone that are relevant for astrophysical references.

Finally, we went further than the framework of the experiment by exhibiting the structure of the compressed field when the compression sheet is subject to a higher particle inflow velocity and enters an unstable regime. In this case, the excessive energy fragments the sheet into plasmoids and is dissipated in the compression zone during unstable phases until a progressive and partial homogenization of the magnetic field and the stabilization of the sheet is achieved. To go further in the study of this type of compression, it would be interesting to deepen the investigations and characterize the turbulent aspect observed in the sheet during the broken magnetic mirror regime and the stabilization aftermath. This part of the work is also a first step toward more detailed studies of compression between relativistic plasmas, that could be supported by laboratory experiments using ultra-intense lasers able to produce relativistic plasma flows.

References

[1] GitHub NeutrinoToolkit/Neutrino. Image analysis for plasma physics. https://github.com/NeutrinoToolkit/Neutrino. Website accessible in 2026.

[2] P. Tomassini and A. Giulietti, "A generalization of Abel inversion to non-axisymmetric density distribution", Optics Communications, Volume 199, Issue 1-4, p.143-148 (November *2001).*
https://doi.org/10.1016/S0030-4018(01)01575-9

[3] J.H. Ha *et al*, "A improved Abel inversion method modified for tangential interferometry in tokamak", Rev. Sci. Instrum. 75, 3408-3410 (October 2004).
https://doi.org/10.1063/1.1788891

[4] A. Marocchino, S. Atzeni and A. Schiavi, « Magnetic field generation and diffusion by a laser-produced blast wave propagating in non-homogeneous plasma », New Journal of Physics, Volume 17 (April 2015).
https://doi.org/10.1088/1367-2630/17/4/043052

[5] E.D. Filippov *et al*, « X-ray self-emission imaging of hydrodynamic laser-induced astrophysical phenomena », Symmetry, Volume 14 (November 2022).
https://doi.org/10.3390/sym14122536

[6] E.D. Filippov *et al*, « Enhanced X-ray emission arising from laser-plasma confinement by a strong transverse magnetic field », Scientific Reports, Volume 11, 8180 (April 2021).
https://doi.org/10.1038/s41598-021-87651-8

[7] A. Sladkov, C. Fegan *et al*, « Saturation of the compression of two interacting magnetic flux tubes evidenced in the laboratory », Nature Comunications (April 2024).
https://doi.org/10.48550/arXiv.2404.12110

[8] A. Bott *et al*, « Proton imaging of stochastic magnetic fields », Journal of Plasma Physics, Volume 83, 6, 905830614 (Decembre 2017).
https://doi.org/10.1017/S0022377817000939

[9] James F. Young, Experimental Methods in the Physical Sciences, Academic Press, 1997.

[10] C.A.J. Palmer *et al*, « Field reconstruction from proton radiography of intense laser driven magnetic reconnection », Phys. Plasmas, Volume 26, 8, 083109 (Août 2019).
https://doi.org/10.1063/1.5092733

[11] D. Mihalas *et al*, « Foundations of Radiation Hydrodynamics », Physics Today, Volume 39, 6 (1986).
https://doi.org/10.1063/1.2815048

[12] C. Scolini *et al*, « CME-CME Interactions as sources of CME geoeffectiveness: the formation of the complex ejecta and intense geomagnetic storm in 2017 early september », The Astrophysical Journal Supplement Series, Volume 241, 1 (February 2020).
https://doi.org/10.3847/1538-4365/ab6216

[13] https://smileipic.github.io/Smilei/Understand/units.html (website still available in April 2026).

[14] F.F. Chen, Introduction to Plasma Physics and controlled fusion, Springer (January 2016). https://doir.org/10.1007/978-3-319-22309-4

[15] A. Pe'er, « Plasmas in Gamma-Ray bursts: Particle acceleration, magnetic fields, radiative processes and environments », Galaxies, Volume 7, 33 (February 2019). https://doi.org/10.3390/galaxies7010033

[16] A. Galeev and L. Zelenyi, « Tearing instability in plasma configurations », Zh. Eksp. Teor. Fiz., Volume 70, p. 2133-2151 (1976).

Chapitre 6

Study of the dynamics of the elongated current sheet in magnetic reconnection between laser-driven magnetized plasmas

As mentioned in Chapter 3, plasmoid-driven magnetic reconnection in an elongated current sheet is the most frequent configuration in astrophysical events and observations but still remains only partially understood. Indeed, even if the existence of plasmoids in a reconnection sheet can be explained, the temporal and spatial evolution of a reconnecting current sheet in which plasmoids get formed is still an open question. Also, the previous experimental studies were mostly relying on short pulse laser. Here, we performed a barely studied before configuration where we trigger magnetic reconnection with long pulse lasers to characterize the evolution of the reconnecting current sheet. Besides, it is crucial to determine which physical mechanisms dominate the current sheet and ultimately how they contribute to its fragmentation into plasmoids. In this chapter, we are going to demonstrate how we did manage to observe and track the evolution of the current sheet, from its formation to the establishment of the plasmoid regime. As only a very few laboratory experiments ever focus on this topic, we will present how our own experimental setup allowed us to monitor the evolution of the elongated current sheet by showing our different experimental data obtained through several diagnostics to exhibit the various properties of the reconnection process. Furthermore, we will complete our experimental observations with SMILEI PIC simulations to support our conclusions.

6.1 Characterisation of the current sheet in the laboratory

6.1.1 Context of the experiment

Magnetic reconnection is expected to occur naturally in astrophysical environments when the necessary conditions are met, and leads to a local and spontaneous rearrangement of the magnetic field topology during transient plasma events. However, magnetic reconnection is less likely to take place in one specific point (modelized by the X-point model described in Chapter 3), but rather develops spatially elongated current sheets, containing multiple reconnection sites between the interacting plasmas.

High power lasers permit to generate in the laboratory magnetized plasmas via the Biermann battery effect, that can be used to reproduce such mechanisms happening in space. However, lately laboratory astrophysics experiments on magnetic reconnection between HED magnetized plasmas mainly focused on the X-point configuration [1]. Even if the punctual configuration is not the most common between space plasmas, these works did show that creating and observing magnetic reconnection in experimental laser-driven plasmas is possible which paved the way for more complex future configurations.

The experiment described in this chapter was conducted to reproduce the elongated current sheet in magnetic reconnection between two magnetized plasmas. This specific magnetic structure was reproduced thanks to the 5 ns high power laser beams, aligned on the targets with lengthened and anisotropic focal spots (600 μm long and 80 μm wide, see Chapter 4). This permitted to generate a current sheet whose dimensions exceeded the different kinetic scales of the plasma, such as the electron and ion inertial lengths and which presented a high aspect ratio A (such as $A >> 1$), where $A = L/\delta$, where L is the length of the sheet and δ its width. In this case, the current sheet becomes unstable and is subject to resistive tearing instabilities that will fragment the sheet and lead to the formation of plasmoids (see Chapter 3).

6.1.2 Experimental highlight of the reconnection

The principal aim of the experiment was to exhibit the formation and the dynamics of the plasmoids in a high aspect ratio sheet. Time-resolved proton radiography was the main diagnostic to image the structure of the reconnection sheet, from its formation to the establishment of the plasmoid regime and the different instabilities occuring in this sequence.

6.1.2.1 Case of coplanar targets

The main configuration used in the experiment described in Chapter 4, section 4.1.3.1. consisted in two coplanar targets, i.e. with an aperture angle $\theta = 180°$. Proton radiography was used to image the temporal evolution of the structure of the reconnection sheet, the same way we used this diagnostic to image the compression zone in the magnetic field compression experiment (see Chapter 5, Figure 38). Here, the deflected protons highlight the topology of the reconnection sheet between the two interacting plasmas, as the magnetic field around the current sheet alters the

trajectories of the probing protons. We performed shots on the same coplanar configuration in order to track the temporal evolution of the current sheet. Indeed, we applied various delays between the irradiation of the copper interaction targets and the TNSA proton beam. Therefore, we were able to image the different stages of the evolution of the process and the regimes the current sheet goes through.

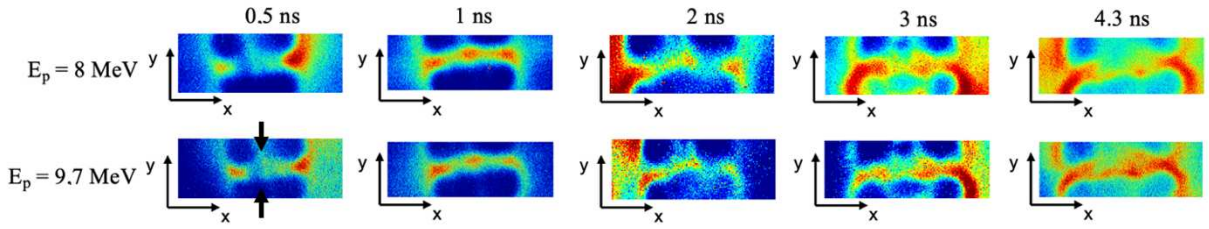

Figure 58. Experimental RCFs representing the time evolution of the magnetic reconnection figure. A voluntary close-up has been made on the films to focus on the current sheet between the plasmas. The times indicated on the upper line correspond to the delay between the start of the ionization of the interacting targets and the TNSA proton beam. Here we do not take into account the proton time-of-flight to reach the different RCFs in the stack as its is negligible (a few picoseconds) compared to the delay between the interaction beams and the proton beam. The energies E_p correspond to the proton energy ranges detected by the RCFs in the stack described in 4.1.3.2.2. (see Figure 28). The black arrows on the bottom left RCF model the propagating plasmas with the reconnection current sheet in between.

As the experimental setup was designed such as the two counter-propagating magnetic fields are aligned in an anti-parallel configuration in their interaction zone, their collision triggers the magnetic reconnection process. Figure 58 shows then the temporal evolution of the resulting reconnection structures (embodied by the central thick sheet between the interacting fields) as captured by proton radiography for different proton energy ranges. At early times, RCFs reveal first a thin and stable current sheet before it starts getting distorted and widens into a thicker sheet around t ~ 2 ns. Around the end of the 5 ns pulse, at t = 4.3 ns, the plasmoids are fully formed.

The formation of plasmoids is a recurring phenomenon in the elongated sheet resulting from the fragmentation of the plasma due to the development of tearing instabilities within the sheet during the process. As a result, the plasmoids were observed multiple times in similar experimental conditions. Figure 59 shows experimental proton radiographies of two different shots performed in the same configuration. Here, the aim was to prove the repeatability of the process. In both cases, reconnection occurs between the plasmas magnetized via the Biermann battery effect and plasmoids get formed at the latest times of the reconnection (around t ~ 4 ns). Consequently, we show here that it is possible to observe the configuration that leads to their formation in the laboratory, in presence of only self-generated magnetic fields.

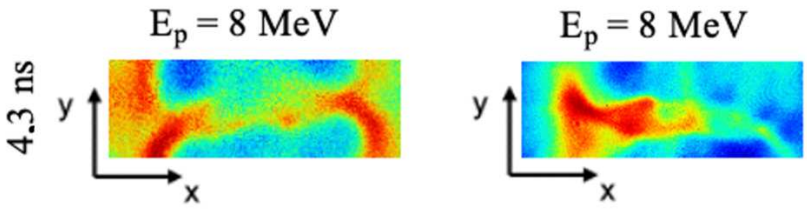

Figure 59. Experimental RCFs of two distinct shots in the same conditions at t = 4.3 ns showing the repeatability of the occurrence of the plasmoids in the elongated sheet configuration. For the shot represented on the right, a voluntary close-up was made during the experiment by putting the RCF stack closer to the interaction targets to increase the magnification on the current sheet.

From the experimental RCFs, we can extract the deposited proton flux as well as the path-integrated magnetic field, to represent the accumulation of protons in the reconnection zone and how they are deflected within the sheet as the process happens. A map of the path-integrated magnetic field also provides the amplitude and the orientation of the magnetic fields carried by the plasma and reconnecting in the sheet (see Figure 60).

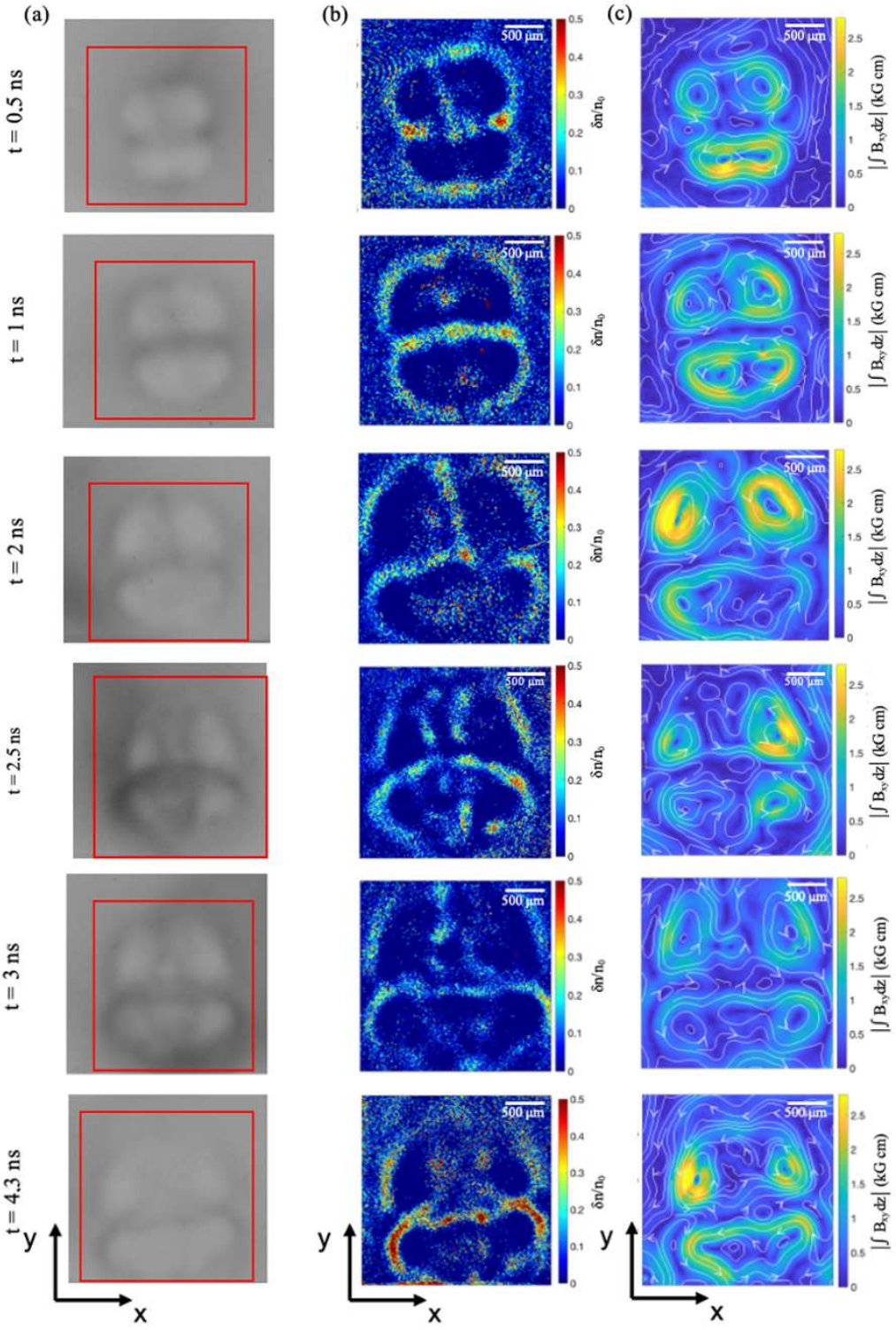

Figure 60. Analyses of the RCFs showed in Figure 59 for E_p = 8 MeV with PROBLEM. Column (a): Scans of the raw experimental RCFs. The red squares correspond to the part of the RCF where a gaussian blur was applied for the analysis. The times on the left correspond to the delay between the start of the target ionization and the TNSA beam pulse. Column (b): Corresponding maps of proton flux representing $\delta n/n_0$, where n_0 is the reference flux. A positive ratio reflects a local increase of the proton flux. Column (c): Corresponding intensity maps of the path-integrated magnetic field. The white arrows correspond to the field lines in the xy-plane, the color bar represents the amplitude of the line-integrated magnetic field along the normal z-axis.

Like in the analysis of the RCFs for the experiment on magnetic compression, we used the code PROBLEM. As mentioned in Chapter 5, the first step was to add a routine to convert the scan of the raw RCF into a dose map (in Gy) and to apply a gaussian blur as reference, which models the shape of the unperturbated proton beam, in the absence of any magnetic structure [3].

PROBLEM provides first the map of the proton flux, which directly represents the proton deflection by the Lorentz force when interacting with the reconnection region. At t = 0.5 ns, the reconnection sheet is getting formed, between the converging plasma flows. This time corresponds to the onset of the magnetic reconnection process, as the converging anti-parallel fields are compressed against each other by the plasma expansions. The current sheet and the reconnection process are fully established around t = 1 ns. At this stage of the process, the current sheet is confined, continuous and stable, as represented by a nearly constant proton flux. Moreover, the sheet is an elongated and narrow structure, and the estimated experimental aspect ratio is approximately A ~ 8. A stable flux suggests that the plasma flows entering the sheet and the outflows are balanced at the beginning of the process and that no magnetic structures such as plasmoids are developed in the sheet.

The regime transition begins and becomes visible as early as t = 2 ns, as the current sheet is broadening. As a consequence, the aspect ratio decreased compared to the initial phase of the reconnection, with A ~ 4 during the transition regime. The proton distribution becomes more diffuse within the sheet, showing emerging structures inside the sheet, as we can notice at t = 2.5 ns. At this stage the current sheet is wider and becomes unstable to tearing instabilities, which induce the fragmentation of the current sheet into multiple localised plasmoids. At later times around t = 4.3 ns, the plasmoid regime is fully established and stabilized. Then, areas of proton accumulation appear at the boundaries of the sheet, which is the sign that the dynamics of the reconnection is altered by the plasmoid formation [4] and that it becomes then a plasmoid-driven process.

From the proton flux, we then get maps of the path-integrated magnetic field (Figure 60c)), showing the field lines and their evolution, respectively along the normal z-axis and in the plane of the reconnection sheet. We notice for the different times on Figure 60c) the tearing between the anti-parallel field lines along the zone of reconnection. The areas where the amplitude of the magnetic field is strong correspond to the field loops confined in the reconnecting plasmas. If these maps show an unperturbated and structured sheet at t = 1 ns with perfectly aligned anti-parallel field lines when the reconnection is stable and confined, they also show the widening of the sheet and the regime change starting from approximately t = 2 ns. The apparition of magnetic islands in the sheet and of internal points of reconnection indicates that the field lines have started to reconnect inside the sheet, leading to multiple reconnection sites and the emergence of plasmoids (see Figure 61).

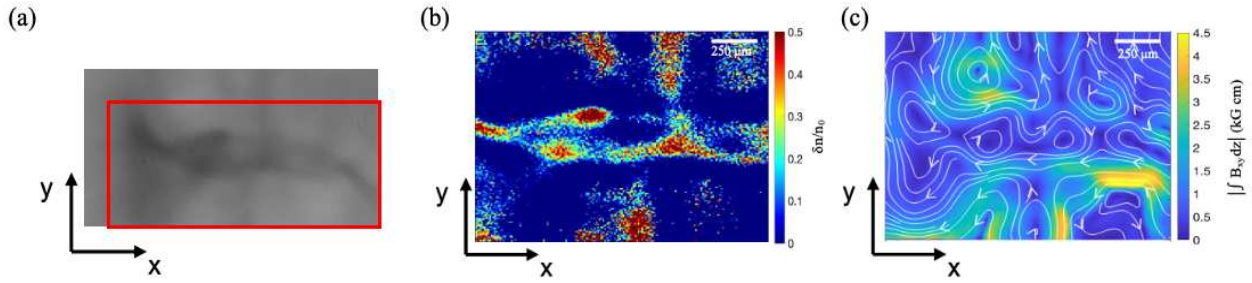

Figure 61. Close-up at t = 4.5 ns of the current sheet in the plasmoid regime showed by (a) the raw RCF, (b) the map of proton flux $\delta n/n_0$ and (c) the map of the path-integrated magnetic field. The film corresponds to an energy range of Ep = 8 MeV.

In the case where the reconnection sheet is stable, before the formation of plasmoids, |B| ~ 0 in the core of the current sheet (see Figure 60c) at t = 1 ns. Indeed, the reconnection process implies the tearing of the oppositely directed magnetic fields in the current sheet, which leads to the diffusion of the magnetic flux in the sheet followed by the reconnection of the field lines. However, at this stage of the reconnection, no field lines have started to reconnect in the zone and the magnetic flux is still being accumulated in the zone. At later times, plasmoid ejections are observed and |B| ≠ 0 near the reconnection sites in the current sheet. These fluctuations of the magnetic fields are visible on Figure 60c), along the field lines reconnecting in the sheet. We also note that a secondary sheet of reconnection is also in formation, orthogonal to the main sheet and within a field loop. This effect can be seen mostly in Figure 60. This specific phenomenom had not been investigated in details, however it would be interesting to do so. Indeed, we observed the formation of this second reconnection sheet repeatedly during the campaign.

In this first part, with the help of proton radiography, we proved that we succeeded in capturing experimentally the time evolution of the topology of the elongated current sheet, showing that it is possible to reproduce this configuration in the laboratory to assimilate typical events happening between space plasmas. We will now focus on a more general setup to reproduce configurations more common in space plasmas, which is the case of reconnection between non-coplanar magnetic fields.

6.1.2.2 Non-coplanar targets: introduction of an out-of-plane guide field

As described in Chapitre 4, our experimental settings presented the possibility to apply an angle φ to tilt the targets toward each other. This mechanism was introduced to generate of an out-of-plane field B_z, normal to the reconnection plane and corresponding to a guide field. In the coplanar configuration presented in the previous section, the counterpropagating magnetic fields remain mostly confined within the reconnection plane and the interaction of the oppositely directed fields leads to |B| ~ 0 T in the core of the current sheet. On the contrary, tilted targets change the geometry of the expanding plasma plumes, such as the magnetic fields they carry become non-coplanar with the reconnection plane. As a result, this induces a component of the magnetic fields, perpendicular to the reconnection plane and which does not get suppressed in the current sheet. Therefore, the field remains during the reconnection and in this case, |B| ≠ 0 T. This out-of-the plane guide field appears then when non-coplanar magnetized plasmas interact, which is the most frequent configuration in space.

Previous studies performed by the group [5] demonstrated that the presence of an out-of-plane field B_z has a direct influence on the reconnection process. As a consequence, the targets have been tilted toward each other during the experiment and the angle φ varied to adjust the strength of this guide field. In total, three configurations have been used during the experiment: coplanar targets (φ = 0°), targets tilted by φ =15° and by φ = 30° each. Besides, we can define the angle θ, which is the aperture angle between the targets, such as θ = 180 – (2φ). With the value of θ, it is possible to estimate the amplitude of the guide field compared to the reconnecting field B_0 such as the z-component of the field is defined by:

$$B_z = B_0 \cos\left(\frac{\theta}{2}\right) \tag{6.1}$$

The presence of a guide field modifies the dynamics of the reconnection as it maintains the magnetization and reduces the diffusion in the sheet. As the evolution of the process is altered by

the guide field, we used proton radiography to visualise experimentally these effects on the reconnection regimes and the plasmoid evolution. The same experimental setup was used for each target configuration, so that a direct comparison of the process can be done.

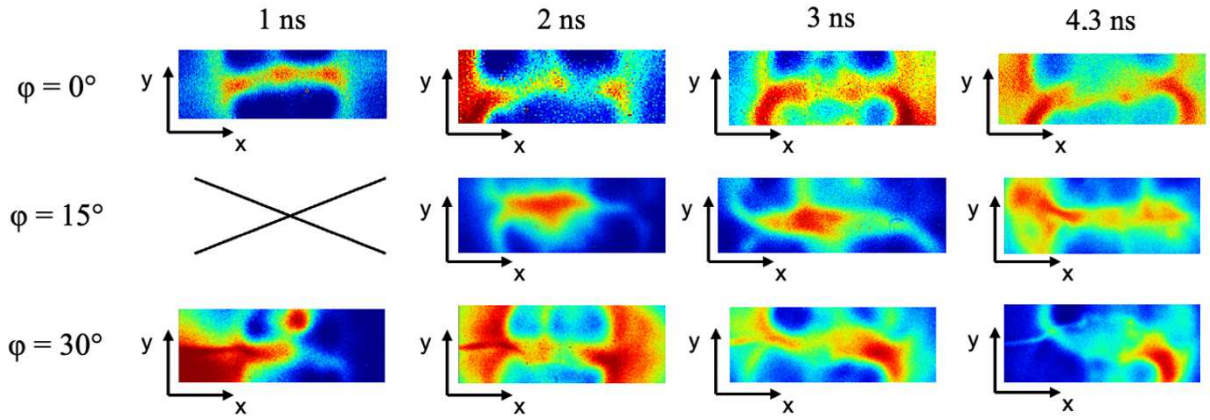

Figure 62. Experimental RCFs for each target configuration. A voluntary close-up has been made on the films to focus on the current sheet between the plasmas. The times indicated on the upper line correspond to the delay between the start of the target ionization and the TNSA proton beam. No measure was performed at t = 1 ns for φ = 15° as the reconnection is slower in this specific case. All the RCFs presented here correspond to a proton energy of E_p = 8 MeV.

On Figure 62, we observe that for coplanar targets (φ = 0°), the reconnection process goes through the phases described previously (first a thin central line indicating a stable current sheet followed by the transition to the plasmoid-dominated regime with the widening of the reconnection sheet and instabilities), with a transition around t ~ 2 ns. However, for φ = 15°, the reconnection sheet starts to broaden and to appear on RCF at t = 3 ns, and is still evolving after t = 4.3 ns. Adding an out-of-plane guide field changes the configuration of the reconnection, bringing the additional component B_z into the process. Indeed, we have $B_z \neq 0$ in the current sheet, even at the beginning of the process. In this case, we have θ = 150°, so from eq. 6.1, we have $B_z/B_0 = 0.26$. As a result, the reconnecting field is not entirely dissipated in the reconnection sheet as it is the case for the coplanar targets. The magnetic flux accumulates in the current sheet (see Figure 63b) at t = 2 ns) and the reconnection is slowed down due to the residual magnetic energy that persists in the sheet [6]. Moreover, the presence of the guide field does not just change the internal geometry of the current sheet, its presence also influences the trajectories of the charged particles. In the coplanar case (B_z = 0 T), the particles are demagnetized as soon as they penetrate the current sheet. On the contrary, if $B_z \neq 0$ T, these particles remain magnetized and are more likely to propagate along the z-axis. However, the amplitude of the guide field remains moderate compared to the reconnecting fields carried by the interaction plasmas. Consequently, the global evolution of the structure of the reconnection sheet is still similar to the one for coplanar targets.

We applied the same methodology to analyze the RCFs for the tilted targets by using the code PROBLEM to track the temporal evolution of the current sheet and the proton deflection in the reconnection structure. In the case where the targets are tilted with an angle φ = 15°, the proton flux maps showed on Figure 63b) reveal indeed that the transition to the plasmoid regime is only getting started at t = 3 ns. Unlike the coplanar configuration, at t = 2 ns the current sheet is still thin and well confined, with a more intense amplitude of the flux inside the sheet. This excessive storage of energy in the sheet also implies a heavy distortion of the magnetic fields carried by the

plasma (Figure 63c)). In this case, the phenomenom of secondary reconnection as mentioned before is less likely to get formed correctly. As the plasmoid regime is finally reached, it is also noticeable that the current sheet does not evolve much spatially in time, keeping a relatively stable aspect ratio A.

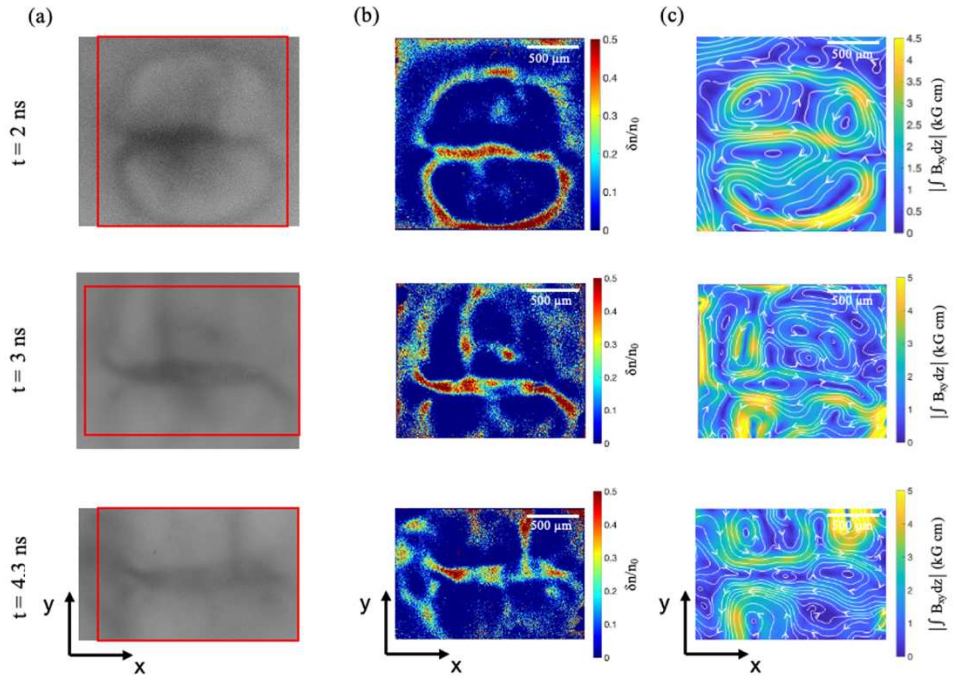

Figure 63. Analyses of the RCFs with PROBLEM in the configuration with φ = 15°. Column (a): Scans of the raw experimental RCFs used to track the temporal evolution of the reconnection. The red squares correspond to the part of the RCFs where the gaussian blur was applied for the analysis. The times on the left correspond to the delay between the start of the target ionisation and the TNSA beam pulse. All the films correspond to an energy range of E_p = 8 MeV. For the shots at t = 3 ns and t = 4.3 ns, a voluntary close-up was made to increase the magnification on the current sheet. Column (b): Corresponding maps of protons flux $\delta n/n_0$. Column (c): Corresponding intensity maps of the path-integrated magnetic field.

However, the reconnection process in the case of a weak out-of plane field is only slowed down compared to the case with coplanar target. Applying a stronger guide field by tilting the targets of φ = 30° changes the process of reconnection itself. On Figure 64, the current sheet is already wider at the beginning of the reconnection at t ~ 2 ns, which is even sooner than for the coplanar targets. Unlike the configuration with φ = 15°, the amplitude of the guide field is higher than previously, with B_z/B_{xy} = 0.5. It induces that more magnetic energy is accumulated in the sheet. This high quantity of stored energy can precipitate the transition toward the plasmoid regime as the current sheet becomes unstable more quickly.

A stronger out-of-plane field restores a fast reconnection, with a wider but more stable current sheet over time, but it is more sensible to tearing instabilities than the regular plasmoid-dominated regime. On Figure 64, at t = 4.3 ns, the current sheet is already distorted and the magnetic energy has already been evacuated from the reconnection region. Also, in this configuration, the secondary reconnection process mentioned before in the coplanar case is established sooner, splitting the magnetic field loops within the plasmas, whose field lines reconnect between one another due to the expansion of the current sheet. Consequently, a quadri-shaped reconnection structure is quickly visible on the RCFs.

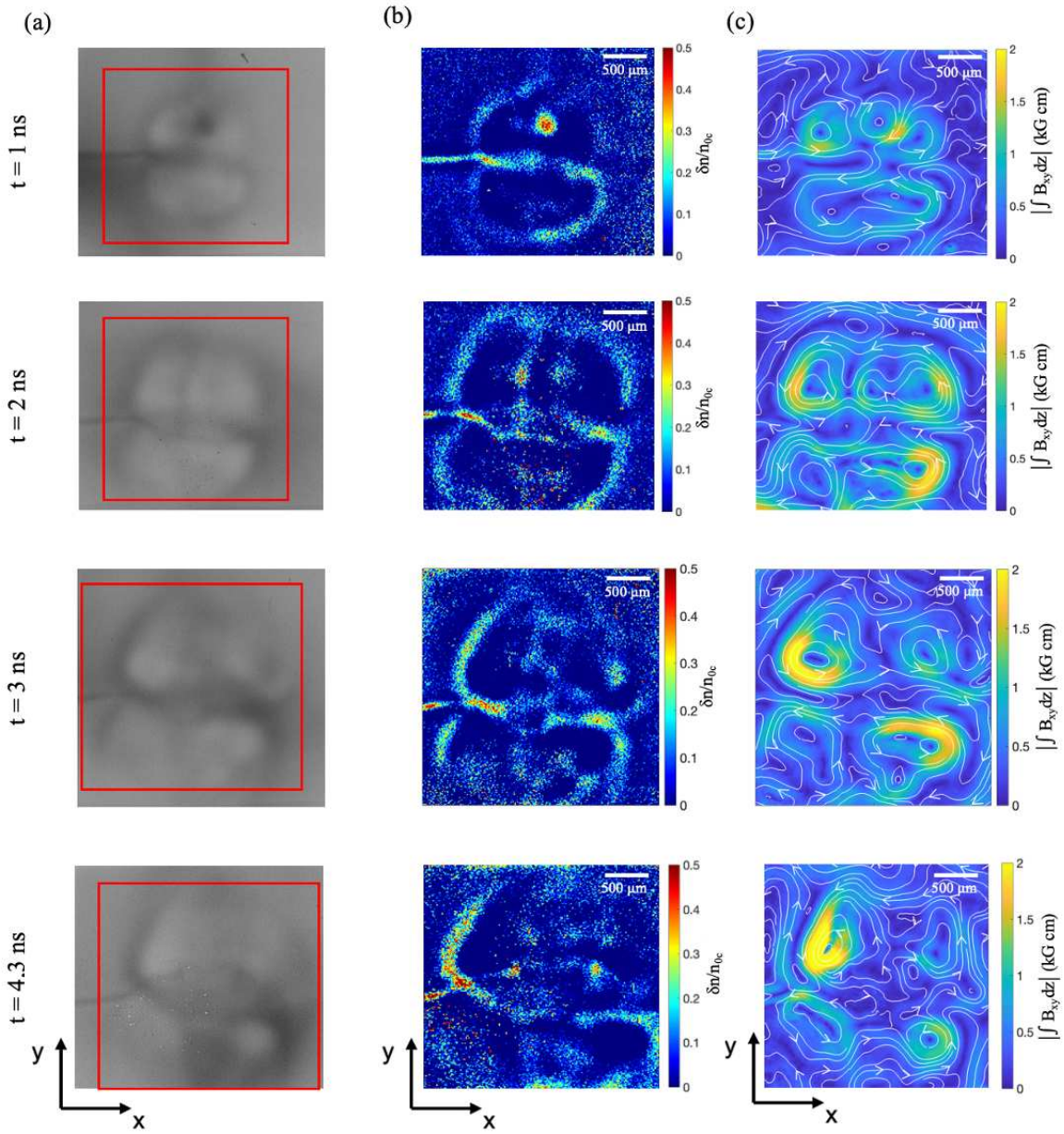

Figure 64. Analyses of the RCFs with PROBLEM in the configuration with φ = 30°. Column (a): Scans of the raw experimental RCFs used to track the temporal evolution of the reconnection. The red squares correspond to the part of the RCFs where the gaussian blur was applied for the analysis. The times on the left correspond to the delay between the start of the target ionisation and the TNSA proton beam. The films all correspond to an energy range of E_p = 8 MeV. Column (b): Corresponding maps of protons flux $\delta n/n_0$. Column (c): Corresponding intensity maps of the path-integrated magnetic field.

This comparative analysis of RCFs between the three configurations showed the influence of the presence of a normal guide field B_z on the formation of the plasmoids and on the way the energy is converted and redistributed during the reconnection process. Indeed, we show here that the apparition of the plasmoid chain within the current sheet is not only relying on the aspect ratio and the Lundquist number of the sheet, but it also depends on the ratio B_z/B_0. If the reconnection goes through the different regimes leading to the plasmoid mode, introducing a normal field to the current sheet either slows down the mechanism or precipitates its progress. These perturbations of the current sheet reorganize the particle distribution within the reconnecting current sheet,

modifying also the dynamics of the plasmas involved and the expansion of the interacting flows during the process.

We completed these observations with the interferometer experimental results. We tracked the expansion of the plasmas at different times during the laser pulse duration, for both the coplanar and the φ = 30° configurations. With this diagnostic, we intended to measure the difference in the expansion of the plasma both with and without the out-of-plane guide field. The methodology used here is similar with the compression experiment, as the interferograms were analyzed with Neutrino to extract the surface and volume electron density maps and the temporal evolution of the characteristic length of the plasma. Figure 65 shows the evolution of the plasma for the two different regimes. The plasmas expand as predicted for the coplanar targets, with a characteristic length growing over time during the laser pulse. However, for the φ = 30° case, the plasmas stay confined closer to the target surfaces and their expansion is limited by the presence of B_z acting like a magnetic confinement mechanism. Furthermore, the expansion reaches a maximum characteristic length around t = 2.5 ns. At this time, the current sheet is already opened for tilted targets and the secondary reconnection process is also proceeding.

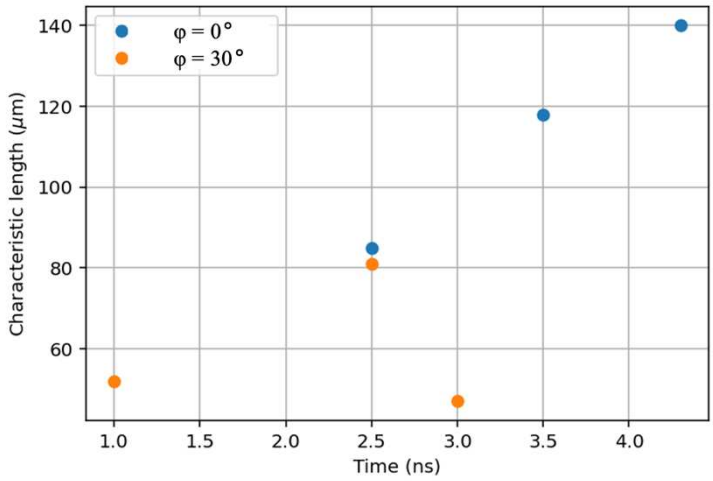

Figure 65. Temporal evolution of the characteristic length of the expanding plasmas during the laser pulse duration, with the coplanar case represented by the blue dots and the case where a 30° angle is induced is represented by the orange ones. The value of the characteristic length for each dot has been calculated from the volume electron density map by analysing the corresponding interferogram with Neutrino.

In this section, we showed that we were able to generate experimentally elongated reconnection current sheets and to observe the formation of plasmoids on RCFs. Here magnetic reconnection is driven only by Biermann battery self-generated magnetic fields and these plasmoids are visible on the RCFs. This diagnostic provides important insights and qualitative descriptions of the reconnection process and permits to detail the development of the current sheet and the global evolution of the magnetic reconnection mechanism. By adapting our setup, we tested different configurations to model the diverse situations occuring in spatial events. We showed therefore that we were not only capable to observe an altered reconnection by inducing experimentally an out-of-plane field, but also that we could observe how these variations affected directly the interacting plasmas. This will be detailed in the following sections.

6.1.3 Dynamics of the current sheet

As we were able to distinguish the different phases of the reconnection process by using RCFs, it is also possible to link the results of proton radiography with optical pyrometry. Indeed, the changes of reconnection regimes were also measured by capturing the emissivity in the visible range of the plasma in the sheet. Therefore, we measured the emissivity of the plasma by being aligned with the axis normal to the current sheet for the three configurations as well as for the situation where only 1 laser beam is shooting, so we can compare with the behavior of a free expanding plasma.

In the case of the coplanar configuration shown on Figure 66, the first peaks of emissivity correspond to the collision of the magnetized plasmas leading to the establishment of the stable regime, when the current sheet remains thin and confined. This high emissivity is linked to the earliest stages of the reconnection, characterized by high values of electron temperature T_e and density n_e, as well as strong reconnecting electric field E_z. The amplitude of the plasma emissivity decreases starting from t = 2 ns, corresponding to the time when the RCFs show the beginning of the regime transition. Secondary peaks can be observed at this stage as the broadening of the sheet goes with energy releases. Around t ~ 4 ns, final peaks are observed, during the plasmoid regime. However, these peaks remain weaker than the first ones, as the current sheet is here more extended and the plasma least dense due to plasmoid formation and ejection. Therefore, proton radiography and optical pyrometry results are complementary. We notice that the emissivity of the plasma reflects the reconnection topology. In comparison, in absence of reconnection, when only one target is irradiated and only one plasma is generated by 1 beam, the emissivity remains low and quasi-constant as expected during the whole plasma lifetime.

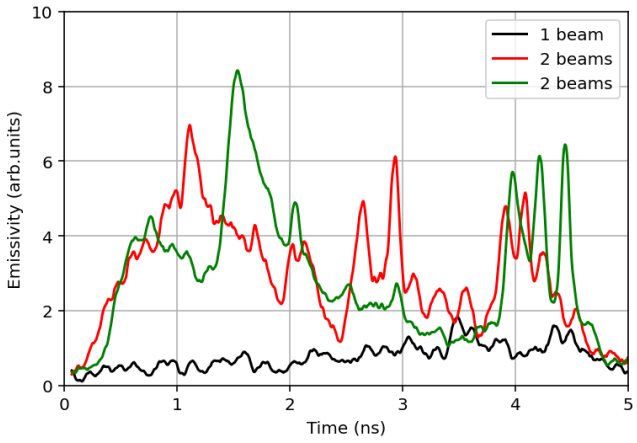

Figure 66. Temporal 1D lineouts of optical pyrometry measurements integrated toward the z-axis of plasma self-emission as a function of time, inducing the plasmas heating of the reconnection region for coplanar targets in the 2 beams configuration (two distinct shots presenting the same configuration are shown by the red and green curves for the reproducibility) and in the 1 beam configuration (no reconnection). The starting time t = 0 ns corresponds to the start of the laser irradiation of the targets.

Furthermore, as mentioned before, proton radiography results presented in Section 6.1.2 reveal the emergence of a secondary reconnection process, orthogonal to the primary one [10]. We noted this phenomenon in the coplanar targets and for φ = 30°, when the plasmoid-dominated regime is precipated by the presence of a strong guide field. This second current sheet does not get

formed between two distinct interacting plasmas but results directly from the reconnection of the magnetic fields advected by the interacting plasmas, which undergo perturbations from the main reconnection process and start to reconnect with themselves. This mechanism can be observed at early times in the process and can develop simultaneously with the rest of the structure, especially during the transition between the distinct reconnection regimes. As this regime change induces a wider and more diffusive current sheet, the diffusion of the thermal energy is more isotropic. Colder regions are heated outside of the current sheet, which will nurture the growth of secondary processes [11]. The second reconnection sheet widens simultaneously with the main one and evolves toward the plasmoid regime. However, this orthogonal reconnection remains more diffused and less stable than the principal. The current sheet is less energetic and magnetic topologies obtained with proton radiography indicate that they last for short timescales, making it a process complementary to the first one.

Similar measurements with optical pyrometry were performed for $\varphi = 15°$ and $\varphi = 30°$. On Figure 67, the primary peaks of emission for $\varphi = 0°$ and $\varphi = 30°$ happen quasi-simultaneously (between t = 1 ns and t = 2 ns). However, the emission is significantly higher for coplanar targets. As we observed with proton radiography, the current sheet is still thin and contained at these times when no guide field is involved while the sheet is already extended for $\varphi = 30°$. In this case, the density of the reconnection zone is already lower than for the thiner current sheet. Consequently, the main peak of emission is weaker for $\varphi = 30°$, similarely to the secondary peaks presented on Figure 66 during the plasmoid regime. It is also possible to observe a second prominent peak for $\varphi = 30°$, shortly before t = 4 ns. At this time, the plasmoid regime is already ongoing and the secondary reconnection process, which is well established in this configuration, distorts the main wider sheet and fragments the plasma. Moreover, the weaker emissivity of the plasma observed for this configuration is correlated with the corresponding interferometry results, as the plasma was way less expanded and remained more confined near the targets than it was for coplanar targets. Finally, for $\varphi = 15°$, the reconnection process is slowed down such as the emissivity remains low and quasi-constant before the opening of the current sheet (around t = 4 ns). The emission in two distinct peaks is similar to the emissivity profile for $\varphi = 30°$ but remains lower as parts of the energy has already been converted during an extending duration of the process. The plasma has not been observed on the RCFs after t = 4.5 ns but the emission is still occuring after the end of the laser pulse at t = 5 ns. Indeed, we see here the second peak around $t \sim 6$ ns, as the reconnection is slowed down by the presence of the guide field in this configuration.

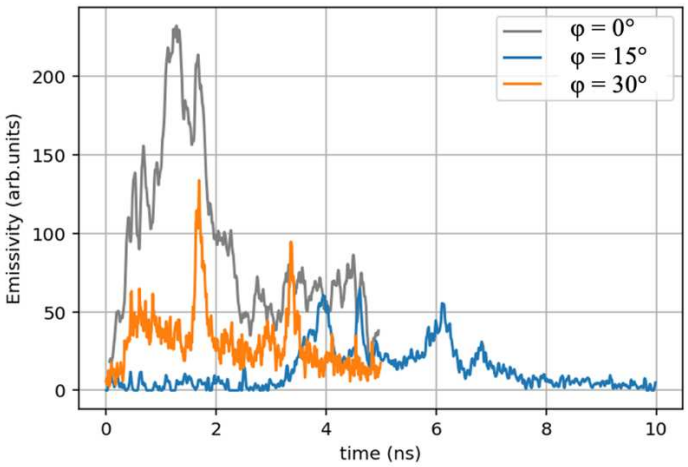

Figure 67. Temporal 1D lineouts of optical pyrometry measurements integrated toward the z-axis of plasma self-emission as a function of time, inducing the plasmas heating of the reconnection region for the three different target configurations. The coplanar configuration is represented by the gray curve, the targets tilted with an angle of 15° and 30° are represented respectively by the blue and orange curves. The starting time t = 0 ns corresponds to the start of the laser irradiation of the targets.

6.1.4 Plasma parameters in the current sheet

Magnetic reconnection is a fundamental process that modifies the magnetic field topology, which impacts directly the charged particles dynamics. Therefore, we determine the plasma dimensionless characteristic parameters to characterize the reconnecting plasma in the current sheet. The magnetic field amplitude can be estimated from assuming balance between the thermal and the magnetic pressure. This assumption is commonly used to get an estimation of the order of magnitude of the involved magnetic field strength. We can approximate $\beta_{th} \sim 1$, therefore we have:

$$n_e k_B T_e \sim \frac{B^2}{2\mu_0} \tag{6.2}$$

$$B \sim \sqrt{2\mu_0 n_e k_B T_e} \ , \tag{6.3}$$

therefore, we can write:

$$B \sim 6{,}34 \times 10^{-13} \sqrt{n_e T_e} \tag{6.4}$$

We consider here that $T_i << T_e$, and the electron temperature T_e was experimentally estimated at around $T_e \sim 175$ eV in the expanding plasmas. Consequently, we have $B \sim 20$ T at the edges of the current sheet, where we assume $\beta_{th} \sim 1$. We determine also the Mach and Alfvén numbers to estimate the β_{th} ratio in the sheet. As $B \sim 0$ T in the core of the sheet, we expect to have $\beta_{th} > 1$. Therefore, we first calculate the sound velocity c_S (see Chapter 1, eq. 1.27). For $T_e = 175$ eV and an ionization level $Z = 14$, we have $c_S = 60$ km/s. If we refer to the experimentally estimated velocity for the expansion of the plasma, we have $v = 300$ km/s. Therefore, the Mach number M_S is:

$$M_S = \frac{v}{c_S} = \frac{300}{60} = 5 \tag{6.5}$$

Similarly, we also calculate the Alfvén velocity v_A (see Chapter 1, eq. 1.29). For a density $n_i \sim 10^{19}$ part/cm^3 $\sim 10^{25}$ part/m^3, we have $v_A = 22$ km/s. Therefore, the Alfvén Mach number M_A is:

$$M_A = \frac{v}{v_A} = \frac{300}{22} \sim 13.6 \quad (6.6)$$

We have M_A, $M_S > 1$, so the plasma inflows entering the current sheet are both super-Alfvénic and supersonic. As shown in Chapter 5 (eq. 5.5), the resulting β_{th} ratio is:

$$\beta_{th} = \left(\frac{M_A}{M_S}\right)^2 \quad (6.7)$$

$$\beta_{th} = \left(\frac{13,6}{5}\right)^2 \sim 7.4 \quad (6.8)$$

We indeed have β_{th} larger than unity, which indicates that the plasma in the sheet is dominated by the thermal pressure. Unlike for magnetic compression (where $\beta_{th} < 1$ in the compression zone), magnetic reconnection here does not induce a transition toward a regime dominated by the magnetic field inside the current sheet. Here both the expanding laser-driven plasmas and the reconnection sheet evolve in a high-β_{th} regime. Furthermore, as $T_i << T_e$, the current sheet is dominated by the electron thermal pressure P_{th}.

From the reconnection figures on the RCFs, we can also estimate the dimensions of the current sheet, and consequently calculate the aspect ratio $A = L/\delta$. For the coplanar targets and the tilted targets with $\varphi = 15°$, which are the two configurations where we can visualize the thin current sheet in the primary stable regime, the aspect ratio is around $A \sim 7.5 – 10$, with an average width of the current sheet estimated around $\delta \sim 100$ µm in this regime (we showed on Figure 64 that the current sheet is thiner for $\varphi = 15°$ than for coplanar targets). It is also interesting to measure the dimensions of the sheet out of the stable regime. Indeed, the thin current sheet widens during the process and leads to a thicker sheet when it enters the plasmoid regime. In this case, for the three target configurations, we have rather $A \sim 4 – 6$.

Finally, we can estimate that the Lundquist number is around $S \sim 100$. $S >> 1$, but usually, the threshold value for the formation of plasmoids during magnetic reconnection is $S \sim 10^4$. We have here a smaller value of S but as we still observe and measure a plasmoid-dominated regime getting established in the current sheet, we can assume that the necessary conditions for the development of plasmoids are not exclusively linked to the Lundquist number. Indeed, the stable current sheet width corresponds to $\delta = 2 – 3d_i$, where d_i is the ion inertial length and $d_i = 40$ µm for copper ions and an ionization level $Z = 14$. Besides, the electron inertial length was estimated to $d_e = 1.7$ µm. Consequently, as the current sheet thickness is of the order of a few d_i, the magnetic reconnection process is driven mainly by kinetic effects and collisionless dynamics, beyond the resistive MHD model on which depends the condition on the Lundquist number. Mechanisms such as the dissipation of magnetic energy or the anistropy within the sheet can favour the apparition of plasmoids. Consequently, even if we have a global estimation of $S \sim 100$, kinetic effects imply local values of S depending on the inner fluctuations of the fields in the sheet, such as locally we have $S_{local} > S$. Therefore, it is coherent to observe experimentally the formation of plasmoids in the elongated current sheet despite a Lundquist number lower than require in the MHD framework.

Plasma parameters	Approximate values
Plasma density (n_e [part/cm^3])	10^{19}
Average ionization level	14 – 15
Electron temperature (T_e [eV])	175
Magnetic field (B [T])	20
Plasma beta ratio (β_{th})	7.4
Sound speed (c_S [km/s])	60
Alfvén speed (v_A [km/s])	22
Aspect ratio (L / δ)	8 – 10
Lundquist number (S)	100
Ion skin depth (d_i [μm])	40
Electron skin depth (d_e [μm])	1.7

Tableau 6. Summary of the main plasma parameters in the current sheet. The plasma density, the average ionization level and the electron temperature were measured experimentally with the appropriate diagnostic; the rest of the parameters were calculated with the experimentally measured quantities. These parameters represent the characteristics of the sheet in the stable regime.

We showed here how we were capable to generate and induce magnetic reconnection in an elongated and large aspect ratio current sheet in the laboratory, in between high-β_{th} magnetized plasmas. The anisotropic geometry of our experimental setup and the long duration of the laser pulses generating the magnetized plasmas permitted to observe the complete temporal evolution of the current sheet: the stable first stage, followed by the progressive fragmentation due to tearing instabilities and then the plasmoid-dominated regime. With our diagnostics, we demonstrated how the evolution of the current sheet influences the properties of the plasma. Through the characterization of our experimental plasma with the calculation of the plasma parameters, we exhibited that the dynamics of the current sheet depends also on the anisotropy of the setup that favours the apparition of the plasmoids, as well as on inner mechanisms, such as magnetic energy dissipation or local variations of pressure. Furthermore, we generalize our experimental results by inducing adding a guide field in our setup. We complete the experimental analysis with PIC simulations to investigate the influence of kinetic effects on the plasmoids formation and estimate how the particle flows and the energy is redistributed in the current sheet during the reconnection process.

6.2 PIC study of the reconnection process

In this part, we will describe the simulations ran to support the experimental results. By using the plasma parameters presented in 6.1.4., we built a setup with the PIC code SMILEI (described in Chapter 4, section 4.2.2.) to reproduce the experimental setup and recreate the interaction of the two magnetized plasmas colliding with anti-parallel magnetic flux.

6.2.1 Relevance of PIC simulations over hydrodynamic models

Contrary to magnetic compression, here for the study of the reconnection process we did not perform any simulations with FLASH modeling the MHD aspects of the current sheet and the reconnection process. Indeed, our work in the laboratory was focused on the precise configuration of the reconnection process where the current sheet presents a large aspect ratio and is likely to be fragmented into chains of plasmoids during the reconnection. These plasmoids are formed as the current sheet becomes unstable and is subject to tearing instabilities, which is a mechanism that can be predicted within the framework of resistive MHD. However, this macroscopical approach only models the plasma as a collisional fluid characterized by a Maxwellian distribution. As a result, kinetic effects that play a crucial role in the reconnection process, such as here Hall effects, or physical aspects at the particle inertial scales, are not taken into account and remain under-resolved with this specific description. We showed in the previous section that the current sheet has a large aspect ratio, meaning that it is both elongated and thin. Also, the width of the current sheet corresponds to a few ion inertial lengths, which indicates that ion-scale effects are relevant in the dynamics of the sheet. Even if the global structure of that current sheet can be described in the MHD framework, the fluid approximation is not valid at scales such as ion and electron inertial lengths, so the internal structures in the current sheet need to be addressed with a kinetic description.

Therefore, here we performed PIC simulations to provide a complete kinetic description of the dynamics of the plasma in the current sheet. This will underline the collisionless aspects of magnetic reconnection and more particularly, we aim to represent the kinetic effects involved in the different stages of the evolution of the current sheet, as well as the formation and the establishment of the plasmoid-dominated regime.

6.2.2 Kinetic model of the current sheet

6.2.2.1 Numerical setup

To build the SMILEI setup to model magnetic reconnection, we used the different plasma parameters calculated previously to adapt our initial conditions on quantities like the magnetic field amplitude or the density. Besides, to visualize the entirety of the sheet, the simulation was set in a 500 μm x 1000 μm domain, for a 1024 x 512 resolution (16 x 6 patches) and 128 particles per cell. The typical timestep was 0.3 fs and the boundary conditions were set to « periodic » for both the electromagnetic fields and the particle flows. The simulations were performed in cartesian

2D, like we did for SMILEI simulations of magnetic compression. We used the same referency frequency ω_r for the variable **reference_angular_frequency_SI**, such as $\omega_r = 1.74.10^{14}$ rad/s. To model the amplitude of the Biermann battery magnetic fields colliding in the zone of reconnection, we set an initial magnetic field whose form is:

$$B_y = B_0 \tanh\left(\frac{x-\frac{L_x}{2}}{4}\right), \tag{6.9}$$

where $B_0 = 20$ T is the initial amplitude of the reconnecting fields (see eq. 6.4) and L_x is the longitudinal dimension of the simulation domain. The velocity model of the particles to advect the flows toward each other to form the current sheet in the middle of the simulation domain is defined by a similar shape:

$$v_{e,i} = -v_0 \tanh\left(x - \frac{L_x}{2}\right), \tag{6.10}$$

where the amplitude of the velocity is set to $v_0 = 0.001c$, so $v_0 = 300$ km/s, to match the experimental value. The initial electron temperature is set at $T_e = 300$ eV and the corresponding ion temperature is $T_i = T_e / 2$. In order to simulate the two incoming plasmas converging from each side of the simulation domain, we set two gaussian density profiles, with n_1 propagating along **x** and n_2 along **-x**, so we have:

$$n_1 = n_0 e^{\frac{\left(x-\frac{L_x}{4}\right)^2}{2\sigma^2}} \tag{6.11}$$

$$n_2 = n_0 e^{\frac{\left(x-3\frac{L_x}{4}\right)^2}{2\sigma^2}}, \tag{6.12}$$

where $\sigma = L_x / 15$ and $n_0 = 20$ is the initial normalized density. Here we simulate two quasi-neutral interacting plasmas, so the initial electron and proton densities are identical. The hyperbolic tangential profile for the magnetic field is commonly used to model numerically magnetic reconnection [12]. Here, we add the velocity and density profiles to model the plasma inflows. Here we ran SMILEI simulations to support the evolution of the sheet as seen in the laboratory experiment. We performed several simulations to be adapted to the different configurations investigated during the experiment.

6.2.2.2 General evolution of the current sheet

PIC simulations permit to investigate the collisionless aspects of the formation and the evolution of the current sheet through its different stages at the scales of the charged particles involved in the reconnection process. We mentioned that, in absence of an out-of-plane guide field, the particles become demagnetized while entering the current sheet. If the magnetic field strength |B| is negligeable in the core of the sheet comparing to the electric field, the Lorentz force acting on electrons and ions is dominated by the electric field. Therefore, the magnetic confinement in the sheet decreases so the charged particles decouple from the magnetic flux and their motion and dynamics are mostly governed by the reconnecting electric field E_z. Besides, at scales close to the inertial length in the current sheet, electrons and ions decouple from the magnetic field lines and the particle diffusion induced by the local electric field generates local variations of the current. Therefore, the demagnetized electrons and ions can be tracked with the evolution of the out-of-

plane z-component of the current density **J**. The evolution of the current density depends on the particle velocities that change with the different regimes within the current sheet. Here, we first simulated the coplanar configuration.

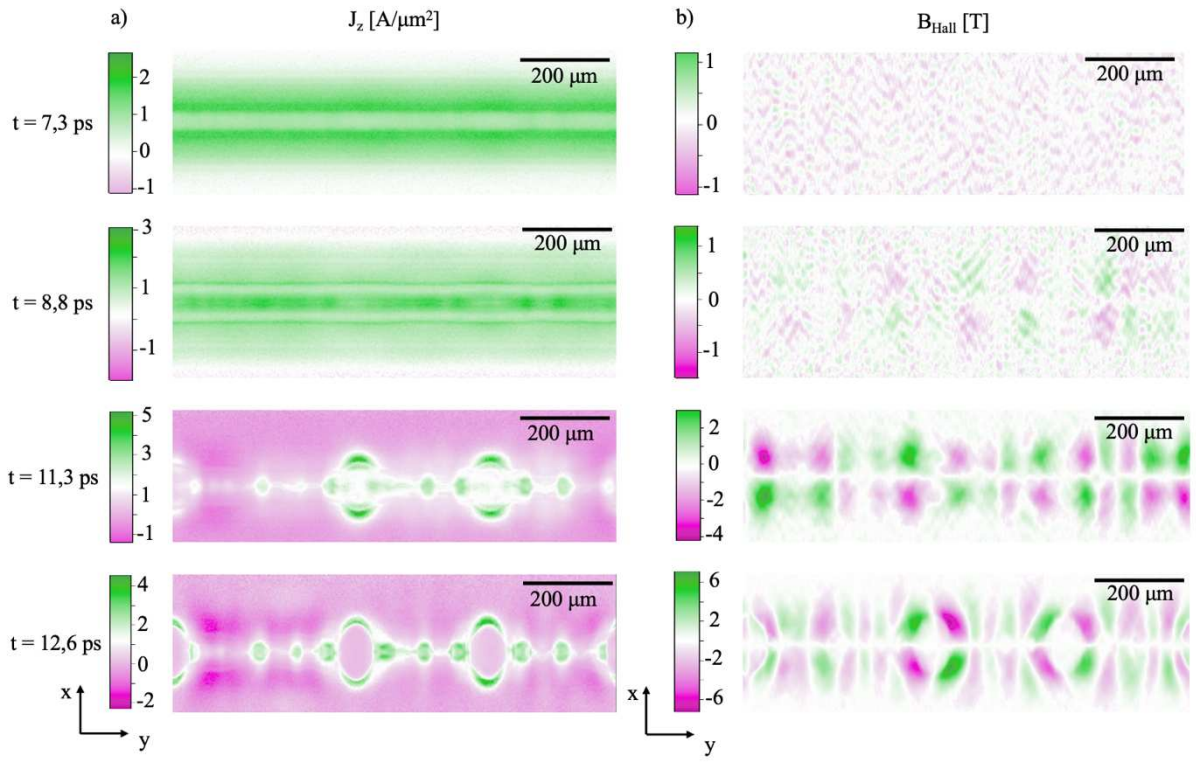

*Figure 68. 2D cartesian SMILEI simulations of the temporal evolution of the elongated current sheet with a large aspect ratio A ~ 10. The simulation parameters are set to the experimental measurements. a) Temporal evolution of the z-axis component of the current density **J**, showing the different stages of the current sheet, including its fragmentation and the formation of the plasmoids. b) Temporal evolution of the corresponding Hall magnetic field in the current sheet B_{Hall}, oriented toward the z-axis and orthogonal to the reconnection plane.*

The evolution of the topology of the sheet influences the internal current density. On Figure 68a), we identify the three main phases of the reconnection process that were highlighted with experimental measurements. When the reconnection sheet is in the stable regime, the current density is uniform and constant around the central neutral zone in the current sheet. The transition toward the plasmoid-driven regime becomes explicit at t = 8.8 ps, as the current sheet progressively starts to be torn by growing internal instabilities and presents fluctuations consistent with tearing. At t = 11.3 ps, the current sheet is fully fragmented into a chain of plasmoids, which gather the charged particles. As the magnetic field lines reconnect around the successive X-points between the plasmoids, the local electromagnetic field is perturbed, which leads to local variations of the ion and electron velocities. In these zones of particle diffusion, the non-ideal terms of the generalized Ohm law dominate (see Chapter 3, eq. 3.2), especially the electronic pressure as the gradients are strong in the X-points. The plasmoids are then characterized by a locally enhanced amplitude of J_z. Furthermore, Figure 68b) exhibits the multiple X-points of reconnection, characterized by the quadrupolar structures of the out-of-plane Hall magnetic field along the z-axis, which appear in the plasmoid regime and are localized in between each magnetic structure. Besides, from the Maxwell equations we have:

$$\nabla \times \mathbf{B} = \mu_0 \mathbf{J} \tag{6.13}$$

The fluctuations of J_z are correlated with the variations of the magnetic field structure. Besides, in the plasmoid-dominated phase, the ejection of particles in the X-points induces variations of the local magnetic field, especially the reconnecting component B_y, occuring at kinetic temporal scales (a few ω_{pe}^{-1}, ω_{pi}^{-1}). PIC simulations permit to follow the evolution of the dynamic of the plasmoids in the current sheet once the plasmoid regime is established. As mentioned previously, plasmoids are not static over time, as they get formed, can merge with one another and eject matter out of the current sheet. These variations modify the electron pressure and dynamics within the current sheet fragmented between the plasmoids and the reconnection sites. Plasmoids are zones of strong pressure gradients and enhanced current density J_z while reconnection points are regions of intense particle acceleration. Here, we have $J_z > 0$ in the plasmoids and $J_z \sim 0$ outside surrounding the X-points. Indeed, the electrons are confined in between closed field lines and induce a stable current structure. More generally, the fluctuations of J_z in the current sheet reflect the constant evolution of its topology, of the magnetic field configuration during the evolution of the chain of plasmoids and X-points as well as of the direction changes of the charged particles velocity.

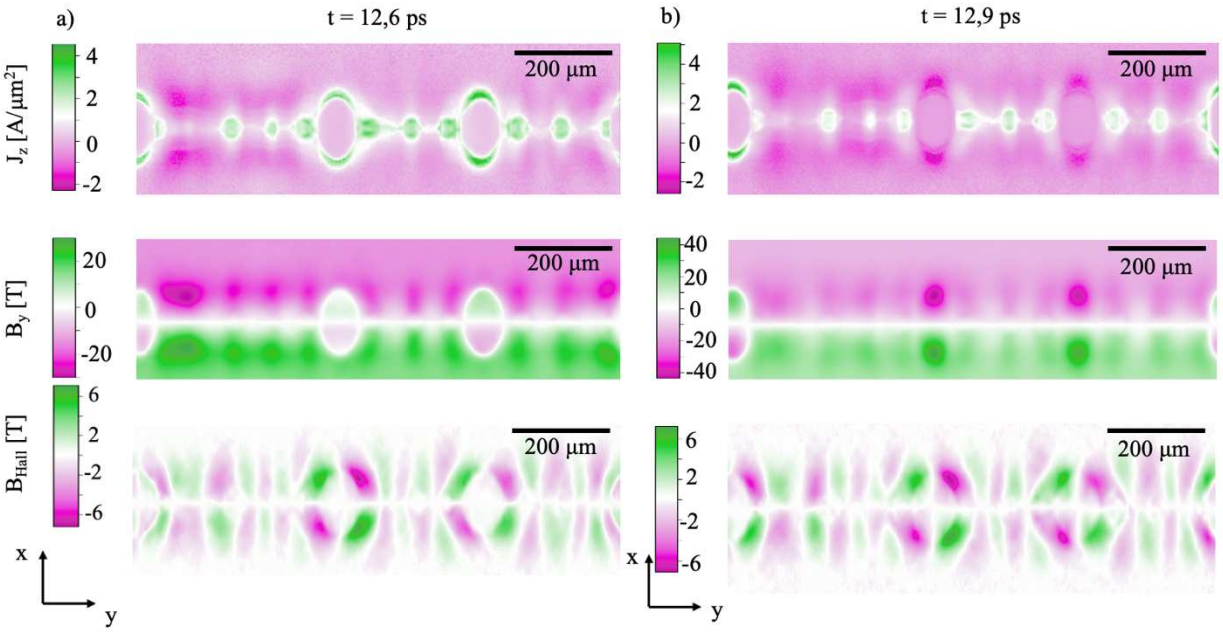

Figure 69. 2D cartesian SMILEI simulations showing the evolution of the current sheet in the plasmoid regime within short time interval. The fluctuations of the z-component of the current density J_z present the dynamics and the merging of the plasmoids and their influence on the reconnecting component of the magnetic field B_y. The evolution of the Hall magnetic field B_{Hall}, orthogonal to the reconnection plane, reflects the spatial evolution of the reconnection sites.

We note that the dynamics of the flows in the current sheet induce variations of the amplitude of the hyperbolic tangential shaped reconnecting magnetic field B_y around the neutral zone (where $B_y = 0$ T in the center of the sheet). These fluctuations are directly linked to the presence of plasmoids, as noticed in Figure 69. Moreover, the current density map exhibits open and distinct structures, representing the dissipation of plasmoids within the current sheet. In this regime, the particles released by the disruption of the plasmoids contribute to the redistribution of

currents and electric fields within the sheet. The energy release induced by the rapid reconfiguration magnetic field topology implied by the dissipation of the plasmoids leads to $J_z \sim 0$.

Besides, during the whole duration of the reconnection process, the particle density is related to the current density. Indeed, if the charged particles velocities define the local sign of J_z, the particle densities also contribute to its intensity. The density variations over time are also an indicator to follow the regime changes in the current sheet and the evolution of the plasmoids. Electron and ion densities are homogeneous during the stable phase of the reconnection before the onset of tearing instabilities in the sheet. As a result, pressure anisotropy can develop along the direction axis of the reconnection sheet, resulting from the particle acceleration and demagnetization. This leads to the formation of small-scale fluctuations of the local field and induces instabilities. Electrons and ions become trapped in the plasmoids formed between the field lines that reconnect in the X-points. Consequently, plasmoids are localized zones of increased density. On the contrary, the X-points are less dense, as particles are accelerated by the reconnecting electric field and ejected out of the sheet within these specific zones of active reconnection.

6.2.2.3 Influence of the guide field

By using the previously described numerical setup, we also modeled the influence of the guide field on the current sheet. We applied the general form of the magnetic field describe in 6.2.2.1., and set a uniform field along the z-axis. We showed in Section 6.1.2.2. that when the targets are each tilted toward each other by $\varphi = 15°$ or $\varphi = 30°$, the guide fields were respectively defined by $B_z = 0.26B_0$ and $B_z = 0.5B_0$, where B_0 is the reconnecting field (here with a 20 T amplitude). Consequently, we launched sets of simulations with the accurate amplitude of B_z for each configuration.

As mentioned in Section 6.1.2.2., the presence of a guide field B_z, normal to the reconnection plane, affects the temporal evolution of the inner topology of the current sheet. When $\varphi = 15°$, the targets are tilted toward each other by a small angle, therefore $B_z/B_0 = 0.26B_0$. In this configuration, the aperture angle between the targets is $\theta = 150°$, compared to $\theta = 180°$ for the coplanar configuration. The guide field does not fundamentally modify the evolution of the reconnection, as the configuration of the current sheet remains similar to the coplanar configuration. However, we observed experimentally that it slows down the reconnection. Charged particles remain partially coupled to the magnetic field, and their trajectories are more structured in the sheet because less subject to kinetic effects. In this geometry, the guide field plays a role of stabilization of the current sheet, in which the fluctuations of the inner electric field and the instabilities are attenuated and delayed.

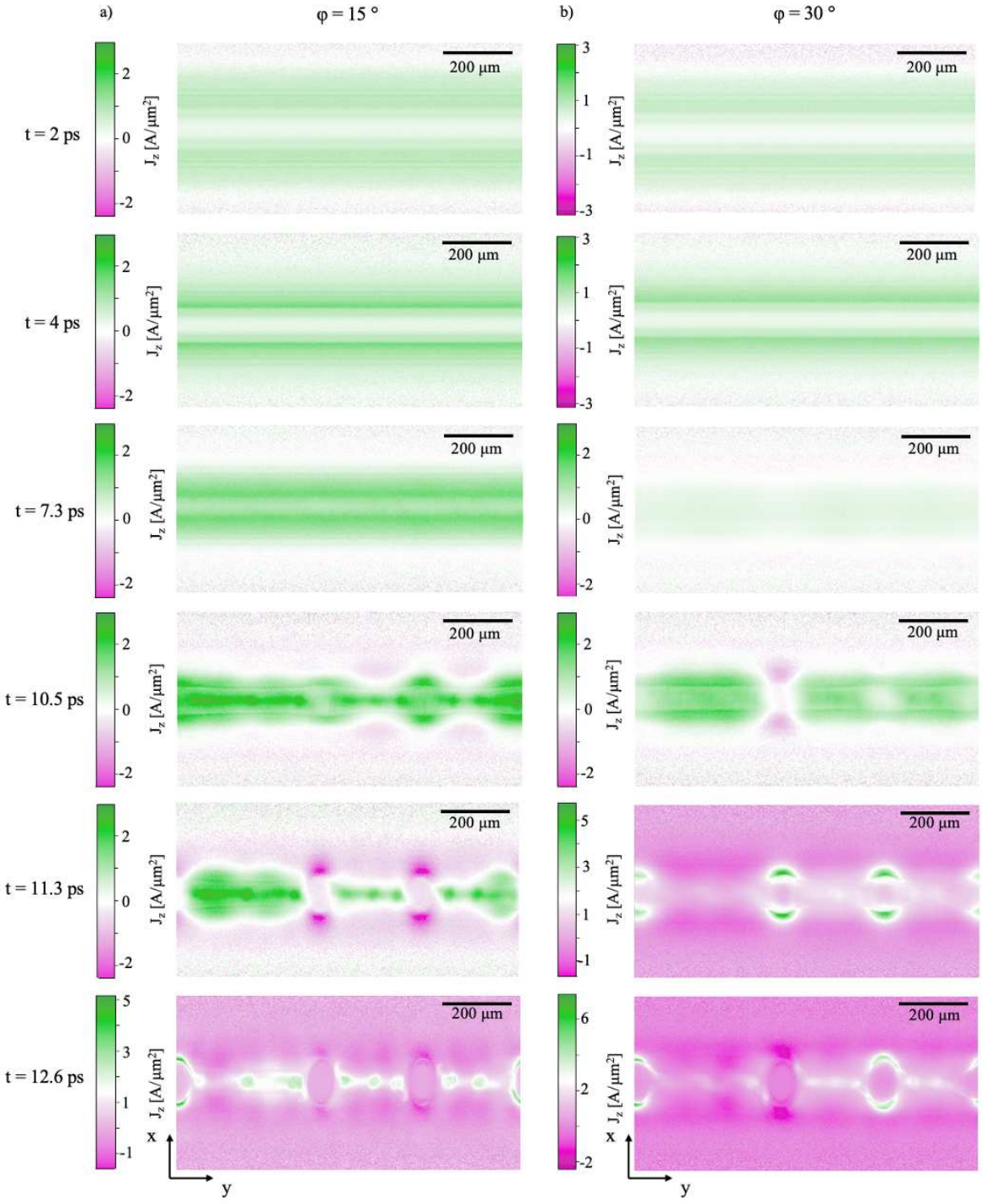

Figure 70. 2D cartesian SMILEI simulations showing the temporal evolution of J_z in the current sheet in the presence of an out-of-plane guide field Bz along the z-axis, such as a) $B_z/B_0 = 0.26$ and b) $B_z/B_0 = 0.5$. Here, we highlight the influence of the guide field on the dynamics of the current sheet, more particularly the transition from the stable regime to the formation and establishment of plasmoids which differs from the coplanar case without guide field.

This effect has been observed experimentally and is confirmed here with the simulations, as shown on Figure 70a). The current sheet becomes unstable due to instabilities only around t = 10.5 ps, while the fragmentation of the sheet into plasmoids only begins around t = 11.3 ps.

Before, the sheet remains stable and narrow. In comparison, in the coplanar case presented on Figure 68, the current sheet is already in an established plasmoid-driven regime at t = 11.3 ps.

PIC simulations also confirm the behavior of the current sheet when a higher guide field is imposed with $\varphi = 30°$ and $B_z/B_0 = 0.5$. Here, the stronger out-of-plane field induces a storage of magnetic energy in the sheet through the remaining magnetized particles, which is quickly released and implies an earlier transition to the plasmoid-dominated regime. As the sheet is only stable for a short time in this configuration, the energy is redistributed faster. Indeed, as shown in Figure 70b), the plasmoid dynamic is accelerated, as plasmoids dissipate faster than in the coplanar case.

With the PIC simulations, we recreated the experimental conditions by modeling two counter-propagating collinding plasmas, magnetized via Biermann battery, to investigate the reconnection process between such magnetic fields. Similarly to the experiment, we modeled an elongated current sheet with a large aspect ratio. This numerical part of the study permitted to validate both our experimental setting for the study of this particular case of magnetic reconnection and the observations made from the experimental results. Consequently, we confirm here our conclusions on the temporal evolution of the current sheet, with and without a guide field.

6.2.3 Characterisation of the magnetic reconnection

6.2.3.1 Evolution of the β_{th} parameter

In the reconnection sheet, β_{th} is expected to be signigicantly larger than unity, as shown experimentally. The sheet is a diffusion region dominated by the plasma pressure, which is characteristic of collisionless reconnection. Such a result for β_{th} has already been highlighted with the experimental measurements, as it is detailed in 6.1.4. However, the experimental assumptions only permit to estimate a global value of β_{th}, which fluctuates in the current sheet over time. As the β_{th} parameter is the ratio of the plasma thermal and magnetic pressures, its value depends on the regime of reconnection. In the stable regime (narrow and uniform current sheet during the earliest times of the process), β_{th} is constant as the charged particles are diffused within the sheet by the reconnecting field. Besides, $\beta_{th} >> 1$, as the dynamic of the sheet is governed by the thermal particles and the reconnection region is formed by the collision of two high - β_{th} magnetized plasmas.

β_{th} is maximal in the center of the sheet where $|B| \sim 0$ T (so does the magnetic pressure P_B). Figure 71 a-d) show the 1D profiles of β_{th} measured in the sheet over time for the coplanar targets ($\varphi = 0°$). If β_{th} remains constant in the sheet during the stable regime (at t = 4 ps, β_{th} is stable around $\beta_{th} \sim 2.1$), fluctuations occur as soon as the first instabilities take place. The chain of plasmoids is formed by the reconnecting magnetic field lines, which trap the charged particles. Their densities n_e, n_i increase considerably but the peaks of density remain localized, confined within the plasmoids. Besides, the local dissipation of the stored magnetic enegy by these plasmoids accelerates the particles but is also partially converted to thermal energy. The plasma is then heated locally, starting with the heat of the electrons. Consequently, β_{th} is significantly higher in the plasmoids (with $\beta_{th} >> 1$), where it reaches its maximum during the plasmoid-driven regime. On Figure 71c) and 71d), showing the profile of β_{th} in the plasmoid-dominated regime, the maximal

values of β_{th} reach $\beta_{th} \sim 40$ in the plasmoids while $\beta_{th} \sim 0$ outside. This distribution of the pressure in the sheet underlines that plasmoids are mostly governed by the plasma pressure $P_{th} = n_e k_B T_e$.

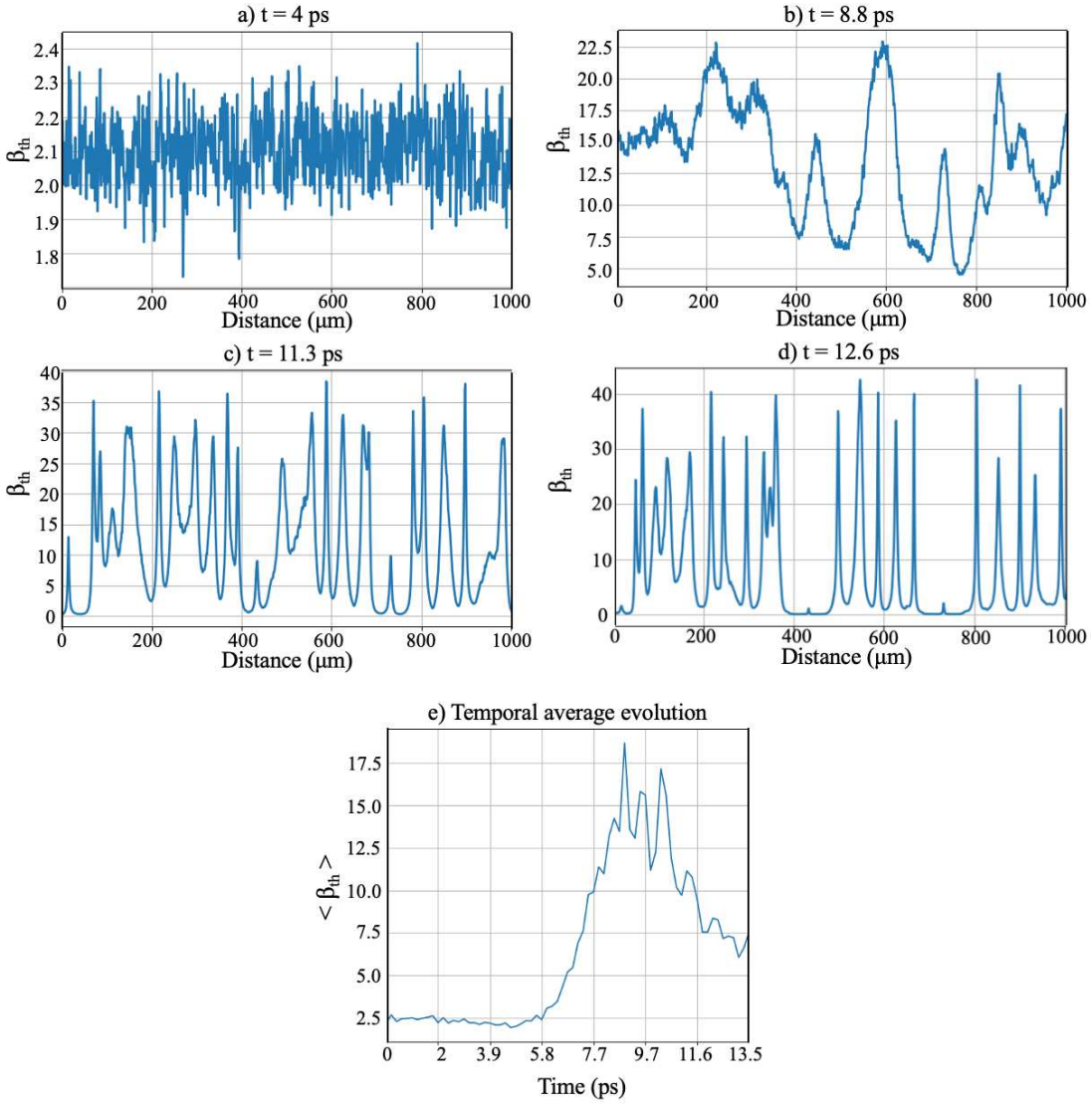

Figure 71. a-d) 1D profiles of β_{th} over time measured on 2D cartesian SMILEI simulations for the coplanar target configuration, measured in the current sheet. The profiles of β_{th} show successively the stable regime of reconnection (a), the formation of tearing instabilities in the sheet (b) and the plasmoid-driven regime (c – d). e) Temporal evolution of β_{th} averaged with time on the totality of the current sheet.

Furthermore, the β_{th} parameter not only exhibits the inner dynamics of the plasmoids, but also reflects the global evolution of the current sheet as a whole. Figure 71e) shows the temporal evolution of β_{th}, this time averaged on the totality of the width of the current sheet. This measurement identifies three main stages in the evolution of β_{th} and of the sheet. Firstly, $\beta_{th} \sim 2.5$ is constant in the stable regime. The global value of β_{th} corresponds to its value measured with the 1D profile taken in the center of the sheet, highlighting the initial uniformity and the narrowness of the large aspect ratio sheet (see Figure 71a)).

β_{th} increases quickly toward higher values, reaching an average $\beta_{th} \sim 18$ at its maximum. This corresponds to a regime transition and the formation of the first plasmoids that confine the

plasma. As shown previously, β_{th} is the highest in the plasmoids, as they are confining hot electrons and dissipate the magnetic energy. Besides, during the transition between the stable and the plasmoid-driven regimes, the current sheet remains narrow, which triggers the development of the tearing instabilities (see Figure 71b)). Consequently, the rise of the global β_{th} reflects the increasing thermal pressure P_{th} in the plasmoids that are getting formed in a still thin current sheet.

Finally, we observe a decreasing average value of β_{th} during the plasmoid regime, despite the ongoing reconnection process and the high - β_{th} plasmoids. The topology of the sheet changes while in the plasmoid regime, as the current is fragmented and mostly concentrated in the plasmoids along the thermal electrons and ions. The sheet widens around the plasmoids and $J_z \sim 0$ A/μm^2 outside. Moreover, as much as plasmoids confined the magnetic energy, the part of this energy converted in thermal energy is balanced by the advection of the heated plasma out of the sheet and the acceleration of the charged particles. Consequently, the temperature within the plasmoids reaches a maximum value and so does β_{th}. This configuration corresponds to the plasmoid quasi-stationary state and saturated values of β_{th} in the plasmoids, associated to a larger current sheet, and induces a decreasing average β_{th}.

6.2.3.2 Influence of the guide field on the reconnection characteristic parameters

We detailed the fluctuations of β_{th} in the current sheet that depend on the regime of the sheet. In this part, we extend this study to the cases of reconnection in presence of a guide field. Figure 72 shows the comparison of the average β_{th} for the coplanar targets with the configurations presenting a guide field along the normal axis. Once again, here β_{th} is calculated on the totality of the sheet. The presence of an out-of-plane guide field, such as $B_z \neq 0$, has a major influence on the global dynamics of the sheet. Indeed, if $B_z \neq 0$, then the total magnetic field is not dissipated in the sheet, even in the neutral zone (see Chapter 3, eq. 3.9). Consequently, the magnetic pressure P_B is not negligeable comparing to the thermal pressure anymore, as $P_B \propto B^2$ and $B^2 \neq 0$.

The presence of a guide field significantly modifies the plasma dynamics in the current sheet. In Figure 71, we note that the coplanar configuration is characterized by $<\beta_{th}> >> 1$. Consequently, in this configuration the magnetic pressure is negligible within the current sheet. However, the presence of a guide field imposes a global low-β_{th} regime in the sheet, with $<\beta_{th}> < 1$ [13]. The guide field induces a remaining magnetic pressure in the sheet, partially balancing the thermal pressure and β_{th} decreases as the sheet enters a more balanced state.

However, we remind that we present here the general aspect of the sheet, where the incoming particles remain partially magnetized in the presence of a guide field $B_z \neq 0$. The guide field affects the dynamics of the sheet, as shown experimentally and numerically with PIC simulations, but we can still measure high values of β_{th} in the current in presence of a guide field, more particularly due to the presence of plasmoids. However, outside of the plasmoids the magnetic pressure is more dominant due to the guide field. This highlights the spatial anisotropy between the plasmoids and the rest of the current sheet. Moreover, the presence of $B_z \neq 0$ favours the particle ejection along the z-axis, leading to structured distribution of the density between the plasmoids which gather the hot plasma and the rest of the sheet.

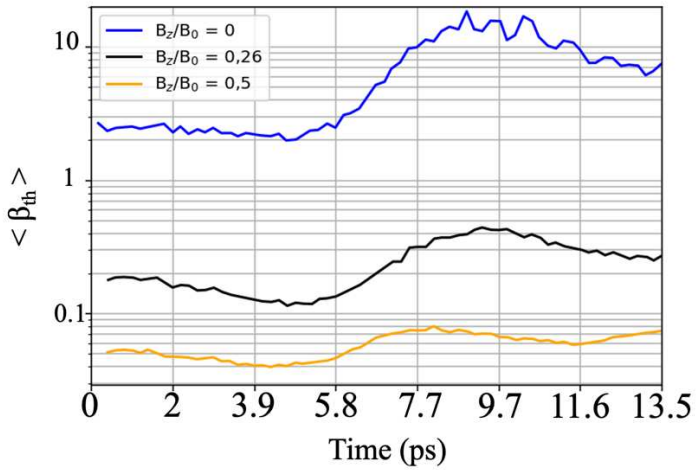

Figure 72. Comparison of the temporal evolution of β_{th} averaged in time on the totality of the current sheet in 2D cartesian SMILEI simulations for the three configurations, with guide field (φ = 15° and φ = 30°) and without guide field (φ = 0°). The ordinate axis has been set on logarithmic scale to highlight the variations of $<\beta_{th}>$.

The presence of the guide field alters the global dynamics of the elongated and large aspect ratio current sheet, as it influences both the temporal and spatial evolution of the sheet and the distribution of the charged particles involved in the reconnection process. To represent the global effect of a guide field on the evolution of the current sheet, we modeled spatio-temporal 2D Fourier transforms from the 2D PIC simulations for each configuration (see Figure 73). As a result, the (ω, k_y) Fourier transforms represent the fluctuations of the structure of the sheet along the y-axis (the direction axis of the current sheet in the SMILEI simulations) over the temporal frequency ω. The Fourier transform does not depend on a specific time, during which the current sheet is stable or under the plasmoid dynamics and the (ω, k_y) spectrum is computed over the total temporal window of the simulation on the entirety of the current sheet. Therefore, it consistutes a general diagnostic for the global dynamics of the sheet during the whole process.

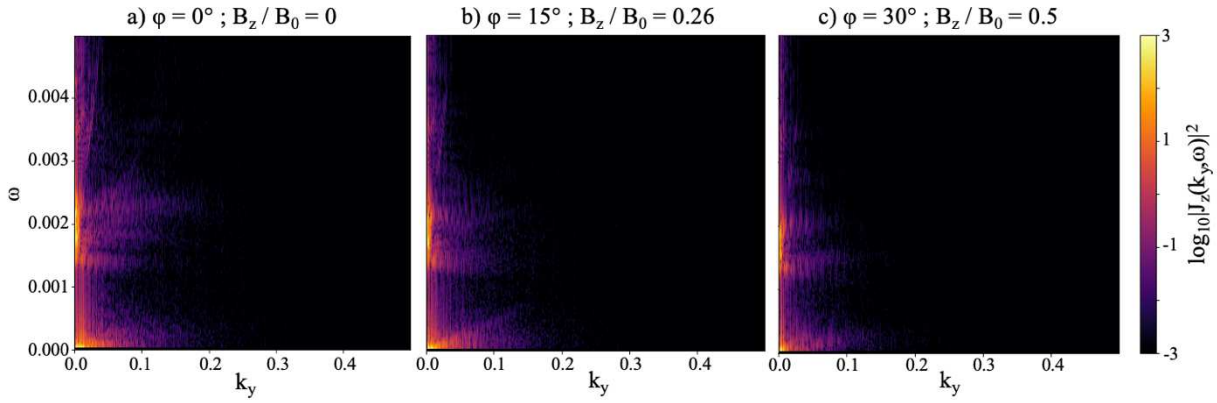

Figure 73. Comparison of the spatial 2D Fourier transforms using the 2D cartesian SMILEI simulations for the three configurations. The spatial Fourier transforms present each two axes of symetry, along ω = 0 and k_y = 0. The totality of the transforms is not represented; here we chose to focus on the quarter where ω > 0 and k_y > 0.

The analysis of the spatio-temporal Fourier transforms permits to identify the different modes and instabilities within each system. For every configuration, a peak of intensity along $k_y = 0$ represents the global evolution of the system and the main mode of the sheet, so here the energy is concentrated around medium frequencies (around $\omega \sim 0.002$). The less intense oscillations localized at higher k_y represent the different secondary modes resulting from the fragmentation of the current sheet and the formation of plasmoids.

The most scattered Fourier transform is the one representing the coplanar configuration (see Figure 73a)), where the oscillations are expanding until around $k_y \sim 0.1$ at low and medium frequencies. In absence of guide field, higher modes are excited in the current sheet. As the charged particles, and especially the electrons, are demagnetized in the sheet in this configuration, their dynamics ease the development of small-scale instabilities in the sheet. Indeed, the higher the k_y mode is, the thinner the corresponding structure is. The Fourier transform presents the spectrum of the different modes triggering the instabilities and the plasmoid regime in the sheet.

These oscillations are more gathered around the central $k_y = 0$ axis when the magnetic reconnection occurs with a guide field (see Figure 73b and 73c)). The spectrum is even less expanded for a higher amplitude of B_z. Therefore, the presence of the normal guide field and the remaining magnetization of the particles stabilize the inner dynamic of the sheet by easing particle acceleration and ejection along the sheet. This mechanism prevents from particle accumulation and the formation of small-scale instabilities. Besides, Figure 73a) reveals the presence of secondary modes for higher frequencies (around $\omega \sim 0.004$) in absence of guide field. These modes transcribe the formation in the sheet of succint and short timescale structures in the sheet. As the guide field improves the stability of the current, these structures are less likely to appear as the amplitude of the guide field grows and the reconnection sheet evolves toward a more stable regime.

Finally, we estimate the evolution of the reconnection rate $R = E_z/v_A B_0$ in the sheet for the three configurations. In all cases (see Figure 74), we observe the clear transitions of reconnection regimes in the sheet. Indeed, $R \sim 0.01$ at the start of the process when the sheet is stable and dominated by the diffusion of particles. Overall, R remains low at the earliest times of the reconnection. However, the rate grows as soon as the instabilities fragment the sheet, implying the formation of multiple reconnection sites. Consequently, the reconnection rate reaches $R \sim 0.06 – 0.08$, depending on the configuration. During this transition, the dynamic of the sheet is not linear and is subject to the ongoing formation of the plasmoids, which induces a faster reconnecting regime. Later in the process, the established plasmoid regime is characterized by a decreasing rate (around $R \sim 0.02$), as the plasmoids dissipate and merge, reducing the amount of reconnection points.

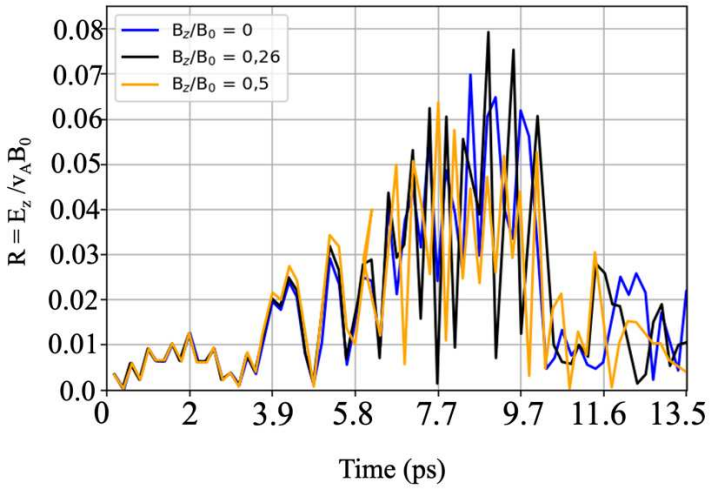

Figure 74. Comparison of the temporal evolution of the reconnection rate R on the totality of the current sheet in 2D cartesian SMILEI simulations for the three configurations, with and without guide field where the coplanar configuration is represented by the blue curve, the configuration φ = 15° by the black curve and the configuration φ = 30° by the orange curve.

It is interesting to emphasize that the evolution of the global reconnection rate remains similar with and without a guide field out of the reconnection plane. Consequently, the guide field influences the evolution of the local structure of the reconnection sheet as we showed with the 2D Fourier spectrum, but does not affect the global reconnection process. Besides, at its maximal value, the reconnection rate almost tends to R ~ 0.1 when the sheet enters the plasmoid regime. This is characteristic of an efficient collisionless reconnection process.

In this part, we showed different diagnostics, relevant between each other and which permit to address the different kinetic effects affecting the reconnection process and the evolution of the elongated current sheet. We also investigated the effects of guide fields on the temporal evolution and the dynamics of the current sheet. We exhibited the main phases occuring in the current sheet and how they impact the energy distribution and the fluctuations of densities, as well as the specific characteristics of an elongated current sheet, such as the fragmentation of the sheet in multiple reconnection sites or the energy transport around and within the plasmoids. We also investigated the effects of the guide fields on the physical quantities and how they are decisive in the evolution of the reconnection zone. Above all, this numerical part of the study not only permits to validate the main properties of the current sheet observed in laboratory, but also provides explaination of these phenomena based on the kinetic framework.

6.3 Conclusion

We presented here the different experimental observations we obtained with the diagnostics that we installed. We exhibited that we were able to generate the necessary conditions in the laboratory to trigger magnetic reconnection in an elongated and large aspect ratio current sheet.

The magnetic fields involved in the process were Biermann battery self-generated fields. In this case, magnetic reconnection does not require any external sources of magnetic field.

We demonstrated that the data acquired experimentally with our diagnostics exhibited coherent mechanisms taking part or resulting from the regime changes within the elongated current sheet. Proton radiography permits to have an insight of the magnetic structure of the current sheet and to track the variations of flux and field around the sheet during the multiple stages of the reconnection, especially in between the stable and plasmoid-dominated regimes. In addition, the self-emission of the plasma in the sheet and the inner variation of temperatures highlighting the different dynamics of the current sheet were measured with optical pyrometry and Thomson scattering.

Numerical simulations were run to support the experimental conclusions and detail the different mechanisms observed with the diagnostics. This theoretical part of our study confirms the model of evolution of the current sheet deduced from the experimental observations. The reconnection process is first evolving in a fully thermal pressure-dominated plasma, within a non stationnary lasting regime, influenced mostly by the charged particles, as they are diffused in the current sheet. After the fragmentation of the sheet due to increasing inner instabilities, the plasmoid regime is established, and we demonstrated how the pressure is balanced in the sheet in this configuration. We also exhibit here the anisotropic aspects of the current sheet, whether it is about the inner pressure of the particles, the dissipiation of energy or the difference of dynamics between the plasmoids and the rest of the sheet. The anisotropy of the current sheet is fully associated to the non-uniform evolution of the current sheet, i.e. the apparition of tearing instabilities leading to the fragmentation of the sheet into plasmoids after a stable initial regime.

Moreover, we showed an equilibrium between the plasma heating and the ejection of matter out of the sheet. These observations, underlined by the inner variations of β_{th}, corroborate the stability of the ion temperatures and electron density measured experimentally with the Thomson scattering diagnostic. Finally, our calculation of the reconnection rate over time shows an efficient conversion of the magnetic energy in the sheet, especially when the plasmoids are established in the sheet, nurturing the plasma heating and the particle kinetic energy. This observation is general and does not depend on whether a guide field is present. Therefore, even if the presence of a guide field in an elongated current sheet does influence the regime changes and impact the formation of plasmoids, it does not affect the efficiency of such a process. Furthermore, a value of the reconnection rate close to $R \sim 0.1$ is typical of the measurements made in astrophysical events where magnetic reconnection intervenes.

This numerical study focusing on the kinetic aspects of the current sheet is also interesting as it underlines the role of kinetic effects in the evolution of the reconnection process. In particular, it was shown in this chapter that the plasmoid-driven regime can be initiated for a Lundquist number that is smaller than the MHD expectations. Consequently, it would be interesting to further investigate these kinetic aspects through future studies, such as focusing on particle acceleration through the current sheet and once again compare cases where a guide field is present or not.

Overall, we provided here a description of the evolution of the sheet, both in experimental conditions and theoretically within the kinetic framework. We succeeded in building an experimental setup to observe plasmoids and regime changes in the elongated current sheet, using self-generated Biermann battery magnetic fields. The numerical simulations enabled us to detail the kinetic aspects involved in the variations of the current sheet, the plasma characteristics and the evolution of the reconnected magnetic field. Finally, several diagnostics, both experimental

like proton radiography or numerical, like the 2D Fourier transform, permitted to cross the different results to highlight their relevancy.

References

[1] P. Nilson *et al*., « Magnetic reconnection and plasma dynamics in two-beam laser-solid interactions », Phys. Rev. Lett., volume 97, 25, 255001, (December 2006).
https://doi.org/10.1103/PhysRevLett.97.255001

[2] A. Bott, C. Graziani, P. Tzeferacos *et al.*, « Proton imaging of stochastic magnetic fields », Journal of Plasma Physics, Volume 83, Issue 6, (Decembre 2017).
https://doi.org/10.1017/S0022377817000939

[3] C.A.J. Palmer *et al.*, "Field reconstruction from proton radiography of intense laser driven magnetic reconnection", Phys. Plasmas, Volume 26, Issue 8 (Août 2019).
https://doi.org/10.1063/1.5092733

[4] Y.M. Huang, L. Comisso and A. Bhattacharjee, « Plasmoid instability in evolving current sheet and onset of fast reconnection », The Astrophysical Journal, Volume 849, 2 (November 2017).
https://doi.org/10.3847/1538-4357/aa906d

[5] S. Bolanos *et al*, « Laboratory evidence of magnetic reconnection hampered in obliquely interacting flux tubes », Nature Communications, Volume 13 (October 2022).
https://doi.org/10.1038/s41467-022-33813-9

[6] S. Majeski *et al*, « Guide field effects on the distribution of plasmoids in multiple scale reconnection », Phys. Plasmas, Volume 28 (September 2021).
https://doi.org/10.1063/5.0059017

[7] H.K. Chung *et al*, « FLYCHK: Generalized population kinetics and spectral model for rapid spectroscopic analysis for all elements », High Energy Density Physics, Volume 1 (2005).
https://nlte.nist.gov/FLY/ (website still available in April 2026).
https://dx.doi.org/10.18434/T4WS3G

[8] D.H. Froula *et al*, Plasma Scattering of Electromagnetic Radiation: Theory and measurement techniques, Academic Press (2011).
https://doi.org/10.1016/C2009-0-20048-1

[9] R. Numata and N.F. Loureiro, « Electron and ion heating during magnetic reconnection in weakly collisional plasmas », Journal of Plasma Physics, Volume 81, 2 (November 2014).
https://doi.org/10.1017/S002237781400107X

[10] L. Chengming, « Observations of electron secondary reconnection in magnetic reconnection front », EGU General Assembly, EGU24-8525 (April 2024).
https://doi.org/10.5194/egusphere-egu24-8525

[11] Q-L. Dong *et al*, « Plasmoid ejection and secondary current sheet generation from magnetic reconnection in laser-plasma interaction », Phys. Rev. Lett, Volume 108, 215001 (May 2012).
https://doi.org/10.1103/PhysRevLett.108.215001

[12] Y.D. Yoon *et al*, « Enablement or suppression of collisionless magnetic reconnection by the background plasma beta and guide field », Geophysical Research Letters, Volume 51 (November 2024).
https://doi.org/10.1029/2024GL112126

[13] H. Ji *et al*, « Study of magnetic reconnection at low- β using laser-powered capacitor coils », Phys. Plasmas, Volume 31 (October 2024). https://doi.org/10.1063/5.0223922

Chapitre 7

General conclusion and perspectives

This thesis is anchored in the study of magnetic field rearrangements occuring during plasma interactions relevant for astrophysics. Electromagnetic fields in space plasmas are ubiquitous across every scale of the Universe and play a key role in energy transfers as well as in the energization and acceleration of charged particle flows, especially during interactions between plasma systems. Currently, modern spacecrafts and both direct or indirect observations are able to detect variations of magnetic fields and plasma flows, mostly in the ISM nearby the Earth and within the Solar System. Indeed, it is possible to detect *in situ* magnetic interactions, more particularly involving the magnetosphere of the planet. However, these observation devices are limited by their very own technologies and instruments. Even nowadays, direct observations of plasma interactions remain quite rare, as these specific phenomena are usually spatially and temporally localized, which makes them difficult to predict.

The purpose of this work for laboratory astrophysics is to design experimental setups in order to generate artificially in laboratory plasmas with equivalent dynamics and characteristics to their space counterparts. The development of the high-power laser technology has permitted the conception and the use of high-power lasers to generate dense plasmas in the laboratory via laser-matter interaction. Consequently, studying laser-driven plasmas analogue to space plasmas erases the scale constraints that are encountered in space *in situ* observations and measurements. Besides, a controlled experimental setup provides repeatatibility, which is not achievable in space conditions.

In this work, we showed how we built successful experimental setups to study two specific mechanims of plasma interactions that are magnetic compression and magnetic reconnection. We adapted our experimental parameters and diagnostics to capture and measure all the main physical quantities to provide a complete experimental description of the phenomena. In both cases, we focused on plasmas magnetized by the Biermann battery effect, inducing a self-generated magnetic field, with no external sources of magnetic field.

These configurations allow to prove that it is possible to observe the main characteristics of magnetic compression in the laboratory. As a result, we measured experimentally the saturation of the accumulated compressed field in the compression zone between two independant magnetic fields advected by counter propagating and free expanding plasmas. We installed adapted experimental diagnostics to track every aspect of the interaction, such as the evolution of the density or the variations of temperature. These different diagnostics gave complementary results which permitted to characterize precisely the observed process. All our experimental results were supported and completed with numerical simulations, in both MHD and kinetic frameworks, respectively with FLASH and SMILEI. This double-sided numerical study covered the entirety of the mechanims involved in magnetic compression, and allowed us to build a complete representation of the process. Not only do the simulations support our experimental conclusions but also, we managed to describe the energy conversions and the regime changes underwent by the plasma entering the compression zone. We highlighted how the energy repartition in the compression sheet induces the saturation of the process, which are the inner mechanisms of the plasma interaction that contribute to reduce to quantity of plasma flow in the compression sheet, and how it also leads to the stabilization of the process.

Through this study, we confirm the effective saturation of the amplitude of the compressed magnetic field, as it has already been measured in space. Moreover, the laser-driven plasma generated in the laboratory as well as the compressed plasma in the zone of interaction present characteristic parameters similar to those measured in space events. Consequently, our work fulfills the main aim of the laboratory astrophysics experiment, as in our case it is relevant for the study of plasma interactions and magnetic compression in space. Finally, with our PIC numerical setup, we were able to adapt the different parameters of the compression in experimental conditions in order to give an insight of the behavior of the compressed plasma from a classical to a relativistic regime. Indeed, here we went further than the experimental limits by simulating plasmas closer to the relativistic regime to highlight the variations of the topology of the compressed magnetic field. As a consequence, we provide here an insight in the dynamics of the compression of relativistic plasmas magnetized with Biermann battery. Therefore, it would be particularly interesting to delve further into the study of magnetic compression. With future experimental campaigns joined to theoretical models, we would be able to estimate in more details the role of each parameter, like the initial magnetic field amplitude, the plasma density or the plasma incoming velocity, on the evolution of the compression process and on the maximum value of the compression rate. Then, it would be possible to draw predictions of the behaviour of the compressed plasma in different situations. Moreover, experimental diagnostics permitting the measurement of the dissipation of the energy accumulated in the compression sheet would be interesting too, in order to address possible mechanisms of energy conversion once the compression process is over and once the compression sheet is not alimented with incoming plasma anymore. Finally, the configuration we used in the laboratory can lead to future experimental campaigns, this time generating laboratory plasmas with high-intensity lasers that are now available in various facilities in the world.

Our study of magnetic reconnection enables us to provide the first observation in the laboratory of the formation and the evolution of the plasmoid-dominated regime in a current sheet during magnetic reconnection. If previous experiments already focused on magnetic reconnection, they were mainly investigating the single X-point configuration of magnetic reconnection. Here, we demonstrated how to study experimentally the elongated and large aspect ratio reconnection sheet configuration. We proved therefore that the formation and the evolution of plasmoids are

likely to occur in between plasmas exclusively magnetized by the Biermann battery effect and observable in the framework of laboratory astrophysics.

We detailed the main stages of magnetic reconnection and the different regimes that shape the current sheet overtime. Experimental diagnostics allowed to capture the temporal evolution of the reconnection process as well as the variation of quantities such as the temperature or the density within the current sheet. Our experimental observations allowed us to identify the specific stages of evolution of the reconnection process in the current sheet, which depend on its internal dynamic. We managed to track the formation and the temporal evolution of the plasmoid chains following the disruption of the large aspect ratio current sheet, and we also detected the particle ejections resulting from the dynamic of the plasmoids regime by measuring the temperature and density variations, as well as the plasma emissivity. The introduction of an out-of-plane guide field, introduced artificially during the experimental campaign by steping out of the coplanar target configuration, permitted to observe the effect of a remaining magnetic field in the current sheet and the consequences on the evolution of the reconnecting process in the case where the incoming charged particles entering the sheet with the plasma flows stay partially magnetized. Once again, the target configurations used to introduce a guide field were designed with the astrophysical relevance of our work in mind. Indeed, the events in space in which magnetic reconnection is verified or likely to take place imply multiple and diverse configurations between the interacting plasmas. The coplanar setting is then an ideal configuration which is not predominant. Consequently, the guide field is supposed to interviene in many reconnection processes, so our experimental setup tends to recreate a more universal configuration to match the astrophysical context.

PIC simulations with SMILEI were performed to complete the study conducted during the experiment. Here, we set the parameters measured in the experiment to bring a theoretical support to the experimental observations. With SMILEI 2D simulations, we showed the same evolution and regime changes over time in the current sheet, underlining the collisionless aspect of magnetic reconnection and the kinetic aspects involved in the process. By setting guide fields, analogue to their experimental counterparts, we investigated the effects of the magnetic field within the sheet by measuring directly the evolution of physical quantities, like the current density, and of characteristic plasma parameters in the sheet, such as the β_{th} ratio or the reconnection rate R. We exhibited that a remaining magnetic field does alter the general evolution of the current sheet, in particular by stabilizing the sheet with a reduction of the inner instabilities and assisting the transport of the charged particles that remain magnetized during the interaction. However, the reconnection process and the global energy exchanges are not impacted, as it is evidenced by the similar aspects of the different reconnection rates for each configuration.

Finally, we showed that the reconnection mechanism can be suject to radical changes during the process within the current sheet, as we exhibit that β_{th} can be high in the stable regimes or within the confined particles in plasmoids but remains low outside of these magnetic structures. Indeed, during the plasmoid-driven regime, PIC results demonstrated that, outside the plasmoids which gather particles while heating the plasma, the current sheet in between presents a low β_{th} ratio such as $\beta_{th} < 1$, meaning that in the same regime, the sheet can be dominated by the thermal pressure of the charged particles, especially the electrons, inside the plasmoids and governed by the reconnecting magnetic field outside and around the reconnection sites. This dynamic has been observed with and without the presence of a guide field.

Both our experimental and theoretical works on magnetic reconnection are anchored in the framework of laboratory astrophysics, similarly to our study of magnetic compression. In both

cases, we study magnetic field interactions by only relying on Biermann battery self-generated fields. With this work, we provide an efficient experimental setup to the study of the formation and the evolution plasmoid-driven regime in elongated current sheet for magnetic reconnection, whose kinetic aspects are supported and validated by PIC simulations. Also, we observed, both experimentally and theoretically through our simulations, phenomena that deserve to be investigated further and which are respectively the second reconnection sheet that appears orthogonal to the main one and particle acceleration out of the current sheet.

Furthermore, the different mechanisms detailled in this work also bring perspectives in the studies of magnetized plasmas generated for magnetic confinement fusion researches. Fusion is a current ever-growing field of research which can be bonded inherently with laboratory astrophysics laser-driven experiments. Indeed, beyond the fundamental aspects of the study of magnetic field interactions such as compression and reconnection in space plasmas, these mechanisms are also already encountered in fusion plasmas and consist in a subject of study, as they play crucial roles in the energization and the heating of plasmas in fusion experiments. In magnetically confined plasma experiments for fusion, such as in tokamaks, compression and reconnection can influence directly energy transport, like in laboratory astrophysics observations, as well as the confinement properties of the plasmas and the particles, as we showed these processes are sources of particle acceleration. Also, it is interesting to mention that the formation of compression and reconnection sheets has already been observed in fusion-related works.

As a result, our work on the temporal evolution of the magnetic compression and reconnection in elongated sheet can support futur experimental studies, both in laboratory astrophysics and fusion researches. Consequently, the entirety of this work, in both its experimental and theoretical aspects, contributes to a better understanding of the interactions in between magnetized plasmas at various scales and their impact on their environment.

List of figures

Chapter 1

FIGURE 1. PANNEL OF EXAMPLES OF THE VISIBLE MATTER PRESENT UNDER DIFFERENT FORMS IN THE UNIVERSE [7]. TOP LEFT : STELLAR ERUPTION AND EJECTION OF CORONAL MASS. TOP RIGHT : GAS CLOUD, PLACE OF HIGH STELLAR FORMATION RATE [8]. BOTTOM LEFT : SUPERNOVAE REMNANT HOSTING A WHITE DWARF IN ITS CORE. THE EJECTA ARE A PLACE OF TURBULENCES AND INSTABILITIES [9]. BOTTOM RIGHT : GALAXIES CONCENTRATE THE MATTER IN THE UNIVERSE AND ARE ORGANISED IN SUPERAMAS [10]. 2

FIGURE 2. CHARACTERIZATION OF THE DIVERSITY OF HED PLASMAS IN SPACE IN A TEMPERATURE-DENSITY-DIAGRAM [26]. THE HED PLASMAS ARE LOCATED OVER THE BLACK ISOBAR LINE, THE WARM DENSE MATTER (WDM) AND HOT DENSE MATTER (HDM) ARE REPRESENTED BY AREAS IN THE CENTER OF THE GRAPH..... *5*

FIGURE 3. ILLUSTRATION OF THE « FROZEN-IN-FLOW » MAGNETIC FIELD APPROXIMATION. THIS SHOWS THAT THE MAGNETIC FLUX GOING THROUGH S(T1) AND S(T2) IS THE SAME [37]. *9*

FIGURE 4. PROPERTIES OF DIFFERENT LASER FACILITIES IN THE WORLD, PRESENTING HIGH-POWER AND HIGH-INTENSITY LASERS. THIS IS A SELECTION AMONG THE DIFFERENT LASER INSTALLATIONS IN THE WORLD, ALL WITH SPECIFIC BEAM CHARACTERISTICS. TO EASE THE LECTURE, WE ONLY SHOW HERE THE FACILITIES WHERE THE AUTHOR PARTICIPATED IN EXPERIMENTS DURING THE THESIS. THE LASERS DESCRIBED IN THE PRESENT MANUSCRIPT AND USED FOR THE THESIS RESEARCHES ARE MARKED IN ORANGE..... *14*

FIGURE 5. HISTORY OF LASER INTENSITY, SHOWING THE PROGRESS ACCELERATION MADE POSSIBLE WITH THE CPA AND THE DIFFERENT REGIMES AVOILABLE [61]. *15*

FIGURE 6. PLASMA ABLATION BY LASER-MATTER INTERACTION ACHIEVABLE IN LABORATORY [66]. *17*

FIGURE 7. MODELING OF THE BIERMANN BATTERY EFFECT IN LASER-DRIVEN PLASMA. (A) SCHEMATIZATION OF THE LASER-MATTER INTERACTION INDUCING GRADIENTS OF ELECTRON DENSITY NE AND TEMPERATURE TE DURING THE PLASMA EXPANSION. THE ROTATION AXIS OF THE TOROIDAL MAGNETIC FIELD IS REPRESENTED BY THE OUT-OF-PLANE VECTORS. (B) KINETIC SIMULATIONS [68] SHOWING THE SPATIAL EVOLUTION OF THE DENSITY AND TEMPERATURE GRADIENTS, AND CONSEQUENTLY THE DEVELOPMENT OF THE OUT-OF-PLANE TOROIDAL MAGNETIC FIELD. 17

Chapter 2

FIGURE 8. SCHEMATIZATION OF THE MAGNETIC COMPRESSION MECHANISM IN THE COMPRESSION ZONE BETWEEN TWO MAGNETIZED PLASMAS. THE FIELD LINES ARE REPRESENTED BY THE THIN BLACK ARROWS, ORIENTED ALONG THE Y-AXIS. A CLOSE-UP OF THE COMPRESSION ZONE SHOWS THE FIELD LINES BEFORE AND AFTER THE INTERACTION

BETWEEN THE TWO PLASMAS THAT INDUCES THE COMPRESSION. THE INFLOWS OF PARTICLES BROUGHT IN BY THE PLASMAS IN THE COMPRESSION AND THEIR MOTION ARE REPRESENTED BY THE LARGE SYMMETRICAL ARROWS FOLLOWING THE X-AXIS. 30

FIGURE 9. SCHEME OF THE EARTH MAGNETOSPHERE (A) [10] AND REPRESENTATION OF THE INTERACTION BETWEEN THE MAGNETIC FIELD OF THE SOLAR WIND (RED ARROWS) AND THE PLANETARY FIELD (BLUE ARROWS) IN THE CASES WHERE THE IMF FIELD LINES ARE PARALLEL (B) OR PERPENDI CULAR (C) TO THE EARTH FIELD LINES. THE MAGNETOPAUSE IS REPRESENTED BY THE THICK GREEN LINE AND THE BOW SHOCK UPSTREAM THE MAGNETOSPHERE BY THE PURPLE LINE. THE PLOTS ARE REPRESENTED IN THE GEOCENTRIC SOLAR MAGNETOSPHERIC (GSM) COORDINATES AND SCALED WITH THE RADIUS OF THE EARTH (R_E) AS A REFERENCE [11]. 32

FIGURE 10. SCHEMES OF THE TWO SITUATIONS IN THE CASE OF THE INTERACTION OF PARTICLES OF DENSITIES N_A, N_B AND VELOCITIES V_A, V_B WITH THE MAGNETIC MIRROR. (A) THE INFLOW PARTICLES, WHOSE TRAJECTORIES ARE MODELED BY THE GREEN LINES, HAVE AN INCIDENT ANGLE $\Theta < \Theta_0$ AND ENTER THE COMPRESSION SHEET. (B) THE INFLOW PARTICLES, WHOSE TRAJECTORIES ARE MODELED BY THE RED LINES, HAVE AN INCIDENT ANGLE $\Theta > \Theta_0$ AND ARE DEFLECTED 36

Chapter 3

FIGURE 11. SCHEMATIZATION OF MAGNETIC RECONNECTION BETWEEN TWO MAGNETIZED PLASMAS. THE FIELD LINES AND THEIR OPPOSED DIRECTIONS ARE REPRESENTED BY THE BLUE AND RED ARROWS, ORIENTED ALONG THE Y-AXIS. THE CONVERGING INFLOWS ARE MODELED BY THE LARGE SYMETRICAL ARROWS FOLLOWING THE X-AXIS. (A) SHOWS THE SYSTEM BEFORE THE BEGIN OF THE RECONNECTION PROCESS, WHEN THE MAGNETIC FIELDS ARE FROZEN IN THE PLASMA FLOWS. (B) REPRESENTED THE BEGINING OF THE PROCESS. CONTRARY TO MAGNETIC COMPRESSION DURING WHICH THE MAGNETIC FLUX ACCUMULATES IN THE INTERACTION REGION, IN MAGNETIC RECONNECTION WE OBSERVE A NEUTRAL ZONE BETWEEN THE PLASMA. (C) CLOSE-UP OF THE RECONNECTED FIELD LINES IN THE RECONNECTION SHEET, INDUCING THE FORMATION OF A CROSSED-MAGNETIC FIELD. 42

FIGURE 12. SOLAR ARCHES AND MAGNETIC RECONNECTION. (A) VISUALIZATION OF A SOLAR ARCH DISTORTED BY THE INTERACTION WITH THE CORONA [7]. A PLASMOID IS GETTING FORMED AS MAGNETIC RECONNECTION IS OCCURING ISIDE OF THE ARCH. (B) SCHEME OF THE SAME PROCESS [8]. *44*

FIGURE 13. SCHEME OF THE EARTH MAGNETOSPHERE. THE ZONE WHERE MAGNETIC RECONNECTION IS THE MOST LIKELY TO HAPPEN (ON DAY SIDE AND WITHIN THE PLASMA SHEET IN THE MAGNETO TAIL) ARE HIGHLIGHTED IN ORANGE [10]. *45*

FIGURE 14. SCHEMATIC VIEW OF THE STRUCTURE OF MAGNETIC RECONNECTION IN (A) AN ISOLATED X-POINT MAGNETIC CONFIGURATION AND IN (B) AN ELONGATED CURRENT SHEET CONSTITUTED BY A SUCCESSION OF MULTIPLE RECONNECTION SITES AND PLASMOIDS. *47*

FIGURE 15. SCHEMATIC REPRESENTATION OF ELECTRON (IN GREEN) AND ION (IN ORANGE) DECOUPLED TRAJECTORIES IN THE CURRENT SHEET. THE ELECTRON DIFFUSION LAYER (LIGHT GREEN) IS MUCH THINNER THAN THE ION ONE (LIGHT ORANGE). THE QUADRIPOLAR

HALL MAGNETIC FIELD B IS REPRESENTED IN BLACK ON EACH SIDES OF THE SEPARATIVE AXIS (BLACK DASHED LINES) AND THE UNIFORM CURRENT DENSITY J_C IN PURPLE. 49

FIGURE 16. MAGNETIC RECONNECTION IN THE PLANE (X0Y). THE SURFACE S THROUGH WHICH WE ESTIMATE THE FLUX IS REPRESENTED IN GREEN IN THE PLANE (Y0Z). *50*

Chapter 4

FIGURE 17. PHOTOGRAPHS OF THE LULI2000 FACILITY. ON THE LEFT : THE LASER HALL WITH THE NORTH AND SOUTH BEAMS. ON THE RIGHT : THE EXPERIMENTAL ROOM N°1 OF THE FACILITY WITH THE TARGET CHAMBER, THE DIAGNOSTICS, THE NORTH AND SOUTH LINES, THE QUANTARAY LASER AND THE BLUE LINE. *56*

FIGURE 18. CLOSE UP SCHEME OF THE DOUBLE TARGETS CONFIGURATION AND THE MAGNETIC FIELDS DISPOSITION FOR COMPRESSION. A) TOP VIEW OF THE DISPOSITIVE (IN THE XY-PLANE). A AND Δ, RESPECTIVELY THE HEIGHT BETWEEN THE TWO TARGETS SURFACES AND THE DISTANCE BETWEEN THE CENTER OF THE TWO FOCAL SPOTS, ARE THE TWO GEOMETRICAL PARAMETERS THAT VARIED DURING THE EXPERIMENT. 57

FIGURE 19. SCHEME OF THE EXPERIMENTAL SETUP USED FOR THE MAGNETIC COMPRESSION EXPERIMENT WITH THE TOP VIEW (A) AND THE SIDE VIEW (B). THE NANOSECOND-LONG LASERS ARE REPRESENTED IN YELLOW (N1 AND N2), THE PICOSECOND LASER IN DARK BLUE, THE THREE TARGETS T1, T2 AND T3 IN LIGHT BLUE AND THE QUANTARAY LASER FOR THE INTERFEROMETRY DIAGNOSTIC IN DARK GREEN. 58

FIGURE 20. SCHEME OF THE TNSA PROTONS DEFLECTION THROUGH THE INTERACTION WITH THE SELF-GENERATED MAGNETIC FIELD ON THE SURFACE OF THE TARGET. THE ORIGINAL UNBOTHERED PROTON TRAJECTORIES (SHOWING THE PROTON PATH WITHOUT MAGNETIC FIELD) ARE MODELED BY THE DOTTED ARROWS AND THE DEFLECTED TRAJECTORIES ARE REPRESENTED BY THE PLAIN ONES. 60

FIGURE 21. RESPONSE CURVES OF THE RCF STACK SHOWING THE ENERGY LEVELS DEPOSITED BY THE INCIDENT PROTONS IN EACH RCF FILM. EACH BRAGG PEAK CORRESPONDS TO A FILM. PROTONS WITH THE LOWEST ENERGY WILL IRRADIATE THE HDV2 FILMS CLOSEST TO THE TARGETS WHILE PROTONS WITH HIGHEST LEVEL OF ENERGY WILL PROPAGATE AND REACH THE EBT3 FILMS AT THE BACK OF THE STACK. 61

FIGURE 22. (A) SCHEME OF THE MACH-ZEHNDER INTERFEROMETER AS IT WAS SETUP DURING THE EXPERIMENT. ALONG THE PATH WITHIN THE INTERFEROMETER, THE BEAM COMING FROM THE LASER PROBE IS COLLIMATED. IT IS BEING FOCUSED BY THE IMAGING LENS UPSTREAM THE CAMERA SO THE INTERFEROGRAM IS ON THE CCD CAPTOR. THE ARMS OF THE INTERFEROMETER ARE ALIGNED IN SUCH A WAY SO THE INTERFEROGRAM APPEARS CORRECTLY ON THE CAMERA. (B) INTERFEROGRAM WITHOUT PERTURBATIONS BEFORE THE SHOT (REFERENCE IMAGE). (C) INTERFEROGRAM A FEW NANOSECONDS AFTER THE SHOT, THE INTERFERENCES ARE DISTORTED BY THE PRESENCE OF THE PLASMA ON THE PROBING ARM. *62*

FIGURE 23. (A) SCHEME OF THE OPTICAL PYROMETRY DIAGNOSTIC AS IT WAS SETUP DURING THE EXPERIMENT. THE LIGHT COMING FROM THE EXPANDING PLASMAS IS DIVIDED BY THE

BEAM SPLITTER SO ONLY HALF OF IT REACHES THE STREAK CAMERA. (B) IMAGE OF THE PLASMA LIGHT EMISSION OBTAINED WITH THE STREAK CAMERA FOR THE CONFIGURATION WHEN BOTH THE TARGETS ARE IRRADIATED BY THE LASER BEAMS TO INDUCE THE COMPRESSION. DURING THIS SHOT, THE DURATION OF APERTURE OF THE STREAK CAMERA WAS 5 NS AND AN OD OF 2,1 WAS PLACED UPSTREAM THE CAMERA ENTRANCE. 63

FIGURE 24. (A) SCHEME OF THE SIDE VIEW OF THE FSSR SETUP WITH THE EXPANDING PLASMA (X-RAYS SOURCE), THE SPHERICAL CRYSTAL ALIGNED ON THE SAME HEIGHT THAN THE TARGET AND THE DETECTOR (IP) BELOW. THE DISTANCE BETWEEN THE CRYSTAL AND THE DETECTOR IS EQUIVALENT TO THE CRYSTAL CURVATURE RADIUS. (B) CLOSE UP IN CAVALIER PERSPECTIVE OF THE IP INSIDE ITS BOX. THE DIFFERENT FILTERS DISPOSED ON THE TOP OF THE BOX ARE NOT REPRESENTED HERE. (C) SCAN OF AN IP OPENED WITH IMAGEJ FOR A SINGLE SHOT WITH THE NORTH BIS BEAM ONLY. 64

FIGURE 25. CLOSE UP SCHEMES OF THE TARGETS AND BEAMS ARRANGEMENT AND THE MAGNETIC FIELDS DISPOSITION FOR RECONNECTION. THE NORTH AND NORTH BIS BEAMS ARE HITTING THE TARGETS ALONG AN AXIS OF SYMMETRY WHICH THE NORMAL AXIS SEPARATING THE TWO TARGETS AND WITH AN INCIDENT ANGLE OF 45° EACH. HERE THE TARGETS ARE COPLANAR. 65

FIGURE 26. SCHEME OF THE EXPERIMENTAL SETUP WITH THE TARGETS REPRESENTED IN LIGHT BLUE, THE TWO NANOSECOND-LONG LASERS IN YELLOW, THE LASER GENERATING THE PROTON BEAM IN DARK BLUE AND THE RCF STACK IN GREEN. THE ANGLE Θ CORRESPONDS TO THE APERTURE ANGLE BETWEEN THE TWO TARGETS AND VARIES FROM SHOT TO SHOT. 66

FIGURE 27. RESPONSE CURVES OF THE RCF STACK SHOWING THE ENERGY LEVELS DEPOSITED IN EACH FILM FROM THE RCF STACK BY PROTONS INITIAL ENERGIES. *67*

FIGURE 28. EXAMPLE OF THE ADAPTATION OF THE MESH AROUND THE TARGET HIT BY THE LASER IN CARTESIAN COORDINATES IN 2D FLASH SIMULATIONS. A) REPRESENTS A COPPER TARGET AT T = 0 NS. THE MESH AROUND THE TARGET IS SMALLER BECAUSE OF THE DIFFERENCE OF DENSITY BETWEEN THE TARGET AND THE VACUUM. B) REPRESENTS THE FIRST STEP OF THE SIMULATION. THE MESH ADAPTED ITSELF AS THE LASER BEAM PROPAGATES AND TARGET STARTS TO BE IONIZED AND THE PLASMA TO EXPAND. 70

FIGURE 29. SCHEME OF THE ADAPTATIVE MESH REFINEMENT PROCESS IN A FLASH SIMULATION [31] SHOWING THE ADAPTATION OF THE DIMENSION OF THE CELLS, SUBDIVIDED BY BLOCKS. THE REFINEMENT PROCESS ENSURES THAT EVERY CELL IN THE COMPUTATIONAL GRID IS SYSTEMATICALLY PROBED AND REFINED. *71*

FIGURE 30. SCHEMATIC ILLUSTRATION OF THE EXPERIMENTAL SETUP FOR THE MAGNETIC COMPRESSION CAMPAIGN WITH THE EXPANDING PLASMA, REPRODUCED AND ADAPTED FOR FLASH IN 2D. THE BLACK BORDER REPRESENTS THE BOX OF THE SIMULATION. *72*

Chapter 5

FIGURE 31. ANALYSES OF THE EXPANSION OF THE PLASMA THROUGH THE INTERFEROMETRY DIAGNOSTIC WITH NEUTRINO AT T = 1 NS AFTER THE BEGINNING OF THE LASER PULSE. A) RAW IMAGE OF THE INTERFEROGRAM DURING THE SHOT AS ITW AS CAPTURED BY THE GOI

CAMERA. THE TARGET IS REPRESENTED BY THE ORANGE DOTTED LINE. B) MAP OF THE CORRESPONDING ELECTRON SURFACE DENSITY OBTAINED FROM THE RAW INTERFEROGRAM WITH NEUTRINO. HERE THE TARGET IS MODELED BY THE BLACK DOTTED LINE. C) MAP OF THE ELECTRON VOLUME DENSITY OBTAINED FROM THE SURFACE DENSITY MAP VIA ABEL INVERSION. THE SECTION OF THE SURFACE DENSITY MAP USED TO INTEGRATE THE DENSITY WITH ABEL INVERSION IS CIRCLED IN BLACK. 81

FIGURE 32. A) ELECTRON VOLUME DENSITY MAP USED FOR THE ESTIMATION OF THE EXPONENTIAL DECAY OF THE SPATIAL EXPANSION OF THE PLASMA. B) PROFILE OF THE ELECTRON DENSITY ALONG THE LINE OF MEASUREMENT, FOLLOWING THE DIRECTION OF PROPAGATION OF THE PLASMA. THE EXPERIMENTAL CURVE CALCULATED ESTABLISHED WITH THE NEUTRINO ANALYSIS (IN BLUE) IS FITTED WITH AN EXPONENTIAL MODEL (DASHED RED CURVE), WHOSE EXPRESSION IS WRITTEN IN THE LEGEND. 82

FIGURE 33. 2D FLASH SIMULATION MODELING THE TEMPORAL EVOLUTION OF THE ELECTRON DENSITY. THE SIMULATED COPPER TARGET IS IRRADIATED BY A 2 NS LONG PULSE WITH A POWER OF P = 1010 W, A WAVELENGTH Λ = 1 MM, A FOCAL SPOT WITH A 25 MM DIAMETER AND A 45° INCIDENCE ANGLE. *83*

FIGURE 34. MEASUREMENT OF THE PLASMA ELECTRON DENSITY PROFILE WITH FLASH AT T = 1 NS. THE WHITE LINE DRAWNON THE ELECTRON DENSITY MAP ON (A) CORRESPONDS TO THE LINEOUT DRAWN ON (B). *83*

FIGURE 35. 2D FLASH SIMULATION OF THE TEMPORAL EVOLUTION OF THE Z-COMPONENT BZ OF THE MAGNETIC FIELD GENERATED BY BIERMANN BATTERY. THE SIMULATED COPPER-MADE TARGET IS IRRADIATED BY A 2 NS LONG LASER BEAM WITH A POWER OF P = 1010 W, A WAVELENGTH Λ = 1 MM, A FOCAL SPOT WITH A 25 MM DIAMETER AND A 45° INCIDENT ANGLE. 84

FIGURE 36. 2D FLASH SIMULATION OF THE TEMPORAL EVOLUTION OF THE ELECTRON TEMPERATURE TE IN EV. THE COPPER-MADE TARGET WAS IRRADIATED WITH A 2 NS LONG LASER BEAM, WITH A POWER OF P = 1010 W, A WAVELENGTH Λ = 1 MM, A FOCAL SPOT WITH A 25 MM DIAMETER AND A 45° INCIDENT ANGLE. *86*

FIGURE 37. TEMPORAL EVOLUTIONS OF BOTH THE AVERAGE ELECTRON TEMPERATURE TE AND ION TEMPERATURE TI MEASURED IN THE CORONA OF THE PLASMA PLUME FOR THE SINGLE TARGET CONFIGURATION. IONS STAY COLDER THAN ELECTRONS BECAUSE MORE ENERGY AND TIME ARE NEEDED TO HEAT THE IONS AT A SIMILAR TEMPERATURE THAN THE ELECTRONS. *87*

FIGURE 38. HIGHLIGHT OF THE MAGNETIC COMPRESSION ON EXPERIMENTAL PROTON RADIOGRAPHY FILMS, ANALYZED BY CONOR FEGAN [7]. (A) PROTON FLUX MEASURED ON RCF AT T = 1,25 NS AFTER THE BEGINNING OF THE LASER PULSE, FOR THE TWO TARGETS CONFIGURATION (THE TWO TARGETS ARE 400 MM AWAY FROM EACH OTHER). (B) CORRESPONDING INTENSITY MAP OF THE PATH-INTEGRATED MAGNETIC FIELD. THE WHITE ARROWS CORRESPOND TO THE LINES OF FIELD IN THE XY-PLAN, THE COLORBAR REPRESENTS THE INTENSITY OF THE FIELD TOWARD THE NORMAL Z-AXIS. BOTH ANALYSES WERE MADE WITH PROBLEM. 88

FIGURE 39. STRUCTURE OF THE ELECTRON DENSITY DURING THE COMPRESSION PROCESS. (A) EXPERIMENTAL INTERFEROGRAM SHOWING THE MAGNETIC COMPRESSION HAPPENING IN BETWEEN TWO TARGETS (SCHEMATIZED BY THE TWO ORANGE DOTED LINES) SEPARATED BY 200 MM. THE MOST DENSE PARTS OF THE PLASMA CORRESPOND TO THE DARK ZONES ON THE INTERFEROGRAM AROUND THE TARGETS. THE INCREASING GRADIENTS OF DENSITY REFRACT THE PROBING LASER BEAM FROM THE INTERFEROMETER UNTIL IT CANNOT BE COLLECTED BY THE IMAGING OPTICS OF THE DIAGNOSTIC ANYMORE. (B) CORRESPONDING FLASH SIMULATION RECREATING THE DOUBLE TARGETS CONFIGURATION AT T = 0,9 NS. THE SAME TILTED STRUCTURE DUE TO THE ACCUMULATION OF THE PLASMA IN THE ZONE IS OBSERVED FOR PARAMETERS SIMILAR TO THE EXPERIMENT. 90

FIGURE 40. LINEOUTS SHOWING THE TEMPORAL EVOLUTION OF OPTICAL PYROMETRY MEASUREMENTS OF PLASMA SELF-EMISSION, INTEGRATED ALONG THE COMPRESSION SHEET NORMAL AXIS, AND INDUCED BY THE PLASMA HEATING IN THE COMPRESSION SHEET IN THE TWO TARGETS CONFIGURATION (WITH COMPRESSION) AND IN THE SINGLE TARGET CONFIGURATION (WITHOUT COMPRESSION). THE INITIAL TIME T = 0 NS CORRESPONDS TO THE BEGINNING OF THE LASER PULSE AND THE IRRADIATION OF THE TARGETS. 91

FIGURE 41. 2D FLASH CARTESIAN SIMULATIONS OF THE EVOLUTION OF THE OUT-OF-PLANE Z-COMPONENT BZ OF THE FIELD, PRESENTING THE EVIDENCE OF THE COMPRESSION OF MAGNETIC FIELDS. (A) ONE TARGET CONFIGURATION SHOWING THE UNPERTURBED EXPANSION OF THE MAGNETIZED PLASMA FROM THE LASER IONIZATION OF THE TARGET (REPRESENTED IN BLACK). (B) TWO TARGETS CONFIGURATION PRESENTING THE FORMATION OF THE COMPRESSION SHEET IN BETWEEN THE TARGETS. 92

FIGURE 42. 1D PROFILES SHOWING THE TEMPORAL EVOLUTION OF THE ACCUMULATED FIELD IN THE COMPRESSION ZONE IN THE FLASH SIMULATIONS. THE 1D PROFILES WERE MADE TAKING THE CENTER OF THE COMPRESSION SHEET AS A REFERENCE, IN BETWEEN THE TWO LASER FOCAL SPOTS ON THE TARGETS. *93*

FIGURE 43. TEMPORAL EVOLUTION OF THE ELECTRONIC DENSITY IN THE CENTER OF THE COMPRESSION ZONE IN THE 2D FLASH SIMULATIONS. *94*

FIGURE 44. TEMPORAL EVOLUTION OF THE MAGNETIC FIELD BZ IN THE COMPRESSION REGION FOR A = B = 200 MM IN THE 2D FLASH SIMULATIONS. AS THE AMPLITUDE OF THE MAGNETIC FIELD VARIES IN THE SHEET, WE CAN ESTIMATE AN AVERAGE AMPLITUDE (RED PLAIN LINE) AS WELL AS THE EXTREMA VALUES (GREY DASHED LINES). 95

FIGURE 45. TEMPORAL EVOLUTION OF THE COMPRESSION RATE IN THE COMPRESSION REGION FOR A = Δ = 200 MM IN THE 2D FLASH SIMULATIONS. AS THE AMPLITUDE OF THE MAGNETIC FIELD VARIES IN THE SHEET, THE AVERAGE RATE (RED PLAIN LINE) CORRESPONDS TO THE AVERAGE AMPLITUDE OF THE FIELD IN THE ZONE WHILE THE EXTREMA (GRAY DASHED LINES) REPRESENT THE LOWEST AND HIGHEST VALUES OF B_Z. 96

FIGURE 46. EVOLUTION OF THE COMPRESSION RATE FOR DIFFERENT A IN 2D FLASH SIMULATIONS, A REPRESENTING THE DISTANCE BETWEEN THE IRRADIATED TARGET SURFACES. THE ERROR BARS CORRESPOND TO THE EXTREMA VALUES OF BZ MEASURED IN THE SHEET DURING THE TIME OF THE SIMULATION. *97*

FIGURE 47. TEMPORAL EVOLUTION OF THE ELECTRON TEMPERATURE MEASURED IN THE FLASH SIMULATIONS IN THE CENTER OF THE COMPRESSION ZONE..... 97

FIGURE 48. MODELING OF THE COMPRESSION SHEET AT T = 12 PS AFTER THE COLLISION BETWEEN THE MAGNETIZED PLASMAS IN 2D SMILEI CARTESIAN SIMULATIONS FOR B0 = 30 T AND V0 = 0.0015C. (A) GENERAL VIEW OF THE COMPRESSION SHEET AND THE AMPLITUDE OF BZ. THE VELOCITIES ARE REPRESENTED BY THE WHITE ARROWS. (B) 1D PROFILE ALONG THE Y-AXIS OF THE AVERAGE ACCUMULATED FIELD IN THE COMPRESSION ZONE. THE PROFILE SHOWED HERE CORRESPOND TO THE WHITE DASHED BOX AS THE CALCULATION WAS MADE OVER THE ENTIRE X-AXIS. (C) 1D PROFILE OF THE FLUCTUATIONS OF B_Z IN THE CORE OF THE SHEET ALONGSIDE THE X-AXIS (WHITE DASHED LINE). 103

FIGURE 49. TEMPORAL EVOLUTION OF THE COMPRESSION PROCESS IN 2D SMILEI SIMULATIONS. (A) GENERAL VIEW OF THE FORMATION AND THE EVOLUTION OF THE COMPRESSION SHEET AND ITS AMPLITUDE BZ. AT T = 4 PS, THE COMPRESSION SHEET IS STILL GETTING FORMED AND IN A TRANSITION STAGE WHILE SINCE T = 7 PS, THE COMPRESSION IS ESTABLISHED AND THE DIMENSIONS OF THE SHEET STAY CONSTANT. (B) PROFILES OF THE AVERAGE ACCUMULATED FIELD IN THE COMPRESSION ZONE. THE PROFILES SHOWED HERE CORRESPOND TO MEASURES OVER THE X-AXIS. 104

FIGURE 50. TEMPORAL EVOLUTION OF THE COMPRESSION RATE IN THE COMPRESSION REGION IN 2D SMILEI SIMULATION FOR B0 = 30 T AND V0 = 0,0015C. AS THE AMPLITUDE OF THE MAGNETIC FIELD IS DIFFUSED AND VARIES IN THE SHEET, THE AVERAGE RATE (RED PLAIN LINE) CORRESPONDS TO THE AVERAGE AMPLITUDE OF THE FIELD IN THE ZONE (PRESENTED ON FIG. 18B)) WHILE THE EXTREMA (GREY DASHED LINES) REPRESENT THE COMMPRESSION RATE FOR THE HIGHEST VALUES OF B_Z MEASURED IN THE SHEET. 105

FIGURE 51. TEMPORAL EVOLUTION OF THE INTERNAL ENERGY OF THE SYSTEM IN 2D SMILEI SIMULATION. THE CUT OFFS OF ENERGY TEND TO A STABLE VALUE (AROUND E = 900 EV), SIGN OF AN EQUILIBRIUM OF THE DYNAMIC OF THE SHEET. 106

FIGURE 52. FORMATION AND TEMPORAL EVOLUTION OF THE COMPRESSION SHEET IN THE BROKEN MIRROR CONFIGURATION IN 2D SMILEI SIMULATIONS FOR B0 = 20 T AND V1 = 0,02C. THE PLASMOIDS ARE FORMED QUICKLY AFTER THE BEGINNING OF THE COMPRESSION DUE TO THE HIGH VELOCITY OF THE INFLOWS. THEY FIRST PRESENT A REGULAR PATTERN BEFORE BEING DISSIPATED. (A) 2D MAP OF THE MAGNITUDE FIELD AMPLITUDE B_Z. (B) 1D PROFILES ALONG THE X-AXIS OF THE CENTER OF THE COMPRESSION SHEET SHOWING THE EVOLUTION OF THE PERIOD OF APPARATION OF THE PLASMOIDS. 109

FIGURE 53. FORMATION AND TEMPORAL EVOLUTION OF THE COMPRESSION SHEET IN A BROKEN MIRROR CONFIGURATION IN 2D SMILEI SIMULATIONS FOR B0 = 20 T AND V0 = 0,05C. THE PLASMOIDS ARE FORMED QUICKLY AFTER THE BEGINNING OF THE COMPRESSION DUE TO THE HIGH VELOCITY OF THE INFLOWS. (A) 2D MAP OF THE MAGNITUDE FIELD AMPLITUDE B_Z. (B) 1D PROFILES ALONG THE X-AXIS OF THE CENTER OF THE COMPRESSION SHEET SHOWING THE EVOLUTION OF THE PERIOD OF APPARATION OF THE PLASMOIDS. 110

FIGURE 54. TEMPORAL EVOLUTION OF BZ IN THE COMPRESSION IN THE BROKEN MAGNETIC MIRROR CONFIGURATION IN 2D SMILEI FOR B0 = 20 T AND V0 = 0,02C. THE TIME INTERVAL WHEN THE ENTER SHEET ENTERS THE BROKEN MAGNETIC MIRROR CONFIGURATION IS HIGHLIGHTED IN GRAY. THIS PERIOD IS CHARACTERIZED BY A PEAK OF THE AVERAGE

COMPRESSION RAGE AND A STRONG COMPRESSED FIELD CONTAINED IN THE PLASMOIDS. 111

FIGURE 55. TEMPORAL EVOLUTION OF BZ IN THE COMPRESSION IN THE BROKEN MAGNETIC MIRROR CONFIGURATION IN 2D SMILEI SIMULATIONS FOR (A) B0 = 20 T AND FOR (B) B0 = 50 T. IN BOTH WE HAVE V2 = 0,05C. THE TIME INTERVALS WHEN THE ENTER SHEET ENTERS THE BROKEN MAGNETIC MIRROR CONFIGURATION ARE HIGHLIGHTED IN BEIGE. 112

FIGURE 56. COMPARISON OF THE DOMINANT MODES OF THE BROKEN MAGNETIC MIRROR IN 2D SMILEI SIMULATIONS FOR THE TWO DIFFERENT VELOCITIES V1 = 0,02C AND V2 = 0,05C, AND FOR B0 = 20 T. *113*

FIGURE 57. COMPARISON OF THE COMPRESSION SHEET FOR THE THREE DIFFERENT VELOCITIES IN 2D SMILEI SIMULATIONS, FOR B0 = 20 T AT (A) T = 10,5 PS AND (B) T = 17 PS, SHOWING THE TEMPORAL EVOLUTION OF THE TOPOLOGY OF THE SHEET WHETHER IT WENT THROUGH ONE OR SEVERAL BROKEN MAGNETIC MIRROR PHASE OR NOT. *114*

Chapter 6

FIGURE 58. EXPERIMENTAL RCFS PRESENTING THE TIME EVOLUTION OF THE MAGNETIC RECONNECTION FIGURE. A VOLUNTARY CLOSE-UP HAS BEEN MADE ON THE FILMS TO FOCUS ON THE EVOLUTION OF THE CURRENT SHEET BETWEEN THE PLASMAS. THE TIMES INDICATED ON THE UPPER LINE CORRESPOND TO THE DELAY BETWEEN THE START OF THE TARGET IONISATION AND THE TNSA PROTON BEAM. HERE WE DO NOT TAKE INTO ACCUNT THE PROTON TIME OF FLIGHT TO REACH THE DIFFERENT RCFS IN THE STACK. THE ENERGIES E_P CORRESPOND TO THE PROTON ENERGY RANGES DETECTED BY THE RCFS IN THE STACK DESCRIBED IN 4.1.3.2.2. (SEE FIGURE 11). 121

FIGURE 59. EXPERIMENTAL RCFS OF TWO DISTINCT SHOTS IN THE SAME CONDITIONS AT T = 4,3 NS SHOWING THE REPEATABILITY OF THE PLASMOID OCCURRENCE IN THE ELONGATED SHEET CONFIGURATION. FOR THE SHOT REPRESENTED ON THE RIGHT, A VOLUNTARY CLOSE-UP WAS MADE DURING THE EXPERIMENT BY PUTTING THE RCF STACK CLOSER TO THE TARGETS TO INCREASE THE MAGNIFICATION AND ZOOM OUT ON THE CURRENT SHEET. 122

FIGURE 60. ANALYSES OF THE RCF SHOWED IN FIGURE 1AT EP = 8 MEV WITH PROBLEM. COLUMN (A) : SCANS OF THE RAW EXPERIMENTAL RCSF USED TO TRACK THE TEMPORAL EVOLUTION OF THE RECONNECTION. THE RED SQUARES CORRESPOND TO THE PART OF THE RCF WHERE A GAUSSIAN BLUR WAS APPLIED FOR THE ANALYSIS. THE TIMES ON THE LEFT CORRESPOND TO THE DELAY BETWEEN THE START OF THE TARGET IONISATION AND THE TNSA BEAM PULSE. COLUMN (B) : CORRESPONDING MAPS OF PROTON FLUX. COLUMN (C) : CORRESPONDING INTENSITY MAPS OF THE PATH-INTEGRATED MAGNETIC FIELD. THE WHITE ARROWS CORRESPOND TO THE FIELD LINES IN THE XY-PLAN, THE COLOR BAR REPRESENTS THE INTENSITY OF THE FIELD TOWARD THE NORMAL Z-AXIS. 123

FIGURE 61. CLOSE-UP AT T = 4,5 NS OF THE CURRENT SHEET IN THE PLASMOID REGIME SHOWED BY (A) THE RAW RCF, (B) THE MAP OF PROTON FLUX AND (C) THE MAP OF THE PATH-INTEGRATED MAGNETIC FIELD. THE FILM CORRESPONDS TO AN ENERGY RANGE OF EP = 8 MEV. *124*

FIGURE 62. EXPERIMENTAL RCFS FOR EACH TARGET CONFIGURATION. A VOLUNTARY CLOSE-UP HAS BEEN MADE ON THE FILMS TO FOCUS ON THE EVOLUTION OF THE CURRENT SHEET BETWEEN THE PLASMAS. THE TIMES INDICATED ON THE UPPER LINE CORRESPOND TO THE DELAY BETWEEN THE START OF THE TARGETS IONISATION AND THE TNSA PROTON BEAM. NO MEASURE WAS PERFORMED AT T = 1 NS FOR Θ = 15° AS THE RECONNECTION IS TOO SLOWED DOWN BY THE OUT-OF-PLANE FIELD B_Z IN THIS SPECIFIC CASE. 126

FIGURE 63. ANALYSIS OF THE RCFS WITH PROBLEM IN THE CONFIGURATION WITH Φ = 15°. COLUMN (A) : SCANS OF THE RAW EXPERIMENTAL RCFS USED TO TRACK THE TEMPORAL EVOLUTION OF THE RECONNECTION. THE RED SQUARES CORRESPOND TO THE PART OF THE RCFS WHERE THE GAUSSIAN BLUR WAS APPLIED FOR THE ANALYSIS. THE TIMES ON THE LEFT CORRESPOND TO THE DELAY BETWEEN THE START OF THE TARGET IONISATION AND THE TNSA BEAM PULSE. THE FILMS ALL CORRESPOND TO AN ENERGY RANGE OF E_P = 8 MEV. FOR THE SHOTS AT T = 3 NS AND T = 4,3 NS, A VOLUNTARY CLOSE-UP WAS MADE TO INCREASE THE MAGNIFICATION AND ZOOM OUT ON THE CURRENT SHEET. COLUMN (B) : CORRESPONDING MAPS OF PROTONS FLUX. COLUMN (C) : CORRESPONDING INTENSITY MAPS OF THE PATH-INTEGRATED MAGNETIC FIELD. 127

FIGURE 64. ANALYSIS OF THE RCFS WITH PROBLEM IN THE CONFIGURATION WITH Φ = 30°. COLUMN (A) : SCANS OF THE RAW EXPERIMENTAL RCFS USED TO TRACK THE TEMPORAL EVOLUTION OF THE RECONNECTION. THE RED SQUARES CORRESPOND TO THE PART OF THE RCFS WHERE THE GAUSSIAN BLUR WAS APPLIED FOR THE ANALYSIS. THE TIMES ON THE LEFT CORRESPOND TO THE DELAY BETWEEN THE START OF THE TARGET IONISATION AND THE TNSA PROTON BEAM. THE FILMS ALL CORRESPOND TO AN ENERGY RANGE OF E_P = 8 MEV. COLUMN (B) : CORRESPONDING MAPS OF PROTONS FLUX. COLUMN (C) : CORRESPONDING INTENSITY MAPS OF THE PATH-INTEGRATED MAGNETIC FIELD. 128

FIGURE 65. SPATIAL EVOLUTION OF THE PLASMA DURING THE IMPULSION. THE VALUE OF THE CHARACTERISTIC LENGTH FOR EACH DOT HAS BEEN CALCULATED FROM THE VOLUME ELECTRON DENSITY MAP BY ANALYSING THE CORRESPONDING INTERFEROGRAM. *129*

FIGURE 66. TEMPORAL LINEOUTS OF OPTICAL PYROMETRY MEASUREMENTS INTEGRATED TOWARD THE Z-AXIS OF PLASMA SELF-EMISSION AS A FUNCTION OF TIME, INDUCING THE PLASMAS HEATING OF THE RECONNECTION REGION FOR COPLANAR TARGETS IN THE 2 BEAMS CONFIGURATION (RECONNECTION OCCURING, TWO SHOTS ARE SHOWN FOR REPRODUCIBILITY) AND IN THE 1 BEAM CONFIGURATION (NO RECONNECTION). THE STARTING TIME T = 0 NS CORRESPONDS TO THE START OF THE LASER IRRADIATION OF THE TARGETS. 130

FIGURE 67. TEMPORAL LINEOUTS OF OPTICAL PYROMETRY MEASUREMENTS INTEGRATED TOWARD THE Z-AXIS OF PLASMA SELF-EMISSION AS A FUNCTION OF TIME, INDUCING THE PLASMAS HEATING OF THE RECONNECTION REGION FOR THE THREE DIFFERENT TARGET CONFIGURATION. THE COPLANAR CONFIGURATION IS REPRESENTED BY THE GRAY CURVE, THE TARGETS TILTED BY AN ANGLE OF 15° AND 30° ARE REPRESENTED RESPECTIVELY BY THE BLUE AND ORANGE CURVES. THE STARTING TIME T = 0 NS CORRESPONDS TO THE START OF THE LASER IRRADIATION OF THE TARGETS. 132

FIGURE 68. 2D CARTESIAN SMILEI SIMULATIONS OF THE EVOLUTION OF THE ELONGATED CURRENT SHEET AND LARGE ASPECT RATIO A ~ 10. THE SIMULATION PARAMETERS ARE SET TO THE EXPERIMENTAL MEASUREMENTS. A) TEMPORAL EVOLUTION OF THE Z-AXIS COMPONENT OF THE CURRENT DENSITY J, SHOWING THE DIFFERENT STAGES OF THE

CURRENT SHEET, INCLUDING ITS FRAGMENTATION AND THE FORMATION OF PLASMOIDS. B) TEMPORAL EVOLUTION OF THE HALL MAGNETIC FIELD IN THE CURRENT SHEET B_{HALL}, ORIENTED TOWARD THE Z-AXIS AND ORTHOGONAL TO THE RECONNECTION PLANE. 137

FIGURE 69. 2D CARTESIAN SMILEI SIMULATIONS SHOWING THE EVOLUTION OF THE CURRENT SHEET IN THE PLASMOID REGIME WITHIN SHORT TIME INTERVALLE BY REPRESENTING THE FLUCTUATIONS OF THE Z-COMPONENT OF THE CURRENT DENSITY JZ, THE RECONNECTING COMPONENT OF THE MAGNETIC FIELD BY AND THE HALL MAGNETIC FIELD IN THE CURRENT SHEET B_{HALL}, ORIENTED TOWARD THE Z-AXIS AND ORTHOGONAL TO THE RECONNECTION PLANE. 138

FIGURE 70. 2D CARTESIAN SMILEI SIMULATIONS SHOWING THE EVOLUTION OF JZ IN THE CURRENT SHEET IN THE PRESENCE OF AN OUT-OF-PLANE GUIDE FIELD BZ ALONG THE Z-AXIS, SUCH AS A) BZ / B0 = 0,26 AND B) BZ / B0 = 0,5. HERE, WE HIGHLIGHT THE INFLUENCE OF THE GUIDE FIELD ON THE DYNAMICS OF THE CURRENT SHEET, MORE PARTICULARLY THE TRANSITION FROM THE STABLE REGIME TO THE FORMATION AND ESTABLISHMENT OF PLASMOIDS WHICH DIFFERS FROM THE COPLANAR CASE WITHOUT GUIDE FIELD. *140*

FIGURE 71. A-D) 1D PROFILES OF BTH OVER TIME MEASURED ON 2D CARTESIAN SMILEI SIMULATIONS FOR THE COPLANAR TARGET CONFIGURATION, MEASURED IN THE CENTER OF THE CURRENT SHEET (CORRESPONDING TO THE MIDDLE OF THE SIMULATION DOMAIN FOLLOWING THE LONGITUDINAL DIMENSION). THE PROFILES OF B_{TH} SHOW SUCCESSIVELY THE STABLE REGIME OF RECONNECTION (A), THE FORMATION OF TEARING INSTABILITIES IN THE SHEET (B) AND THE PLASMOID-DRIVEN REGIME (C – D). E) TEMPORAL EVOLUTION OF B_{TH} AVERAGED WITH TIME ON THE TOTALITY OF THE CURRENT SHEET. 142

FIGURE 72. COMPARISON OF THE TEMPORAL EVOLUTION OF BTH AVERAGED WITH TIME ON THE TOTALITY OF THE CURRENT SHEET IN 2D CARTESIAN SMILEI SIMULATIONS FOR THE THREE CONFIGURATIONS, WITH GUIDE FIELD (Φ = 15° AND Φ = 30°) AND WITHOUT GUIDE FIELD (Φ = 0°). THE ORDINATE AXIS HAS BEEN SET ON LOGARITHMIC SCALE TO HIGHLIGHT THE VARIATIONS OF $<B_{TH}>$. 144

FIGURE 73. COMPARISON OF THE SPATIAL 2D FOURIER TRANSFORMS USING THE 2D CARTESIAN SMILEI SIMULATIONS FOR THE THREE CONFIGURATIONS. THE SPATIAL FOURIER TRANSFORMS PRESENT EACH TWO AXIS OF SYMETRY, ALONG Ω = 0 AND KY = 0. THE TOTALITY OF THE TRANSFORMS ARE NOT REPRESENTED ; HERE WE CHOSE TO FOCUS ON THE QUARTER WHERE $\Omega > 0$ AND $K_Y > 0$. 144

FIGURE 74. COMPARISON OF THE TEMPORAL EVOLUTION OF THE RECONNECTION RATE R WITH TIME ON THE TOTALITY OF THE CURRENT SHEET IN 2D CARTESIAN SMILEI SIMULATIONS FOR THE THREE CONFIGURATIONS, WITH AND WITHOUT GUIDE FIELD. *146*

List of tables

Chapter 1

TABLEAU 1. EXAMPLES OF PHYSICAL QUANTITIES IN A HED REGIME WITH A PRESSURE OF 1 MBAR [62]. *16*

Chapter 4

TABLEAU 2. SUMMARY OF THE DIFFERENCES OF THE TWO DESCRIPTION AND OF THE COMPLEMENTARITY OF THE TWO STUDY. *74*

Chapter 5

TABLEAU 3. COMPARISON OF THE SOUND AND ALFVEN NUMBERS RELATED PLASMA PARAMETERS IN THE EXPANDING PLASMA AND INSIDE THE COMPRESSION SHEET IN 2D FLASH SIMULATIONS. *99*

TABLEAU 4. COMPARISON OF PLASMA PARAMETERS IN THE MHD FRAMEWORK IN THE EXPANDING PLASMA AND INSIDE THE COMPRESSION SHEET IN 2D FLASH SIMULATIONS. *99*

TABLEAU 5. COMPARISON OF SELECTED PLASMA PARAMETERS ADAPTED FROM SLADKOV ET AL, IN THE CASE OF MAGNETIC COMPRESSION FOR INTERACTION BETWEEN CMES (ASTROPHYSICAL REFERENCE), FOR THE EXPERIMENTAL LASER-DRIVEN PLASMAS AND FOR THE PLASMAS WITH 2D FLASH SIMULATION. *100*

Chapter 6

TABLEAU 6. SUMMARY OF THE MAIN PLASMA PARAMETERS IN THE CURRENT SHEET. THE PLASMA DENSITY, THE AVERAGE IONIZATION LEVEL AND THE ELECTRON TEMPERATURE WERE MEASURED EXPERIMENTALLY WITH THE APPROPRIATE DIAGNOSTIC ; THE REST OF THE PARAMETERS WERE CALCULATED WITH THE EXPERIMENTALLY MEASURED QUANTITIES. THESE PARAMETERS REPRESENT THE CHARACTERISTICS OF THE SHEET IN THE STABLE REGIME. *134*

Publications

Magnetic compression

- **T. Waltenspiel**, J. Fuchs, P. Antici and E. d'Humières, « Numerical study of the saturated compression of self-generated magnetic fields in laser-driven plasmas relevant for Astrophysics » (Article in the submission process to MRE).
- A. Sladkov, C. Fegan, W. Yao, A.F.A. Bott, S.N. Chen, H. Ahmed, E.D. Filippov, R. Lelièvre, P. Martin, A. McIlvenny, **T. Waltenspiel** *et al,* « Saturation of the compression of two interacting magnetized toroidal plasmas evidenced in the laboratory », Nature Communications, 15 (November 2024). https://doi.org/10.1038/s41467-024-53938-3

Magnetic reconnection

- A. Sladkov, **T. Waltenspiel** *et al*, « Laboratory evidence of electron pressure anisotropy driving plasmoid mediated magnetic reconnection » (Article in the submission process to MRE).

Contributions to other studies

- W. Yao, I. Cohen, P. Suarez Gerona, H. Ahmed, A.F.A. Bott, S.N. Chen, M. Cook, R. Lelièvre, P. Martin, **T. Waltenspiel** *et al*, « Efficient ion re-acceleration in laboratory-produced interpenetrating collisionless shocks » (Article in the submission process to Nature).
- C.L.C. Lacoste, D. Oportus, J. Béard, S.N. Chen, I. Cohen, R. Lelièvre, **T. Waltenspiel** *et al*, « Investigation of laser plasma instabilities driven by coupled high-power laser beams in magnetized underdense plasmas » (Article in the submission process to Physics of Plasma).
- W. Yao, R. Lelièvre, I. Cohen, **T. Waltenspiel** *et al*, « Characterization and performance of the Apollon main short-pulse laser beam following its commissioning at 2 PW level », *Physics of Plasmas* 32 (April 2025). https://doi.org/10.1063/5.0252874
- W. Yao, R. Lelièvre, **T. Waltenspiel** *et al*, « Enhanced energy, conversion efficiency and collimation of protons driven by high-contrast and ultra-short laser pulses », *Applied Sciences*, 14(14) :6101 (July 2024). https://doi.org/10.3390/app14146101
- R. Lelièvre, W. Yao, **T. Waltenspiel** *et al*, « A comprehensive characterization of the neutron fields produced by the Apollon petawatt laser », *The European Physical Journal Plus,* 139,1035 (November 2024). https://doi.org/10.1140/epjp/s13360-024-05679-x

Étude en laboratoire des processus d'échange d'énergie particules-plasma magnétisé pertinents pour l'astrophysique

Résumé :

L'observation *in situ* dans l'espace d'interactions magnétiques et de processus d'énergisation des particules reste difficile avec les appareils en orbite autour de la Terre ou voyageant dans le Sytème Solaire. En effet, ces mécanismes sont rapides (à peine quelques heures pour les plus longs d'entre eux), très localisés spatialement et quasiment impossible à prédire. Par conséquent, l'essor de la technologie laser depuis le milieu du siècle dernier et le développement des lasers de haute puissance aujourd'hui disponibles nous permettent de recréer en laboratoire et à échelle réduite ces phénomènes survenant dans divers évènements et au sein de différents objects dans l'Univers. Ainsi, on se place dans le cadre de l'Astrophysique de laboratoire. Une caractéristique essentielle du champ magnétique en Astrophysique est la magnétisation spontanée des plasmas. En effet, l'effet Biermann battery, qui engendre la formation d'un champ magnétique auto-généré quand les conditions de densité et de température électronique sont réunies, permet la magnétisation d'un milieu sans requérir de sources externes de champ. Notre étude a été portée sur les interactions magnétiques se basant uniquement sur des plasmas magnétisés par cet effet. Le projet de thèse porte sur l'étude en laboratoire de deux processus d'interactions entre plasmas magnétisés : la compression magnétique et la reconnexion magnétique. Ces deux mécanismes, dont l'apparition dépend de l'orientation des champs magnétiques les uns par rapport aux autres, sont tous les deux les objets d'intenses recherches en raison de leur rôle présumé dans le chauffage prompt du plasma et l'énergisation des particules qui sont observés dans diverses situations astrophysiques, comme par exemple au sein des arches solaires ou lors d'interactions entre le vent solaire et le champ magnétique terrestre. Cette étude s'est focalisée sur des aspects caractéristiques de ces interactions magnétisées et de leur évolution, notamment la saturation du champ magnétique compressé par le phénomène de compression magnétique, ou la fragmentation de la couche de reconnexion due aux instabilités de déchirement y survenant. Nous avons développé une plateforme de laboratoire pour étudier en détail ces processus. Les travaux dans ce cadre s'appuient en partie sur des études antérieures pour affiner notre compréhension, mais aussi en introduisant de nouvelles spécificités, notamment liées à l'étude des champs magnétiques auto-générés par l'effet Biermann battery ou des configurations 3D qui s'écartent des topologies 2D idéalisées utilisées jusqu'à présent en laboratoire. De plus, aucune source extérieure de champ magnétique n'a été apportée, pour se placer dans des configurations similaires aux conditions astrophysiques. Avec ce projet, nous procurons de nouveaux outils de compréhension de ces phénomènes plasma qui, grâce à la combinaison de techniques accessibles aujourd'hui, deviennent accessibles à l'expérimentation en laboratoire. Ainsi, nous présentons de nouveaux résultats sur ces sujets très importants pour l'ensemble des questions de production de particules hautement énergétiques dans l'Univers.

Mots clés : Astrophysique - Physique des plasmas – Magnétisme - Laser

Investigating in the laboratory particle-magnetized plasma energy exchange processes relevant for astrophysics

Summary:

The direct *in situ* observation in space of magnetized plasma interactions and particle energy exchange processes remain difficult nowadays, even with space devices orbiting around Earth or traveling within the Solar System. Indeed, these mechanisms are succinct (lasting only a few hours at best), very spatially localized and it is almost impossible to predict them. As a consequence, the rise of laser technology since the middle of the XXth century that leads to the development of high power lasers that are available today enables to recreate these phenomena in the laboratory as they could occur in different spatial objects, but at reduced scales. This is the framework of Laboratory Astrophysics. One of the main characteristics of the magnetic field in Astrophysics is the spontaneous magnetization of plasmas. Indeed, the Biermann battery effect, which provocates the formation of a self-generated magnetic field when the required conditions on the electron density and temperature are met, permits the magnetization of a medium without external sources of field. Our study focused on the interactions between magnetic fields in plasmas that are only relying on the Biermann battery effect. Our project for this thesis was to study in the laboratory two of the main processes between magnetized plasmas: magnetic compression and magnetic reconnection. These two mechanisms, whose apparitions depend on the orientation of the involved magnetic fields toward each other, are both subjects of intense research as they are suspected of contributing to the heating of the plasma and to the energization of particles. These effects are observed in various astrophysical events, such as in solar arches or within the interaction between the solar wind and the Earth magnetosphere. Our study focused on the characteristic aspects of these magnetized processes and their evolution, detailing mechanisms such as the saturation of the compressed magnetic field during magnetic compression or the fragmentation of the reconnection sheet due to the apparition of inner tearing instabilities. We developed an experimental setup to investigate these two processes in the laboratory. Our work also relies partially on previous studies in order to detail our comprehension, but also introduces new specificities, most particularly about the study of interactions between Biermann battery self-generated magnetic fields or more complex 3D configurations, to go further than ideal 2D topologies that were already studied in the laboratory. Moreover, no external sources of magnetic field were used during our experimental campaigns, to get as close as possible to the astrophysical context and provide relevant results. With this work, we propose new means of comprehension about these plasma phenomena whose detailed studies become possible in the laboratory. Consequently, we present new results about these important topics for the overall question of the production of highly energetic particles in the Universe.

Keywords : Astrophysics - Plasma physics – Magnetism - Laser

Unité de recherche :

Centre pour l'Étude des Lasers Intenses et Applications, UMR 5107
Domaine du Haut – Carré Bâtiment C6 43, rue Pierre Noailles – 33405 Talence, France